Stochastic Geometry Perspective of Massive MIMO Systems

by

Priyabrata Parida

Dissertation submitted to the Faculty of the
Virginia Polytechnic Institute and State University
in partial fulfillment of the requirements for the degree of

Doctor of Philosophy
in
Electrical Engineering

Harpreet S. Dhillon, Chair
R. Michael Buehrer
Walid Saad
Yaling Yang
Xi Chen

August 9, 2021
Blacksburg, Virginia

Keywords: Stochastic geometry, massive MIMO, fractional pilot reuse, Poisson point process, Johnson-Mehl cells, cell-free massive MIMO, random sequential adsorption, binomial point process, spectrum sharing, Matérn hard core process.

Stochastic Geometry Perspective of Massive MIMO Systems

Priyabrata Parida

(ABSTRACT)

Owing to its ability to improve both spectral and energy efficiency of wireless networks, massive multiple-input multiple-output (mMIMO) has become one of the key enablers of the fifth-generation (5G) and beyond communication systems. For successful integration of this promising physical layer technique in the upcoming cellular standards, it is essential to have a comprehensive understanding of its network-level performance. Over the last decade, stochastic geometry has been instrumental in obtaining useful system design insights of wireless networks through accurate and tractable theoretical analysis. Hence, it is only natural to consider modeling and analyzing the mMIMO systems using appropriate statistical constructs from the stochastic geometry literature and gain insights for its future implementation.

With this broader objective in mind, we first focus on modeling a cellular mMIMO network that uses fractional pilot reuse to mitigate the sole performance-limiting factor of mMIMO networks, namely, pilot contamination. Leveraging constructs from the stochastic geometry literature, such as Johnson-Mehl cells, we derive analytical expressions for the uplink (UL) signal-to-interference-and-noise ratio (SINR) coverage probability and average spectral efficiency for a random user. From our system analysis, we present a partitioning rule for the number of pilot sequences to be reserved for the cell-center and cell-edge users that improves the average cell-edge user spectral efficiency while achieving similar cell-center user spectral efficiency with respect to unity pilot reuse. In addition, using the analytical approach developed for the cell-center user performance evaluation, we study the performance of a small cell system where user and base station (BS) locations are coupled. The impact of distance-dependent UL power control on the performance of an mMIMO network with unity pilot reuse is analyzed and subsequent system design guidelines are also presented.

Next, we focus on the performance analysis of the cell-free mMIMO network, which is a distributed implementation of the mMIMO system that leads to the second and third contributions of this dissertation. Similar to the cellular counterpart, the cell-free systems also suffer from pilot contamination due to the reuse of pilot sequences throughout the network. Inspired by a hardcore point process known as the random sequential adsorption (RSA) process, we develop a new distributed pilot assignment algorithm that mitigates the effect of pilot contamination by ensuring a minimum distance among the co-pilot users. This pilot assignment scheme leads to the construction of a new point process, namely the multilayer RSA process. We study the statistical properties of this point process both in one and two-dimensional spaces by deriving approximate but accurate expressions for the density and pair correlation functions. Leveraging these new results, for a cell-free network with the proposed RSA-based pilot assignment scheme, we present an analytical approach that determines the minimum number of pilots required to schedule a user with

probabilistic guarantees. In addition, to benchmark the performance of the RSA-based scheme, we propose two optimization-based centralized pilot allocation schemes using linear programming principles. Through extensive numerical simulations, we validate the efficacy of the distributed and scalable RSA-based pilot assignment scheme compared to the proposed centralized algorithms.

Apart from pilot contamination, another impediment to the performance of a cell-free mMIMO is limited fronthaul capacity between the baseband unit and the access points (APs). In our fourth contribution, using appropriate stochastic geometry-based tools, we model and analyze the downlink of such a network for two different implementation scenarios. In the first scenario, we consider a finite network where each AP serves all the users in the network. In the second scenario, we consider an infinite network where each user is served by a few nearby APs in order to limit the load on fronthaul links. From our analyses, we observe that for the finite network, the achievable average system sum-rate is a strictly quasi-concave function of the number of users in the network, which serves as a key guideline for scheduler design for such systems. Further, for the user-centric architecture, we observe that there exists an optimal number of serving APs that maximizes the average user rate.

The fifth and final contribution of this dissertation focuses on the potential improvement that is possible by the use of mMIMO in citizen broadband radio service (CBRS) spectrum sharing systems. As a first concrete step, we present comprehensive modeling and analysis of this system with omni-directional transmissions. Our model takes into account the key guidelines by the Federal Communications Commission for co-existence between licensed and unlicensed networks in the 3.5 GHz CBRS frequency band. Leveraging the properties of the Poisson hole process and Matérn hardcore point process of type II, a.k.a. ghost RSA process, we analytically characterize the impact of different system parameters on various performance metrics such as medium access probability, coverage probability, and area spectral efficiency. Further, we provide useful system design guidelines for successful co-existence between these networks. Building upon this omni-directional model, we also characterize the performance benefits of using mMIMO in such a spectrum sharing network.

Stochastic Geometry Perspective of Massive MIMO Systems

Priyabrata Parida

GENERAL AUDIENCE ABSTRACT

The emergence of cloud-based video and audio streaming services, online gaming platforms, instantaneous sharing of multimedia contents (e.g., photos, videos) through social networking platforms, and virtual collaborative workspace/meetings require the cellular communication networks to provide high data-rate as well as reliable and ubiquitous connectivity. These constantly evolving requirements can be met by designing a wireless network that harmoniously exploits the symbiotic co-existence among different types of cutting-edge wireless technologies. One such technology is massive multiple-input multiple-output (mMIMO), whose core idea is to equip the cellular base stations (BSs) with a large number of antennas that can be leveraged through appropriate signal processing algorithms to simultaneously accommodate multiple users with reduced network interference. For successful deployment of mMIMO in the upcoming cellular standards, i.e., fifth-generation (5G) and beyond systems, it is necessary to characterize its performance in a large-scale wireless network taking into account the inherent spatial randomness in the BS and user locations. To achieve this goal, in this dissertation, we propose different statistical methods for the performance analysis of mMIMO networks using tools from stochastic geometry, which is a field of mathematics related to the study of random patterns of points.

One of the major deployment issues of mMIMO systems is pilot contamination, which is a form of coherent network interference that degrades user performance. The main reason behind pilot contamination is the reuse of pilot sequences, which are a finite number of known signal waveforms used for channel estimation between a user and its serving BS. Further, the effect of pilot contamination is more severe for the cell-edge users, which are farther from their own BSs. An efficient scheme to mitigate the effect of pilot contamination is fractional pilot reuse (FPR). However, the efficiency of this scheme depends on the pilot partitioning rule that decides the fraction of total pilot sequences that should be used by the cell-edge users. Using appropriate statistical constructs from the stochastic geometry literature, such as Johnson-Mehl cells, we present a partitioning rule for efficient implementation of the FPR scheme in a cellular mMIMO network.

Next, we focus on the performance analysis of the cell-free mMIMO network. In contrast to the cellular network, where each user is served by a single BS, in a cell-free network each user can be served by multiple access points (APs), which have less complex hardware compared to a BS. Owing to this cooperative and distributed implementation, there are no cell-edge users. Similar to the cellular counterpart, the cell-free systems also suffer from pilot contamination due to the reuse of pilot sequences throughout the network. Inspired by a hardcore point process known as the random sequential adsorption (RSA) process, we develop a new distributed pilot assignment algorithm that mitigates the effect of pilot contamination by ensuring a minimum distance among the co-pilot users. Further, we show that the performance of this distributed pilot assignment scheme is appreciable compared

to different centralized pilot assignment schemes, which are algorithmically more complex and difficult to implement in a network. Moreover, this pilot assignment scheme leads to the construction of a new point process, namely the multilayer RSA process. We derive the statistical properties of this point process both in one and two-dimensional spaces.

Further, in a cell-free mMIMO network, the APs are connected to a centralized baseband unit (BBU) that performs the bulk of the signal processing operations through finite capacity links, such as fiber optic cables. Apart from pilot contamination, another implementational issue associated with the cell-free mMIMO systems is the finite capacity of fronthaul links that results in user performance degradation. Using appropriate stochastic geometry-based tools, we model and analyze this network for two different implementation scenarios. In the first scenario, we consider a finite network where each AP serves all the users in the network. In the second scenario, we consider an infinite network where each user is served by a few nearby APs. As a consequence of this *user-centric* implementation, for each user, the BBU only needs to communicate with fewer APs thereby reducing information load on fronthaul links. From our analyses, we propose key guidelines for the deployment of both types of scenarios.

The type of mMIMO systems that are discussed in this work will be operated in the sub-6 GHz frequency range of the electromagnetic spectrum. Owing to the limited availability of spectrum resources, usually, spectrum sharing is encouraged among different cellular operators in such bands. One such example is the citizen broadband radio service (CBRS) spectrum sharing systems proposed by the Federal Communications Commission (FCC). The final contribution of this dissertation focuses on the potential improvement that is possible by the use of mMIMO in the CBRS systems. As our first step, using tools from stochastic geometry, we model and analyze this system with a single antenna at the BSs. In our model, we take into account the key guidelines by the FCC for co-existence between licensed and unlicensed operators. Leveraging properties of the Poisson hole process and hardcore process, we provide useful theoretical expressions for different performance metrics such as medium access probability, coverage probability, and area spectral efficiency. These results are used to obtain system design guidelines for successful co-existence between these networks. We further highlight the potential improvement in the user performance with multiple antennas at the unlicensed BS.

Dedicated to my parents.

Acknowledgments

To begin with, I am eternally grateful to my advisor Dr. Harpreet S. Dhillon. While an advisor plays the most important role in a graduate student's professional life, Dr. Dhillon went beyond his responsibilities as an advisor to inspire me to complete this dissertation. His positive attitude is something that I aspire to emulate in every sphere of my life.

I am also thankful to my committee members Dr. Mike Buehrer, Dr. Walid Saad, Dr. Yaling Yang, Dr. Xi Chen for their valuable inputs at different stages of my Ph.D. I feel privileged to have taken the courses taught by Dr. Buehrer and Dr. Allen MacKenzie. In the future, if I get the opportunity to be in academia, I will look up to their teaching methodologies. I am grateful to the administrative staff at the Department of ECE and at Wireless@ VT, especially Hilda Reynolds, whose tireless efforts have made the journey of my graduate life easier. Apart from the regular Ph.D. curriculum, I have also learned a lot from my internship mentors. During these periods, I am grateful for having worked with Dr. Pavan Nuggehalli at MediaTeck Inc., Dr. Ramesh Palat and Dr. Dilip Bethanabhotla at Blue Danube Systems.

I would also like to thank my lab mates and friends at Wireless@VT, especially Mohammad (Mozaffari), Mustafa, Mehrnaz, Chiranjib, Vishnu, Kartheek, Praful, Raghu, Chris, (Sundar) Aditya, Tengchan, Akshay, Morteza, Mohamed (Abd-Elmagid), Anish, and Keerthana. I will always cherish the numerous technical as well as light-hearted discussions that we had in and outside of the lab. I am also grateful to my friends at Blacksburg: Ishan, Suvankar, Bidisha, Mehdi, Haroun, Vikram, and Anshul. My life at Blacksburg would have been extremely monotonous without their presence.

I am very grateful to my brother, whose periodic visits to Blacksburg were something I always looked forward to. Finally, I express my heartfelt gratitude to my parents whose scarifies throughout their lives have helped both me and my brother to be the persons that we are.

Contents

List of Figures

List of Tables

Chapter 1

Introduction

With the emergence of cloud-based streaming services, the ubiquity of handheld wireless devices, and the desire to make the world more connected, the pursuit of higher throughput seems never-ending. Moreover, the job of a wireless engineer has only become more difficult as current and future wireless systems need to provide not only higher throughput but also reliable ubiquitous coverage, uniform user experience, ultra-low latencies, better energy efficiency, and secure communication links to name a few. These requirements are usually conflicting in nature and need to be achieved by multiplexing a multitude of physical layer technologies and designing the network that exploits the symbiotic relationships among them. At the forefront of these technologies is massive multi-input-multi-output (mMIMO) that facilitates many-fold improvement in spectral efficiency (`SE`), energy efficiency, and reliability in communication links, especially in the sub-6 GHz spectrum, which has the preferred frequency bands for mMIMO implementation. These attractive attributes of mMIMO have propelled it to be a part of fifth-generation new radio (5G NR) standards. However, this is not the end of the story for mMIMO rather the end of the beginning as there lie myriads of challenges that need to be overcome for its successful integration into the future wireless networks [1].

1.1 Background

Fundamentally, mMIMO is an extension of the conventional multi-user MIMO technique, where a large number of antennas at the BSs simultaneously serve an order of magnitude less number of users than the antennas. The promise of this technology lies in the fact that under ideal conditions it eliminates the deleterious effect of channel fading and additive noise while negating the effect of network interference using simple-to-implement linear beamforming schemes [2, 3, 4]. The availability of accurate channel state information (CSI) at the BSs is indispensable to perform beamforming/filtering operations. Since the number of antennas in the network is much larger than the number of users, the usual approach is to estimate the channel in the uplink through a set of orthogonal pilot sequences. Due to the limited channel coherence interval, the number of orthogonal sequences is limited. As a result, the pilot sequences need to be spatially reused throughout the network. In his seminal work [2], Marzetta showed that using low-complexity but suboptimal linear processing schemes, such as maximal ratio combining (MRC), the reuse of pilot sequences gives rise to an inherent

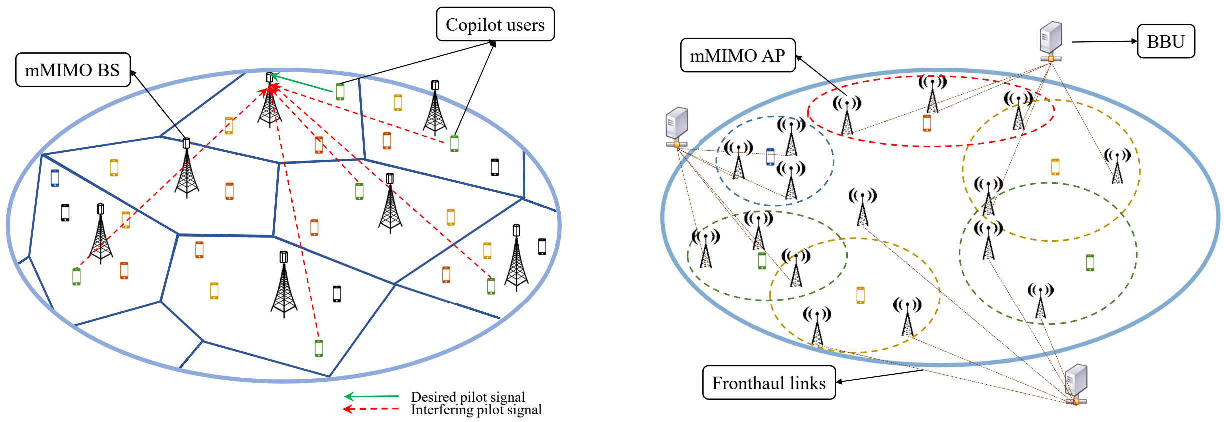

Figure 1.1: Two different architectures of mMIMO networks: the cellular architecture (left), the cell-free architecture (right).

interference known as *pilot contamination*, which fundamentally limits the performance of mMIMO networks. Further, in a cellular architecture (Fig. 1.1 (left)), where BSs do not cooperate and transmit only to their associated users, the impact of pilot contamination is more severe for the cell-edge users compared to the cell-center users. A promising approach to overcome this disparate user experience is by deploying mMIMO in a distributed manner as envisioned in the form of cell-free mMIMO [5, 6]. In the cell-free architecture (Fig. 1.1 (right)), a large number of geographically separated access points (APs), which are centrally controlled by baseband units (BBUs) through finite capacity fronthaul links, serve users in the network. This form of implementation eliminates the concept of cell-edge due to cooperation among APs that results in a uniform user experience throughout the network. Although cell-free mMIMO can be interpreted as an incarnation of the cooperative communications concept, along the same lines as coordinated multipoint (CoMP) and cloud radio access network (C-RAN), it is different from these technologies from an operational point of view. While in CoMP the cooperation is performed among a limited set of existing BSs in a cellular network, in C-RAN all the APs in the network are connected to a "cloud" based processor that performs all the baseband operation including joint precoding or decoding of the data. Such implementations are not *scalable* owing to the overwhelming amount of data and CSI sharing among the BSs or the APs and the cloud processor. On the other hand, in a cell-free mMIMO network, each AP (possibly with multiple antennas) performs beamforming/filtering operation using locally available CSI and forwards the I-Q symbols to the BBU that performs the rest of the baseband operations. Although this functional split is necessary, it is not sufficient to guarantee a scalable implementation especially when the numbers of APs and users in the network grow. Moreover, in the limiting case of the number of antennas per unit area, pilot contamination becomes one of the performance-limiting factors of the cell-free mMIMO network as well.

From the above discussion, it is immediately clear that the successful integration of both the architectures of mMIMO in upcoming cellular networks requires a comprehensive understanding of how pilot contamination affects network performance and what are the effective ways to mitigate it. Further, as scalable implementation is a priority for cell-free architecture, it is imperative to understand the impact of the fronthaul link capacity constraints on system performance as the network size grows and provide useful guidelines for network dimensioning to enable scalable implementation. Additionally, the flavors of mMIMO that are discussed in this dissertation are from the perspective of a network that operates in the sub-6 GHz spectrum. Since the available spectrum in these frequency bands is scarce, spectrum sharing is encouraged. One such example is the proposal by the Federal Communications Commission (FCC) under the banner of citizen broadband radio service (CBRS) at the 3.5 GHz frequency range. The proposal encourages co-existence between licensed and unlicensed networks along with important deployment guidelines. It is imperative to understand the improvement that can be obtained over omni-directional transmission if the spectrum sharing entities employ mMIMO and if there lie any associated trade-offs that must be taken into account during the deployment phase.

Although one can study the different types of mMIMO networks through extensive system simulations and answer the questions highlighted in the previous paragraph, these large networks simulations do not have a favorable computational scaling. A useful complementary approach is to contain the curse of dimensionality by modeling the node locations with certain spatial distribution rather than assuming them to be deterministic. This allows one to conveniently compute network-wide metrics by spatially averaging over all possible topologies using powerful tools from stochastic geometry and, in certain cases, obtain tractable theoretical expressions that result in useful insights. Stochastic geometry has already been applied successfully to analyze different types of cellular networks over the last decade [7, 8, 9, 10, 11, 12, 13]. Hence, following the natural course, in this dissertation, we discover useful stochastic-geometry constructs in the literature that can be leveraged to model, analyze, and provide implementation guidelines for mMIMO networks.

1.2 Selected prior works

Pilot contamination mitigation in cellular architecture: To address the issue of pilot contamination in a cellular mMIMO, a number of works have focused on pilot contamination suppression or mitigation methods that can be categorized into protocol-based methods [14], base station (BS) coordination based methods [15, 16], and pilot reuse or hopping based methods [17, 18]. While protocol and coordination-based methods are effective in removing the pilot contamination, they are usually complex and require a higher degree of coordination among BSs. On the other hand, the gains obtained by pilot hopping-based methods are limited to scenarios with larger channel coherence times. Another promising method to reduce the pilot contamination is to have orthogonal pilot sequences in neighboring cells following a certain reuse factor. This is similar to frequency reuse in traditional cellular networks. However, this scheme usually results in `SE` degradation compared to unity reuse, where all the available pilot sequences are reused in each cell of the network. A pilot reuse scheme that partially inherits the benefits of fully orthogonal pilot reuse and unit reuse is fractional pilot reuse (FPR). This scheme is more attractive due to its distributed and lower complexity implementation [19]. The goal of the FPR scheme is to improve the performance of the cell-edge users, which are more severely impacted by pilot contamination compared to the cell-center users, at a minimal reduction in overall system throughput compared to the unity pilot reuse. However, one of the important questions to answer to achieve the above goal is how to partition the set of available pilots for cell-center and cell-edge users. To reliably answer this question, we need to consider a large-scale multi-cellular setup so that the effect of pilot contamination can be accurately captured. In Chapter 2 of this dissertation, using the desired set of tools from the stochastic geometry literature, we answer the aforementioned question of pilot partitioning.

Pilot contamination mitigation in cell-free architecture: The pilot contamination mitigation methods for cell-free mMIMO is a completely different challenge owing to different network architecture. In this case, the optimal pilot assignment is non-deterministic polynomial-time (NP)-hard in nature. Therefore, all the works in the literature focus on heuristics-based algorithms, such as random pilot allocation [5] and random access type pilot assignment [20], which are distributed in nature. Various centralized pilot allocation schemes based on graph coloring [21, 22], K-means clustering [23], and meta-heuristics [24] are also available in the literature. While the distributed random pilot allocation schemes are inferior in performance compared to the centralized schemes, the centralized schemes suffer from a lack of scalability, which is an important aspect of cell-free architecture. In Chapter 6, we propose a distributed scalable pilot assignment scheme that is inspired by the random sequential adsorption (RSA) process. As a consequence of the above pilot assignment scheme, we construct a new point process, which is a variant of the multilayer RSA process studied in the statistical physics literature [25, 26, 27, 28, 29]. To facilitate the theoretical evaluation of different performance metrics, such as pilot assignment probability and network interference, in a cell-free mMIMO system, statistical characterization of the new multilayer RSA process is necessary. Chapter 5 of the dissertation is dedicated to deriving and understanding the statistical properties related to the multilayer RSA process that are used in Chapter 6 to derive useful theoretical results for cell-free mMIMO systems.

Impact of limited fronthaul capacity in cell-free mMIMO: Apart from pilot contamination, another performance-limiting factor of cell-free mMIMO is the finite fronthaul capacity that introduces compression/quantization error into the system. The performance of such networks are presented in [30, 31, 32, 33, 34, 35, 36, 37]. In [30, 31, 32, 34] authors present the uplink (UL) performance of cell-free mMIMO with finite fronthaul capacity. In [35], the authors study the performance of a cell-free network with hardware impairments where the authors compare the performance of three transmission strategies between the BBU and the APs through finite capacity links. The UL and downlink (DL) performances of fronthaul constrained cell-free network with low resolutions ADCs are presented in [36]. Note that most of these works focus on *traditional* cell-free architecture where all the APs serve every user in the network. Since the user performance degrades with quantization/-compression error, which depends on the number of users (load) per AP, each AP should serve a subset of users in the network. A network-centric approach that achieves this goal is proposed [31, 34]. However, from the scalability perspective, a *user-centric* architecture is preferred [38, 39, 40, 20, 41, 42, 37] where a user selects its set of serving APs. Further, a user-centric approach can also be implemented in a distributed manner. However, in the literature, there are few works on the DL performance of the user-centric cell-free architecture with finite fronthaul capacity. In Chapter 7, using tools from stochastic geometry along with a spatial construct related to bipartite random geometric graphs, we analyze the DL performance of user-centric cell-free mMIMO systems.

Spectrum sharing in the CBRS band: As mentioned earlier, one of our objectives is to evaluate the benefits of using mMIMO in a sub-6 GHz spectrum sharing environment such as the citizen broadband radio service (CBRS) system. To characterize the performance benefits, we first need a holistic view of the system performance taking into account the main FCC guidelines, such as protection zones around licensed BSs where unlicensed BSs cannot operate, a spectrum sensing, and contention-based channel access mechanism by the unlicensed BSs. While in the literature, networks with contention-based channel access are modeled using Matérn hardcore process of type-II (MHPP-II) [43, 44, 45, 46], a completely new point process is necessary to model the CBRS networks (to accurately capture the unique implementation guidelines by FCC). In Chapter 8, we present a modified MHPP-II process that is obtained from a parent Poisson hole process (PHP) to model and subsequently analyze the CBRS network.

1.3 Contributions

Using tools from stochastic geometry along with scenario specific spatial constructs, we model, analyze, and optimize the cellular mMIMO, the cell-free mMIMO, and the CBRS spectrum sharing networks in this dissertation. The main contributions are summarized below.

1.3.1 Pilot contamination mitigation in cellular mMIMO

In Chapter 2, we analyze the performance of the UL of an mMIMO network considering an asymptotically large number of antennas at the BSs. We model the locations of the BSs as a homogeneous Poisson point process (PPP) and assume that their service regions are limited to their respective Poisson-Voronoi cells (PVCs). Further, for each PVC, based on a threshold radius, we model the cell-center region as the Johnson-Mehl (JM) cell of its BS while the rest of the PVC is deemed as the cell-edge region. We consider the FPR scheme where two different sets of pilot sequences are used for the cell-center and the cell-edge users. For the above system model, we derive analytical expressions for the UL signal-to-interferene-plus-noise ratio (SINR) coverage probability and average SE for randomly selected cell-center and cell-edge users. In addition, we present an approximate expression for the average cell SE. One of the key intermediate results in our analysis is the approximate but accurate characterization of the distributions of the cell-center area, i.e., the typical JM cell area, and the cell-edge area of a typical cell. Another key intermediate step is the accurate characterization of the pair correlation functions (PCF) of the point processes formed by the interfering cell-center and cell-edge users that subsequently enables the coverage probability analysis. From our system analysis, we present a partitioning rule for the number of pilot sequences to be used for cell-center and cell-edge users as a function of the threshold radius that improves the average cell-edge user SE while achieving similar cell-center user SE with respect to unity pilot reuse.

It is worth mentioning that the usefulness of the JM cell goes beyond modeling the mMIMO system with FPR. The analytical methods developed for performance evaluation of a cell-center user are also applicable to model and analyze the performance of a cellular system with coupled user and BS locations where the users are clustered around each BS. The results of this study are presented in Chapter 3. In the above system model for FPR, we do not consider UL power control by the users. Since UL power control is usually desirable in a cellular network, in Chapter 4, for the UL of an mMIMO network with unity reuse, we introduce a new approach based on the application of the displacement theorem involving a PPP to capture the effect of distance-dependent power control by the users. This result can help analyze the soft pilot reuse (SPR) in an mMIMO network.

1.3.2 Pilot contamination mitigation in cell-free mMIMO

One of our key observations from the works in the literature that deal with pilot contamination mitigation in cell-free mMIMO is the co-pilot users in the network should have spatial separation that is reminiscent of the repulsive point processes in the stochastic geometry literature. One such point process is the RSA process where the points have a certain minimum distance among themselves. Hence, the algorithm that generates RSA process from a set up PPP distributed points can be modified as a pilot allocation algorithm. While coming up with the algorithm is relatively straightforward, the most challenging part is to understand the statistical properties of this new multilayer RSA process, where each layer belongs to a set of co-pilot users.

Statistical characterization of multilayer RSA process

In Chapter 5, we focus on the statistical characterization of the multilayer RSA process. Our goal is to obtain the first-order statistic, namely the time-varying density. As our first step, we focus on the one dimensional (1D) version of the problem, where the deposition of overlapping rods on a line is allowed only if they are assigned two different colors, where colors are symbolic of orthogonal resources, such as frequency bands, in communication networks. Owing to a strong spatial coupling among the deposited rods of different colors, finding an exact solution for the density of deposited rods of a given color as a function of time seems intractable. Hence, we propose two useful approximations to obtain the time-varying density of rods of a given color. The first approximation is based on the recursive use of the known monolayer RSA result for the indirect estimation of the density of rods for the multilayer version. The second approximation, which is more accurate but computationally intensive, involves accurate characterization of the time evolution of the gap density function. This gap density function is subsequently used to estimate the density of rods of a given color. To solve the more relevant two-dimensional (2D) version of this problem, we extend the first approximation approach developed for the 1D case to estimate the time-varying density of deposited circles of a given color as a function of time.

Pilot assignment schemes for cell-free mMIMO systems

In Chapter 6, we address the problem of pilot assignment for a cell-free mMIMO system to reduce the effect of pilot contamination. Owing to the prohibitive complexity to get an optimal solution, we focus on devising an efficient heuristic algorithm with a potential scalable distributed implementation. Our first algorithm, which is inspired by the RSA process, achieves this objective while ensuring that a minimum distance is maintained among the co-pilot users to limit the effect of pilot contamination. Leveraging the results of Chapter 5, we present an analytical approach to obtain the density of the co-pilot users. One of our key results is the accurate characterization of the probability of the event that a pilot assigned to a typical user in the network. In addition, to benchmark the performance of the RSA-based scheme, we propose two optimization-based centralized pilot allocation schemes. The first centralized scheme, similar to the RSA-based scheme, only considers the user locations during the decision-making process. This algorithm, namely the max-min distance-based algorithm, partitions the set of users to maximize the minimum distance between two users in a partition (a set of co-pilot users). On the other hand, the second centralized algorithm takes both user and AP locations into account and provides a near-optimal solution in terms of sum-user `SE` with the application of the branch-and-price algorithm. Through extensive system simulations, we observe that the scalable RSA-based pilot assignment provides competitive performance in terms of user `SE` compared to the max-min distance-based algorithm. Further, both the RSA and the max-min distance-based schemes perform as good as the near-optimal scheme as the density of APs increases.

1.3.3 Impact of fronthaul capacity in cell-free mMIMO network

Apart from pilot allocation, one of the important problems related to cell-free mMIMO is studying the impact of limited fronthaul capacity on system performance. In Chapter 7, we analyze the performance of the DL of a cell-free mMIMO system considering finite capacity fronthaul links. Conditioned on the user and AP locations, we first derive an achievable rate for a randomly selected user in the network that captures the effect of finite fronthaul capacity in terms of compression error. From this expression, we establish that for the traditional cell-free architecture where each AP serves all the users in the network the achievable rate becomes zero as the network size grows. Hence, to have a meaningful system analysis, we present the performance of the traditional cell-free architecture over a finite region. To be specific, we model the user and AP locations as two independent binomial point processes (BPPs) and provide an accurate theoretical result to determine the user rate coverage. To reduce the load on fronthaul link for a larger (possibly infinite) network, we consider a user-centric architecture where each user in the network is served by a specified number of nearest APs. For this architecture, we model the AP and user locations as two independent PPPs. Since the rate expression is a function of the number of users served by an AP, we need to statistically characterize the load in terms of the number of users per AP. This problem is equivalent to determine the degree distribution of a bipartite random geometric graph. As the exact derivation of the probability mass function (PMFs) of the load is intractable, we first present the exact expressions for the first two moments of the load. Next, we approximate the load as a negative binomial random variable whose parameters are obtained through the moment matching method. Next, using the derived load results and appropriate tools from stochastic geometry along with a few subtle approximations, we present an accurate theoretical expression to determine the rate coverage of the typical user. From our system analyses, for the traditional architecture, we conclude that the average system sum-rate is a quasi-concave function of the number of users in the finite network. Further, for the user-centric architecture, we observe that there exists an optimal number of serving APs that maximizes the average user rate.

1.3.4 Modeling and analysis of CBRS spectrum sharing system

Since the mMIMO networks discussed in this dissertation are for sub-6 GHz spectrum range, in the near future, these networks can co-exists by spectrum sharing, especially in the under-utilized CBRS band. In Chapter 8, we model and analyze a cellular network that operates in the licensed band of the 3.5 GHz spectrum and consists of a licensed and an unlicensed operators. Using tools from stochastic geometry, we concretely characterize the performance of this spectrum sharing system. We model the locations of the licensed BSs as a homogeneous PPP with protection zones around each BS. Since the unlicensed BSs can not operate within the protection zones, their locations are modeled as a PHP. In addition, we consider carrier sense multiple access with collision avoidance type contention-based channel access mechanism for the unlicensed BSs. For this setup, we first derive an approximate expression and useful lower bounds for the medium access probability of the serving unlicensed operator BS. Further, by efficiently handling the correlation in the interference powers induced due to correlation in the locations of the licensed and unlicensed BSs, we provide approximate expressions for the coverage probability of a typical user of each operator. Subsequently, we study the effect of different system parameters on area `SE` of the network. We have also presented the intial result on the improvement in system performance due to MIMO-enabled BSs at the unlicensed operators.

List of Publications

The dissertation has led to following journal papers:

1. **P. Parida** and H. S. Dhillon, "A Stochastic Geometry-based Analysis of Cell-Free Massive MIMO with Finite Fronthaul Capacity", submitted.
2. **P. Parida** and H. S. Dhillon, "Multilayer Random Sequential Adsorption", submitted.
3. **P. Parida** and H. S. Dhillon, "Modeling and Analysis of CSMA Networks using Random Sequential Adsorption Process", submitted.
4. **P. Parida** and H. S. Dhillon, "Pilot Allocation Schemes for Cell-Free Massive MIMO Systems", submitted.
5. **P. Parida** and H. S. Dhillon, "Stochastic Geometry-based Uplink Analysis of Massive MIMO Systems with Fractional Pilot Reuse", *IEEE Transactions on Wireless Communications*, vol. 18, no. 3, pp. 1651-1668, Mar. 2019.
6. **P. Parida**, H. S. Dhillon, and P. Nuggehalli, "Stochastic Geometry-based Modeling and Analysis of Citizens Broadband Radio Service System", *IEEE Access*, vol. 5, pp. 7326-7349, 2017.
7. P. D. Mankar, **P. Parida**, H. S. Dhillon, M. Haenggi, "Distance from the Nucleus to a Uniformly Random Point in the 0-Cell and the Typical Cell of the Poisson-Voronoi Tessellation", *Journal of Statistical Physics*, vol. 181, no. 5, pp. 1678-1698, Dec. 2020.
8. P. D. Mankar, **P. Parida**, H. S. Dhillon and M. Haenggi, "Downlink Analysis for the Typical Cell in Poisson Cellular Networks", *IEEE Wireless Communications Letters*, vol. 9, no. 3, pp. 336-339, Mar. 2020.

The dissertation has led to following conference papers:

1. **P. Parida** and H. S. Dhillon, "Random Sequential Adsorption-based Pilot Assignment for Distributed Massive MIMO Systems", in *Proc. IEEE Globecom*, Waikoloa, HI, Dec. 2019.

2. **P. Parida**, H. S. Dhillon, and A. F. Molisch, "Downlink Performance Analysis of Cell-Free Massive MIMO with Finite Fronthaul Capacity", in *Proc. IEEE VTC (Fall)*, Chicago, IL, Aug 2018.

3. **P. Parida** and H. S. Dhillon, "Johnson-Mehl Cell based Analysis of UL Cellular Network with Coupled User and BS Locations", in *Proc. IEEE ICC*, Kansas City, MO, May 2018.

4. **P. Parida** and H. S. Dhillon, "New Stochastic Geometry-based Analysis of Uplink Massive MIMO in Asymptotic Antenna Regime", in *Proc. IEEE WCNC*, San Francisco, CA, March 2017.

5. **P. Parida**, H. S. Dhillon and P. Nuggehalli, "Stochastic Geometry Perspective of Unlicensed Operator in a CBRS System", in *Proc. IEEE WCNC Workshops*, San Francisco, CA, March 2017.

Chapter 2

Stochastic Geometry-based Uplink Analysis of Massive MIMO Systems with Fractional Pilot Reuse

2.1 Introduction

In this chapter, we focus on a cellular mMIMO system with asymptotically large number of antennas at the BSs. As shown in the seminal work by Marzetta [2], under the assumption of independent and identically distributed (i.i.d.) Rayleigh fading across BS antennas and sub-optimal low-complexity processing schemes such as maximal ratio combining (MRC), the reuse of pilot sequences gives rise to an inherent interference known as *pilot contamination* (PC), which fundamentally limits the performance of mMIMO networks. As discussed next in detail, a significant amount of research effort has been focused on overcoming the effect of PC. Amongst all the solutions, a relatively simple scheme, namely fractional pilot reuse (FPR), stands out in reducing the effect of PC for the cell-edge (CE) users. In this chapter, our objective is to analyze the performance of a mMIMO network that uses the FPR scheme leveraging tools from stochastic geometry.

2.1.1 Motivation and related works

In the literature, PC suppression or mitigation methods can be broadly categorized into protocol based methods [14], BS coordination based methods [15, 16], and pilot reuse or hopping based methods [17, 18]. Please refer to [47] for a comprehensive survey on this subject. While protocol and coordination based methods are effective in removing the PC, they are usually complex. Further, these techniques require some degree of coordination among BSs. On the other hand, the gains obtained by pilot hopping based methods is primarily due to interference randomization and is hence limited to scenarios with larger channel coherence times. In contrast, a low complexity and distributed scheme to counter the effect of PC is to forbid reusing the same pilots in every cell, which requires no coordination among BSs [48, 49]. The concept of pilot reuse is similar to the frequency reuse in cellular networks. In [48], the optimal pilot reuse factor is obtained for a network with linear topology. From the numerical simulations, authors show that higher than unity pilot reuse factor is beneficial for average cell throughput. In [49], for a hexagonal cellular network model, authors show that reuse-1 may not be optimal in all scenarios. These works considered the use of completely orthogonal sets of pilots in neighboring cells. However, the spectral efficiency (SE) can be further improved by using a more aggressive pilot reuse scheme, namely FPR, instead of completely orthogonal reuse across cells. Conceptually, FPR is similar to that of fractional frequency reuse (FFR) used in LTE systems to mitigate the effect of inter-cell interference. To the best of the knowledge of the authors, the concept of FPR was first introduced in [19]. In FPR, similar to FFR, depending on the channel condition, users in a cell are classified into two categories, namely cell-center (CC) and CE users. While the set of pilots reserved for CC users are reused in every cell, the set of pilots for CE users are reused in specific cells depending upon the reuse factor.

For the performance analysis of mMIMO systems with FPR, it is imperative to consider a large-scale multi-cell setup so that the effect of interference on the performance can be accurately modeled. For such problems, stochastic geometry provides a rigorous set of tools for the spatial modeling and performance analysis, as discussed in detail in [12, 50]. For a pedagogical treatment of the subject with emphasis on the application to cellular network, interested readers are advised to refer to [12]. Although stochastic geometry has been used for the performance analysis of mMIMO systems in [51, 52, 53, 54, 55, 56, 57, 58, 59, 60], the analyses presented in these works cannot be trivially extended to analyze the FPR scheme. To begin with, in contrast to our network topology, in [60] a cooperative mMIMO network is considered. In [51, 52, 53, 54, 55, 56, 57], where a cellular topology is considered, the UL interference field generated by the users from unity pilot reuse scheme is different from the FPR scheme. Further, the analyses [52, 53, 54, 55, 56, 57] are limited to the consideration of a fixed number of users in each BS which does not take into account the varying load (number of users) in each cell. In this work, we propose a new approach to analyze the performance of a cellular mMIMO network considering FPR scheme that results in the following key contributions.

2.1.2 Contributions of the work

Analytical model for UL analysis of a mMIMO system with FPR

A new generative model is proposed to analyze the performance of the UL of a mMIMO system in the asymptotic antenna regime under the consideration of FPR scheme. We model the BS locations as a PPP. Based on a threshold distance R_c, we characterize the CC regions as the Johnson-Mehl (JM) cells associated with the BSs. The complementary region in each cell is modeled as the CE region. One important result in our analyses is the approximate but accurate distribution functions for the CC and CE areas of a typical Poisson-Voronoi Cell (PVC). These results are subsequently used to model the load (number of CC and CE users) distribution of each cell. Using these distributions, we provide key intermediate results, such as the pilot assignment probability to a randomly selected CC (CE) user and utilization probability of a pilot. These results are later used in the coverage probability and SE analyses.

SINR coverage, average user and cell SEs analysis

We present SINR coverage probability of a user assigned to a given CC (CE) pilot. The derivation of exact probability is difficult as the exact statistical characterization of the interference field is extremely challenging. In fact, derivation of this result for a relatively simpler scenario of the classical UL system, where the segregation between CC and CE users is not present, is also intractable. Hence, to lend tractability to this problem, we resort to a careful approximation of the interference statistics in the UL. Motivated by [61], first, we derive the pair correlation function (PCF) of the interfering user locations with respect to (w.r.t.) the BS of interest. Using this PCF, we approximate the point process formed by the CC (CE) interfering users as a non-homogeneous PPP. Next, based on the *dominant interferer* based approach, we provide useful theoretical expressions for the coverage probability of a user assigned to a CC (CE) pilot. This result is extended to obtain analytical expressions for the average SEs of a randomly selected CC (CE) user and average SE of a typical cell.

System design guidelines

Our analysis leads to following system design guidelines. First, our analyses show that for a certain range of threshold radius by allocating $1 - \exp(-c_2\pi\lambda_0 R_c^2)$, where λ_0 is the BS density and c_2 is a constant, fraction of pilots for the CC users, FPR scheme improves the average SE of a CE user with marginal reduction in the average SE of a CC user compared to unity reuse. Second, for a given threshold radius, it is possible to achieve higher average cell SE using FPR scheme compared to unity reuse by a suitable partitioning (different from the aforementioned rule) of the set of the pilots. Third, the coverage probability of a user on a CE pilot decreases with increasing R_c in the higher SINR regime, however, the reverse trend is observed for the lower SINR regime.

2.2 System model

2.2.1 Network model

BS and user locations

In this work, we analyze the UL performance of a cellular network where each BS is equipped with $M \to \infty$ antennas. The locations of the BSs belong to the set $\Psi_b = \Phi_b \cup \{\mathbf{o}\}$, where $\mathbf{o}$

represents the origin, and Φ_b is a realization of homogeneous PPP of density λ_0. In this work, we present our analysis condition on the location of the BS at $\mathbf{o}$. By virtue of Slivnyak's theorem, the reduced palm measure of Ψ_b is equal to the original measure of Φ_b [10]. The location of the j-th BS is denoted by $\mathbf{b}_j \in \Psi_b$, where the index j does not represent any ordering and $\mathbf{b}_0 = \mathbf{o}$. In a cell, the region that is within a distance R_c from its BS is defined as the CC region. For the typical cell at the origin (referred to as 0-th cell hereafter), the CC region is given as

$$\mathcal{X}_C(\mathbf{o}, R_c, \Psi_b) = \{\mathbf{x} \in \mathcal{V}_{\Psi_b}(\mathbf{o}) : \|\mathbf{x}\| \leq R_c\} = \mathcal{V}_{\Psi_b}(\mathbf{o}) \cap \mathcal{B}_{R_c}(\mathbf{o}), \tag{2.1}$$

where $\mathcal{V}_{\Psi_b}(\mathbf{o}) = \{\mathbf{x} \in \mathbb{R}^2 : \|\mathbf{x}\| \leq \|\mathbf{x} - \mathbf{b}_j\|, \forall \mathbf{b}_j \in \Psi_b\}$ is the PVC associated with $\mathbf{b}_0$ and $\mathcal{B}_{R_c}(\mathbf{o})$ denotes a ball of radius R_c centered at $\mathbf{o}$. Note that the CC regions are equivalent to the JM cells associated with the BSs [62]. These JM cells are usually defined from the perspective of random nucleation and growth process. However, we follow (3.2) for simpler exposition. The region of the cell that is beyond R_c from the BS is the CE region and is given as

$$\mathcal{X}_E(\mathbf{o}, R_c, \Psi_b) = \{\mathbf{x} \in \mathcal{V}_{\Psi_b}(\mathbf{o}) : \|\mathbf{x}\| > R_c\} = \mathcal{V}_{\Psi_b}(\mathbf{o}) \cap \mathcal{B}^C_{R_c}(\mathbf{o}). \tag{2.2}$$

The locations of the CC and CE users attached to the j-th BS are uniformly and randomly distributed within $\mathcal{X}_C(\mathbf{b}_j, R_c, \Psi_b)$ and $\mathcal{X}_E(\mathbf{b}_j, R_c, \Psi_b)$, respectively. We denote the CC area of the j-th cell as $X_{Cj}(\lambda_0, R_c) = |\mathcal{X}_C(\mathbf{b}_j, R_c, \Psi_b)|$ and the CE area as $X_{Ej}(\lambda_0, R_c) = |\mathcal{X}_E(\mathbf{b}_j, R_c, \Psi_b)|$. If the typical cell does not have a CE region, then $\mathcal{X}_E(\mathbf{b}_j, R_c, \Psi_b) = \varnothing$ and $X_{Ej}(\lambda_0, R_c) = 0$. Let N_{Cj} and N_{Ej} be the numbers of CC and CE users present in the j-th cell. We assume that both the random variables N_{Cj} and N_{Ej} follow zero-truncated Poisson distribution with parameters $\lambda_u X_{Cj}(\lambda_0, R_c)$ and $\lambda_u X_{Ej}(\lambda_0, R_c)$, respectively. Accordingly, conditioned on the CC (CE) area of the j-th cell, the `PMF`s of N_{Cj} and N_{Ej} for $n > 0$ are given as

$$\begin{aligned}\mathbb{P}\left[N_{Cj} = n | x_{cj}\right] &= \frac{e^{-\lambda_u x_{cj}} (\lambda_u x_{cj})^n}{n!(1 - e^{-\lambda_u x_{cj}})},\\ \mathbb{P}\left[N_{Ej} = n | x_{ej}, \mathcal{E}_3^C\right] &= \frac{e^{-\lambda_u x_{ej}} (\lambda_u x_{ej})^n}{n!(1 - e^{-\lambda_u x_{ej}})},\end{aligned} \tag{2.3}$$

where $\mathcal{E}_3^C$ is the event that the j-th cell has a CE region and is defined in Section 2.3, x_{cj} and x_{ej} are the realizations of the CC and CE areas [1]. The main motivation behind consideration of the truncated Poisson distribution for users is to ensure that each BS in the network has at least one CC and CE user within its Voronoi cell. Since mMIMO will be primarily used for macro cells, from the system perspective, this is a reasonable assumption. Further, this allows us to model the user point process (to be defined shortly) as a Type-I

[1]Throughout this manuscript, we have represented a random variable in capital letter and its realization in small letter.

process introduced in [61] facilitating a rigorous system analysis from the perspective of a typical cell. Note that λ_u is used to vary the load (number of users) in a cell.

Let us define a point process $\Psi_{\mathtt{u,CC}}$ that is constructed by randomly and uniformly distributing one point in the CC region of each cell. Mathematically, this can be expressed as

$$\Psi_{\mathtt{u,CC}} = \{U(\mathcal{X}_C(\mathbf{b}_j, R_c, \Psi_b)) : \forall \mathbf{b}_j \in \Psi_b\},$$

where $U(B)$ denotes a uniformly distributed point in $B \subset \mathbb{R}^2$. On the other hand, let Ψ_{bE} denote the set of BSs having a CE region that is defined as $\Psi_{bE} = \{\mathbf{b}_j : \forall \mathbf{b}_j \in \Psi_b, \mathcal{X}_E(\mathbf{b}_j, R_c, \Psi_b) \neq \varnothing\}$. Now, for the CE case we define the point process $\Psi_{\mathtt{u,CE}} = \{U(\mathcal{X}_E(\mathbf{b}_j, R_c, \Psi_b)) : \forall \mathbf{b}_j \in \Psi_{bE}\}$. Except the users attached to the BS at $\mathbf{o}$, rest of the users in the network belong to the interfering cells. Let the CC and CE point processes formed by the points in the interfering cells be

$$\Phi_{\mathtt{u,CC}} = \{U(\mathcal{X}_C(\mathbf{b}_j, R_c, \Psi_b)) : \forall \mathbf{b}_j \in \Phi_b\},$$
$$\Phi_{\mathtt{u,CE}} = \{U(\mathcal{X}_E(\mathbf{b}_j, R_c, \Psi_b)) : \forall \mathbf{b}_j \in \{\Psi_{bE} \setminus \mathbf{b}_0\}\}.$$

Table 2.1: Summary of notations used in this chapter.

Notation	**Description**
Ψ_b and λ_0	Homogeneous PPP modeling the locations BSs and density of Ψ_b
$\mathbf{b}_j$ and $\mathbf{u}_{j_k}$	Locations of the j-th BS and a user in the j-th cell using k-th pilot
R_c and $\kappa = R_c\sqrt{\pi c_2 \lambda_0}$	Threshold radius and normalized threshold radius
$\mathcal{V}_{\Psi_b}(\mathbf{b}_j)$	Voronoi cell associated with the j-th BS
$\mathcal{X}_C(\mathbf{b}_j, R_c, \Psi_b)$	CC region of the j-th cell
$\mathcal{X}_E(\mathbf{b}_j, R_c, \Psi_b)$	CE region of the j-th cell
$X_{Cj}(\lambda_0, R_c)$	CC area of a typical cell in a network of BS density λ_0
$X_{Ej}(\lambda_0, R_c)$	CE area of a typical cell in a network of BS density λ_0
$\Phi^{\mathtt{CC}}_{\mathtt{u,k}}$ and $\lambda^{\mathtt{CC}}_{\mathtt{u,k}}(r, \kappa)$	Point processes of users using k-th CC pilot and its density function
$\mathcal{I}_{\mathtt{CC}}(j, k)$	Indicator variable for the usage of the k-th CC pilot in the j-th cell
$\mathcal{I}_{\mathtt{CE}}(j, l)$	Indicator variable for the usage of the l-th CE pilot in the j-th cell
$\mathcal{A}_{\mathtt{0,CC}}$ ($\mathcal{A}_{\mathtt{0,CE}}$)	Indicator variable for pilot assignment to CC (CE) user of interest
$\mathcal{A}_{\mathtt{0n,CC}}$ ($\mathcal{A}_{\mathtt{0m,CE}}$)	Indicator variable for n-th (m-th) pilot assignment to CC (CE) user
D_{ij_k}	Random distance between the BS at $\mathbf{b}_j$ and user at $\mathbf{u}_{j_k}$
$\mathbf{g}_{ij_k} \sim \mathcal{CN}(\mathbf{0}_M, d_{ij_k}^{-\alpha}\mathbf{I}_M)$	Channel vector between i-th BS and the user at $\mathbf{u}_{j_k}$
$\mathtt{SINR}_{0_k}$	$\mathtt{SINR}$ of the user using the k-th pilot in the 0-th cell
$\mathtt{P}^{\mathtt{CC}}_{\mathtt{c,k}}$ and $\mathtt{P}^{\mathtt{CE}}_{\mathtt{c,l}}$	Coverage probability of a user using k-th CC and l-th CE pilots
B, B_C, and B_E	Total number of pilots, number of CC, and number of CE pilots
T_c, B	Length of coherence time and pilot sequence (in symbol durations)

Pilot sequences

We restrict our analysis to a narrowband single-carrier system. Extension to a multi-carrier system is straightforward and hence is skipped in favour of simpler exposition. In order to get the CSI at the BS, in the j-th cell, each user is assigned a pilot (sequence) that is selected from a set of orthogonal pilots $\mathcal{P}_j \subset \mathcal{P}$, where $\mathcal{P} = \{\mathbf{p}_1, \mathbf{p}_2, \cdots, \mathbf{p}_B\}$ and $\mathbf{p}_i \in \mathbb{C}^{B\times 1}$ for $i = 1, 2, \ldots, B$, where B is the number of orthogonal pilots. Hence, the duration of each pilot sequence is B symbol duration. For convenience, we denote the pilots by their indices. Therefore, the set of indicies of the pilots used in the j-th cell is denoted as $\mathcal{K}_j \subset \mathcal{K}$, where $\mathcal{K} = \{1, 2, 3, \ldots, B\}$. Owing to the limited channel coherence time of T_c symbol duration, the cardinality of this set $|\mathcal{K}| = B \leq T_c$. While the pilots remain orthogonal in each cell, due to the consideration of FPR, orthogonality among cells is not guaranteed. In each cell, the pilots are partitioned into two different sets, i.e. for the j-th BS $\mathcal{K}_j = \mathcal{C} \cup \mathcal{E}_j$ where $\mathcal{C} = \{1, 2, \ldots, B_C\}$ contains the indices of the CC pilots that are reused in each cell. Moreover, $|\mathcal{C}| = B_C \leq B$. On the other hand, $\mathcal{E}_j$ contains the indices of the CE pilots used in the j-th cell, which are reused in other cells depending on the reuse factor β_f. Further, $|\mathcal{E}_j| = B_E$ and $(B - B_C)/\beta_f = B_E$ for all $\mathbf{b}_j \in \Psi_b$. The choice for B_C, B_E, and β_f is made such that all three are integers.

These pilots are assigned randomly to the user in a particular cell. For the k-th CC pilot sequence in the j-th cell, where $k \in \mathcal{C}$, we define a binary random variable $\mathcal{I}_{\mathtt{CC}}(j,k)$ as follows

$$\mathcal{I}_{\mathtt{CC}}(j,k) = \begin{cases} 1, & \text{if } k\text{-th CC pilot is used in the } j\text{-th cell,} \\ 0, & \text{if } k\text{-th CC pilot is not used in the } j\text{-th cell.} \end{cases} \tag{2.4}$$

On the similar lines, for the l-th CE pilot in the j-th cell, we define the binary random variable $\mathcal{I}_{\mathtt{CE}}(j,l)$. Let $\Phi_{\mathtt{u,k}}^{\mathtt{CC}}$ and $\Phi_{\mathtt{u,l}}^{\mathtt{CE}}$ be the point processes formed by the interfering CC and CE users that use the k-th CC and l-th CE pilots, respectively. Since the user locations in $\Phi_{\mathtt{u,k}}^{\mathtt{CC}}$ are uniformly distributed points in the CC region of their respective cells, $\Phi_{\mathtt{u,k}}^{\mathtt{CC}}$ can be defined to inherit the user locations from $\Phi_{\mathtt{u,CC}}$ when $\mathcal{I}_{\mathtt{CC}}(j,k) = 1$. Similar argument is true for $\Phi_{\mathtt{u,l}}^{\mathtt{CE}}$ and $\Phi_{\mathtt{u,CE}}$. Hence,

$$\begin{aligned} \Phi_{\mathtt{u,k}}^{\mathtt{CC}} &= \{\mathbf{u} : \mathbf{u} \in \Phi_{\mathtt{u,CC}}, \mathcal{I}_{\mathtt{CC}}(j,k) = 1\}, \text{and} \\ \Phi_{\mathtt{u,l}}^{\mathtt{CE}} &= \{\mathbf{u} : \mathbf{u} \in \Phi_{\mathtt{u,CE}}, \mathcal{I}_{\mathtt{CE}}(j,l) = 1\}. \end{aligned} \tag{2.5}$$

We defer the discussion on the statistical properties of these point processes to Section 2.5. Note that the point process formed by the users using other pilot sequences in the network can be defined on the similar lines as that of $\Phi_{\mathtt{u,k}}^{\mathtt{CC}}(\Phi_{\mathtt{u,l}}^{\mathtt{CE}})$, where the points will be inherited from a point process that has the same definition as $\Phi_{\mathtt{u,CC}}(\Phi_{\mathtt{u,CE}})$. In the illustrative network diagram (Fig. 4.1), one CC pilot that is reused in each cell and one CE pilot that is reused in a few of the cells.

Distance distributions

Let the location of the user that uses the k-th sequence in the j-th cell be denoted as $\mathbf{u}_{j_k}$. The random distance between a user at $\mathbf{u}_{j_k}$ and a BS at $\mathbf{b}_i$ is denoted by the random variable $D_{ij_k} = \|\mathbf{u}_{j_k} - \mathbf{b}_i\|$ and d_{ij_k} is its realization. To obtain the coverage probability of a randomly selected user CC (CE) user, we need the distribution of the serving distance D_{00_k} (D_{00_l}) between $\mathbf{b}_0$ and the CC (CE) user using the k-th (l-th) pilot in the 0-th cell. For a typical PVC, the distance distribution between the BS and a randomly located point in the PVC is approximated as Rayleigh distribution with scale parameter $(\sqrt{2\pi\lambda_0 c_2})^{-1}$, where $c_2 = 5/4$ is an empirically obtained correction factor [63]. Since the user at $\mathbf{u}_{0_k}$ can not lie beyond $\mathcal{B}_{R_c}(\mathbf{o})$, it is reasonable to approximate the distribution of D_{00_k} to follow truncated Rayleigh distribution as given below

$$F_{D_{00_k}}(d_{00_k}|R_c) = \frac{1 - \exp(-\pi c_2 \lambda_0 d_{00_k}^2)}{1 - \exp(-\pi c_2 \lambda_0 R_c^2)}, \quad d_{00_k} \leq R_c. \tag{2.6}$$

On the other hand, the distribution of distance D_{00_l} can also be approximated as

$$F_{D_{00_l}}(d_{00_l}|R_c) = 1 - \exp(-\pi c_2 \lambda_0 (d_{00_l}^2 - R_c^2)), \quad d_{00_l} > R_c. \tag{2.7}$$

At this point, in order to make R_c invariant to the BS density λ_0, we define a normalized radius κ as $R_c = \frac{\kappa}{\sqrt{\pi c_2 \lambda_0}}, \kappa \in [0, \infty)$. In Sec. 2.5, κ will be used in the statistical characterization of $\Phi_{\mathtt{u,k}}^{\mathtt{CC}}(\Phi_{\mathtt{u,l}}^{\mathtt{CE}})$. Further, κ also provides perspective regarding the size of the CC region without the knowledge of λ_0. Next, we define the system parameters from the perspective

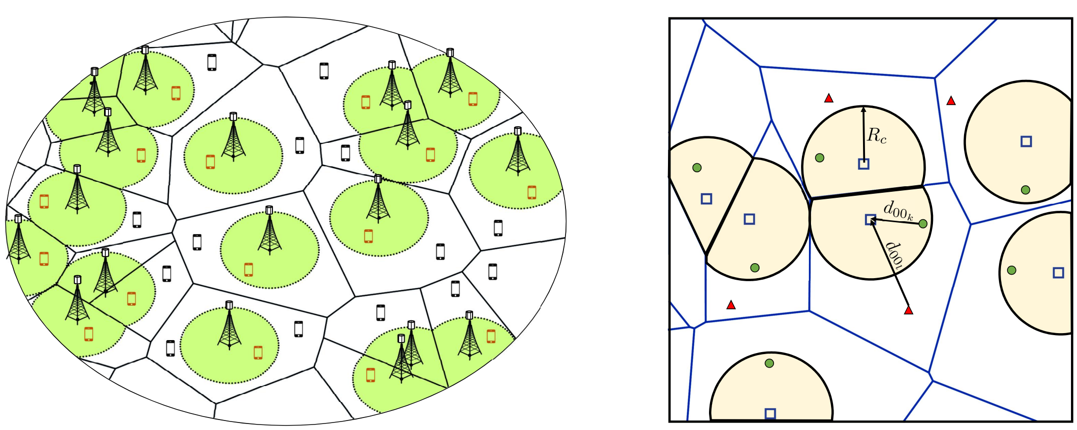

Figure 2.1: A representative network diagram (left) and a network realization illustrating the users using the k-th CC and l-th CE pilot (right). In a few of the cells the CE pilot is not in use.

of the CC user using the k-th pilot sequence. The extension of these definitions for CE case is straightforward.

2.2.2 Channel model and channel estimation

Channel model

We consider a system where each link suffers from two multiplicative wireless channel impairments, namely distance-dependent pathloss and multi-path fading. Consideration of the effect of shadowing is left as a promising future work. The channel vector between the user located at $\mathbf{u}_{j_k}$ and the M antenna elements of the BS located at $\mathbf{b}_i$ is given as $\mathbf{g}_{ij_k} = d_{ij_k}^{-\alpha/2}\mathbf{h}_{ij_k}(\in \mathbb{C}^{M\times 1})$, where α is the pathloss exponent, $\mathbf{h}_{ij_k} \sim \mathcal{CN}(\mathbf{0}_M, \mathbf{I}_M)$ is a $M \times 1$ complex Gaussian vector. We assume that these channel vectors exhibit quasi-orthogonality, i.e.

$$\lim_{M\to\infty} \frac{1}{M}\mathbf{h}_{ij_m}^H \mathbf{h}_{ij_n} = \mathbf{1}(j_m = j_n). \tag{2.8}$$

Further, we consider user transmit power ρ_u to be fixed for both pilot and data symbols.

Channel estimation

In a cell, using the orthogonal pilots, corresponding BS obtains the least square channel estimate of the users attached to them. Hence, for the CC user using the k-th pilot, the channel estimate at the 0-th BS is given as $\tilde{\mathbf{g}}_{00_k} = \sqrt{\rho_u}\mathbf{g}_{00_k} + \sum_{\mathbf{u}_{j_k}\in\Phi_{\mathrm{u,k}}} \sqrt{\rho_u}\mathbf{g}_{0j_k} + \mathbf{v}_0 \in \mathbb{C}^{M\times 1}$, where $\mathbf{v}_0 \sim \mathcal{CN}(\mathbf{0}_M, \mathbf{I}_M)$ is a complex Gaussian noise vector.

2.2.3 Asymptotic UL SINR of a CC (CE) user assigned to k-th (l-th) pilot sequence

The received signal vector at the 0-th BS is given as

$$\mathbf{r}_0 = \mathbf{h}_{00_k} x_{0k} d_{00_k}^{-\alpha/2} + \sum_{i=1, i\neq k}^{B} \mathcal{I}_{\mathtt{CC}}(0,i)\mathbf{h}_{00_i} x_{0i} d_{00_i}^{-\alpha/2} + \sum_{i=1}^{B} \sum_{\mathbf{u}_{j_i}\in\Phi_{\mathrm{u,i}}^{\mathtt{CC}}} \mathbf{h}_{0j_i} x_{ji} d_{0j_i}^{-\alpha/2} + \mathbf{n}_0, \tag{2.9}$$

where x_{ji} is the data symbol transmitted by the user using the i-th pilot in the j-th cell, $\mathbf{n}_0 \sim \mathcal{CN}(\mathbf{0}_M, \mathbf{I}_M)$ is a complex Gaussian noise vector. We assume that $\mathbb{E}[x_{ji}] = 0$ and $\mathbb{E}[\|x_{ji}\|^2] = \rho_u$. In order to estimate the symbol transmitted by the CC user of interest, the 0-th BS uses MRC detection scheme, where the filter coefficients are given as $\mathbf{w}_{0_k} = \frac{1}{M}\tilde{\mathbf{g}}_{00_k}^H$. As demonstrated in various works in the literature (cf. [64]), the asymptotic SINR of a user is independent of the detection scheme. Now, the detected symbol for the CC user using the k-th pilot in the 0-th BS is given as $\hat{x}_{0k} = \mathbf{w}_{0_k}\mathbf{r}_0$. As the number of antennas $M \to \infty$, due to quasi-orthogonality of the channel, it can be shown that the detected symbol is only affected by the interference from the users using the k-th pilot in other cells (a.k.a. pilot contamination). Hence, the $\texttt{SINR}$ of the CC and CE users that are assigned the k-th and l-th pilots, respectively, are given as

$$\texttt{SINR}_{0_k} = d_{00_k}^{-2\alpha}\Bigg(\sum_{\mathbf{u}_{j_k}\in\Phi_{\mathrm{u,k}}^{\mathrm{CC}}} d_{0j_k}^{-2\alpha}\Bigg)^{-1}, \quad \texttt{SINR}_{0_l} = d_{00_l}^{-2\alpha}\Bigg(\sum_{\mathbf{u}_{j_l}\in\Phi_{\mathrm{u,l}}^{\mathrm{CE}}} d_{0j_l}^{-2\alpha}\Bigg)^{-1}. \tag{2.10}$$

The proof of the above $\texttt{SINR}$ expression is readily available in the literature (cf. [2, 53]). Since the above expressions are independent of ρ_u, we assume $\rho_u \equiv 1$.

2.2.4 Performance metrics

In this work, the following metrics are considered for the network performance analysis.

1) $\texttt{SINR}$ *coverage probability:* The $\texttt{SINR}$ coverage probabilities of a CC and CE user using the k-th and l-th pilots for a target $\texttt{SINR}$ threshold T are

$$\begin{aligned} \mathtt{P}_{\mathtt{c,k}}^{\mathtt{CC}}(T) &= \mathbb{P}\left[\texttt{SINR}_{0_k} \geq T | \mathcal{I}_{\mathtt{CC}}(0,k) = 1\right], \quad \text{and} \\ \mathtt{P}_{\mathtt{c,l}}^{\mathtt{CE}}(T) &= \mathbb{P}\left[\texttt{SINR}_{0_l} \geq T | \mathcal{I}_{\mathtt{CE}}(0,l) = 1 | \mathcal{E}_3^C\right], \end{aligned} \tag{2.11}$$

where $\mathcal{E}_3^C$ is the event that the typical cell has a CE region (detailed discussion is in Sec. 2.3).

2) Average user SE: The average user SEs of the CC and CE users of interest are given as

$$\begin{aligned} \overline{\texttt{SE}}_{\mathtt{u,CC}} &= \omega\mathbb{E}\left[\mathcal{A}_{\mathtt{0,CC}}\log_2(1+\texttt{SINR}_{\mathtt{0,CC}})\right], \quad \text{and} \\ \overline{\texttt{SE}}_{\mathtt{u,CE}} &= \omega\mathbb{E}\left[\mathcal{A}_{\mathtt{0,CE}}\log_2(1+\texttt{SINR}_{\mathtt{0,CE}})\middle|\mathcal{E}_3^C\right], \end{aligned} \tag{2.12}$$

where $\omega = (1 - B/T_c)$ accounts for the fact that out of the total coherence time of T_c symbol duration, B symbol duration is dedicated for channel estimation leaving only $T_c - B$ duration for data transmission. Note that while the coverage probability is defined for a user conditioned on a pilot, the average user SE is defined for a randomly selected CC (CE) user that can be assigned any one of the CC (CE) pilots. Hence, $\texttt{SINR}_{\mathtt{0,CC}}$ and $\texttt{SINR}_{\mathtt{0,CE}}$ is the $\texttt{SINR}$ of a randomly selected CC (CE) user that we term as *CC (CE) user of interest*. Further, the indicator variable $\mathcal{A}_{\mathtt{0,CC}} = 1$, if the CC user of interest is assigned a pilot sequence, and $\mathcal{A}_{\mathtt{0,CC}} = 0$, otherwise. Similarly, we define the indicator variable $\mathcal{A}_{\mathtt{0,CE}}$ for a random CE user of interest.

3) Average cell SE: The cell SE of the 0-th cell is given as

$$\texttt{CSE} = \omega\left[\sum_{n=1}^{B_C}\mathcal{I}_{\mathtt{CC}}(0,n)\log_2(1+\texttt{SINR}_{0_n}) + \sum_{m=1}^{B_E}\mathcal{I}_{\mathtt{CE}}(0,m)\log_2(1+\texttt{SINR}_{0_m})\right], \tag{2.13}$$

where $\omega = (1 - B/T_c)$. Our metric of interest is $\mathbb{E}\left[\texttt{CSE}\right]$. In the following sections, we derive theoretical expressions for the aforementioned quantities.

2.3 Distributions of the CC and CE areas of a typical cell

As discussed in the previous section, the distribution of the number of CC (CE) users and subsequently the pilot utilization in an interfering cell depends on its CC (CE) area. Since exact characterization of CE area is challenging (it is an open problem), we provide an approximate area distribution for the CE area using the well-known Weibull distribution. In our approach, we first derive the exact expressions for the first two moments of the CE area of a typical cell. In the second step, using moment matching method, we approximate this area as Weibull distribution. We use the similar method to approximate the CC area distributions as a truncated beta distribution. While the exact characterization of the distribution of a typical JM cell area, hence the CC area, is given in [65], the expression of the probability density function (PDF) involves an infinite summation over multi-dimensional integrations. Further, the order of integration (hence the complexity of the expression) increases with the increasing value of R_c. Hence, our approximate truncated beta distribution lends tractability to the analysis. We validate the accuracy of the proposed distributions through Monte Carlo simulations using statistical metrics such as Kulback-Leibler divergence (KLD) and Kolmogorov-Smirnov distance (KSD). It is worth mentioning that the area of a typical PVC is approximated to follow gamma distribution, whose properties are used to provide load-based analysis of cellular networks [66, 67].

2.3.1 Distribution of CE area of a typical cell

To begin with, in the following lemma, we present the first two moments of the CE area.

Lemma 2.1. *For a given R_c and λ_0, the mean CE area of a typical Voronoi cell is*

$$m_{1,X_{E0}}(\lambda_0, R_c) = \mathbb{E}\left[X_{E0}(\lambda_0, R_c)\right] = \frac{\exp(-\pi\lambda_0 R_c^2)}{\lambda_0}, \tag{2.14}$$

and the second moment of the area is $m_{2,X_{E0}}(\lambda_0, R_c) =$

$$\mathbb{E}\left[X_{E0}(\lambda_0, R_c)^2\right] = 2\pi \int\limits_{r_1=R_c}^{\infty} \int\limits_{r_2=R_c}^{\infty} \int\limits_{u=0}^{2\pi} \exp\left(-\lambda_0 V(r_1, r_2, u)\right) \mathrm{d}u r_2 \mathrm{d}r_2 r_1 \mathrm{d}r_1, \tag{2.15}$$

where $V(r_1, r_2, u)$ is the area of union of two circles. The radii of these circles are r_1 and r_2, and the angular separation between their centers with respect to origin is u. Further,

$$\begin{aligned} V(r_1, r_2, u) =& r_1^2 \left(\pi - v(r_1, r_2, u) + \frac{\sin(2v(r_1, r_2, u))}{2}\right) \\ &+ r_2^2 \left(\pi - w(r_1, r_2, u) + \frac{\sin(2w(r_1, r_2, u))}{2}\right), \end{aligned} \tag{2.16}$$

where $v(r_1, r_2, u) = \cos^{-1}\left(\frac{r_1 - r_2\cos(u)}{\sqrt{r_1^2 + r_2^2 - 2r_1r_2\cos(u)}}\right)$ *and* $w(r_1, r_2, u) = \cos^{-1}\left(\frac{r_2 - r_1\cos(u)}{\sqrt{r_1^2 + r_2^2 - 2r_1r_2\cos(u)}}\right)$.

Proof: Please refer to Appendix A.1. ■

Before proceeding further, some intuition on the type of distribution that provides an accurate approximation is necessary. Note that a Voronoi cell has two characteristic radii R_m and R_M [68]. While R_m corresponds to the radius of the largest circle that completely lies inside a Voronoi cell, R_M is the radius of the smallest circle that encircles a Voronoi cell. Using R_m and R_M, we define following three disjoint events: (i) $\mathcal{E}_1 = \{R_c < R_m\}$, i.e. the CC region completely lies inside the Voronoi cell, (ii) $\mathcal{E}_2 = \{R_m \leq R_c < R_M\}$, i.e. the circle $\mathcal{B}_{R_c}(\mathbf{o})$ and the Voronoi cell $\mathcal{V}_{\Psi_b}(\mathbf{o})$ intersects, and (iii) $\mathcal{E}_3 = \{R_M \leq R_c\}$, i.e. there is no CE region. So, the CE area PDF can be expressed as the sum of two components:

$$f_{X_{E0}}(x) = f_{X_{E0}}(x|\mathcal{E}_3)\mathbb{P}\left[\mathcal{E}_3\right] + f_{X_{E0}}(x|\mathcal{E}_3^C)(1 - \mathbb{P}\left[\mathcal{E}_3\right]), \tag{2.17}$$

Further, note that $f_{X_{E0}}(x|\mathcal{E}_3)$ is given as

$$f_{X_{E0}}(x|\mathcal{E}_3) = \delta(0), \tag{2.18}$$

where $\delta(x)$ is the Dirac-delta function. Next we obtain $\mathbb{P}\left[\mathcal{E}_3\right]$ and $f_{X_{E0}}(x|\mathcal{E}_3)$. Since $\mathcal{E}_3 = \{R_M \leq R_c\}$, $\mathbb{P}\left[\mathcal{E}_3\right] = \mathbb{P}\left[R_M \leq R_c\right]$, where the distribution of R_M is [68, Theorem 1]

$$\mathbb{P}\left[R_M \leq r\right] = 1 - e^{-4\pi\lambda_0 r^2}\left(1 - \sum_{k\geq 1}\frac{(-4\pi\lambda_0 r^2)^k}{k!}\xi_k\right), \quad r > 0. \tag{2.19}$$

In the above expression,

$$\xi_k = \int_{\sum_{i=1}^{k} u_i = 1, u_i \in [0,1]}\left[\prod_{i=1}^{k} F(u_i)\right] e^{4\pi\lambda_0 r^2 \sum_{i=1}^{k}\int_0^{u_i} F(t)\mathrm{d}t}\mathrm{d}\mathbf{u},$$

where $F(t) = \sin^2(\pi t)\mathbf{1}(0 \leq t \leq \frac{1}{2}) + \mathbf{1}(t > \frac{1}{2})$, where $\mathbf{1}(\cdot)$ is the indicator function. Based on moment matching method, we approximate $f_{X_{E0}}(x|\mathcal{E}_3^C)$ as Weibull PDF. Intuitively, the CE area is likely to exhibit similar properties of the Voronoi cell area, especially when R_c is small. Hence, the gamma distribution, which is used to approximate the Voronoi cell area, is the first preference. However, for larger R_c, gamma PDF fails to capture the decay of the PDF of CE area. Hence, Weibull distribution, which has similar Kernel as gamma distribution[2] along with the flexibility to control the decay factor of the PDF, is used for the aforementioned approximation. Now, we present the mean and variance of X_{E0} conditioned on $\mathcal{E}_3^C$.

[2]The kernel of gamma PDF is $f_G(x) \propto x^{\xi-1}\exp(-x/\theta)$, and Weibull PDF is $f_W(x) \propto x^{\xi-1}\exp(-(x/\theta)^{\xi})$.

Lemma 2.2. *The mean and variance of the CE area conditioned on $\mathcal{E}_3^C$ are*

$$\mathbb{E}\left[X_{E0}|\mathcal{E}_3^C\right] = \mathbb{E}\left[X_{E0}\right](\mathbb{P}\left[\mathcal{E}_3^C\right])^{-1} \text{ and}$$
$$\mathtt{Var}\left[X_{E0}|\mathcal{E}_3^C\right] = \frac{\mathtt{Var}\left[X_{E0}\right]}{\mathbb{P}\left[\mathcal{E}_3^C\right]} - \mathbb{P}\left[\mathcal{E}_3\right](\mathbb{E}\left[X_{E0}|\mathcal{E}_3^C\right])^2.$$

Proof: The proof of this Lemma follows from law of total expectation and law of total variance that are given as $\mathbb{E}\left[X_{E0}\right] = \mathbb{E}\left[X_{E0}|\mathcal{E}_3\right]\mathbb{P}\left[\mathcal{E}_3\right] + \mathbb{E}\left[X_{E0}|\mathcal{E}_3^C\right]\mathbb{P}\left[\mathcal{E}_3^C\right]$, and

$$\begin{aligned}\mathtt{Var}\left[X_{E0}\right] =& \mathtt{Var}\left[X_{E0}|\mathcal{E}_3\right]\mathbb{P}\left[\mathcal{E}_3\right] + \mathbb{P}\left[\mathcal{E}_3\right](1-\mathbb{P}\left[\mathcal{E}_3\right])(\mathbb{E}\left[X_{E0}|\mathcal{E}_3\right])^2\\ &+ \mathtt{Var}\left[X_{E0}|\mathcal{E}_3^C\right]\mathbb{P}\left[\mathcal{E}_3^C\right] + \mathbb{P}\left[\mathcal{E}_3^C\right]\mathbb{P}\left[\mathcal{E}_3\right](\mathbb{E}\left[X_{E0}|\mathcal{E}_3^C\right])^2\\ &- 2\mathbb{E}\left[X_{E0}|\mathcal{E}_3\right]\mathbb{P}\left[\mathcal{E}_3\right]\mathbb{E}\left[X_{E0}|\mathcal{E}_3^C\right]\mathbb{P}\left[\mathcal{E}_3^C\right].\end{aligned}$$

Rearranging the terms and replacing $\mathbb{E}\left[X_{E0}|\mathcal{E}_3\right] = 0$ and $\mathtt{Var}\left[X_{E0}|\mathcal{E}_3\right] = 0$, we obtain the expressions presented in the lemma. ∎

The conditional PDF of X_{E0} is given as

$$f_{X_{E0}}(x|\mathcal{E}_3^C) = \frac{\eta}{\zeta}\left(\frac{x}{\zeta}\right)^{\eta-1}\exp\left(-\frac{x^\eta}{\zeta^\eta}\right), \tag{2.20}$$

where η and ζ are shape and scale parameters. These parameters are obtained by matching the first two moments and solving the following system of equations:

$$\begin{aligned}\eta\Gamma(1+1/\zeta) &= \mathbb{E}\left[X_{Ej}|\mathcal{E}_3^C\right],\\ \eta^2(\Gamma(1+2/\zeta) - \Gamma(1+1/\zeta)^2) &= \mathtt{Var}\left[X_{Ej}|\mathcal{E}_3^C\right].\end{aligned} \tag{2.21}$$

Now, (2.20), (2.19), (2.18), and (2.17) together provide us the approximate PDF for CE area.

2.3.2 Distribution of CC area of a typical cell

Similar to the CE case, in the next lemma, we derive the first two moments of the CC area.

Lemma 2.3. *For a given λ_0 and R_c, the mean of the CC area a typical Voronoi cell is given by*

$$m_{1,X_{C0}}(\lambda_0, R_c) = \mathbb{E}\left[X_{C0}(\lambda_0, R_c)\right] = \frac{1-\exp(-\pi\lambda_0 R_c^2)}{\lambda_0}, \tag{2.22}$$

and the second moment of the area is given by $m_{2,X_{E0}}(\lambda_0, R_c) =$

$$\mathbb{E}\left[X_{C0}(\lambda_0, R_c)^2\right] = 2\pi\int_{r_1=0}^{R_c}\int_{r_2=0}^{R_c}\int_{u=0}^{2\pi} e^{-\lambda_0 V(r_1,r_2,u)}\mathrm{d}u r_2\mathrm{d}r_2 r_1\mathrm{d}r_1, \tag{2.23}$$

where $V(r_1, r_2, u)$ is the area of union of two circles given in (2.16).

Proof: On the similar lines of the proof of Lemma 2.1, the mean CC area of the 0-th cell is

$$\mathbb{E}\left[|\mathcal{X}_C(\mathbf{o}, R_c, \Psi_b)|\right] = 2\pi \int_{r=0}^{R_c} \exp(-\pi\lambda_0 r^2) r \mathrm{d}r.$$

Similarly, the second moment of the j-th CC area is given as

$$\mathbb{E}\left[|\mathcal{X}_C(\mathbf{o}, R_c, \Psi_b)|^2\right] = \mathbb{E}\Big[\int_{\mathbf{x}\in\mathbb{R}^2} \mathbf{1}_{(\mathbf{x}\in\mathcal{V}_{\Psi_b}(\mathbf{o})\cap\mathcal{B}_{R_c}(\mathbf{o}))} \mathrm{d}\mathbf{x} \int_{\mathbf{y}\in\mathbb{R}^2} \mathbf{1}_{(\mathbf{y}\in\mathcal{V}_{\Psi_b}(\mathbf{o})\cap\mathcal{B}_{R_c}(\mathbf{o}))} \mathrm{d}\mathbf{y}\Big],$$

On the similar lines as in Appendix A.1, after a few steps (2.23) follows from the above expression. ■

Now, the PDF of the CC area can be expressed as

$$f_{X_{C0}}(x) = f_{X_{C0}}(x|\mathcal{E}_1)\mathbb{P}\left[\mathcal{E}_1\right] + f_{X_{C0}}(x|\mathcal{E}_1^C)(1 - \mathbb{P}\left[\mathcal{E}_1\right]), \tag{2.24}$$

where $\mathbb{P}\left[\mathcal{E}_1\right] = \mathbb{P}\left[R_m > R_C\right]$. Note that R_m is half of the nearest neighbor distance of a PPP, which follows Rayleigh distribution with parameter $(\sqrt{8\pi\lambda_0})^{-1}$ and CDF $F_{R_m}(r_m) = 1 - \exp(-4\pi\lambda_0 r_m^2)$. Hence, the probability of $\mathcal{E}_1$ is given as

$$\mathbb{P}\left[\mathcal{E}_1\right] = \mathbb{P}\left[R_m > R_c\right] = \exp(-4\pi\lambda_0 R_c^2) = 1 - \mathbb{P}\left[\mathcal{E}_1^C\right]. \tag{2.25}$$

Observe that, the PDF of X_{C0} conditioned on $\mathcal{E}_1$ is

$$f_{X_{C0}}(x|\mathcal{E}_1) = \delta(\pi R_c^2). \tag{2.26}$$

Now, to approximate $f_{X_{C0}}(x|\mathcal{E}_1^C)$, we have used generalized truncated beta distribution, i.e.

$$f_{X_{C0}}(x|\mathcal{E}_1^C) \approx g(x; v, w, y, z, \gamma, \beta) = \frac{(x-y)^{\gamma-1}(z-x)^{\beta-1}}{B(v, w, y, z; \gamma, \beta)}, \quad 0 \le x < \pi R_c^2, \tag{2.27}$$

where γ and β are shape parameters; the support of the untruncted beta distribution is $[y, z]$ (since beta distribution has finite support); the support of the truncated beta distribution is $[v, w]$; and the normalization factor $B(v, w, y, z; \gamma, \beta) = \int_{\mathfrak{v}}^{\mathfrak{w}} (x-y)^{\gamma-1}(z-x)^{\beta-1}\mathrm{d}x$, where $\mathfrak{v} = \frac{v-y}{y-z}$ and $\mathfrak{w} = \frac{w-y}{z-y}$. The choice of beta distribution is motivated by the fact that the distribution function of X_{C0} has a finite support $[0, \pi R_c^2]$. Based on this support set, we set $v = 0$ and $w = \pi R_c^2$ for the PDF presented in (2.27). Another motivation behind selection of beta is the presence of an additional shape parameter compared to conventional distributions such as Gamma or Weibull, which are parametrized by a single shape parameter. Further, we are introducing truncation to the above distribution that gives us an additional degree of freedom to closely match any arbitrary shape of the actual PDF. Here, we set $y = 0$ and $z = 3/2\pi R_c^2$. To obtain the shape parameters γ and β using moment matching method, we need the mean and variance of X_{C0} conditioned on $\mathcal{E}_1^C$, which is presented next.

Lemma 2.4. *The mean and variance of the area X_{C0} conditioned on $\mathcal{E}_1^C$ is given as*

$$\mathbb{E}\left[X_{C0}|\mathcal{E}_1^C\right] = \frac{(1-e^{-\pi\lambda_0 R_c^2})\lambda_0^{-1} - \pi R_c^2 e^{-4\pi\lambda_0 R_c^2}}{1-e^{-4\pi\lambda_0 R_c^2}},$$
$$\mathtt{Var}\left[X_{C0}|\mathcal{E}_1^C\right] = \frac{\mathtt{Var}\left[X_{C0}\right]}{\mathbb{P}\left[\mathcal{E}_1^C\right]} - \mathbb{P}\left[\mathcal{E}_1\right]\left(\mathbb{E}\left[X_{C0}|\mathcal{E}_1\right] - \mathbb{E}\left[X_{C0}|\mathcal{E}_1^C\right]\right)^2. \tag{2.28}$$

Proof: The proof is done on the similar lines as that of Lemma 2.2. Using the law of total expectation, we write

$$\mathbb{E}\left[X_{C0}|\mathcal{E}_1^C\right] = \left(\mathbb{E}\left[X_{C0}\right] - \mathbb{E}\left[X_{C0}|\mathcal{E}_1\right]\mathbb{P}\left[\mathcal{E}_1\right]\right)/(1-\mathbb{P}\left[\mathcal{E}_1\right]).$$

The mean of the conditional area in the Lemma is obtained by substituting $\mathbb{E}\left[X_{C0}|\mathcal{E}_1\right] = \pi R_c^2, \mathbb{P}\left[\mathcal{E}_1\right] = e^{-4\pi\lambda_0 R_c^2}$, and using the value of $\mathbb{E}\left[X_{C0}\right]$ from Lemma 2.3. Further, the conditional variance is obtained from the law of total variance and using the fact that $\mathtt{Var}\left[X_{C0}|\mathcal{E}_1\right] = 0$. ■

The parameters γ, β in (2.27) are obtained by solving the following simultaneous equations

$$\frac{\mathtt{B}(v,w,y,z;\gamma+1,\beta)}{\mathtt{B}(v,w,y,z;\gamma,\beta)} = \mathbb{E}\left[X_{C0}|\mathcal{E}_1^C\right],$$
$$\frac{\mathtt{B}(v,w,y,z;\gamma+2,\beta)}{\mathtt{B}(v,w,y,z;\gamma,\beta)} - \mathbb{E}\left[X_{C0}|\mathcal{E}_1^C\right]^2 = \mathtt{Var}\left[X_{C0}|\mathcal{E}_1^C\right].$$

Substituting (2.25) and (2.26) in (2.24), the approximate CC area PDF is given as

$$f_{X_{C0}}(x) = \delta(\pi R_c^2)e^{-4\pi\lambda_0 R_c^2} + f_{X_{C0}}(x|\mathcal{E}_1^C)(1-e^{-4\pi\lambda_0 R_c^2}), \tag{2.29}$$

where $f_{X_{C0}}(x|\mathcal{E}_1^C)$ is given in (2.27).

Remark 2.5. *It is possible to approximate the* PDF *of the area of a typical Voronoi cell using the expressions for $f_{X_{C0}}(x)$ in (2.17) or $f_{X_{C0}}(x)$ in (2.29). While in the former case, the typical Voronoi cell area* PDF *is obtained by setting $R_c = 0$, in the latter case it is obtained by setting a sufficiently large value of R_c such that $\mathbb{P}\left[\mathcal{E}_1\right] = \exp(-\pi\lambda_0 R_c^2) \approx 0$.*

2.3.3 Accuracy of the approximate distributions

The approximate theoretical results are validated through Monte Carlo simulations. We use KLD (KSD) to compare the approximate and the true PDFs (CDFs) obtained through simulations. In Table 2.2 these two metrics are presented for different values of R_c for both CC and CE areas. The low values of KSD and KLD for different R_c verifies the accuracy of the distributions. For visual verification, in Fig. 2.2, we compare the true and approximate PDFs of CC and CE areas.

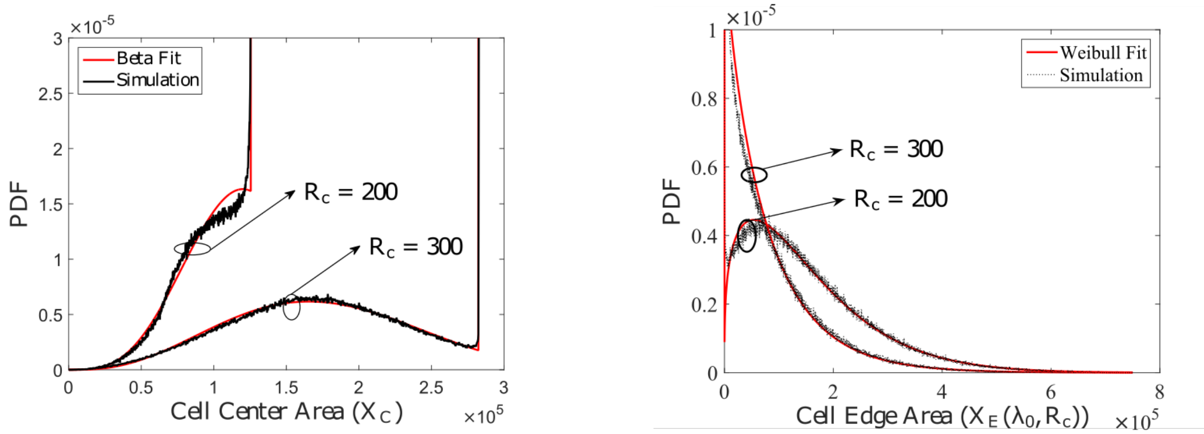

Figure 2.2: The PDFs (left) of the CC area and CE area (right) of a typical cell. $\lambda_0 = 4 \times 10^{-6}$.

$R_c \vert \kappa$	100|0.4	200|0.8	250|1	300|1.2	500|2
KS Distance (CC)	0.0230	0.0238	0.0123	0.0104	0.002
KL Divergence (CC)	0.0125	0.0095	0.0055	0.0032	0.0007
KS Distance (CE)	0.0164	0.0107	0.0233	0.0347	
KL Divergence (CE)	0.0098	0.0087	0.0160	0.0208	

Table 2.2: Comparison between simulation and approximate PDFs and CDFs for different R_c. $\lambda_0 = 4 \times 10^{-6}$.

2.4 Pilot assignment and pilot utilization probability

In this section, we present theoretical expressions for the probability of assigning a pilot to the CC (CE) user of interest (Lemma 2.6) and the probability that the k-th CC (l-th CE) pilot is being used in the j-th cell (Lemma 2.7). As we will see in the following section, the former quantity is useful in obtaining the average SE of the CC (CE) user of interest, and the latter quantity is useful in determining the average cell SE as well as the density function of interfering CC (CE) user point process. Before proceeding further, let us define the binary variable $\mathcal{A}_{\mathtt{0n,CC}} = 1$, if the CC user of interest is assigned the n-th pilot sequence, and $\mathcal{A}_{\mathtt{0n,CC}} = 0$, otherwise. Similarly, the indicator variable $\mathcal{A}_{\mathtt{0m,CE}}$ can be defined for CE user of interest and the m-th CE pilot. Next, we present the probability of pilot assignment to the CC (CE) user of interest.

Lemma 2.6. *The probability that CC user of interest is assigned the k-th pilot is*

$$\mathbb{E}\left[\mathcal{A}_{\mathtt{0k,CC}}\right] = \mathbb{P}\left[\mathcal{A}_{\mathtt{0k,CC}} = 1\right] = \frac{\mathbb{P}\left[\mathcal{A}_{\mathtt{0,CC}} = 1\right]}{B_C} = \frac{\int_0^{\pi R_c^2} \mathbb{P}\left[\mathcal{A}_{\mathtt{0,CC}} = 1 | x_{c0}\right] f_{X_{C0}}(x_{c0}) \mathrm{d}x_{c0}}{B_C},$$

where

$$\mathbb{P}\left[\mathcal{A}_{0,\mathtt{CC}}=1|x_{c0}\right]=\sum_{n=1}^{B_C}\mathbb{P}\left[N_{C0}=n|x_{c0}\right]+\sum_{n>B_C}\frac{B_C}{n}\mathbb{P}\left[N_{C0}=n|x_{c0}\right] \tag{2.30}$$

is the probability that CC user of interest is assigned a pilot in the 0*-th cell. Further, conditioned on the event that the* 0*-th cell has a CE region, the probability of CE user of interest is assigned the* l*-th pilot is given as*

$$\mathbb{E}\left[\mathcal{A}_{01,\mathtt{CE}}|\mathcal{E}_3^C\right]=\mathbb{P}\left[\mathcal{A}_{01,\mathtt{CE}}=1|\mathcal{E}_3^C\right]=\frac{\mathbb{P}\left[\mathcal{A}_{0,\mathtt{CE}}=1|\mathcal{E}_3^C\right]}{B_E}$$
$$=B_E^{-1}\int_0^\infty\mathbb{P}\left[\mathcal{A}_{0,\mathtt{CE}}=1|\mathcal{E}_3^C,x_{e0}\right]f_{X_{E0}}(x_{e0}|\mathcal{E}_3^C)\mathrm{d}x_{e0},$$

where

$$\mathbb{P}\left[\mathcal{A}_{0,\mathtt{CE}}=1|\mathcal{E}_3^C,x_{e0}\right]=\sum_{n=1}^{B_E}\mathbb{P}\left[N_{E0}=n|\mathcal{E}_3^C,x_{e0}\right]+\sum_{n>B_E}\frac{B_E}{n}\mathbb{P}\left[N_{E0}=n|\mathcal{E}_3^C,x_{e0}\right].$$

Proof: The probability of assigning a pilot to the CC user of interest is given as

$$\mathbb{P}\left[\mathcal{A}_{0,\mathtt{CC}}=1\right]=\mathbb{P}\left[\cup_{n=1}^{B_C}\{\mathcal{A}_{0\mathtt{n},\mathtt{CC}}=1\}\right]=\sum_{n=1}^{B_C}\mathbb{P}\left[\mathcal{A}_{0\mathtt{n},\mathtt{CC}}=1\right]=B_C\mathbb{P}\left[\mathcal{A}_{0\mathtt{k},\mathtt{CC}}=1\right],$$

where the last step follows from the fact that the events $\{\{\mathcal{A}_{0\mathtt{n},\mathtt{CC}}=1\},n=1,\ldots,B_C\}$ are equi-probable. Conditioned on the CC area of the 0-th cell, the distribution of the number of users in this region is given by (3.3). Hence, the probability that the CC user of interest is assigned a pilot is given by (2.30). The final result is obtained by de-conditioning w.r.t. CC area of the 0-th cell. The pilot assignment probability for the CE user follows from the similar argument. ∎

As discussed in Sec. 2.2, since our analysis is performed for the k-th CC (l-th CE) pilot, the aggregate network interference perceived at the 0-th BS depends on the utilization of the k-th CC (l-th CE) pilot in the interfering cells. In the following Lemma, we present the probability of the usage of the k-th CC (l-th CE) pilot in an interfering cell.

Lemma 2.7. *The probability that the* k*-th pilot is used in an interfering cell (say* j*-th cell) is*

$$\mathbb{E}\left[\mathcal{I}_{\mathtt{CC}}(j,k)\right]=\mathbb{P}\left[\mathcal{I}_{\mathtt{CC}}(j,k)=1\right]=\int_0^{\pi R_c^2}\mathbb{P}\left[\mathcal{I}_{\mathtt{CC}}(j,k)=1|x_{cj}\right]f_{X_{Cj}}(x_{cj})\mathrm{d}x_{cj}, \tag{2.31}$$

where

$$\mathbb{P}\left[\mathcal{I}_{\texttt{CC}}(j,k)=1|x_{cj}\right]=\sum_{n=1}^{B_C}\frac{n}{B_C}\mathbb{P}\left[N_{Cj}=n|x_{cj}\right]+\sum_{n>B_C}\mathbb{P}\left[N_{Cj}=n|x_{cj}\right]. \quad (2.32)$$

Similarly, conditioned on the event that the j-th cell has a CE region, the probability that the l-th CE pilot is used in the j-th cell is given as $\mathbb{E}\left[\mathcal{I}_{\texttt{CE}}(j,l)|\mathcal{E}_3^C\right]=$

$$\mathbb{P}\left[\mathcal{I}_{\texttt{CE}}(j,l)=1|\mathcal{E}_3^C\right]=\int_{x_{ej}=0}^{\infty}\mathbb{P}\left[\mathcal{I}_{\texttt{CE}}(j,l)=1|\mathcal{E}_3^C,x_{ej}\right]f_{X_{Ej}}(x_{ej}|\mathcal{E}_3^C)\mathrm{d}x_{ej}, \quad (2.33)$$

where

$$\mathbb{P}\left[\mathcal{I}_{\texttt{CE}}(j,l)=1\middle|\mathcal{E}_3^C,x_{ej}\right]=\sum_{n=1}^{B_E}\frac{n}{B_E}\mathbb{P}\left[N_{Ej}=n\middle|x_{ej},\mathcal{E}_3^C\right]+\sum_{n>B_E}\mathbb{P}\left[N_{Ej}=n\middle|x_{ej},\mathcal{E}_3^C\right].$$

Proof: For the CC case, first we condition on area of the j-th cell. Now, the probability that the k-th pilot is used on the j-th cell is given by (2.32). The expression in (2.31) follows from de-conditioning w.r.t. X_{Cj}. On the similar lines, (2.33) can be derived. ∎

2.5 SINR coverage and SE analysis

In this section, we characterize the statistical properties of the point processes $\Phi_{\texttt{u,k}}^{\texttt{CC}}(\Phi_{\texttt{u,l}}^{\texttt{CE}})$ to obtain the coverage probability and SE of a randomly selected CC (CE) user.

2.5.1 SINR coverage analysis of a user assigned to the k-th CC pilot

As discussed in Sec. 2.2, $\Phi_{\texttt{u,k}}^{\texttt{CC}}$ is obtained from $\Phi_{\texttt{u,CC}}$. Therefore, the first step is to understand the properties to $\Phi_{\texttt{u,CC}}$, which is discussed next.

Density function of $\Phi_{\texttt{u,CC}}$

Conditioned on the 0-th BS location, $\Phi_{\texttt{u,CC}}$ is isotropic. In addition, since $\Phi_{\texttt{u,CC}}$ is defined excluding the point in $\mathcal{X}_c(\mathbf{o},R_c,\Psi_b)$ from $\Psi_{\texttt{u,CC}}$, it is non-homogeneous. Now, our objective is to characterize $\Phi_{\texttt{u,CC}}$ conditioned on the 0-th BS location $\mathbf{o}$. To achieve this objective, we first determine the PCF $g(r)$ of the points in $\Phi_{\texttt{u,CC}}$ w.r.t. $\mathbf{o}$. Next, using this PCF, we approximate the point process as a non-homogeneous PPP. The approach that we have followed for the statistical characterization of $\Phi_{\texttt{u,CC}}$ is inspred by the work presented in [61], where the interfering users are uniformly distributed within the Voronoi cell of each BS. In contrast, in our case the users are uniformly distributed within the CC region of each cell. Hence, our result is slightly more general, i.e. for a sufficiently large value of κ we arrive at the result presented in [61]. Further, as we will see shortly, the derivation of the `PCF` is also not straightforward as the geometry of the region that we encounter is a little more complex compared to the Voronoi cells considered in [61]. Note that in this case, the `PCF` $g_\lambda(r,\kappa)$ is also a function of κ. By definition, $g_\lambda(r,\kappa)$ presents the likelihood of finding a point of $\Phi_{\mathtt{u,CC}}$ at a distance r from the 0-th BS in a network with $\lambda_0 = \lambda$ and threshold radius $R_c = \kappa/\sqrt{\pi c_2 \lambda}$. Further, in this case, the `PCF` is scale-invariant, i.e. $g_\lambda(r,\kappa) = g_1(r\sqrt{\lambda},\kappa)$. Using the scale invariance property, next, we present the `PCF` of $\Phi_{\mathtt{u,CC}}$ w.r.t. origin for $\lambda_0 = 1$.

Lemma 2.8. *The* `PCF` *of* $\Phi_{\mathtt{u,CC}}$ *w.r.t. the* 0*-th BS location is*

$$g_1^{\mathrm{CC}}(r,\kappa) \approx 1 - e^{-2\pi r^2 \mathbb{E}\left[X_{C0}(1,\kappa/\sqrt{\pi c_2})^{-1}\right]}, \tag{2.34}$$

where $X_{C0}(1,\kappa/\sqrt{\pi c_2})$ *is the CC area of a typical cell of a PV tessellation with unity BS density.*

Proof: Please refer to Appendix A.2. ∎

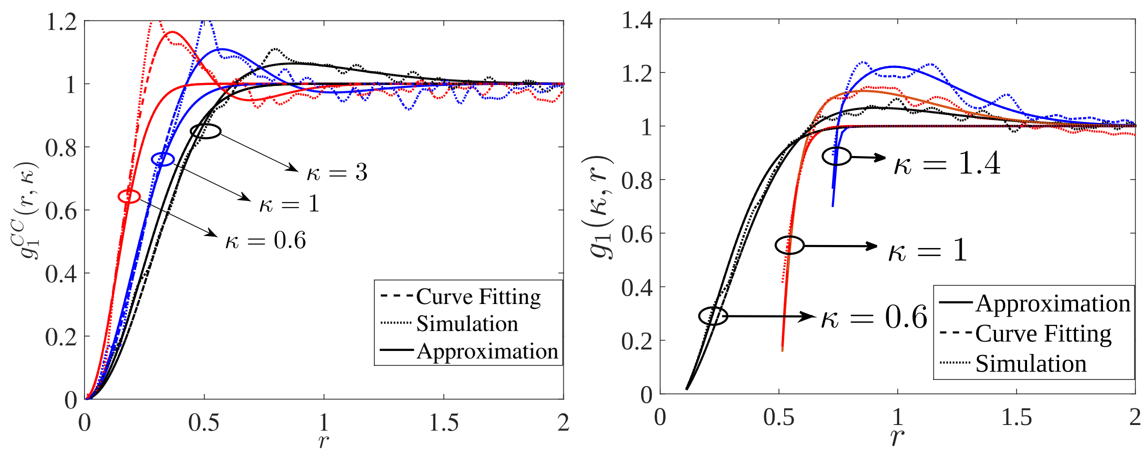

Figure 2.3: `PCF`s of $\Phi_{\mathtt{u,CC}}$ (left) and $\Phi_{\mathtt{u,CE}}$ (right) for different κ. The approximation and curve-fitting are based on (2.39) and (2.40), respectively.

In Fig. 2.3, we present the `PCF` $g_1^{\mathrm{CC}}(r,\kappa)$ for different values of κ. The approximate theoretical expression presented in (2.34) is compared with the simulation results. Further, following prototype function is also used to approximate the `PCF` for comparison purpose

$$\hat{g}_1^{\mathrm{CC}}(r,\kappa) = 1 - \exp(-ar^2) + br^2\exp(-cr^2), \tag{2.35}$$

where the values of the parameters a, b, c are obtained through curve fitting with simulated `PCF`. Based on the figure, we make the following remark on the `PCF` in (2.34).

Remark 2.9. *For smaller values of κ, the* PCF *obtained from simulation indicates that $\Phi_{\mathtt{u,CC}}$ exhibits clustering behaviour. However, by approximating the* PCF *using the exponential function presented in (2.34), it is not possible to capture this clustering nature. More complicated functions such as (2.35) can be used for this purpose. However, determining the values of the parameters $a, b,$ and c analytically is not tractable. Hence, we resort to the exponential* PCF *for the rest of the analysis, which is accurate for smaller values of r, i.e. in the neighborhood of the BS at $\mathbf{o}$.*

Using the PCF in (2.34), we approximate $\Phi_{\mathtt{u,CC}}$ as a non-homogeneous PPP such that for all $f : \mathbb{R}^2 \mapsto \mathbb{R}^+$, $\mathbb{E}\left[\sum_{x\in\Phi_{\mathtt{u,CC}}} f(x)\right] \equiv \mathbb{E}\left[\sum_{x\in\Phi^{\rm PPP}_{\mathtt{u,CC}}} f(x)\right] \implies$

$$\lambda_0 \int_{\mathbf{x}\in\mathbb{R}^2} f(\mathbf{x}) g_1^{\rm CC}(\|\mathbf{x}\|\sqrt{\lambda_0}, \kappa){\rm d}\mathbf{x} = \int_{\mathbf{x}\in\mathbb{R}^2} f(\mathbf{x})\lambda^{\rm PPP}_{\mathtt{u,CC}}(\|\mathbf{x}\|, \kappa){\rm d}\mathbf{x},$$

where the second step follows from the application of Campbell's theorem and replacing the intensity measure by the reduced second factorial moment measure [10, Chapter 8]. Hence, the density function of $\Phi_{\mathtt{u,CC}}$, if approximated as a non-homogeneous PPP, is given as

$$\lambda^{\rm PPP}_{\mathtt{u,CC}}(r, \kappa) = \lambda_0 \left(1 - e^{-2\pi\lambda_0 r^2 \mathbb{E}\left[X_{C0}(1,\kappa/\sqrt{\pi c_2})^{-1}\right]}\right). \tag{2.36}$$

Density function of $\Phi^{\mathtt{CC}}_{\mathtt{u,k}}$

Since $\Phi^{\mathtt{CC}}_{\mathtt{u,k}} \subseteq \Phi_{\mathtt{u,CC}}$, one can obtain $\Phi^{\mathtt{CC}}_{\mathtt{u,k}}$ by independently thinning the points in $\Phi_{\mathtt{u,CC}}$ with probability $1 - \mathbb{E}\left[\mathcal{I}_{\mathtt{CC}}(j,k)\right]$. Note that due to correlation in CC areas of neighbouring cells, the number of users in each cell, as well as the pilot utilization probability among neighbouring cells are correlated. Hence, the independent thinning is an approximation. However, to maintain tractability, this approximation is necessary. Approximating $\Phi^{\mathtt{CC}}_{\mathtt{u,k}}$ as a PPP, in the following Lemma, we present its density function.

Lemma 2.10. *The density function of $\Phi^{\mathtt{CC}}_{\mathtt{u,k}}$ is*

$$\lambda^{\mathtt{CC}}_{\mathtt{u,k}}(r, \kappa) = \lambda_0 \mathbb{E}\left[\mathcal{I}_{\mathtt{CC}}(j,k)\right] \left(1 - e^{-2\pi\lambda_0 r^2 \mathbb{E}\left[X_{C0}(1,\frac{\kappa}{\sqrt{\pi c_2}})^{-1}\right]}\right),$$

where $\mathbb{E}\left[\mathcal{I}_{\mathtt{CC}}(j,k)\right]$ is given in Lemma 2.7. The intensity measure is

$$\Lambda^{\mathtt{CC}}_{\mathtt{u,k}}(r, \kappa) = 2\pi \int_0^r \lambda^{\mathtt{CC}}_{\mathtt{u,k}}(t, \kappa) t {\rm d}t.$$

Proof: By independently thinning $\Phi^{\rm PPP}_{\mathtt{u,CC}}$ with probability $1 - \mathbb{E}\left[\mathcal{I}_{\mathtt{CC}}(j,k)\right]$, we arrive at the expression for the density function. ∎

Remark 2.11. *In the above expression, for* $\kappa \to \infty$, $\mathbb{E}\left[X_{C0}(1, \kappa/\sqrt{\pi c_2})^{-1}\right] \approx 7/5$. *This corresponds to the interfering user density* $\lambda^{\mathrm{PPP}}_{\mathtt{u,CC}}(r,\kappa) \approx \lambda_0\left(1 - \exp\left(-\frac{14}{5}\pi\lambda_0 r^2\right)\right)$, *which is the density function for interfering users in case of pilot reuse-1 [61].*
Moreover, since $\lim_{\kappa\to\infty} \mathbb{E}\left[X_{C0}(1, \frac{\kappa}{\sqrt{\pi c_2}})^{-1}\right] \leq \mathbb{E}\left[X_{C0}(1, \frac{\kappa}{\sqrt{\pi c_2}})^{-1}\right]$, *the intensity measure of the user point process of pilot reuse-1 is less than* $\Lambda^{\mathtt{CC}}_{\mathtt{u,k}}(r,\kappa)$. *As a consequence, the distance of the nearest interfering user in case of FPR is stochastically dominated by pilot reuse-1 for a randomly selected CC user.*

Coverage probability of the CC user of interest

In stochastic geometry-based works, for coverage analysis, one key intermediate step is to characterize the interference by the Laplace transform (LT) of its distribution [12]. The main advantage of this approach is that in the presence of exponential fading gain, the coverage probability can be readily expressed in terms of this LT [12]. However, in the SINR expression given in (2.10), the small scale fading term is absent due to spatial averaging. Hence, the conventional LT based approach is not applicable in this scenario. Although classical approaches such as Gil-Palaez inversion theorem [69, 70] can be used to obtain coverage probability, it is computationally inefficient, hence, usually avoided wherever possible. A more useful solution to this problem can be obtained by observing the fact that due to pathloss the total interference is likely to be dominated by interference contributions from a few *dominant* users [71]. Based on this intuition, we approximate the total interference power as the sum of the interference power from the *most* dominant interferer and the mean of the rest of the terms conditioned on the dominant term.

Dominant interferer approximation: Let $\hat{D}_{01_k}$ be the distance between the 0-th BS and its nearest interferer. Then, the CDF and the PDF of $\hat{D}_{01_k}$ are given as

$$\begin{aligned} F_{\hat{D}_{01_k}}(\hat{d}_{01_k}|\kappa) &= 1 - e^{-\Lambda^{\mathtt{CC}}_{\mathtt{u,k}}(\hat{d}_{01_k},\kappa)}, \\ f_{\hat{D}_{01_k}}(\hat{d}_{01_k}|\kappa) &= 2\pi\hat{d}_{01_k}\lambda^{\mathtt{CC}}_{\mathtt{u,k}}(\hat{d}_{01_k},\kappa)e^{-\Lambda^{\mathtt{CC}}_{\mathtt{u,k}}(\hat{d}_{01_k},\kappa)}, \end{aligned} \tag{2.37}$$

which are obtained using void probability of the PPP [12]. Now, the total interference is approximated as the sum of interference from the most dominant interferer and the expected interference from rest of the interferers in the network. Hence, we write $I_{\mathtt{agg},k} = \hat{D}_{01_k}^{-2\alpha} + \mathbb{E}\left[\sum_{\hat{\mathbf{u}}_{j_k}\in\Phi^{\mathtt{CC}}_{\mathtt{u,k}}\setminus\hat{\mathbf{u}}_{1_k}} \hat{D}_{0j_k}^{-2\alpha}\middle|\hat{D}_{01_k}\right] = \hat{D}_{01_k}^{-2\alpha} + \mathbb{E}\left[I_{\mathtt{rem,k}}|\hat{D}_{01_k}\right]$, where $\hat{\mathbf{u}}_{1_k}$ is the location of the dominant interferer in $\Phi^{\mathtt{CC}}_{\mathtt{u,k}}$. In the following Lemma, we present an expression for $\mathbb{E}\left[I_{\mathtt{rem,k}}|\hat{D}_{01_k}\right]$.

Lemma 2.12. *Conditioned on the distance to the dominant interferer* $\hat{D}_{01_k}$, *the expected* *interference from the rest of the interfering users is*

$$\mathbb{E}\left[I_{\mathtt{rem,k}}|\hat{D}_{01_k} = \hat{d}_{01_k}\right] = 2\pi \int_{\hat{d}_{01_k}}^{\infty} r^{-2\alpha} \lambda_{\mathtt{u,k}}^{\mathtt{CC}}(r,\kappa) r \mathrm{d}r.$$

Proof: Above expression follows from the application of Campbell's theorem. ■

With the knowledge of the expected interference and the distribution of $\hat{D}_{01_k}$, in the following proposition, we present the coverage probability for a CC user assigned to the k-th pilot.

Proposition 2.13. *Conditioned on the event that the k-th pilot is used in the 0-th cell, the coverage probability of the user that is assigned this sequence is given as* $\mathtt{P}_{\mathtt{c,k}}^{\mathtt{CC}}(T) =$

$$\mathbb{E}_{D_{00_k},\hat{D}_{01_k}}\left[\mathbf{1}\left(\hat{d}_{01_k}^{-2\alpha} + \mathbb{E}\left[I_{\mathtt{rem,k}}|\hat{d}_{01_k}\right] < \frac{d_{00_k}^{-2\alpha}}{T}\right)\middle|\mathcal{I}_{\mathtt{CC}}(0,k) = 1\right], \tag{2.38}$$

where $f_{\hat{D}_{01_k}}(\hat{d}_{01_k})$ is given in (2.37), and the CDF *of D_{00_k} is given in (3.4).*

Proof: Conditioned on $\mathcal{I}_{\mathtt{CC}}(0,k) = 1$, the coverage probability of the user assigned the k-th sequence is $\mathbb{P}\left[\mathtt{SINR}_{0_k} > T|\mathcal{I}_{\mathtt{CC}}(0,k) = 1\right] =$

$$\mathbb{P}\left[\frac{D_{00_k}^{-2\alpha}}{T} > I_{\mathtt{agg,k}}\middle|\mathcal{I}_{\mathtt{CC}}(0,k) = 1\right]$$
$$=\mathbb{E}\left[\mathbf{1}\left(\hat{d}_{01_k}^{-2\alpha} + \mathbb{E}\left[I_{\mathtt{rem,k}}|\hat{d}_{01_k}\right] < \frac{d_{00_k}^{-2\alpha}}{T}\right)\middle|\mathcal{I}_{\mathtt{CC}}(0,k) = 1\right],$$

where the expectation is taken over $D_{00_k}, \hat{D}_{01_k}$. This completes the proof of the above proposition. ■

2.5.2 SINR coverage analysis of a CE user assigned to the l-th CE pilot

Most of the intermediate steps necessary for the coverage probability result in this case can be derived on the similar lines as that of the previous section. Hence, we omit a few of the proofs to avoid repetition.

Density function of $\Phi_{\mathtt{u,l}}^{\mathtt{CE}}$

To begin with, we present the density function of the point process $\Phi_{\mathtt{u,CE}}$. Similar to the CC case, we first present the PCF $g_{\lambda}^{\mathrm{CE}}(r,\kappa)$ for $\Phi_{\mathtt{u,CE}}$ w.r.t. the 0-th BS. Due to scale invariance, we consider a network with unit BS density and threshold radius $\kappa/\sqrt{\pi c_2}$. In the following Lemma, we present the expression for $g_{1}^{\mathrm{CE}}(r,\kappa)$.

Lemma 2.14. *The* PCF *of* $\Phi_{\mathtt{u,CE}}$ *w.r.t. the* 0*-th BS is given as*

$$g_1^{\rm CE}(r,\kappa) \approx 1 - e^{-\pi\left(r^2 - \frac{\kappa^2}{\pi c_2}\right)\frac{14}{5}\mathbb{P}\left[\mathcal{E}_3^C\right]\exp(\kappa^2/c_2)}, \quad r \geq \frac{\kappa}{\sqrt{\pi c_2}}. \tag{2.39}$$

Proof: Please refer to Appendix A.4. ■

Similar to the CC case, in Fig. 2.3, we present the PCF for different values of κ for $\Phi_{\mathtt{u,CE}}$. The approximate theoretical expression presented in (2.39) is compared with the simulation results. We use the following prototype function to approximate the PCF for comparison purpose

$$\hat{g}_1^{\rm CE}(r,\kappa) = 1 - e^{-a_1(r^2 - R_c^2)} + b_1(r^2 - R_c^2)e^{-c_1(r^2-R_c^2)}, \tag{2.40}$$

where the values of the parameters a_1, b_1, c_1 are obtained through curve fitting with simulated PCF. Based on the figure, we make the following remark for the PCF in (2.39).

Remark 2.15. *As κ increases, the* PCF *obtained from simulation indicates that $\Phi_{\mathtt{u,CE}}$ exhibits clustering behaviour beyond R_c. By approximating the* PCF *using the exponential function presented in (2.39), it is not possible to capture this clustering nature. However, note that from the network deployment perspective higher values of R_c may not be desirable, because it would result in a higher fraction of cells without CE regions. Hence, the benefit of FPR will be reduced due to unutilized CE pilots in the cells without the CE regions. Therefore, the range of κ for which the approximation of* PCF *using (2.39) is poor is of lesser practical importance.*

Now, we approximate $\Phi_{\mathtt{u,CE}}$ as a non-homogeneous PPP with density function

$$\lambda_{\mathtt{u,CE}}^{\rm PPP}(r,\kappa) = \lambda_0 \mathbb{P}\left[\mathcal{E}_3^C\right]\left(1 - e^{-\pi\lambda_0(r^2-R_c^2)\mathbb{P}\left[\mathcal{E}_3^C\right]\frac{14}{5}\exp(\kappa^2/c_2)}\right), \quad r \geq R_c. \tag{2.41}$$

Recall that $\Phi_{\mathtt{u,l}}^{\mathtt{CE}} \subseteq \Phi_{\mathtt{u,CE}}$ contains the locations of the interfering CE users that use the l-th pilot. Similar to the CC case, we approximate $\Phi_{\mathtt{u,l}}^{\mathtt{CE}}$ as a non-homogeneous PPP whose density function is presented in the following lemma.

Lemma 2.16. *For $r \geq R_c$, the density function of the $\Phi_{\mathtt{u,l}}^{\mathtt{CE}}$ containing the locations of the active CE interfering users is approximated as*

$$\lambda_{\mathtt{u,l}}^{\mathtt{CE}}(r,\kappa) \approx \lambda_0 \mathbb{E}\left[\mathcal{I}_{\mathtt{CE}}(j,l)\right]\mathbb{P}\left[\mathcal{E}_3^C\right]\left(1 - e^{-\pi\frac{14}{5}\exp(\kappa^2/c_2)\mathbb{P}\left[\mathcal{E}_3^C\right]\lambda_0(r^2-R_c^2)}\right),$$

and corresponding intensity measure is given as

$$\Lambda_{\mathtt{u,l}}^{\mathtt{CE}}(r,\kappa) = 2\pi\int_{t=0}^{r}\lambda_{\mathtt{u,l}}^{\mathtt{CE}}(t,\kappa)t\mathrm{d}t.$$

Proof: The density function is obtained on the similar arguments as that of Lemma 2.10. ■

Coverage probability of the CE user of interest

Using the intensity measure and density function of $\Phi^{\mathtt{CE}}_{\mathtt{u,l}}$, the CDF and PDF of the distance to the dominant CE interferer are given as

$$F_{\hat{D}_{01_l}}(\hat{d}_{01_l}|\kappa) = 1 - e^{-\Lambda^{\mathtt{CE}}_{\mathtt{u,l}}(\hat{d}_{01_l},\kappa)}, \tag{2.42}$$

$$f_{\hat{D}_{01_l}}(\hat{d}_{01_l}|\kappa) = 2\pi\hat{d}_{01_l}\lambda^{\mathtt{CE}}_{\mathtt{u,l}}(\hat{d}_{01_l},\kappa)e^{-\Lambda^{\mathtt{CE}}_{\mathtt{u,l}}(\hat{d}_{01_l},\kappa)}. \tag{2.43}$$

Now, conditioned on the distance to the dominant interferer $\hat{D}_{01_l}$, the aggregate interference at the 0-th BS from the CE users is approximated as

$$\begin{aligned} I_{\mathtt{agg,l}} = \hat{d}_{01_l}^{-2\alpha} + \mathbb{E}\left[\sum_{\hat{\mathbf{u}}_{j_l}\in\Phi^{\mathtt{CE}}_{\mathtt{u,l}}\setminus\hat{\mathbf{u}}_{1_l}} \hat{d}_{0j_l}^{-2\alpha}\middle|\hat{d}_{01_l}\right] &= \hat{d}_{01_l}^{-2\alpha} + \mathbb{E}\left[I_{\mathtt{rem,l}}\middle|\hat{d}_{01_l}\right] \\ &\overset{(a)}{=}\hat{d}_{01_l}^{-2\alpha} + 2\pi\int_{\hat{d}_{01_l}}^{\infty} r^{-2\alpha}\lambda^{\mathtt{CE}}_{\mathtt{u,l}}(r,\kappa)r\mathrm{d}r, \end{aligned}$$

where (a) follows from the application of Campbell's theorem. Using the above expression for aggregate interference, the coverage probability of the CE user of interest is presented next.

Proposition 2.17. *Conditioned on the event that $\mathcal{I}_{\mathtt{CE}}(0,l) = 1$, the coverage probability of a user assigned to l-th pilot is given as*

$$\begin{aligned} \mathtt{P}^{\mathtt{CE}}_{\mathtt{c,l}}(T) &= \mathbb{P}\left[\mathtt{SINR}_{\mathtt{0,l}} > T|\mathcal{E}_3^C, \mathcal{I}_{\mathtt{CE}}(0,l) = 1\right] \\ &= \mathbb{E}_{D_{00_l},\hat{D}_{01_l}}\left[\mathbf{1}\left(I_{\mathtt{agg,l}} < \frac{d_{00_l}^{-2\alpha}}{T}\right)\middle|\mathcal{E}_3^C, \mathcal{I}_{\mathtt{CE}}(0,l) = 1\right]. \end{aligned}$$

Proof: The proof can be done on the similar lines as that of Proposition 2.13. ∎

2.5.3 Average user SE and cell SE

Using the coverage probability results, in the following Proposition, we present the approximate expressions for average SE of the CC and CE users of interest, and average cell SE. It is worthwhile mentioning that alternate methods such as the one presented in [72, 73] can also be used to characterize the SE.

Proposition 2.18. *The average SE of a randomly selected CC user is given as*

$$\overline{\mathtt{SE}}_{\mathtt{u,CC}} \approx \omega B_C\mathbb{E}\left[\mathcal{A}_{\mathtt{0k,CC}}\right]\int_{t=0}^{\infty}\mathtt{P}^{\mathtt{CC}}_{\mathtt{c,k}}(2^t-1)\mathrm{d}t, \tag{2.44}$$

where $\omega = (1 - B/T_C)$, $\mathtt{P}^{\mathtt{CC}}_{\mathtt{c,k}}(\cdot)$ *is presented in Proposition 2.13 and* $\mathbb{E}\left[\mathcal{A}_{\mathtt{0k,CC}}\right]$ *is presented in Lemma 2.6. Similarly, the average SE of a randomly selected CE user is given as*

$$\overline{\mathtt{SE}}_{\mathtt{u,CE}} \approx \omega B_E \mathbb{E}\left[\mathcal{A}_{\mathtt{0l,CE}} | \mathcal{E}_3^C\right] \int_{t=0}^{\infty} \mathtt{P}^{\mathtt{CE}}_{\mathtt{c,l}}(2^t - 1)\mathrm{d}t. \tag{2.45}$$

Proof: From (3.7), the average SE of the CC user of interest can be approximated as

$$\begin{aligned}
\overline{\mathtt{SE}}_{\mathtt{u,CC}} =& \omega\mathbb{E}\left[\mathcal{A}_{\mathtt{0,CC}} \log_2(1 + \mathtt{SINR}_{\mathtt{0,CC}})\right] \\
=& \omega\mathbb{E}\left[\sum_{n=1}^{B_C} \mathcal{A}_{\mathtt{0n,CC}} \log_2(1 + \mathtt{SINR}_{0_n})\right] \\
\overset{(a)}{=}& B_C\mathbb{E}\left[\mathcal{A}_{\mathtt{0k,CC}} \log_2(1 + \mathtt{SINR}_{0_k})\right] \\
\overset{(b)}{\approx}& B_C\mathbb{E}\left[\mathcal{A}_{\mathtt{0k,CC}}\right]\mathbb{E}\left[\log_2(1 + \mathtt{SINR}_{0_k})\right],
\end{aligned}$$

where $\mathtt{SINR}_{0_n}$ is the $\mathtt{SINR}$ of the CC user of interest if it is assigned the n-th CC pilot, (a) follows from the identical distributions of $\{\mathcal{A}_{\mathtt{0n,CC}} \log_2(1 + \mathtt{SINR}_{0_n})\}_{n=1}^{B_C}$, (b) follows from the independence assumption between $\mathcal{A}_{\mathtt{0k,CC}}$ and $\mathtt{SINR}_{0_k}$. The expression in the proposition follows from the last step using the fact that for a positive random variable X, $\mathbb{E}[X] = \int_0^\infty \mathbb{P}[X > t]\,\mathrm{d}t$. Similarly, the average CE user SE is derived. Similarly, the average SE of the CE user of interest is given as

$$\overline{\mathtt{SE}}_{\mathtt{u,l}} = \mathbb{E}\left[\log_2(1 + \mathtt{SINR}_{0_l}) | \mathcal{E}_3^C\right] = \mathbb{E}\left[\log_2(1 + \mathtt{SINR}_{0_l}) | \mathcal{I}(0,l) = 1, \mathcal{E}_3^C\right]\mathbb{P}\left[\mathcal{I}(0,l) = 1 | \mathcal{E}_3^C\right],$$

and the final expression follows from the expectation of a positive random variable. ∎

Proposition 2.19. *The average cell SE of a typical cell is given as*

$$\overline{\mathtt{CSE}} = \omega B_C \mathbb{E}\left[\mathcal{I}_{\mathtt{CC}}(0,k)\right] \int_{t=0}^{\infty} \mathtt{P}^{\mathtt{CC}}_{\mathtt{c,k}}(2^t - 1)\mathrm{d}t + \omega\mathbb{P}\left[\mathcal{E}_3^C\right] B_E \mathbb{E}\left[\mathcal{I}_{\mathtt{CE}}(0,l) | \mathcal{E}_3^C\right] \int_{t=0}^{\infty} \mathtt{P}^{\mathtt{CE}}_{\mathtt{c,l}}(2^t - 1)\mathrm{d}t.$$

Proof: From (2.13), we write $\mathbb{E}[\mathtt{CSE}] \overset{(a)}{=}$

$$\begin{aligned}
&\omega\mathbb{E}\left[\sum_{n=1}^{B_C} \mathcal{I}_{\mathtt{CC}}(0,n) \log_2(1 + \mathtt{SINR}_{0_n})\right] + \omega\mathbb{P}\left[\mathcal{E}_3^C\right]\mathbb{E}\left[\sum_{m=1}^{B_E} \mathcal{I}_{\mathtt{CE}}(0,m) \log_2(1 + \mathtt{SINR}_{0_m}) \middle| \mathcal{E}_3^C\right] \\
\overset{(b)}{\approx}& \omega B_C \mathbb{E}\left[\log_2(1 + \mathtt{SINR}_{0_k}) | \mathcal{I}_{\mathtt{CC}}(0,k) = 1\right]\mathbb{E}\left[\mathcal{I}_{\mathtt{CC}}(0,k)\right] \\
&+ \omega B_E \mathbb{P}\left[\mathcal{E}_3^C\right]\mathbb{E}\left[\mathcal{I}_{\mathtt{CE}}(0,l) | \mathcal{E}_3^C\right]\mathbb{E}\left[\log_2(1 + \mathtt{SINR}_{0_l}) | \mathcal{I}_{\mathtt{CE}}(0,l) = 1, \mathcal{E}_3^C\right],
\end{aligned}$$

where (a) follows from the law of total probability and (b) follows from the fact that $\{\mathtt{SINR}_{0_n}\}_{n=1}^{B_C}$ $(\{\mathtt{SINR}_{0_m}\}_{m=1}^{B_E})$ are identical, and for the final expression we assume independence between the event $\{\mathcal{I}_{\mathtt{CC}}(0,k) = 1\}$ and $\mathtt{SINR}_{0_k}$ and use the identity $\mathbb{E}[X] = \int_0^\infty \mathbb{P}[X > t]\,\mathrm{d}t$. ∎

2.6 Numerical results and discussion

In this section, we validate the approximate theoretical results using Monte Carlo simulations. Further, we study the effect of different system parameters on the SINR coverage probability, average user and cell SEs. In our simulation framework, we consider the BS density $\lambda_0 = 4 \times 10^{-6}$, pathloss exponent $\alpha = 3.7$, the coherence time interval $T_c = 200$ symbol duration, and the pilot length $B = 100$ symbol duration. For comparison purpose, we also provide SE results corresponding to pilot reuse-1 at necessary places. Note that the system model for reuse-1 is the same as described in Sec. 2.2. The key difference is that there is no segregation in terms of CC (CE) pilots and the entire set of B pilots can be assigned to any user attached to a BS. This complicates the pilot utilization analysis. To be specific, to obtain the probability of the event that a CC (CE) user is assigned a given pilot requires the consideration of the joint distribution of the number of CC and CE users. This result does not directly follow from Lemma 2.6 and requires additional analysis, which does not appear tractable as deriving joint distribution for the CC and CE areas of a typical cell is challenging. The similar remark holds for the probability of pilot utilization in case of reuse-1. Hence, to validate the efficacy of FPR scheme with respect to reuse-1, we rely on simulation-based results for reuse-1.

2.6.1 SINR coverage probability of a user assigned to a given pilot

In this subsection, we study the effect of different system parameters on the coverage probability of a CC (CE) user that is assigned the k-th (l-th) pilot. The effect of λ_u on coverage probability for CC and CE cases can be observed from Fig. 2.4 (left and right, respectively). From the figures, we infer that with the increasing density, the coverage probability reduces in both the scenarios. This is intuitive as with increasing λ_u, the pilot usage probability in the interfering cells increases, thereby increasing the aggregate interference. The effect of normalized threshold radius κ on coverage probability is presented in Fig. 2.5 for CC (left) and CE (right) cases. As observed from Fig. 2.5 (left), with decreasing κ (equivalently R_c), the coverage probability improves. This behavior is justified by the fact that with decreasing R_c the serving distance also decreases. In addition, the pilot usage probability in interfering cells also reduces. Combination of both the effects results in SINR coverage probability improvement. For a randomly selected CE user assigned a given CE pilot sequence, above trend is observed for higher SINR thresholds. On the other hand, for lower SINR thresholds, reverse trend is observed. One possible explanation behind this behaviour is that although with increasing R_c serving distance increases, the number of interfering users reduces. This results in improvement of coverage probability. In Fig. 2.6, we have presented coverage probability for different path loss exponent α. As expected with increasing path loss exponent, the coverage probability improves due to less interference.

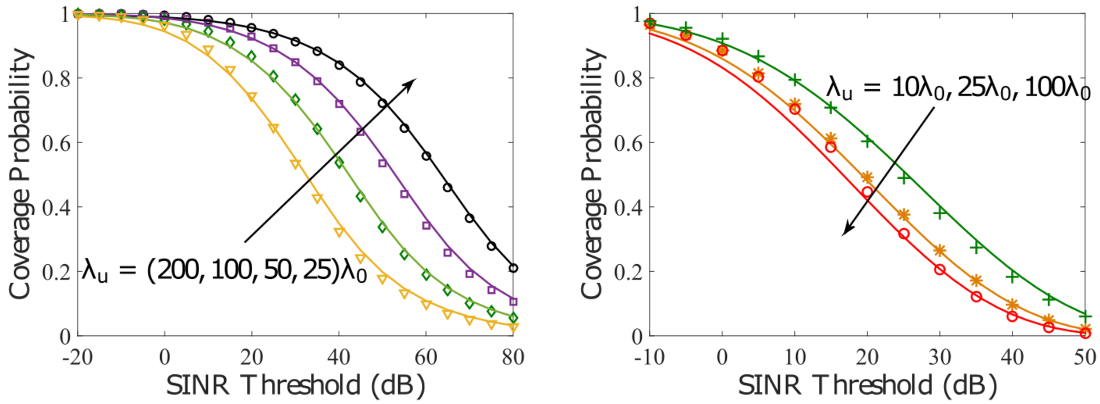

Figure 2.4: Coverage probability of a CC user on a given CC pilot (left) and CE user on a given CE pilot (right) for different λ_u. Markers and solid lines represent the simulation and theoretical results, respectively. $\kappa = 0.6, B_C = 58, B_E = 14, \beta_f = 3$.

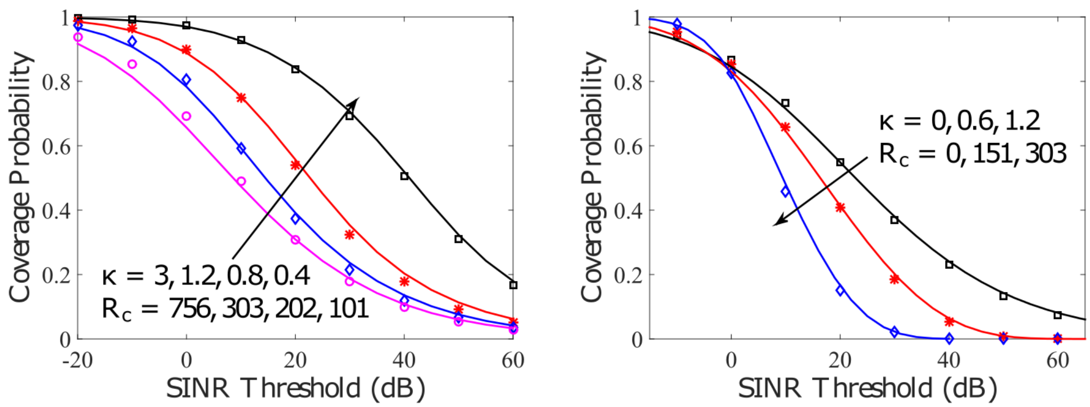

Figure 2.5: Coverage probability of a CC user on a given CC pilot (left) and CE user on a given CE pilot (right) for different R_c. Markers and solid lines represent the simulation and theoretical results, respectively. $B_C = 58, B_E = 14, \beta_f = 3, \mathbb{E}\left[\mathcal{I}_{\mathtt{CC}}(0,k)\right] = \mathbb{E}\left[\mathcal{I}_{\mathtt{CE}}(0,l)|\mathcal{E}_3^C\right] = 1$.

2.6.2 Average CC (CE) user SE and cell SE

SE as a function of B_C/B: In Fig. 2.7, the average SEs of CC and CE users of interest as well as a typical cell are presented for different values of B_C/B, where $B = 100$. For reference, we have also presented the average CC and CE user SEs for unity pilot reuse. From Fig. 2.7 (left), we observe that FPR scheme performs better compared to unity reuse beyond a certain B_C/B. For both the curves (corresponding to $\kappa = 0.8, 1$), this value of B_C/B lies in the neighbourhood of $1-\exp(-\kappa^2)$. Intuitively, in case of unity reuse, the probability of assigning a pilot sequence to a CC user is approximately $1-\exp(-\pi\lambda_0 c_2 R_c^2) = 1-\exp(-\kappa^2)$. Hence, on an average $1-\exp(-\kappa^2)$ fraction of pilot sequences are assigned to CC users. Therefore, by choosing $B_C/B \approx 1-\exp(-\kappa^2)$ in FPR case, the average SE for CC user of interest becomes

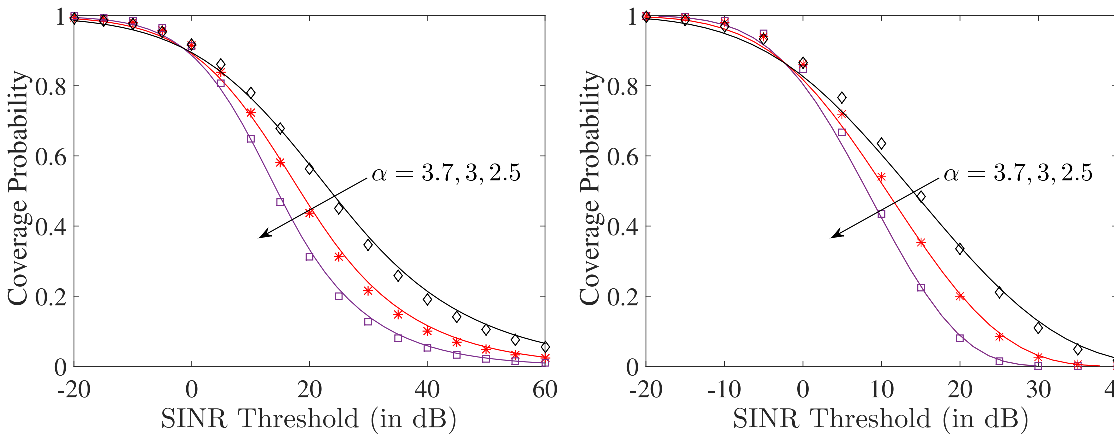

Figure 2.6: Coverage probability of a CC user on a given CC pilot (left) and CE user on a given CE pilot (right) for different path loss exponent α. Markers and solid lines represent the simulation and theoretical results, respectively. $\kappa = 0.8, B_C = 49, B_E = 17, \beta_f = 3$.

close to the SE of a CC user in unity reuse. On the other hand, from Fig. 2.7 (middle), we observe that for a wide-range of B_C/B the average SE of CE user of interest in FPR is higher compared to average CE user SE in case of unity reuse. This result justifies the use of FPR scheme as its main purpose is to improve the performance of CE users. Finally, the average cell SE for FPR scheme is presented in Fig. 2.7 (right) for two different values of κ. For comparison purpose, the cell SEs corresponding to reuse-1 is also presented. Depending on the value of κ, for certain values of B_C/B, sum-cell SE gains over reuse-1 is possible.

SE as a function of κ: The average SEs for the three cases of interest (CC user of interest, CE user of interest, and sum-cell) are presented in Fig. 2.8 for different values of κ. Based on the insights from the previous result, in order to achieve the same CC user SE as reuse-1, we partition the pilot sequences into two sets such that $B_C/B \approx 1-\exp(-\kappa^2)$. From Fig. 2.8 (left), we observe that aforementioned partitioning rule results in marginal reduction in CC user SE compared to reuse-1 scheme. On the other hand, in Fig. 2.8 (middle), we observe that the CE user spectral efficiency of reuse-1 is better compared to the FPR scheme for lower values of κ. This is because of the fact that when κ is low, more number of users lie in the CE region. Since FPR employs reuse-3 scheme, the pilot assignment probability to a randomly selected user reduces, which results in the reduction of user SE compared to the reuse-1 scheme. However, for higher values of κ, FPR performs better compared to the reuse-1 scheme, which is the desired outcome. From Fig. 2.8 (right), we observe that the average sum-cell SE in case of FPR scheme is close to reuse-1 scheme for higher values of κ with the above partitioning rule. System operation at this point is desirable as it improves the CE user SE while providing comparable CC user SE.

SE as a function of B/T_c: From Fig. 2.9, we observe that average SEs are concave functions of B/T_c. Note that with increasing B/T_c, the pilot assignment probability increases and the `SINR` improves due to reduced pilot utilization in the interfering cells. On the other

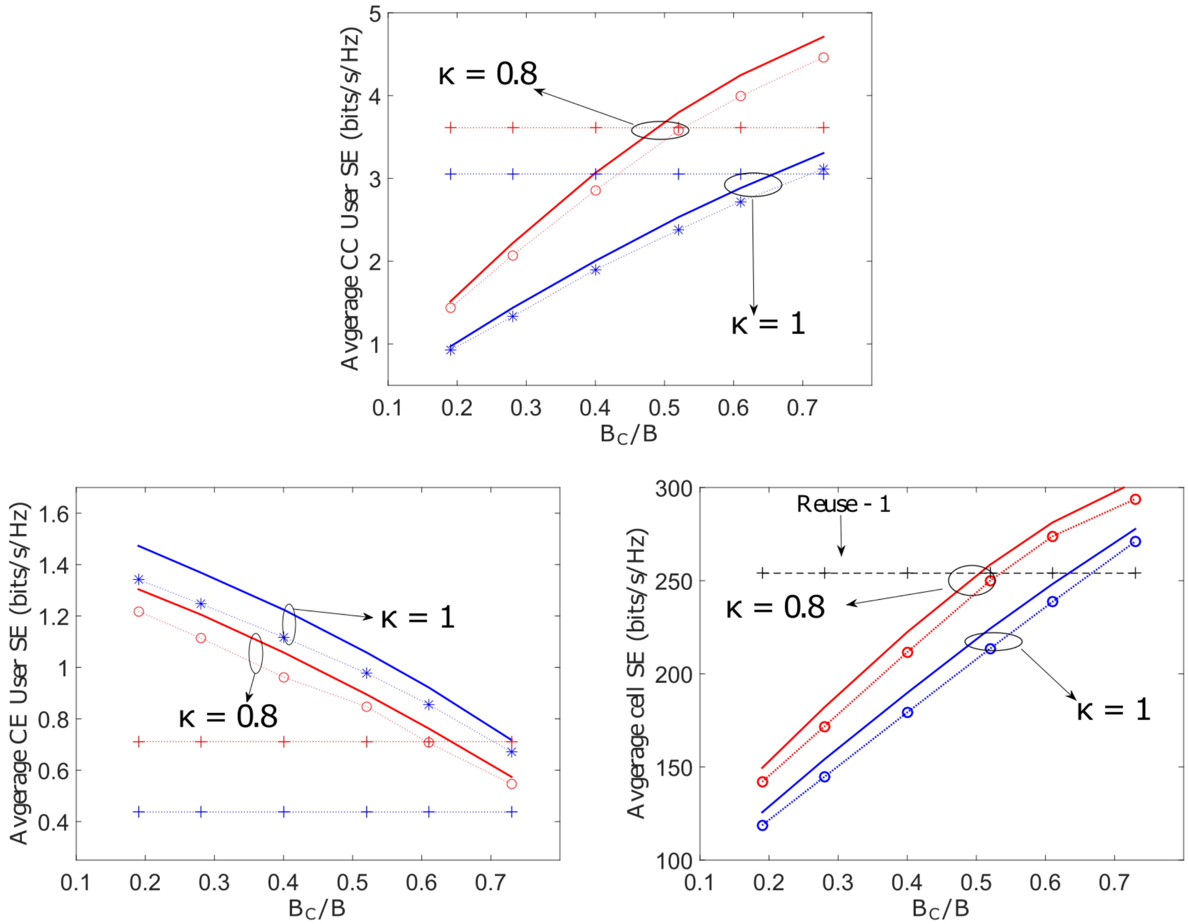

Figure 2.7: The average CC user SE (top), CE user SE (bottom-left), and sum-cell SE (bottom-right) as functions of B_C/B. The solid lines and marked dotted lines represent the theoretical and simulation results, respectively. The dashed lines represent the simulated SEs corresponding to reuse-1. $B = 100, \lambda_{\mathrm{u}} = 150\lambda_0, \lambda_0 = 4 \times 10^{-6}, \beta_f = 3$.

hand, the pre-log factor $(1 - B/T_c)$ reduces with increasing B/T_c. Hence, the concave behavior of the functions is justified. Further, we observe that using the proposed pilot partitioning rule, there is a significant improvement in the CE user SE at the cost of marginal reductions in average CC user SE and average sum-cell SE.

In Fig. 2.10, we show he effect of user density on SE. As expected, with increasing user density, the average user SEs reduces while the sum-cell SE saturates.

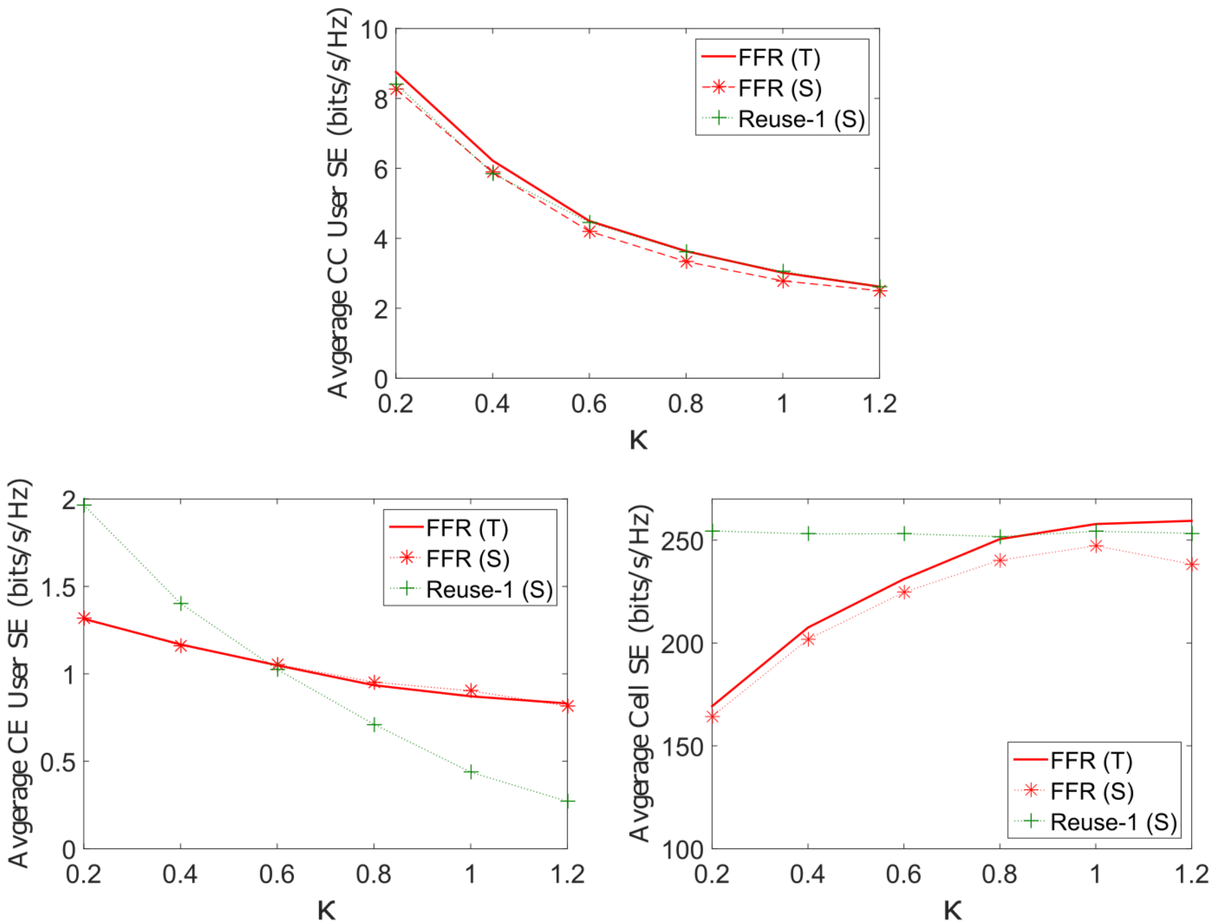

Figure 2.8: The average CC user SE (top), CE user SE (bottom-left), and sum-cell SE (bottom-right) as functions of normalized radius κ. $\lambda_0 = 4 \times 10^{-6}, \lambda_u = 150\lambda_0, B_C/B \approx \left(1 - \exp(-\kappa^2)\right), \beta_f = 3$. The solid lines and marked dotted lines represent the theoretical and simulation results, respectively.

2.7 Concluding remarks and outlook

In this chapter, we have analyzed the UL performance of a mMIMO system with fractional pilot reuse. Using tools from stochastic geometry, we have presented approximate expressions for the SINR coverage probability and average SE of a randomly CC (CE) user in a typical cell. Our analysis begins with the accurate approximations of the area distributions of CC and CE regions of a typical cell. These distributions are used to analyze the pilot assignment probability for the user of interest and utilization probability of a given pilot sequence in a typical cell. While the former quantity is directly used in average user SE evaluation, the latter quantity is helpful in obtaining the average sum-cell SE and statistical characterization of interfering user point processes for both CC and CE cases. All the theoretical results are validated through extensive Monte Carlo simulations. From our system analysis, we arrive at the conclusion that with proper selection of system parameters it is possible to improve the

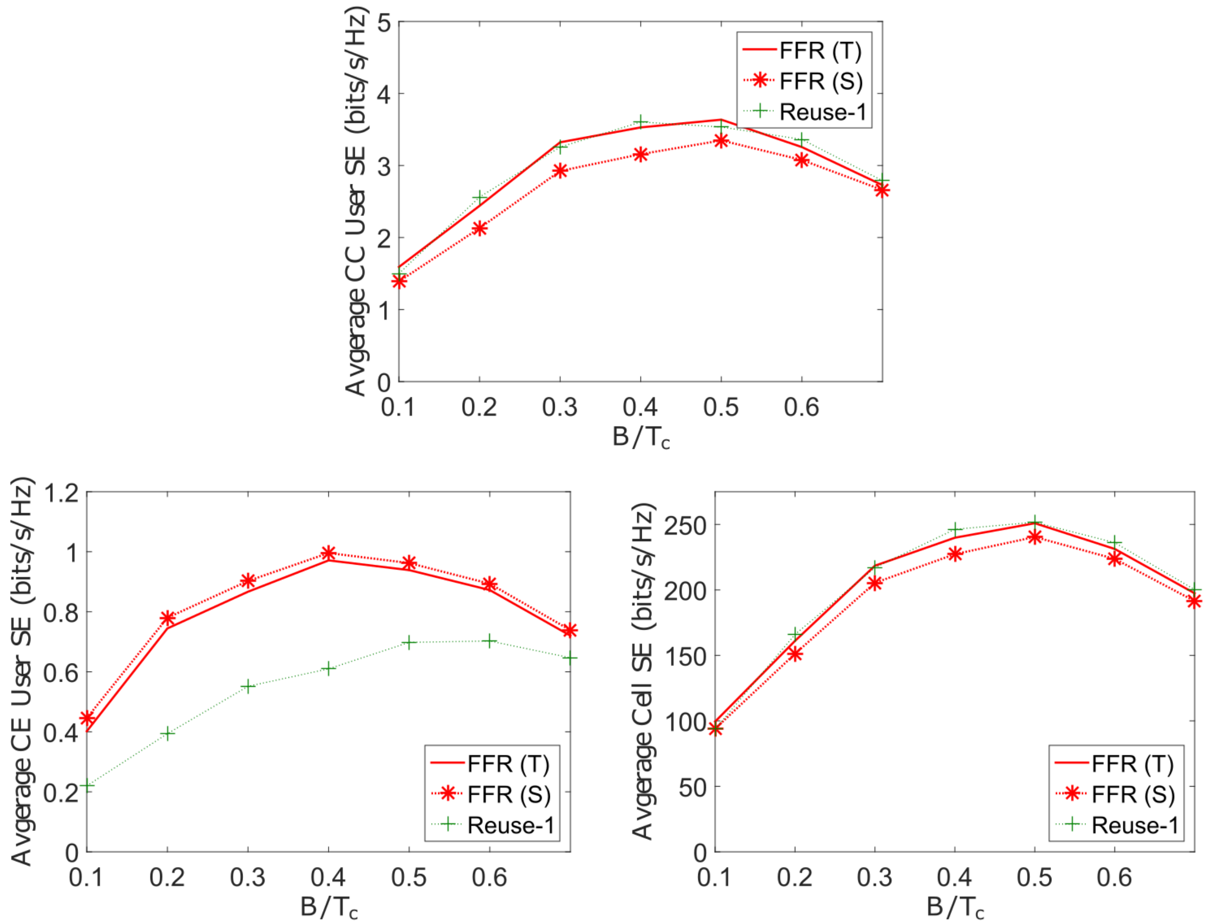

Figure 2.9: The average CC user SE (top), CE user SE (bottom-left), and sum-cell SE (bottom-right) as functions of B/T_c. The solid lines and marked dotted lines represent the theoretical and simulation results, respectively. $\kappa = 0.8, \beta_f = 3, B_C/B \approx \left(1 - \exp(-\kappa^2)\right)$.

CE user SE with negligible performance degradation in the CC user SE and cell SE compared to the unity pilot reuse. There are several possible extensions of this work. In this work, we have considered an asymptotically large number of antennas at the BSs. Hence, a natural extension of this work is to consider a system with finite number of antennas and evaluate the efficacy of FPR. From stochastic geometry perspective, our analysis of interfering user point process formed by CE users can be improved further by modeling this point process as a cluster process or a Poisson hole process [74].

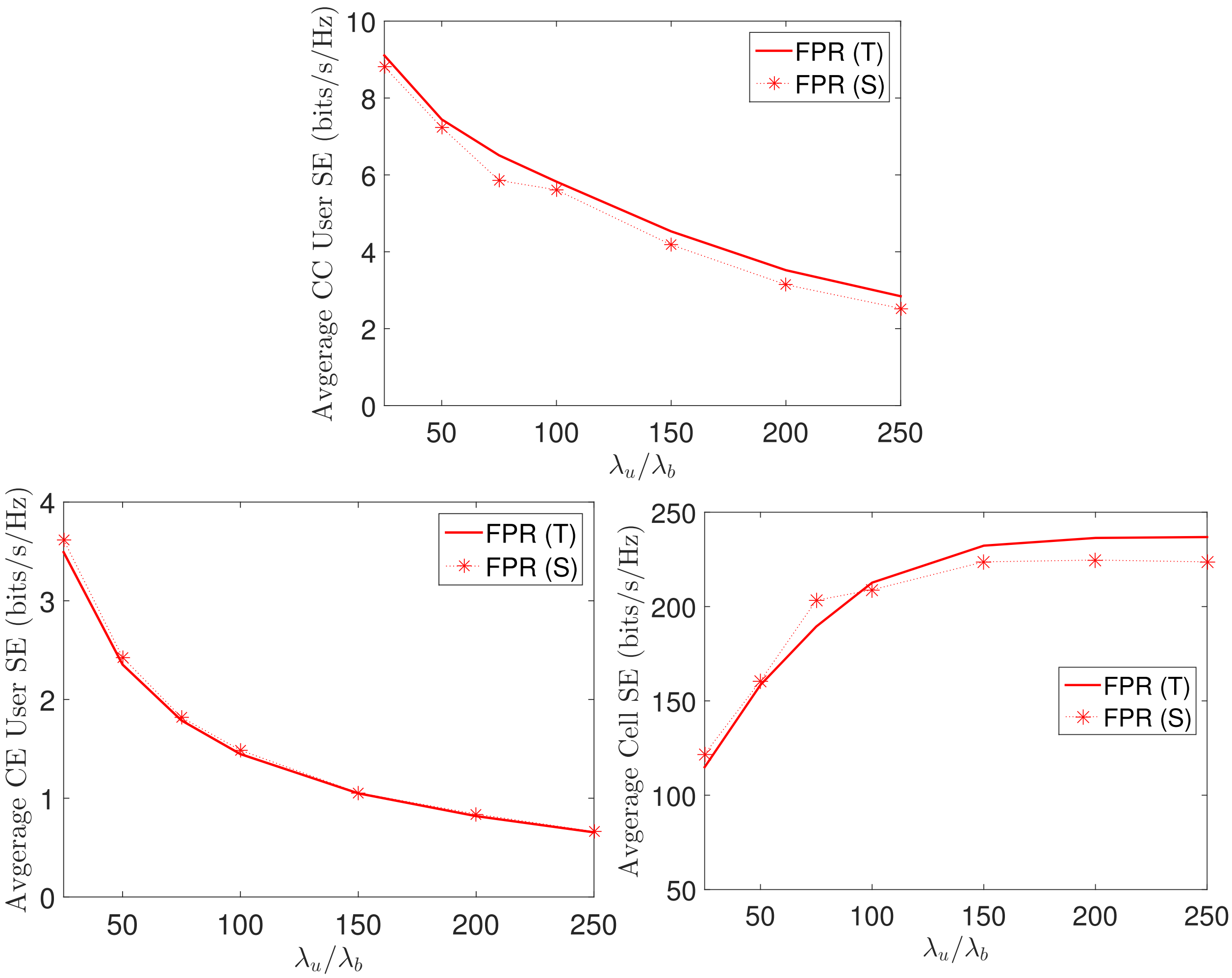

Figure 2.10: Average user SE of a randomly selected CC user (top), CE user (bottom-left), and average sum-cell SE (bottom-right) as a function of λ_u/λ_b. The solid lines and marked dotted lines represent the theoretical and simulation results, respectively. $B = 100, B_C = 31, \kappa = 0.6, \beta_f = 3$.

Chapter 3

Johnson-Mehl Cell-based Analysis of UL Cellular Network with Coupled User and BS Locations

3.1 Introduction

In the stochastic geometry literature, the usual approach is to model the BS and the user locations as two independent stochastic processes. The simplicity and tractability of this model have led to its wide-scale acceptance in the cellular research community. Although it is a good first-order model, it suffers from one key shortcoming of not being able to capture inherent coupling in the user and BS locations, which results from the deployment of BSs in more populated areas. In this chapter, using the approach presented in Chapter 2 to analyze the performance of a cell-center user, we present the uplink (UL) performance for a small cell system where the BS and user locations are coupled. Next, we review the state of the art related to this work and lay out the contributions of this chapter.

3.1.1 Related works and contributions

Since in UL the sources of interference are users, it is necessary to have a thorough understanding of the point processes formed by them. Despite the traction that cellular UL analysis using stochastic geometry has gained (cf. [75, 76, 77]), the understanding of the user point process is still evolving. In a few recent works ([61, 78]), authors have analyzed the statistical properties of the user process for a scenario where the BSs are PPP distributed and the users are uniformly distributed within the Voronoi cell of each BS. While these works take several important steps towards the accurate UL analysis, as mentioned earlier, their model does not capture the real-world location coupling, where the user density will be higher in certain region(s) (ideally in the proximity of a BS), which is a subset of the Voronoi cell of the BS. Building on the analysis presented in [79] for a clustered device-to-device network, the UL performance of a closed-access cellular system is presented in [80], where the coupling in the locations is taken into consideration. To be specific, authors have modeled the user point process as a Matérn cluster process (MCP), where their locations are uniformly distributed within circles centered at cluster head (BS) locations, which follows a Poisson point process (PPP). As a result, two clusters of users can *overlap* resulting in some undesirable artifacts, such as higher density of users in the overlap region, which may not be realistic in a real-world setting. This particular limitation of an MCP model can be overcome by modeling user locations using Johnson-Mehl (JM) cells instead of just circular disks. As shown in Fig. 3.1, this basically restricts the domain of the user locations within circular segments instead of circular disks. Although more realistic, the UL analysis using such a model is not straightforward due to the very fact that the statistical characterization of the point process formed by the interfering users is challenging. As a matter fact, the analysis can be done using the approach developed to analyze the performance of a cell-center user in the previous chapter. In this chapter, on the similar lines as that of cell-center user coverage probability of the previous chapter, we present accurate expression for the UL coverage probability of a typical user in the network. In addition, using the cell-center area distribution result of the previous chapter, we also characterize the average SE of a typical user. Further, using Monte Carlo simulations, we compare the UL coverage in the MCP based model used in [80] and the proposed JM cell-based model.

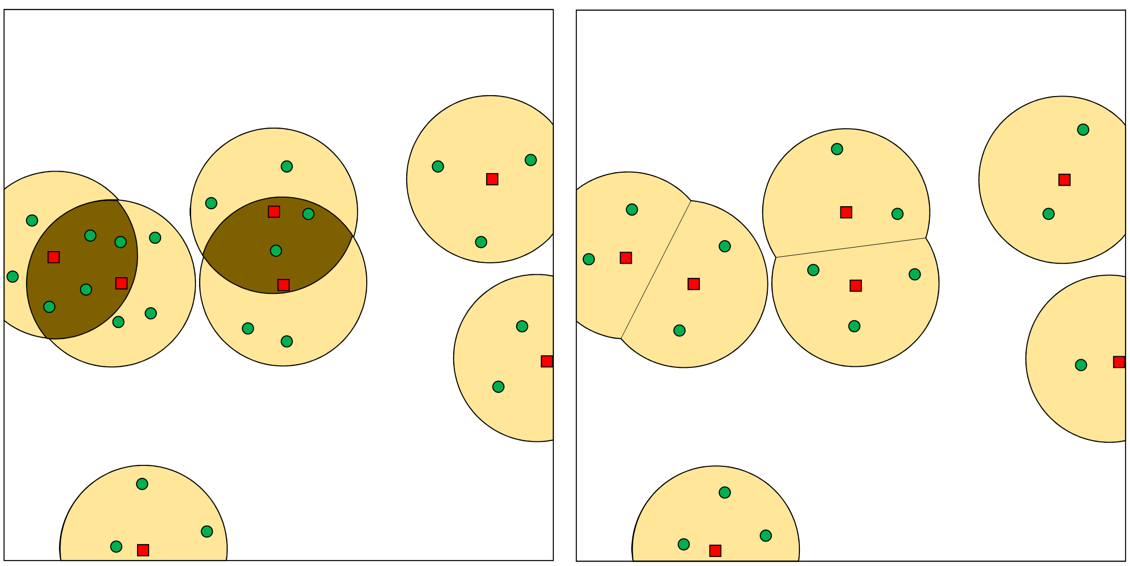

Figure 3.1: (Left) A realization of MCP. Overlapping regions have higher user density. (Right) A realization of JM cell-based modeling that results in uniform user density in the clustered locations.

3.2 System model

3.2.1 Network model

We consider a single tier network, where the locations of the BSs belong to the set $\Psi_b = \Phi_b \cup \{\mathbf{o}\}$, and the locations in Φ_b form a realization of a homogeneous PPP of density λ_0.

By virtue of Slyvniak's theorem, Ψ_b is also a homogeneous PPP of density λ_0. The location of the j-th BS is denoted by $\mathbf{b}_j \in \Psi_b$, where index j does not represent any ordering and $\mathbf{b}_0 = \mathbf{o} = (0, 0)$ is at the origin. In order to capture the coupling among the user and BS locations, we consider that users are uniformly distributed within the JM cell of each BS. While the JM cells can be described from the perspective of random nucleation and growth process [62], we present a more intuitive definition for the JM cell associated with a typical BS. Recall that the locations of the BSs can be used as seed points to form a Poisson-Voronoi tessellation (PVT) that completely covers $\mathbb{R}^2$ with convex sets known as Poisson Voronoi cells (PVC). Mathematically, the PVC of the typical BS at the origin (0-th BS) is given as

$$\mathcal{V}_{\Psi_b}(\mathbf{o}) = \{\mathbf{x} \in \mathbb{R}^2 : \|\mathbf{x}\| \leq \|\mathbf{x} - \mathbf{b}_j\|, \forall \mathbf{b}_j \in \Psi_b\}. \tag{3.1}$$

For a given threshold radius R_c, JM cell of the typical BS is defined as the region of its PVC that is within a distance R_c from its location, i.e. for the typical BS at the origin (0-th BS) we define its JM cell as $\mathcal{X}_C(\mathbf{o}, R_c, \Psi_b) =$

$$\{\mathbf{x} \in \mathcal{V}_{\Psi_b}(\mathbf{o}) : \|\mathbf{x}\| \leq R_c\} = \mathcal{V}_{\Psi_b}(\mathbf{o}) \cap \mathcal{B}_{R_c}(\mathbf{o}), \tag{3.2}$$

where $\mathcal{B}_{R_c}(\mathbf{o})$ denotes a circle of radius R_c centred at $\mathbf{o}$. We denote the area of the JM cell associated with the j-th BS (or with slight abuse of notation any typical BS) as $X_{Cj}(\lambda_0, R_c) = |\mathcal{X}_C(\mathbf{b}_j, R_c, \Psi_b)|$. Let N_{Cj} be the number of users associated with the j-th BS. We assume that N_{Cj} depends on the j-th JM cell area and follows a zero-truncated Poisson distribution with parameters $\lambda_u X_{Cj}(\lambda_0, R_c)$. To be more precise, conditioned on the area of the j-th JM cell X_C, the probability mass function of N_{Cj} is given as

$$\mathbb{P}\left[N_{Cj} = n | x_c\right] = \frac{\exp(-\lambda_u x_c)(\lambda_u x_c)^n}{n!(1 - \exp(-\lambda_u x_c))}. \tag{3.3}$$

One of the motivations behind consideration of the truncated Poisson distributions is to ensure that each BS in the network has at least one active user within its JM cell. Consequently, this truncated Poisson distribution allows to model the user point process (to be defined shortly) as a Type-I process introduced in [61]. Note that λ_u can be used to vary the load (the number of users per JM cell) in the network.

We restrict our analysis to a narrow band single resource block system with bandwidth B. Extension of the analysis to a system with multiple resource block is straightforward and is skipped in favour of simpler exposition. Further, we assume that this resource block is shared among all the users associated to a BS in round robin manner. Note that at any given time, there is one active user in the JM cell of each BS. We present the performance analysis for a randomly selected user associated with the 0-th BS that we term as the typical user in the network. Let the point process formed by the locations of these active users be denoted as $\Psi_{\mathtt{u}}$, which is defined as

$$\Psi_{\mathtt{u}} = \{U(\mathcal{X}_C(\mathbf{b}_j, R_c, \Psi_b)) : \forall \mathbf{b}_j \in \Psi_b\},$$

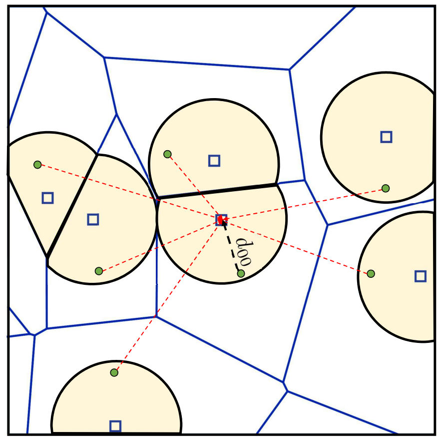

Figure 3.2: A representative network diagram for the UL with a single active user in each JM cell. The BS and user locations are denoted by squares and dots, respectively.

where $U(B)$ denotes a uniformly distributed point in $B \subset \mathbb{R}^2$. From the construction, it is clear that the density of $\Psi_{\mathbf{u}}$ is λ_0. Except the typical user attached to the 0-th BS, rest of the users in the network are interfering users. Hence, the point processes formed by these interfering users is given as

$$\Phi_{\mathbf{u}} = \{U(\mathcal{X}_C(\mathbf{b}_j, R_c, \Psi_b)) : \forall \mathbf{b}_j \in \Phi_b\}.$$

We defer the discussion on the properties of the point process $\Phi_{\mathbf{u}}$ to Section 3.3.

Let the location of the active user attached to the j-th BS is denoted by $\mathbf{u}_j$. Then, the distance between a user at $\mathbf{u}_j$ and a BS at $\mathbf{b}_i$ is given as $d_{ij} = \|\mathbf{u}_j - \mathbf{b}_i\|$. In order to characterize the coverage probability, the first step is the knowledge of the distribution of serving distance D_{00} between the 0-th BS and the typical user. In case of a typical PVC, the distance distribution between the BS and a randomly located point in the PVC is approximated as Rayleigh distribution with scale parameter $(\sqrt{2\pi\lambda_0 c_2})^{-1}$, where $c_2 = 5/4$ is an empirically obtained correction factor [63, 61]. Since, in our case, the user can not lie beyond the threshold radius R_c, it is reasonable to approximate the distribution D_{00} to follow truncated Rayleigh distribution, which is given as

$$F_{D_{00}}(d|R_c) = \frac{1 - \exp(-\pi c_2 \lambda_0 d^2)}{1 - \exp(-\pi c_2 \lambda_0 R_c^2)}. \tag{3.4}$$

At this point, we redefine R_c in terms of normalized radius κ as $R_c = \kappa/\sqrt{\pi c_2 \lambda_0}, \quad \kappa \in [0, \infty)$. In Sec. 3.3, κ will be used to define the scale invariant pair correlation function (PCF) of $\Phi_{\mathbf{u}}$. This scale invariant property provides the flexibility to obtain PCF for $\lambda_0 = 1$, which can later be scaled to get the density function of $\Phi_{\mathbf{u}}$ for any value of λ_0. An illustrative diagram of the network is presented in Fig. 3.2.

The channel gain between a BS and the typical user depends on small scale fading gain on the resource block, as well as the distance-dependent path loss. We assume that the small scale fading gain follows exponential distribution with mean 1 and the path loss between two nodes at a distance d is $d^{-\alpha}$, where α is the path loss exponent. The consideration of shadowing is left for future work. Under the above set of assumptions and in an interference limited scenario, the signal to interference ratio ($\mathtt{SIR}$) of the typical user associated with the 0-th BS is given as

$$\mathtt{SIR}_0 = h_{00} d_{00}^{-\alpha} \Big(\sum_{\mathbf{u}_j \in \Phi_{\mathtt{u}}} h_{0j} d_{0j}^{-\alpha} \Big)^{-1}, \tag{3.5}$$

where h_{0j} is the small scale channel gain between the typical user and the j-th BS.

3.2.2 Performance metrics

In this work, the system performance is evaluated using the following metrics.

$\mathtt{SIR}$ coverage probability

The $\mathtt{SIR}$ coverage probability of the typical user for a target threshold T is defined as

$$\mathtt{P_c}(T, \kappa, \lambda_0) = \mathbb{P}\left[\mathtt{SIR}_0 > T\right]. \tag{3.6}$$

Average user spectral efficiency

Considering round robin scheduling scheme, the average SE of a typical user is given as

$$\overline{\mathtt{SE}}(\kappa, \lambda_0) = \mathbb{E}\left[\frac{B}{N_{C0}} \log_2(1 + \mathtt{SIR}_0)\right], \tag{3.7}$$

where B is the system bandwidth, and N_{C0} is the number of users associated with the 0-th BS. In the following sections, we present our approach to obtain approximate but accurate theoretical expressions for the aforementioned quantities.

3.3 $\mathtt{SIR}$ coverage and $\mathtt{SE}$ analysis

In Section 3.2, we introduced the point process formed by the interfering user locations $\Phi_{\mathtt{u}}$ without providing any details regarding its statistical properties. For coverage analysis the knowledge of the distribution of locations of users is essential. The objective of this section is to characterize the statistical properties of $\Phi_{\mathtt{u}}$ that is subsequently used to get the coverage probability expression. As mentioned earlier, in this case, the point process formed by the interfering users is same as the point process of interfering users corresponding to cell-center region discussed in the previous chapter (please refer to Sec. 2.5). For the sake of completeness, in the following lemma, we present the $\mathtt{PCF}$ of the interfering users.

Lemma 3.1. *The* PCF *of interfering user locations w.r.t. the* 0*-th BS is given as*

$$g_1(r,\kappa) \approx 1 - \exp\left(-2\pi r^2 \mathbb{E}\left[X_{Cj}(1,\kappa/\sqrt{\pi c_2})^{-1}\right]\right). \tag{3.8}$$

Proof: Please refer to Appendix A.2. ■

Using the above PCF, we approximate $\Phi_{\mathbf{u}}$ as a non-homogeneous PPP such that for all $f : \mathbb{R}^2 \mapsto \mathbb{R}^+$

$$\mathbb{E}\bigg[\sum_{x\in\Phi_{\mathrm{u}}} f(x)\bigg] = \mathbb{E}\bigg[\sum_{x\in\Phi_{\mathbf{u}}^{(\mathrm{PPP})}} f(x)\bigg]$$
$$\implies \lambda_0 \int\limits_{\mathbf{x}\in\mathbb{R}^2} f(\mathbf{x}) g_1(\|\mathbf{x}\|\sqrt{\lambda_0},\kappa)\mathrm{d}\mathbf{x} = \int\limits_{\mathbf{x}\in\mathbb{R}^2} f(\mathbf{x})\lambda_{\mathbf{u}}^{(\mathrm{PPP})}(\|\mathbf{x}\|,\kappa)\mathrm{d}\mathbf{x},$$

where the second step follows from the application of Campbell's theorem and replacing the intensity measure by the reduced second factorial moment measure [10, Chapter 8]. Hence, the density of $\Phi_{\mathbf{u}}$, if approximated as a non-homogeneous PPP, is given as

$$\lambda_{\mathbf{u}}^{(\mathrm{PPP})}(r,\kappa) = \lambda_0\left(1 - e^{-2\pi\lambda_0 r^2 \mathbb{E}\left[X_C(1,\kappa/\sqrt{\pi c_2})^{-1}\right]}\right). \tag{3.9}$$

3.3.1 Coverage probability of a typical user

To obtain the coverage probability, we first present the LT of aggregate interference in the following Lemma.

Lemma 3.2. *The* LT *of aggregate interference at the* 0*-th BS is given as*

$$\mathcal{L}_{I_{\mathrm{agg}}}(s) = \exp\left(-2\pi\int_{r=0}^{\infty}\frac{\lambda_{\mathbf{u}}^{(\mathrm{PPP})}(r,\kappa) r\mathrm{d}r}{1+r^\alpha s^{-1}}\right).$$

Proof: As per the definition, the LT of aggregate interference is given as

$$\begin{aligned}\mathcal{L}_{I_{\mathrm{agg}}}(s) =& \mathbb{E}_{\Phi_{\mathrm{u}},\{h_{0j}\}}\left[\exp(-sI_{\mathrm{agg}})\right] = \mathbb{E}\left[\prod_{\mathbf{u}_j\in\Phi_{\mathrm{u}}}\mathbb{E}_{h_{0j}}\left[\exp(-sh_{0j}d_{0j}^{-\alpha})\right]\right]\\ =&\mathbb{E}\left[\prod_{\mathbf{u}_j\in\Phi_{\mathrm{u}}}\frac{1}{1+sd_{0j}^{-\alpha}}\right] = \exp\left(-2\pi\int_{r=0}^{\infty}\frac{\lambda_{\mathbf{u}}^{(\mathrm{PPP})}(r,\kappa)r\mathrm{d}r}{1+r^\alpha s^{-1}}\right),\end{aligned}$$

where the last step follows from the application of PGFL of PPP. ■

Now using the LT of interference, in the following proposition, we present the coverage probability of a randomly selected user associated with the typical BS.

Proposition 3.3. *For a target* $\mathtt{SIR}$ *threshold* T*, the UL coverage probability of a typical user is given as*

$$\mathtt{P_c}(T,\kappa,\lambda_0) = \int_{r=0}^{R_c} \mathcal{L}_{I_{\text{agg}}}(r^{\alpha}T) f_{D_{00}}(r|R_c)\mathrm{d}r. \tag{3.10}$$

Proof: The coverage probability for the typical user is defined as

$$\mathbb{P}\left[\mathtt{SIR}_0 > T\right] = \mathbb{P}\left[h_{00} > d_{00}^{\alpha} T I_{agg}\right] = \mathbb{E}_{D_{00}}\left[e^{-d_{00}^{\alpha} T I_{\text{agg}}}\right],$$

where (3.10) follows from deconditioning w.r.t. D_{00}. ■

Using (3.10) and the area distribution of a typical JM cell (Sec. 2.3.2), in the following proposition, we present the average achievable SE of a typical user.

Proposition 3.4. *The average SE of a typical user is given as*

$$\overline{\mathtt{SE}}(\kappa,\lambda_0,\lambda_u) = B\mathbb{E}\left[N_{C0}^{-1}\right] \int_{t=0}^{\infty} \mathtt{P_c}(2^t - 1,\kappa,\lambda_0)\mathrm{d}t, \tag{3.11}$$

where $\mathbb{E}\left[N_{C0}^{-1}\right] = \int\limits_{x_c=0}^{\pi R_c^2} \sum_{n=1}^{\infty} \frac{\mathbb{P}[N_{C0}=n|x_c]}{n} f_{X_c}(x_c)\mathrm{d}x_c.$

Proof: Assuming independence between N_{C0} and $\mathtt{SIR}_0$, (3.7) can be approximately expressed as

$$\overline{\mathtt{SE}}(\kappa,\lambda_0) = B\mathbb{E}\left[N_{C0}^{-1}\right]\mathbb{E}\left[\log_2(1+\mathtt{SIR}_0)\right].$$

The expression in (3.11) follows from the fact that for a positive random variable X, $\mathbb{E}[X] = \int_{t=0}^{\infty} \mathbb{P}[X > t]\,\mathrm{d}t$. ■

3.4 Results

In this section, we verify the accuracy of the approximate theoretical expressions using Monte Carlo simulations. We consider the BS density $\lambda_0 = 4\times10^{-6}$ BS/m^2, and path loss exponent $\alpha = 3.7$. The system bandwidth B is taken to be 1 Hz to focus on user SE.

The $\mathtt{SIR}$ coverage probability of a typical user in UL is presented in Fig. 3.3 for different values of κ (equivalently R_c). As observed from the figure, with increasing κ reduction in average serving distance results in coverage probability degradation. Further, in order to highlight the usefulness of the proposed model, through Monte Carlo simulations, we present the coverage probability (dashed black lines) of a typical user using MCP based model [80]. As observed from the figure, with respect to the proposed model, the MCP-based model underestimates the coverage probability.

The average SE of the typical user is presented in Fig. 3.4. As observed from the figure, the average SE decreases with increasing κ. This is justified by the fact that with increasing κ the coverage probability reduces. Further, due to increasing number of users, the typical user is assigned the resource block less frequently. From this figure, we also gain insights regarding the achievable average user SE for given λ_u, κ. For example, a network with $\lambda_u = 200\lambda_0$ users/m^2 and $\kappa \geq 0.2$, cannot support an average user SE of 2 bits/s/Hz. In both the figures, the theoretical results closely match with the simulation results, which verifies the accuracy of the theoretical expressions.

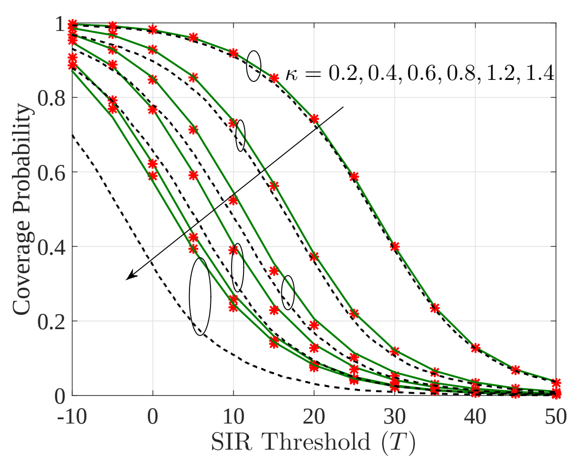

Figure 3.3: The SIR coverage probability of a typical user. Markers and solid lines represent the simulation and theoretical results, respectively, based on the proposed model. The dashed line represent the coverage probability of a typical user based on MCP model. $\lambda_0 = 4 \times 10^{-6}$ BS/m^2, $\lambda_u = 200\lambda_0$ users/m^2.

3.5 Conclusion

In this chapter, we proposed a new model to analyze the UL performance of a cellular network considering coupling between BS and user locations. This coupling is captured by modeling the users to be uniformly distributed in the JM cells of each BS. The first important result of this work is the approximate area distribution of a typical JM cell that can be used to model the load distribution (in terms of the number of users) in a typical BS. The second important outcome of this work is the statistical characterization of the point process formed by the interfering user locations that is later used to derive the UL coverage

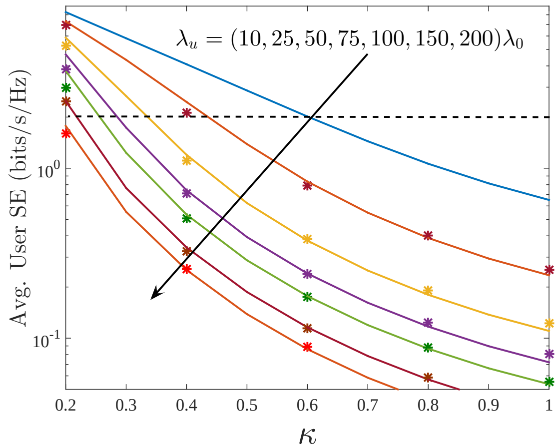

Figure 3.4: The average spectral efficiency of a typical user. Markers represent simulation results. $\kappa = R_c\sqrt{\pi c_2 \lambda_0}, \lambda_0 = 4 \times 10^{-6}$ BS/m^2.

probability for a typical user. The accuracy of the approximate theoretical expressions is verified through Monte Carlo simulations using two key metrics: coverage probability and average user spectral efficiency.

Chapter 4

Stochastic Geometry-based Analysis of Uplink Massive MIMO with Power Control

4.1 Introduction

In Chapter 2, from the perspective of tractability, we considered a mMIMO system without uplink (UL) power control. However, in order to mitigate the near-far effect power control in the UL is considered to be important. Fractional power control (FPC), which is a distance dependent power control scheme, is one of the effective and distributed approaches prevalent in the cellular network. The goal of this chapter is to analyze the UL performance of a mMIMO cellular network with FPC. For simplicity, we restrict out attention to unity pilot reuse.

4.1.1 Motivation and related Work

The stochastic geometry-based UL analysis of cellular networks has been performed in [75, 77, 81] with slightly different approaches. The key intermediate step in these works is the characterization of network interference, which is usually modeled as a power-law shot-noise field. While the characterization of Laplace transform (`LT`) of this shot-noise field is quite tractable, the same is not true for the probability density function (`PDF`) or cumulative distribution distribution function (`CDF`). Therefore, these works mainly rely on the Rayleigh fading assumption under which the UL coverage probability can be directly expressed in terms of the `LT`, thus circumventing the need for characterizing the `PDF` or `CDF` explicitly [12]. On the contrary, in mMIMO systems, small-scale fading gets *spatially* averaged out due to the presence of large number of antennas. Hence, in these scenarios the absence of exponentially distributed term in the received power means that we cannot directly apply the approaches developed in [75, 77, 81]. While the modeling approaches for the DL of a cellular system in the absence of fading can be found in [82, 83, 84], the fundamental differences between the UL and DL models make it difficult to apply them directly for the analysis of UL.

Having said that, authors in [51, 52, 53, 54, 55, 56] do attempt the mMIMO UL system analysis, *albeit* under significant simplifications. While analysis in [51] is limited to the consideration of exponential fading (shadowing), [52, 53, 54] does not incorporate UL power control. In [55], author has analyzed the UL throughput distribution for a hexagonal cellular layout. Authors in [56] have analyzed the performance of the UL massive MIMO system with finite number of antennas. However, the interference field is modeled as a homogeneous PPP beyond an exclusion zone. Further simplification in analysis is made by replacing the aggregate inference by its expected value. Hence, the model does not capture variance of the aggregate interference. We address these shortcomings by providing a more comprehensive analysis in this work. The key contributions are summarized next.

4.1.2 Contributions

In this chapter, we present a comprehensive and accurate approach to the UL analysis of mMIMO networks with asymptotically large number of antennas and fractional power control. As discussed above, due to absence of fading, the conventional `LT`-based approach to evaluate coverage probability is not directly applicable in this case. We use an alternate approach based on classical Gil-Pelaez inversion theorem to obtain the coverage probability from the characteristic function (`CHF`) of the interference. However, this method results in significant computational burden. Hence, we propose a numerically efficient approach that is based on approximate statistical characterization of the total interference power as the sum of two terms: (i) the most dominant term, and (ii) the mean of the rest of the terms conditioned on the dominant term. However, due to power control by users, characterizing the distribution of the dominant interference term is not straightforward. Further, the correlation in the user distances also imposes challenge to the analysis. In order to circumvent these problems, we resort to the careful application of displacement theorem to capture the effect of random UL power and the correlation of UL power of each user with respect to its distance from the BS of interest. Using this approach, we derive tractable and accurate expressions for both coverage probability and spectral efficiency of the typical user. These results also enable the analysis of the ergodic and outage spectral efficiency for different power control fraction.

4.2 System model

4.2.1 Network model

In this work, we focus on the performance analysis of the UL scenario of a cellular system where BSs are equipped with $M \to \infty$ antennas. The locations of the BSs form a realization of homogeneous PPP Ψ_b with density λ_0. The location of the j-th BS is denoted by $\mathbf{b}_j \in \Psi_b$,

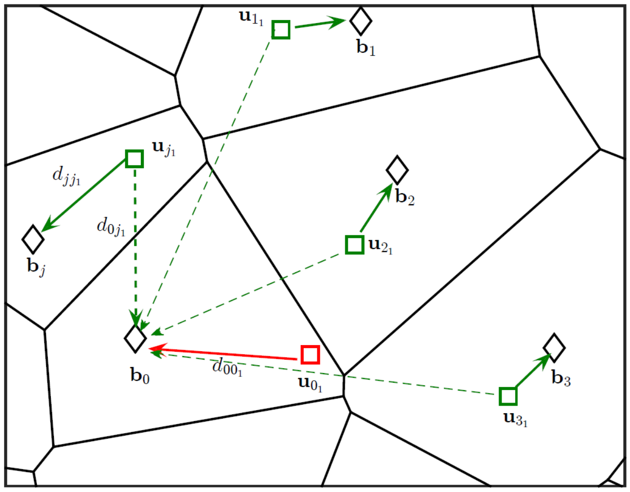

Figure 4.1: A representative network diagram for the UL with $K = 1$. Diamonds and squares represent BS and user locations, respectively. The typical user $\mathbf{u}_{0_1}$ is located at the origin and served by the tagged BS located at $\mathbf{b}_0$.

where the index j does not represent any ordering. We assume that the user locations follow a homogeneous PPP with density λ_a and independent of the BS process Ψ_b. In this work, we consider that each user is attached to the nearest BS. Further, λ_a is assumed to be sufficiently large to ensure that there are at least $K(< M)$ users that get attached to each BS. Out of all the users that are attached to a BS, K users are randomly selected to transmit on a specific resource block. We assume a slotted system in time and frequency such as orthogonal frequency division multiple access, where by definition, the resource blocks are orthogonal both in time and frequency. On the assumption that network interference and channel gain across resource blocks remain i.i.d., we focus our analysis on an arbitrarily selected resource block that we term the *representative resource block*. Exploiting the availability of multiple antennas with suitable signal processing techniques, on the representative resource block, each BS can simultaneously decode the signals transmitted by all the K users attached to it.

For successful decoding of the transmitted data, BSs should posses the CSI of all K users attached to it, which is facilitated by the use of K orthogonal pilot sequences. As a typical consideration, these pilot sequences are reused in each cell. The location of the user attached to the j-th BS and using the k-th pilot sequence is denoted by $\mathbf{u}_{j_k}$. Without loss of generality, we consider that the typical user uses the k-th pilot sequence and is located at the origin. Further, the BS to which it is attached is known as the *tagged BS* and its location is denoted by $\mathbf{b}_0$. The distance between a user at $\mathbf{u}_{j_k}$ and a BS at $\mathbf{b}_i$ is given as $d_{ij_k} = \|\mathbf{u}_{j_k} - \mathbf{b}_i\|$. A representative diagram is presented in Figure 4.1 for $K = 1$. Since each BS has one user attached to it that uses the k-th pilot sequence, we make the following assumption regarding the random locations of these users.

Assumption 4.1. *The locations of all the users using the k-th pilot sequence (typical and* *interfering) form a realization of a homogeneous PPP Ψ_{u_k} with the same intensity $\lambda_u = \lambda_0$ as that of the BSs. Apart from the typical user, the rest of the users in the network belong to $\Phi_{u_k} = \Psi_{u_k} \setminus \mathbf{u}_{0_k}$.*

Above assumption is very typical to the works that focus on the UL system analysis (c.f. [77]). Note that due to the minimum distance associations policy, every user in Φ_{u_k} must satisfy the condition $d_{0j_k} > d_{jj_k}$.

Since the users are attached to respective serving BS based on minimum distance criteria, every user has to lie within the Voronoi cell of its BS. This gives rise to the inherent correlation of the distances of the users from their attached BSs. Accurate characterization of this correlation is a difficult task. Hence, motivated by the results presented in [75], we make the following assumption regarding these distances:

Assumption 4.2. *The distances of users, which use the k-th pilot sequences in each cell, from their attached BSs are independently and identically distributed.*

Since the users are connected to the nearest BS, the PDF of the d_{jj_k} is Rayleigh and is given as

$$f_{d_{jj_k}}(x) = 2\pi\lambda_0 x \exp(-\pi\lambda_0 x^2). \tag{4.1}$$

4.2.2 Channel model

We consider a system where each link suffers from two multiplicative wireless channel impairments, namely distance dependent path loss and multi-path fading. The effect of shadowing can be formally included in the analysis using the displacement theorem [83], but is ignored in favor of a simpler exposition. The channel vector between the user located at $\mathbf{u}_{j_k}$ and the M antenna elements of the BS located at $\mathbf{b}_i$ is given as

$$\mathbf{g}_{ij_k} = d_{ij_k}^{-\alpha/2}\mathbf{h}_{ij_k}, \tag{4.2}$$

where α is the path loss exponent, $\mathbf{h}_{ij_k} \sim \mathcal{CN}(\mathbf{0}_M, \mathbf{I}_M)$ is a $\mathbb{C}^{M\times 1}$ complex Gaussian noise vector. We assume that these channel vectors exhibit quasi-orthogonality, i.e.

$$\lim_{M\to\infty} \frac{1}{M}\mathbf{h}_{ij_k}^H \mathbf{h}_{ij_l} \to \begin{cases} 0 & j_k \neq j_l \\ 1 & j_k = j_l. \end{cases} \tag{4.3}$$

Power control

In this work, we consider the FPC scheme [75]. In this scheme, the transmission power of the user is chosen such that it either partially or fully compensates for the path loss with respect to the attached BS. Therefore, the k-th user attached to the j-th BS transmits at a power level

$$p_{uj_k} = \rho_u d_{jj_k}^{\alpha\epsilon}, \tag{4.4}$$

where ϵ is the power control fraction with $0 \leq \epsilon \leq 1$, and ρ_u is a constant (*open loop* power). When $\epsilon = 0$, we deal with a system where the users transmit with a fixed power ρ_u. On the other hand, when $\epsilon = 1$, the received power at the attached BS is ρ_u irrespective of the distance of the user. To maintain simplicity, we do not put any constraint on the maximum transmission power of a user.

Channel estimation

Under the assumption that each pilot sequence is reused in every cell, the channel estimates of the typical user at the tagged BS is a function of $\{\mathbf{g}_{0j_k}\}_{\mathbf{u}_{j_k}\in\Psi_{u_k}}$, i.e. the channel vectors of all the users in the network using k-th pilot sequence and the tagged BS. For simplicity, we assume

$$\tilde{\mathbf{g}}_{00_k} = \sum_{\mathbf{u}_{j_k}\in\Psi_{u_k}} p_{uj_k}\mathbf{g}_{0j_k} + \mathbf{v}_0, \tag{4.5}$$

where $\mathbf{v}_0 \in \mathbb{C}^{M\times 1}$ is a complex Gaussian noise vector.

4.2.3 Signal model and asymptotic SINR

Under the assumption of a perfectly synchronized network, the received signal vector at the tagged BS is given as

$$\mathbf{r}_0 = d_{00_k}^{-\alpha/2}\mathbf{h}_{00_k}x_{0k} + \underbrace{\sum_{i=1,i\neq k}^{K} d_{00_i}^{-\alpha/2}\mathbf{h}_{00_i}x_{0i}}_{\text{Intracell}} + \underbrace{\sum_{j\in\Psi_b}\sum_{i=1}^{K} d_{0j_i}^{-\alpha/2}\mathbf{h}_{0j_i}x_{ji}}_{\text{Intercell}} + \mathbf{n}_0, \tag{4.6}$$

where x_{ji} is the data symbol transmitted by the user using the i-th pilot sequence in the j-th cell. We assume that $\mathbb{E}[x_{ji}] = 0$ and $\mathbb{E}[\|x_{ji}\|^2] = p_{uj_i}$. Further, $\mathbf{n}_0 \in \mathbb{C}^{M\times 1}$ is a complex Gaussian noise vector whose elements are of zero mean and unit variance. In order to recover the data of the typical user, the tagged BS use MRC detection scheme, where the filter coefficients are given as $\mathbf{w}_{0_k} = \frac{1}{M}\tilde{\mathbf{g}}_{00_k}^H$. As demonstrated in various works in the literature (cf. [64]), the asymptotic SINR of the typical user is independent of the detection scheme used at the tagged BS. Now, the detected symbol for the typical user is given as $\hat{x}_{0k} = \mathbf{w}_{0_k}\mathbf{r}_0$. As the number of antennas $M \to \infty$, due to quasi-orthogonality of the channel, it can be shown that the detected symbol is only affected by the interference from the users using the

k-th pilot sequence in other cells, a.k.a. pilot contamination induced interference. Hence, the SINR of the typical user can be expressed as

$$\mathtt{SINR}_{0_k} = \frac{d_{00_k}^{2\alpha(\epsilon-1)}}{\sum\limits_{\mathbf{u}_{j_k}\in\Phi_{u_k}} d_{jj_k}^{2\alpha\epsilon} d_{0j_k}^{-2\alpha}} = \frac{d_{00_k}^{2\alpha(\epsilon-1)}}{\sum\limits_{\mathbf{u}_{j_k}\in\Psi_{u_k}} d_{jj_k}^{2\alpha\epsilon} d_{0j_k}^{-2\alpha} \mathbf{1}\left(d_{jj_k} < d_{0j_k}\right)}. \tag{4.7}$$

A detalied proof of the above expression is readily available in literature (cf. [2, 53]). Since the above expression is independent of ρ_u, without loss of generality, we assume $\rho_u \equiv 1$. In order to simplify notation, we drop the subscript k in subsequent analysis. With the availability of typical user SINR expression, in the next section we present the coverage probability and user spectral efficiency expressions.

4.3 User coverage probability and spectral efficiency

This is the main technical section of the chapter, where we present the coverage probability and spectral efficiency expressions for the typical user based on the discussed system model.

As highlighted earlier, in case of mMIMO systems, due to the spatial averaging of small scale channel variation, the simpler evaluation of coverage probability leveraging LT of interference in presence of exponential fading term in the desired link is not possible. One alternate approach to get coverage probability is to invert the CHF of interference using Gil-Pelaez inversion theorem [69, 70].

Inversion theorem based approach

From the previous section, it is clear that the UL aggregate interference (I_{agg}) at the tagged BS is given by the denominator of (4.7). In the following Lemma we present the CHF of aggregate interference.

Lemma 4.3. *The* CHF *of aggregate interference is given as*

$$\varphi_{I_{agg}}(w) = \exp\left(-2\pi\lambda_0 \int\limits_{r=0}^{\infty} \left[1 - \exp(-\pi\lambda_0 r^2) - \int\limits_{y=0}^{r} f_{d_{jj}}(y) \exp(jw\frac{r^{-2\alpha}}{y^{-2\alpha\epsilon}})\mathrm{d}y\right] r\mathrm{d}r\right) \tag{4.8}$$

Proof: The proof has been relegated to Appendix B.3. ■

Using the CHF of aggregate interference and Gil-Pelaez inversion theorem, in the following proposition we present the expression for coverage probability of the typical user.

Proposition 4.4. *The coverage probability for the typical user at the origin for the assumed system model is given as*

$$\mathsf{P_c}(\epsilon,\alpha,T) = \frac{1}{2} - \frac{1}{\pi}\mathbb{E}_{d_{00}}\left[\int_0^\infty \frac{\mathrm{Im}\left[\exp(-jwd_{00}^{2\alpha(\epsilon-1)}/T)\varphi_{I_{agg}}(w)\right]}{w}\mathrm{d}w\right], \tag{4.9}$$

where d_{00} is the distance between the typical user and the tagged BS and its PDF *is given in* (4.1).

Above proposition follows from the direct application of Gil-Pelaez inversion theorem [69]. Numerical evaluation of the above expression requires significant amount of computational resources, which motivates us to propose our method based on approximate characterization of interference.

Dominant Interferer Based Approach

A more useful solution to this problem can be obtained by observing the fact that due to path loss the total interference is likely to be dominated by interference contributions from a few *dominant* users. Hence, instead of exact statistical characterization of the interference, we approximate the total interference power as the sum of the interference power from the *most* dominant interferer and the mean of the rest of the terms conditioned on the value of the dominant term. It is worth mentioning that this idea has been exploited in a few recent works, *albeit* only for the downlink analysis [84, 71]. Note that due to the absence of fading, in case of [84] and [71], the dominant interferer is the nearest interferer. On the contrary, in our case, except for $\epsilon = 0$, the users transmit with a power $\rho_u d_{jj}^{\alpha\epsilon}$. Due to this random transmission power, the interfering user located nearest to the tagged BS may not be the most dominant interferer. Hence, the approach in [84, 71] can not be trivially extended to solve the problem at hand as we cannot rely on the Euclidean distance to determine the dominant interferer.

From (4.7), we observe that the received interference power at the tagged BS from the user attached to the j-th BS is given as $\rho_u d_{jj}^{2\epsilon\alpha} d_{0j}^{-2\alpha}$. In order to capture the effect of transmission power of each user, we define an equivalent distance for the j-th interfering user as $\hat{d}_{0j} = d_{0j} d_{jj}^{-\epsilon}$. This equivalent distance is the distance between the tagged BS and the j-th interfering user whose location belong to a new point process $\boldsymbol{\mu}_u$. Note that there is one-to-one correspondence between the points of Φ_u and $\boldsymbol{\mu}_u$ that are governed by the rules: (1) $\hat{d}_{0j} = d_{0j} d_{jj}^{-\epsilon}$, (2) $d_{0j} > d_{jj}$. Further, $\boldsymbol{\mu}_u$ is a non-homogeneous PPP with isotropic density function. Using the above mentioned rules for d_{jj} and d_{0j} along with the displacement theorem for PPP [85], we characterize the point process $\boldsymbol{\mu}_u$ by its intensity measure in the following Lemma.

Lemma 4.5. *The new point process $\boldsymbol{\mu}_u$ formed by the displaced interfering user locations is a non-homogeneous PPP $\boldsymbol{\mu}_u$ with intensity measure $\Lambda_\mu(\mathcal{B}(\mathbf{0},t)) =$*

$$(\pi\lambda_0)^{1-\epsilon}t^2\Gamma_{\mathtt{L}}\left(1+\epsilon,\pi\lambda_0 t^{2/(1-\epsilon)}\right) - \Gamma_{\mathtt{L}}\left(2,\pi\lambda_0 t^{2/(1-\epsilon)}\right), \tag{4.10}$$

and radially symmetric distance dependent density (intensity function)

$$\lambda_\mu(r) = \lambda_0^{1-\epsilon}\pi^{-\epsilon}\Gamma_L(1+\epsilon,\pi\lambda_0 r^{2/(1-\epsilon)}). \tag{4.11}$$

Proof: Please refer to Appendix B.1. ■

Based on Lemma 4.5, the following remark can be made for the special cases of $\epsilon = 0$ and $\epsilon = 1$.

Remark 4.6. *When channel inversion based power control is employed, i.e. $\epsilon = 1$, the resultant PPP is a homogeneous PPP of density $\frac{1}{\pi}$ beyond an exclusion radius of 1. On the other hand for no power control scenario, i.e. $\epsilon = 0$, we obtain a non-homogeneous PPP with density $\lambda_0(1-\exp(-\pi\lambda_0 r^2))$. Note that the remark for $\epsilon = 0$, is consistent with the approach followed in [77], where the location of interfering user is modeled according to a non-homogeneous PPP based on distance dependent intensity function.*

Now, using the expressions in Lemma 4.5, the `PDF` of the distance $\hat{d}_{01}$ of the nearest interfering user is given as

$$f_{\hat{d}_{01}}(x) = 2\pi x\lambda_\mu(x)\exp(-\Lambda_\mu(\mathcal{B}(\mathbf{0},x))). \tag{4.12}$$

The aggregate interference is given as $I_{agg} = \sum_{\hat{u}_j\in\boldsymbol{\mu}_u}\hat{d}_{0j}^{-2\alpha}$. Now, based on the dominant interferer approximation, we write $I_{agg} \approx$

$$\hat{d}_{01}^{-2\alpha} + \mathbb{E}\left[\sum_{\hat{u}_j\in\boldsymbol{\mu}_u\setminus\hat{u}_1}\hat{d}_{0j}^{-2\alpha}\middle|\hat{d}_{01}\right] = \hat{d}_{01}^{-2\alpha} + \mathbb{E}\left[I_{2,\infty}|\hat{d}_{01}\right], \tag{4.13}$$

where $\hat{u}_1$ is the location of the dominant interferer. In the following Lemma, we present the expression for the conditional expected interference in (4.13).

Lemma 4.7. *Conditioned on the distance of the dominant interferer $\hat{d}_{01}$, the expected interference from rest of the interfering users whose locations belong to the point process $\boldsymbol{\mu}_u$ is*

$$\mathbb{E}\left[I_{2,\infty}|\hat{d}_{01}\right] = 2\pi\int_{\hat{d}_{01}}^{\infty} r^{-2\alpha}\lambda_\mu(r)r\mathrm{d}r, \tag{4.14}$$

which under the condition $2-\alpha+\alpha\epsilon > 0$ reduces to

$$\frac{(\pi\lambda_0)^{1-\epsilon}}{(\alpha-1)}\hat{d}_{01}^{2-2\alpha}\Gamma_{\mathtt{L}}\left(1+\epsilon,\pi\lambda_0\hat{d}_{01}^{2/(1-\epsilon)}\right) + \frac{(\pi\lambda_0)^{(\alpha-\alpha\epsilon)}}{(\alpha-1)}\Gamma_{\mathtt{U}}\left(2-\alpha+\alpha\epsilon,\pi\lambda_0\hat{d}_{01}^{2/(1-\epsilon)}\right), \tag{4.15}$$

where $\Gamma_{\mathtt{U}}$ is the upper incomplete gamma function and $\Gamma_{\mathtt{L}}$ is the lower incomplete gamma function.

Proof: Please refer to Appendix B.2 ■

With the knowledge of the expected interference and the distribution of $\hat{d}_{01}$, we present the coverage probability expression based on dominant interferer approach in the following Proposition.

Proposition 4.8. *The coverage probability based on dominant interferer based approach for the UL of the mMIMO system under consideration is given as* $\mathtt{P}_{\mathtt{c,Dom}}(\epsilon, \alpha, T) =$

$$\mathbb{E}_{d_{00}}\mathbb{E}_{\hat{d}_{01}}\left[\mathbf{1}\left(\hat{d}_{01}^{-2\alpha} + \mathbb{E}\left[I_{2,\infty}|\hat{d}_{01}\right] < \frac{d_{00}^{-2\alpha(1-\epsilon)}}{T}\right)\right], \tag{4.16}$$

where the PDF *of* d_{00} *is given in* (4.1)*,* $\hat{d}_{01}$ *is given in* (4.12)*, and* I_{agg} *is characterized by* (4.13) *and* (4.14)*.*

Proof: The proof follows from the standard definition of coverage probability, which is given as $\mathtt{P}_{\mathtt{c,Dom}}(\epsilon, \alpha, T) =$

$$\mathbb{P}\left[\mathtt{SINR}_0 > T\right] = \mathbb{P}\left[d_{00}^{2\alpha(\epsilon-1)} > T I_{agg}\right]. \tag{4.17}$$

Taking the expectation over d_{00} and $\hat{d}_{01}$, we get the expression in the Proposition. ■

Apart from coverage probability, another useful performance metric for the analysis of mMIMO system is the average user spectral efficiency. On the same lines as Proposition 4.8, we present the following Proposition for achievable average UL spectral efficiency of the typical user at the origin.

Proposition 4.9. *The ergodic UL spectral efficiency of the typical user attached to the tagged BS is* $\bar{R} =$

$$\mathbb{E}\left[\log_2(1+\mathtt{SINR}_0)\right] = \int_{t=0}^{\infty} \mathbb{E}_{d_{00}}\mathbb{E}_{\hat{d}_{01}}\left[\mathbf{1}\left(\hat{d}_{01}^{-2\alpha} + \mathbb{E}\left[I_{2,\infty}|\hat{d}_{01}\right] < \frac{d_{00}^{-2\alpha(1-\epsilon)}}{2^t - 1}\right)\right] \tag{4.18}$$

Proof: Since $\log_2(1+\mathtt{SINR}_0)$ is a positive random variable, the mean rate is given as $\mathbb{E}\left[\log_2(1+\mathtt{SINR}_0)\right] =$

$$\int_{t=0}^{\infty} \mathbb{P}\left[\log_2(1+\mathtt{SINR}_0) > t\right] \mathrm{d}t = \int_{t=0}^{\infty} \mathbb{P}\left[\mathtt{SINR}_0 > 2^t - 1\right] \mathrm{d}t. \tag{4.19}$$

Using the coverage probability expression given in (4.17), we get (4.18). ■

This concludes the technical section of the chapter. In the following section, we analyze the performance of the typical user in terms of coverage probability and average user spectral efficiency using the expressions presented in this section.

4.4 Numerical results

In this section, we validate the theoretical results by comparing the derived results with Monte Carlo simulation results. Further, we study the effect of power control fraction on user spectral efficiency as well. The simulation set up considers a BS density of $\lambda_0 = 4 \times 10^{-6}$ BS/m^2 within a radius of $R = 10$ km. Users are dropped uniformly at random in the disk. In order to minimize the possibility of having an inactive BS, the user density λ_a is considered to be 50 times λ_0. As discussed in the system model, we only attach one user (that is assumed to use the k-th pilot sequence) to each BS among all the users that lie in the Voronoi cell of the BS. We have considered a path loss exponent of $\alpha = 3.7$.

In Figure 4.2, we validate the coverage probability expression presented in Proposition 4.8. Further, the coverage probability expression for $\epsilon = 1$ is obtained using Proposition 4.4. We find it pertinent to mention that due to highly oscillatory nature of the CHF, it is difficult to evaluate the coverage probability using Proposition 4.4, which is, in the first place, our motivation to resort to the dominant interferer based approach. As evident from the figure, both theoretical and the simulation results are in close agreement with each other. The ergodic spectral efficiency and outage spectral efficiency for the typical user is presented in Figure 4.3 and Figure 4.4, respectively. The outage spectral efficiency for a given SINR threshold T is defined as

$$R_{\mathtt{out}} = \mathtt{P}_{\mathtt{c,Dom}}(\epsilon, \alpha, T) \log_2(1 + T) \text{ bits/s/Hz}. \tag{4.20}$$

From the figures it is clear that channel inversion based power control, i.e. $\epsilon = 1$, has inferior performance in terms of spectral efficiency compared to other less aggressive power control schemes. This can be explained by the fact that the aggregate interference power is more in case of $\epsilon = 1$ compared to other values of ϵ.

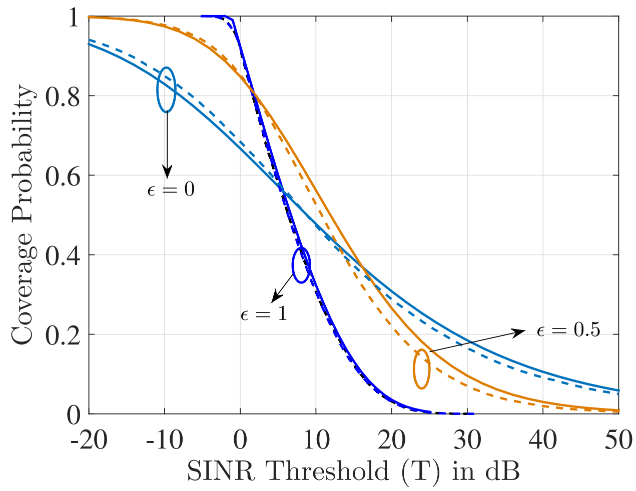

Figure 4.2: Coverage Probability for different values of ϵ. Solid lines represent the theoretical results generated using Proposition 4.8, dashed lines represents the theoretical result obtained using Proposition 4.4.

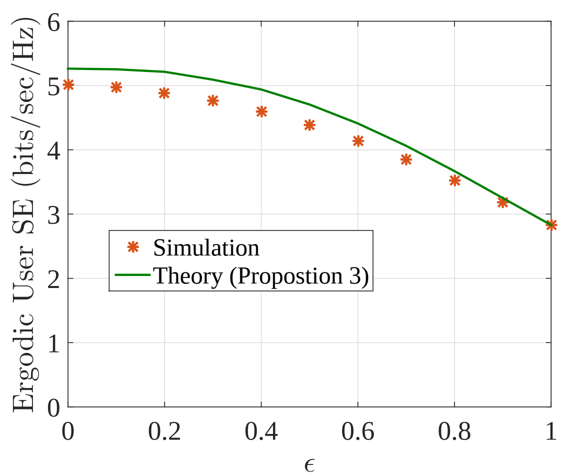

Figure 4.3: Ergodic user spectral efficiency for different power control fraction (ϵ). Theoretical curve is generated using Proposition 4.9.

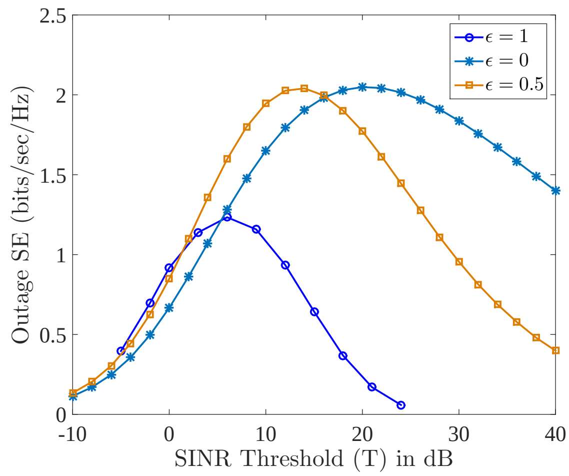

Figure 4.4: Outage user spectral efficiency for different ϵ v/s target SINR threshold. Outage SE is defined in (4.20).

4.5 Concluding remarks

The analysis of the UL of a cellular system is a challenging problem due to UL power control and the correlation among the user distances. All known results for the UL coverage assume Rayleigh fading in order to conveniently express coverage probability in terms of the LT of interference. However, in case of mMIMO due to spatial averaging of fading new methods are required for coverage probability analysis, which was the main focus of this work. The key contribution lies in carefully handling the interference power by splitting it into two terms: (i) the dominant interference power term, and (ii) conditional average of the rest of the terms. Due to the presence of power control, the geographically closest user is not necessarily the most dominant, which has been addressed by the application of the displacement theorem. Using the coverage result, the achievable user spectral efficiency is also derived. The approaches presented in this chapter and in Chapter 2 can be combined to analyze the UL performance of a soft pilot reuse mMIMO system.

Chapter 5

Multilayer Random Sequential Adsorption

5.1 Introduction

Based on the discussion presented in the prior works section in Chapter 1, to mitigate the effect of pilot contamination in a cell-free mMIMO system, one of the promising approaches is to ensure a certain geographical distance among a set of co-pilot users. In this chapter, we propose a variant of the random sequential adsorption (RSA) process that is inspired by this pilot sharing philosophy where a certain minimum distance is ensured among the set of co-pilot users. Moreover, due to the broadcast nature of the wireless networks, this philosophy of resource allocation can be incorporated to reduce the effect of co-channel interference in any other types of orthogonal resource sharing networks such as cellular networks with frequency reuse. In this chapter, we present the preliminary but concrete results to understand the spatial statistics of the co-resource users in such a system.

In order to make a more accurate connection of the above wireless setting with RSA, let us focus on a certain observation window and assume the following: (1) the nodes appear in the network as per a spatio-temporal Poisson point process (PPP), (2) each node transmits on a certain frequency band, which is randomly selected from the set of *available bands*, where a band is said to be available if it is not being used by any other nodes within a certain minimum distance from this node, (3) a node for which the set of available bands is empty because of the minimum distance violation (i.e., all bands are already being used by the other nodes in its vicinity) is not admitted into the system, and (4) once a node is admitted into the system, it will not leave the system. A natural question for this setting is: at any given time what is the density of nodes transmitting on the same frequency band? If we have only a single frequency band in the network, the setup reduces to the well-studied monolayer RSA setting (which is the native setting of the Rény's car parking problem) because of which we can answer this question by using the well-known monolayer RSA results [86, 87]. However, if there are multiple orthogonal resources, one can envision the resulting point process of users as a *multilayer RSA*. As will be discussed shortly, even though one can draw some similarities between this multilayer RSA and some known variants of RSA studied in the literature, the underlying physical phenomenon that generates this process has not been discussed in this context yet. Given the novel setting, we naturally need to derive new results to answer the above question, which is the main contribution of our work.

With this general background, we are now ready to present our new variant of the RSA process in the canonical 1D setting below. After deriving results for the 1D case, we will also tackle the 2D case later in the chapter.

5.2 Problem statement and prior works

Consider a 1D line that is empty at $t = 0$. Hard rods of length σ are arriving uniformly at random at rate r_a per unit length. A rod is placed on the line irreversibly after being assigned a color from a set of colors $\mathcal{K} = \{c_1, c_2, \ldots, c_K\}$. From a communication network perspective, rod centers represent communicating node locations, their lengths represent the communication range, and the set colors represent the orthogonal frequencies. A color is selected randomly from the set of *available colors*, where a color is available if it is not assigned to already existing rods that overlap with the arriving rod. If no colors are available for assignment, the arriving rod is not admitted into the system. An illustrative diagram is presented in Fig. 5.1. The special case of $K = 1$ gives us the celebrated *Rény's car parking* problem. Our goal is to characterize the density of rods of a given color as a function of time, denoted by $\rho_k(t)$ for $c_k \in \mathcal{K}$.

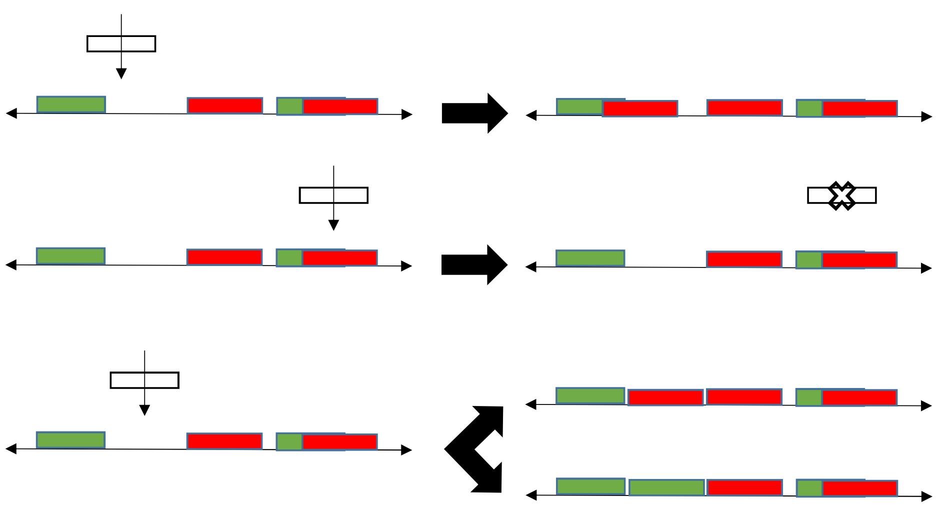

Figure 5.1: An illustrative figure for the deposition of rods that are assigned either red or green color. (Top) Arriving rod overlaps with a deposited rod of green color. Hence, it is assigned red color. (Middle) Arriving rod overlaps with rods of both the colors. Hence, it is discarded. (Bottom) Arriving rods lies in an empty interval. Hence, it can be assigned either of the two colors with equal probability.

5.2.1 Related literature and contributions

The problem described above has similarity to some known multilayer variants of the RSA problem [25, 26, 27, 28, 29]. While we briefly describe these variants next for completeness, the differences in the geometric constraints and dynamics between these and the setup studied in this chapter forbid a direct application of these prior analyses to the current setup. In [25, 26], authors have considered a sequential multilayer deposition of dimers on a lattice. Using mean-field theory, approximate density results are presented by not considering the *screening*[1] effect from higher layers. Additional approximate results for the entire time range based on *empty interval probability*[2] rate equations were also presented. However, the results are limited to the first two layers as the solution rapidly becomes cumbersome for higher layers. Further, in [26] authors provide the large time asymptotic behavior of the densities for different layers for the continuum case. In [27], the authors present asymptotic results for a variant of the multilayer RSA with sequential deposition of objects without screening effect. In addition, the authors consider the length of the objects to be random with a certain distribution. The asymptotic results are presented for 1D and 2D continuum cases that suggest each layer approaches the jamming limit as a power law. In [28], the authors study a variant of the continuum multilayer RSA where variable-length screening due to overhangs from higher layers is considered. For this model, exact results are presented only for the first layer. A generalized version of the multilayer RSA model in [28] is considered in [29] where the three possible events of the particle deposition are taken into account namely adsorption, desorption, and rolling of an object on the surface. Similar to the previous case, the exact results are presented only for the first layer.

Another interesting line of works that are inspired by the process of frequency assignment in wireless networks can be found in [88, 89, 90, 91]. In this variant, the sequential assignment of frequencies gives rise to a space-time process that is similar to the multilayer RSA process without the screening effect. In [88], through numerical simulations, authors propose several conjectures related to the long term asymptotic behavior such as the number of frequency bands necessary to accommodate n users, i.e. the average number of layers formed by deposition of the first n rods. Additional simulation-based results related to packing density are also presented. Inspired by the same model, in [89] a sequential two-layer RSA process is considered on a discrete finite lattice where the arriving objects are dimers. The model also takes into account both "no screening" and screening of dimers from the second layer to the first layer. The density results are presented for local patterns, i.e. occupancy in both the layers over three consecutive sites. In [91], authors extend the previous results from two layers to higher layers for a finite lattice size of five sites where arrival is allowed on consecutive three sites. The analysis is focused on obtaining the occupancy probability of the center site for a given layer at the large time limit. Further, a few simulation-based

[1] Blocking of arriving objects by higher layers to the lower layers due to overhangs. This phenomenon is not a characteristic of our model due to orthogonal frequency bands.

[2] The probability of finding an interval of n or more consecutive sites empty.

results for systems with larger lattice sizes are also discussed.

From this discussion, two key characteristics of the prior works are noteworthy. First, each variant of the multilayer RSA has unique geometrical and dynamical features that are not universal and are strongly driven by the underlying rules of deposition of the objects. Because of this, a unified analysis of all these variants, although desirable, is not possible. As a result, understanding the characteristics of each process requires a unique analytical treatment governed by its underlying physical model. Second, the exact characterization of these features is extremely difficult due to the non-markovian nature of the process as well as strong spatio-temporal interaction among different layers. Hence, accurate approximate results are mostly our best hope unless one considers very specific limiting scenarios, such as finite lattice size or large time system behavior. With this understanding, the contributions of our work are summarized below:

1. as presented at the beginning of this section, we propose a new variant of the multilayer RSA that is inspired from random orthogonal resource sharing in wireless communications networks.

2. Although each step in this variant is random, owing to the infinite memory of the deposition process, it is non-markovian. Hence, obtaining exact results for the kinetics is difficult. Therefore, to tackle this problem, we develop approximations that are reasonably accurate for the entire time range. For the 1D case, we provide two useful approximation methods to obtain the density of rods of a given color. The first method recursively uses the monolayer RSA result with modified arrival rates to obtain the density of rods of a given color. On the other hand, in the second method, we approximately characterize the *gap density function*, which is later used to obtain the density of rods. While the first approach is more amenable to numerical evaluation, the second method is more accurate along with providing useful intermediate results.

3. We also accommodate the 2D version of the problem, which is solved using a method that is similar to the first approximation method for the 1D case. From an application point of view, we present a case study of orthogonal frequency band allocation in Wi-Fi networks where the results derived for the 2D RSA are directly applicable for the system analysis.

The rest of the chapter is organized as follows: in Sec. 5.3, we present the first approximation that leverages the monolayer RSA result to solve the problem. In Sec. 5.4 we present our second approach to solve the problem using gap density function. The density results for the 2D case using the first approximation is presented in Sec. 5.5. We provide concluding remark in Sec. 5.6.

5.3 Density Approximation of 1D Multilayer RSA: An Iterative Approach

In this section, we present our first approach to approximate the density of rods of a given color as a function of time. This approach is based on establishing an equivalence between the proposed color assignment process and an alternate sequential color assignment process that is described below. The equivalence between these two assignment processes is in terms of total density of rods admitted into the system.

The rules for the alternate sequential color assignment scheme are as follows:

1. Let there be K colors $\mathcal{K} = \{c_1, c_2, \ldots, c_K\}$ with a predefined ordering. The coloring scheme is sequential, i.e. for an arriving rod at x, color c_1 is considered first. If a rod of color c_1 overlaps with $B_{\sigma/2}(x)$[3], then color c_2 is considered and so on.

2. If the arriving rod at x overlaps with rods of all the colors, i.e. centers of rods of all colors are present in $B_\sigma(x)$, then the rod is not admitted into the system.

Let $\tilde{\rho}_i(t)$ be the density of rods of color c_i at time t. Due to the sequential nature of the assignment scheme, it is clear that $\tilde{\rho}_1(t) \geq \tilde{\rho}_2(t) \geq \ldots \geq \tilde{\rho}_K(t)$. On the other hand, in case of the random assignment of colors as proposed in the original problem (Sec 5.2), the densities of rods of different colors are the same, i.e. $\rho_1(t) = \rho_2(t) = \ldots = \rho_K(t)$. Note that at time t, in both the schemes, the total density of admitted rods of all colors is the same. Hence, we write

$$\begin{aligned}
\sum_{k=1}^{K} \rho_k(t) &= \sum_{k=1}^{K} \tilde{\rho}_k(t) \\
\Rightarrow K\rho_i(t) &= \sum_{k=1}^{K} \tilde{\rho}_k(t) \\
\Rightarrow \rho_i(t) &= \frac{\sum_{k=1}^{K} \tilde{\rho}_k(t)}{K}, \forall i = 1, 2, \ldots, K. \qquad (5.1)
\end{aligned}$$

To use the above equation to characterize the density of rods of color c_i for the original assignment scheme, we need information regarding $\tilde{\rho}_i(t)$, $\forall i$. Observe that the evolution of density of rods for color c_1, denoted by $\tilde{\rho}_1(t)$, is the same as the monolayer RSA. Hence, the density of rods of color c_1 is given as [87]

$$\tilde{\rho}_1(t) = \frac{1}{\sigma} \int_0^{r_a \sigma t} \exp\left(-2 \int_0^u \frac{1 - e^{-x}}{x} \mathrm{d}x\right) \mathrm{d}u. \qquad (5.2)$$

[3] Throughout the manuscript, we denote a ball of radius $\sigma/2$ centered at x as $B_{\sigma/2}(x)$.

However, characterizing the exact density of rods of color c_n, for $n \geq 2$, is non-trivial. Hence, we approximate $\tilde{\rho}_n(t)$ for $n \geq 2$. In the sequential assignment scheme, at time t, $\tilde{\rho}_1(t)$ rods per unit length have been assigned color c_1. Hence, the number of arrivals per unit length that have been considered for the allocation of color c_2 is $r_a t - \tilde{\rho}_1(t)$. Similarly, the number of arrivals per unit length considered for color c_3 is $r_a t - \tilde{\rho}_1(t) - \tilde{\rho}_2(t)$. To obtain $\tilde{\rho}_2(t)$, we assume that the rods are arriving uniformly at random at a rate $r_a - \frac{\tilde{\rho}_1(t)}{t}$. Note that although reasonable, this assumption is an approximation. Further, assuming that the evolution of color c_2 happens similar to monolayer RSA, the density at time t is given as

$$\tilde{\rho}_2(t) = \frac{1}{\sigma} \int_0^{r_a \sigma t - \tilde{\rho}_1(t)\sigma} \exp\left(-2 \int_0^u \frac{1 - e^{-x}}{x} \mathrm{d}x\right) \mathrm{d}u. \tag{5.3}$$

Proceeding on the similar lines, the density of rods of color c_n for $2 \leq n \leq K$ is given as

$$\tilde{\rho}_n(t) = \frac{1}{\sigma} \int_0^{r_a \sigma t - \sigma \sum_{i=1}^{n-1} \tilde{\rho}_i(t)} \exp\left(-2 \int_0^u \frac{1 - e^{-x}}{x} \mathrm{d}x\right) \mathrm{d}u. \tag{5.4}$$

In the following proposition, we summarize the density result presented in this section:

Proposition 1. The density of rods of a given color for the original random color assignment problem is given as

$$\rho_i(t) = \frac{\sum_{k=1}^{K} \tilde{\rho}_k(t)}{K},$$

where

$$\tilde{\rho}_k(t) = \frac{1}{\sigma} \int_0^{r_a \sigma t - \sigma \sum_{i=1}^{k-1} \tilde{\rho}_i(t)} \exp\left(-2 \int_0^u \frac{1 - e^{-x}}{x} \mathrm{d}x\right) \mathrm{d}u.$$

The validation of the accuracy of the above approximation is presented in Fig. 5.2.

Interestingly, once the equivalence between the original and the alternate sequential color assignment processes was established in (5.1), this approach relied exclusively on the known monolayer result. As we will discuss in Section 4, its tractability also makes it an appealing choice for the RSA analysis in higher dimensions. That said, this approach suffers from a gradual loss of accuracy as the number of colors increases. This motivates us to present an alternate result that is more accurate compared to this approximation and has an added advantage of providing useful intermediate results that have more information regarding the kinetics of the process (whereas the above approach does not provide any other statistical information about the original random color assignment process apart from the time-varying density of rods of a given color).

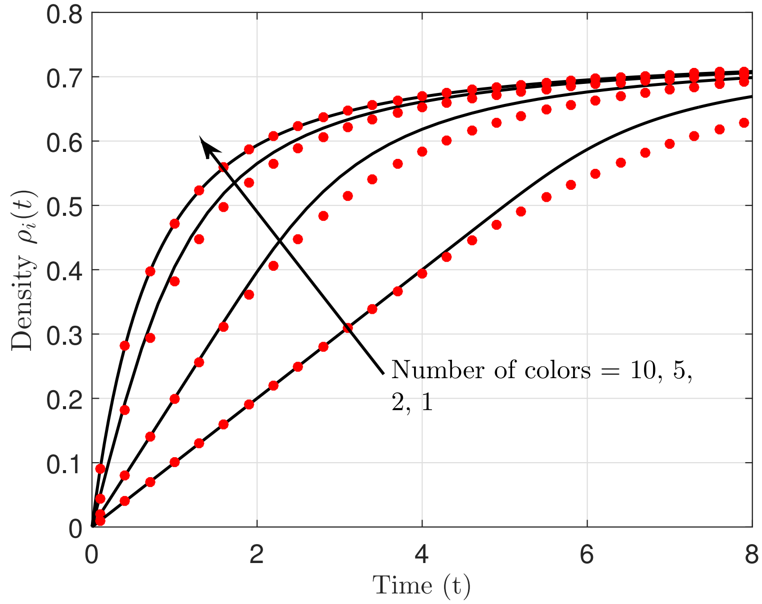

Figure 5.2: The evolution of the density of rods of a particular color as a function of time t for $\sigma = 1$. Markers and solid lines represent simulations and theoretical results, respectively.

5.4 Density Approximation for 1D Multilayer RSA: Gap Density Function-based Approach

In this section, we present our second approximation approach to obtain the density of rods of a given color. It is based on the characterization of the *gap density function*, which is one of the canonical methods to understand the kinetics of the RSA process as well as its different variants. In our case, at time t, the gap density function $G_i(l, t)$ is defined such that $G_i(l, t)\mathrm{d}l$ gives the density of gaps of length between l and $l + \mathrm{d}l$ for rods that are colored c_i. Following properties of $G_i(l, t)$ are useful in the derivation of density of rods of a given color:

1. Since each gap corresponds to an admitted rod of color c_i preceding it (or succeeding it), the density of rods of color c_i is given as

$$\rho_i(t) = \int_0^\infty G_i(l, t)\mathrm{d}l. \tag{5.5}$$

   This direct relationship to the density makes gap density function more attractive to work with compared to other intermediate quantities such as empty interval probability [92].

2. At time t, the fraction of the length (average length over a unit interval) available for

admitting a rod that can be assigned color c_i is

$$\Phi_i(t) = \int_{\sigma}^{\infty} (l - \sigma) G_i(l, t) \mathrm{d}l. \tag{5.6}$$

Above result can be interpreted as the probability of a rod arriving in a gap of length l of color c_i. This relationship is used later in the proposed approximation.

Instead of directly solving the problem for $K \geq 2$ colors, we begin with the simpler case of $K = 2$. The objective is to expose the underlying structure of the problem for the simpler setting of $K = 2$, which will help in identifying key constructs that emerge from the inherent spatial coupling of the RSA and will hence need careful approximations for a tractable analysis. This will then inform our analysis of $K \geq 2$.

5.4.1 Results for two layers $(K = 2)$

Consider the scenario where rods can be assigned either of the two colors $\mathcal{K} = \{c_1, c_2\}$. As mentioned in Sec. 5.2, the assignment of a color is random with equal probability unless the arriving rod overlaps with an admitted rod of a given color. Owing to the random assignment, at a given time t, $G_1(l, t)$ and $G_2(l, t)$ are identical. Hence, without loss of generality, we just focus on deriving $G_1(l, t)$.

Our first step is to characterize the time evolution of $G_1(l, t)$. Consider a gap of length l for rods of c_1 (see Fig. 5.3). The allowable length on which a rod can arrive with the possibility of getting the color c_1 is the segment $[\frac{\sigma}{2}, l - \frac{\sigma}{2}]$. Let us denote this line segment by $L_{l-\sigma}$. For a rod arriving at location $x \in L_{l-\sigma}$, we define the following events:

1. $\mathcal{I}_i(x, t) :=$ {A rod arriving at point x during the time window $(t, t+\mathrm{d}t]$ will be assigned c_i.}

2. $\mathcal{C}_i(x, t, l) :=$ {The rod arrives in gap of length l corresponding to color c_i during time $(t, t + \mathrm{d}t]$.}

3. $\mathcal{E}_n(x, t) :=$ {At time t, the segment $B_{\sigma/2}(x) := \left[x - \frac{\sigma}{2}, x + \frac{\sigma}{2}\right]$ overlaps with n deposited rods}

The evolution of $G_1(l, t)$ depends on the following configurations in the vicinity of x:

1. the rod will be assigned color c_1 (green in the illustrations) with probability 1/2 if $B_{\sigma/2}(x)$ is not partially (or fully) covered by rods of color c_2 (orange in the illustrations), and

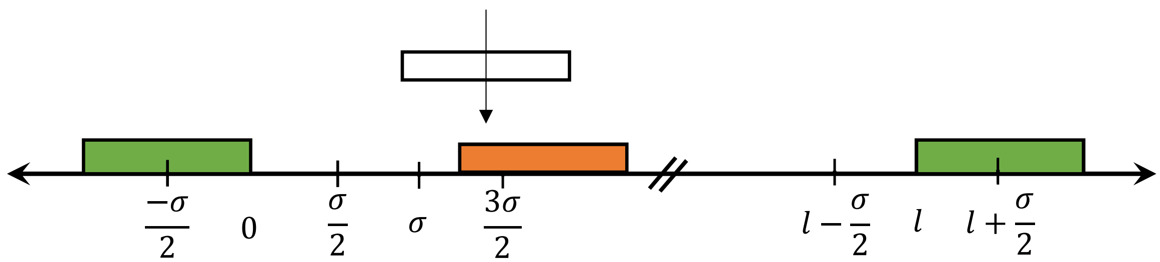

Figure 5.3: A gap of length l for rods of color c_1 (green for the illustration purpose). New arrivals that can destroy this gap are possible only over the segment $L_{l-\sigma} = [\frac{\sigma}{2}, l - \frac{\sigma}{2}]$.

2. the rod will be assigned color c_1 with probability 1 if $B_{\sigma/2}(x)$ is partially (or fully) covered by rods of color c_2. In the illustrative example of Fig. 5.3, the arriving rod will be assigned color c_1 with probability 1 as it overlaps with rod of color c_2.

We write the following set of differential equations to capture the evolution of $G_1(l,t)$ due to an arrival in the gap of length l for rods of color c_1 during an infinitesimally small time window $(t, t + \mathrm{d}t]$:

$$\frac{\partial G_1(l,t)}{\partial t} = \begin{cases} -r_a \displaystyle\int_{x \in L_{l-\sigma}} G_1(l,t)\mathbb{P}[\mathcal{I}_1(x,t)|\mathcal{C}_1(x,t,l)]\mathrm{d}x & \\ \quad +2r_a \displaystyle\int_{y=l+\sigma}^{\infty} G_1(y,t)\mathbb{P}[\mathcal{I}_1(x,t)|\mathcal{C}_1(x,t,y)]\mathrm{d}y & l \geq \sigma, \\ 2r_a \displaystyle\int_{y=l+\sigma}^{\infty} G_1(y,t)\mathbb{P}[\mathcal{I}_1(x,t)|\mathcal{C}_1(x,t,y)]\mathrm{d}y & l < \sigma. \end{cases} \tag{5.7}$$

To obtain (5.7), we first consider the case of $l \geq \sigma$ as it involves the rate of change in the density of gaps between $(l, l + \mathrm{d}l]$ due to the destruction of such gaps as well as creation of such gaps from gaps of larger length. The second case of $l < \sigma$ involves only the creation term that can be obtained using a similar logic as we present for $l \geq \sigma$. The first term on the right hand side (destruction term) captures the rate of change in density $G_1(l,t)$ due to the average number of arrivals over unit length in a gap of length l and is straightforward to obtain. The second term (creation term) captures the rate of change in $G_1(l,t)$ due to average number of arrivals per unit length that can create a gap of length l from a gap of length $y > l + \sigma$. This expression can be derived as follows: for all the gaps of length $(y, y + \mathrm{d}l]$, the fraction of available length for arrival of a rod is $(y - \sigma)G_1(y,t)\mathrm{d}l$. In order to create a gap of length l, the rod needs to arrive on a thin length $\mathrm{d}y$ at a distance $l + \sigma/2$ from either end of the gap y. Due to the uniform arrival of rods, the probability of this event is $\mathrm{d}y/(y - \sigma)$. Further, this arriving rod will be assigned color c_1 with certain probability depending on the configuration of already deposited rods of color c_2 in this gap.

This probability is captured by the term $\mathbb{P}[\mathcal{I}_1(x,t)|\mathcal{C}_1(x,t,y)]$. Hence, the fraction of length that allows an arriving rod to partition y into two smaller gaps of lengths l and $y-l-\sigma$ is

$$\begin{aligned}\frac{2\mathrm{d}y}{(y-\sigma)}&(y-\sigma)[G_1(y,t)\mathrm{d}l]\mathbb{P}[\mathcal{I}_1(x,t)|\mathcal{C}_1(x,t,y)]\\&=2[G_1(y,t)\mathrm{d}l]\mathbb{P}[\mathcal{I}_1(x,t)|\mathcal{C}_1(x,t,y)]\mathrm{d}y,\end{aligned}$$

which gives the desired integrand in (5.7) for the creation term in both the cases.

Our next step is to derive an expression for the probability term presented in (5.7). Using Bayes' theorem and law of total probability, we write $\mathbb{P}[\mathcal{I}_1(x,t)|\mathcal{C}_1(x,t,l)] =$

$$\begin{aligned}&\frac{\mathbb{P}[\mathcal{I}_1(x,t),\mathcal{C}_1(x,t,l)]}{\mathbb{P}[\mathcal{C}_1(x,t,l)]}\\=&\frac{\sum_{n\geq 0}\mathbb{P}[\mathcal{I}_1(x,t),\mathcal{C}_1(x,t,l)|\mathcal{E}_n(x,t)]\mathbb{P}[\mathcal{E}_n(x,t)]}{\mathbb{P}[\mathcal{C}_1(x,t,l)]}\\=&\frac{\sum_{n\geq 0}\mathbb{P}[\mathcal{I}_1(x,t)|\mathcal{C}_1(x,t,l),\mathcal{E}_n(x,t)]\mathbb{P}[\mathcal{C}_1(x,t,l)|\mathcal{E}_n(x,t)]\mathbb{P}[\mathcal{E}_n(x,t)]}{\mathbb{P}[\mathcal{C}_1(x,t,l)]}.\end{aligned}\tag{5.8}$$

Note that the above conditional probability depends on the location of $x \in L_{l-\sigma}$. Deriving an exact expression while considering this location dependence is intractable. This is a manifestation of the spatial coupling because of which exact analyses of multilayer RSA in most settings is intractable. Next we present our approximation approach that is based on a few assumptions including the location independence.

First, we get $\mathbb{P}[\mathcal{E}_n(x,t)]$, i.e. the probability of the event that the interval $[x-\frac{\sigma}{2}, x+\frac{\sigma}{2}]$ overlaps with n deposited rods. Consider the following realizations of this event:

1. For $n=0$ (Fig. 5.4 top): if the arrival occurs at $x \in [\sigma, l-\sigma]$, then it is clear that there has been no prior arrivals in $(x-\sigma, x+\sigma)$ until time t. Otherwise, it would have been assigned one of the colors. Hence, using empty interval probability of 1D Poisson process, $\mathbb{P}[\mathcal{E}_0(x,t)] = e^{-r_a 2\sigma t}$. On the other hand, if the arrival occurs at $x \in \{[\frac{\sigma}{2}, \sigma) \cup (l-\sigma, l-\frac{\sigma}{2}]\}$, then there is a non-zero probability that there has been atleast one arrival in $(x-\sigma, x+\sigma)$ prior to time t. This arrival(s) has been discarded as there are no colors left to assign. Exact evaluation of the probability of this event is cumbersome. Hence, we approximate it as a Poisson arrival and write

$$\mathbb{P}[\mathcal{E}_0(x,t)] = e^{-r_a 2\sigma t}, \quad x \in \left[\frac{\sigma}{2}, l-\frac{\sigma}{2}\right].$$

2. For $n=1$ (Fig. 5.4 bottom): similar to the previous case, if the arrival occurs at $x \in [\sigma, l-\sigma]$, then it is clear that there is one arrival in $(x-\sigma, x+\sigma)$ until time t. Hence, we write $\mathbb{P}[\mathcal{E}_1(x,t)] = r_a 2\sigma t e^{-r_a 2\sigma t}$. However, when arrival occurs at $x \in$

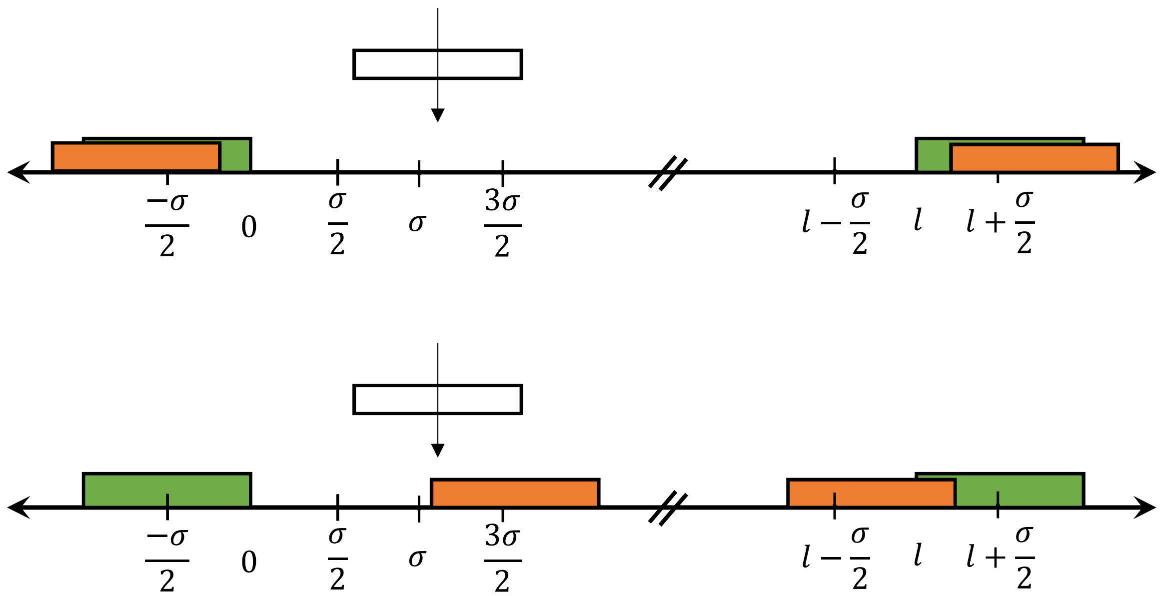

Figure 5.4: An illustrative gap of length l for color green (c_1). The arrivals at $x \in \left[\frac{\sigma}{2}, l-\frac{\sigma}{2}\right]$ are considered for assigning color green.

$\{[\frac{\sigma}{2}, \sigma) \cup (l-\sigma, l-\frac{\sigma}{2}]\}$, it is difficult to derive $\mathbb{P}[\mathcal{E}_1(x,t)]$ as it requires a cumbersome enumeration. To circumvent this, similar to the previous case, we approximate the arrivals in $(x-\sigma, x+\sigma)$ to follow a Poisson process and write

$$\mathbb{P}[\mathcal{E}_1(x,t)] = r_a 2\sigma t e^{-r_a 2\sigma t}.$$

3. For $n=2$: Similar to the previous cases, we approximate that the process is Poisson in $(x-\sigma, x+\sigma)$ for an arrival at $x \in [\frac{\sigma}{2}, l-\frac{\sigma}{2}]$. Hence,

$$\mathbb{P}[\mathcal{E}_2(x,t)] = \frac{(r_a 2\sigma t)^2}{2} e^{-r_a 2\sigma t}.$$

Note that $\mathbb{P}[\mathcal{E}_n(x,t)] = 0$ for $n \geq 3$.

Next, we are interested in $\mathbb{P}[\mathcal{C}_1(x,t,l)|\mathcal{E}_n(x,t)]$, $\forall n$. Let us define the event $C_1(x,t)$ as the event that an arriving rod falls in a gap corresponding to color c_1. As presented earlier, the probability of this event is given as

$$\mathbb{P}[C_1(x,t)] = \Phi_1(t) = \int_\sigma^\infty (z-\sigma) G_1(z,t) \mathrm{d}z.$$

Above probability takes into account all the gaps of length greater than σ, where the probability that the rod lies in a gap of length $(l, l+\mathrm{d}l]$ corresponding to color c_1 is

$(l-\sigma)G_1(l,t)\mathrm{d}l$. Please note that $\mathbb{P}[\mathcal{C}_1(x,t,l)|\mathcal{E}_n(x,t)] = \mathbb{P}[\mathcal{C}_1(x,t,l),\mathcal{C}_1(x,t)|\mathcal{E}_n(x,t)]$ due to the fact that $\mathcal{C}_1(x,t,l) \subseteq \mathcal{C}_1(x,t)$ conditioned on $\mathcal{E}_n(x,t)$. Further, we assume that $\mathbb{P}[\mathcal{C}_1(x,t,l)|\mathcal{C}_1(x,t),\mathcal{E}_n(x,t)] = \mathbb{P}[\mathcal{C}_1(x,t,l)|\mathcal{C}_1(x,t)]$ for all n. Using this relationship, for $n=0$, this conditional probability is simply the probability that $B_{\sigma/2}(x)$ lies in a gap of length $(l, l+\mathrm{d}l]$ of all the gaps and is given as

$$\begin{aligned}
\mathbb{P}[\mathcal{C}_1(x,t,l)|\mathcal{E}_0(x,t)] &= \mathbb{P}[\mathcal{C}_1(x,t,l),\mathcal{C}_1(x,t)|\mathcal{E}_0(x,t)] \\
&= \mathbb{P}[\mathcal{C}_1(x,t,l)|\mathcal{C}_1(x,t),\mathcal{E}_0(x,t)]\mathbb{P}[\mathcal{C}_1(x,t)|\mathcal{E}_0(x,t)] \\
&\overset{(a)}{=} \mathbb{P}[\mathcal{C}_1(x,t,l)|\mathcal{C}_1(x,t)]\mathbb{P}[\mathcal{C}_1(x,t)|\mathcal{E}_0(x,t)] \\
&= \frac{\mathbb{P}[\mathcal{C}_1(x,t,l)]}{\mathbb{P}[\mathcal{C}_1(x,t)]}\mathbb{P}[\mathcal{C}_1(x,t)|\mathcal{E}_0(x,t)] \\
&\overset{(b)}{=} \frac{(l-\sigma)G_1(l,t)\mathrm{d}l}{\Phi_1(t)}
\end{aligned}$$

where (a) follows from the aforementioned assumption, and (b) using the fact that $\mathbb{P}[\mathcal{C}_1(x,t)|\mathcal{E}_0(x,t)] = 1$.

Now consider that the arriving rod $B_{\sigma/2}(x)$ sees one deposited rod in the neighborhood. Its arrival is in in a gap of color c_1 only if the deposited rod is assigned color c_2. The probability of this event is $1/2$. Following the similar principle as $n=0$, we write

$$\begin{aligned}
\mathbb{P}[\mathcal{C}_1(x,t,l)|\mathcal{E}_1(x,t)] &= \mathbb{P}[\mathcal{C}_1(x,t,l),\mathcal{C}_1(x,t)|\mathcal{E}_1(x,t)] \\
&= \mathbb{P}[\mathcal{C}_1(x,t,l)|\mathcal{C}_1(x,t),\mathcal{E}_1(x,t)]\mathbb{P}[\mathcal{C}_1(x,t)|\mathcal{E}_1(x,t)] \\
&= \frac{(l-\sigma)G_1(l,t)\mathrm{d}l}{\Phi_1(t)}\frac{1}{2}.
\end{aligned} \tag{5.9}$$

The event $\mathcal{E}_2(x,t)$ is more interesting compared to the previous cases. First, if the centers of both the deposited rods are not separated by a distance σ, then these two rods need to be assigned two different colors. Hence,

$$\mathbb{P}[\mathcal{C}_1(x,t,l)]|\mathcal{E}_2(x,t),\{\text{Admitted rods are less than } \sigma \text{ apart}\}] = 0$$

as the arrival is no longer in a gap of color c_1. Hence, the event we are interested in is that the centers of both the admitted rods are atleast σ distance apart and both these rods are assigned color c_2. The probability that the two arrivals are at least σ distance apart can be evaluated using order statistics and it comes out to be $5/18$. Further, the probability that these two rods are assigned color c_2 is $1/4$. Overall, we write

$$\begin{aligned}
\mathbb{P}[\mathcal{C}_1(x,t,l)|\mathcal{E}_2(x,t)] &= \mathbb{P}[\mathcal{C}_1(x,t,l),\mathcal{C}_1(x,t)|\mathcal{E}_2(x,t)] \\
&= \mathbb{P}[\mathcal{C}_1(x,t,l)|\mathcal{C}_1(x,t),\mathcal{E}_2(x,t)]\mathbb{P}[\mathcal{C}_1(x,t)|\mathcal{E}_2(x,t)] \\
&= \frac{(l-\sigma)G_1(l,t)\mathrm{d}l}{\Phi_1(t)}\frac{1}{4}\frac{5}{18}.
\end{aligned} \tag{5.10}$$

Using the law of total probability

$$\mathbb{P}[\mathcal{C}_1(x,t,l)] = \frac{(l-\sigma)G_1(l,t)\mathrm{d}l}{\Phi_1(t)}\left(e^{-r_a 2\sigma t} + \frac{1}{2}(r_a 2\sigma t)e^{-r_a 2\sigma t} + \frac{1}{4}\frac{5}{18}(r_a 2\sigma t)^2\frac{e^{-r_a 2\sigma t}}{2}\right). \quad (5.11)$$

Above expression for $\mathbb{P}[\mathcal{C}_1(x,t,l)]$ is exact when

$$\Phi_1(t) = e^{-r_a 2\sigma t} + \frac{1}{2}r_a 2\sigma t e^{-r_a 2\sigma t} + \frac{1}{4}\frac{5}{18}(r_a 2\sigma t)^2\frac{e^{-r_a 2\sigma t}}{2}.$$

Since this is not the case, the result is an approximation whose accuracy is validated at the end of this section.

To reach our final goal, we need to obtain $\mathbb{P}[\mathcal{I}_1(x,t)|\mathcal{C}_1(x,t,l),\mathcal{E}_n(x,t)]$. Owing to the equi-probable random assignment of colors

$$\mathbb{P}[\mathcal{I}_1(x,t)|\mathcal{C}_1(x,t,l),\mathcal{E}_n(x,t)] = \begin{cases} 1/2 & n=0, \\ 1 & n=1,2, \end{cases} \quad (5.12)$$

where for $n=2$, we have the condition that both the arrivals are at least σ distance apart.

Substituting the conditional probability expressions in (5.8), we get

$$\begin{aligned}\mathbb{P}[\mathcal{I}_1(x,t)|\mathcal{C}_1(x,t,l)] =& \frac{\frac{1}{2}e^{-r_a 2\sigma t} + \frac{1}{2}(r_a 2\sigma t)e^{-r_a 2\sigma t} + 5/144(r_a 2\sigma t)^2 e^{-r_a 2\sigma t}}{e^{-r_a 2\sigma t} + \frac{1}{2}(r_a 2\sigma t)e^{-r_a 2\sigma t} + 5/144(r_a 2\sigma t)^2 e^{-r_a 2\sigma t}} \\ =& \frac{1 + r_a 2\sigma t + 5/72(r_a(2\sigma)t)^2}{2 + r_a 2\sigma t + 5/72(r_a(2\sigma)t)^2}.\end{aligned}$$

Using all the intermediate steps described so far, we arrive at the following result to approximately characterizing the density of rods of a given color.

Proposition 2. For $K=2$, the density of rods of a given color c_i is given as

$$\rho_i(t) = \int_{l\geq 0} G_i(l,t)\mathrm{d}l,$$

where the time evolution of $G_i(l,t)$ is given as

$$\frac{\partial G_i(l,t)}{\partial t} = \begin{cases} \left[-r_a(l-\sigma)G_i(l,t) + 2r_a\int_{y=l+\sigma}^{\infty} G_i(y,t)\mathrm{d}y\right] & \\ \quad \frac{1 + r_a 2\sigma t + 5/72(r_a(2\sigma)t)^2}{2 + r_a 2\sigma t + 5/72(r_a(2\sigma)t)^2} & l \geq \sigma, \\ 2r_a\frac{1 + r_a 2\sigma t + 5/72(r_a(2\sigma)t)^2}{2 + r_a 2\sigma t + 5/72(r_a(2\sigma)t)^2}\int_{y=l+\sigma}^{\infty} G_i(y,t)\mathrm{d}y & l < \sigma. \end{cases} \quad (5.13)$$

Following results verify the accuracy of the approximation. In Fig. 6.5, we present $G_i(l,t)$ as a function of l for different t. We have considered the length of a rod as $\sigma = 1$. As evident from the figure, with increasing time, gaps of length $l < 1$ become relatively dominant of all the gaps. This result is also intuitive since only gaps of length $l < 1$ remain in the system as the system reaches the jamming limit. In Fig. 5.6, we present the density $\rho_i(t)$ of rods of a given color. We also observe that the simulations and approximated theory results are remarkably close.

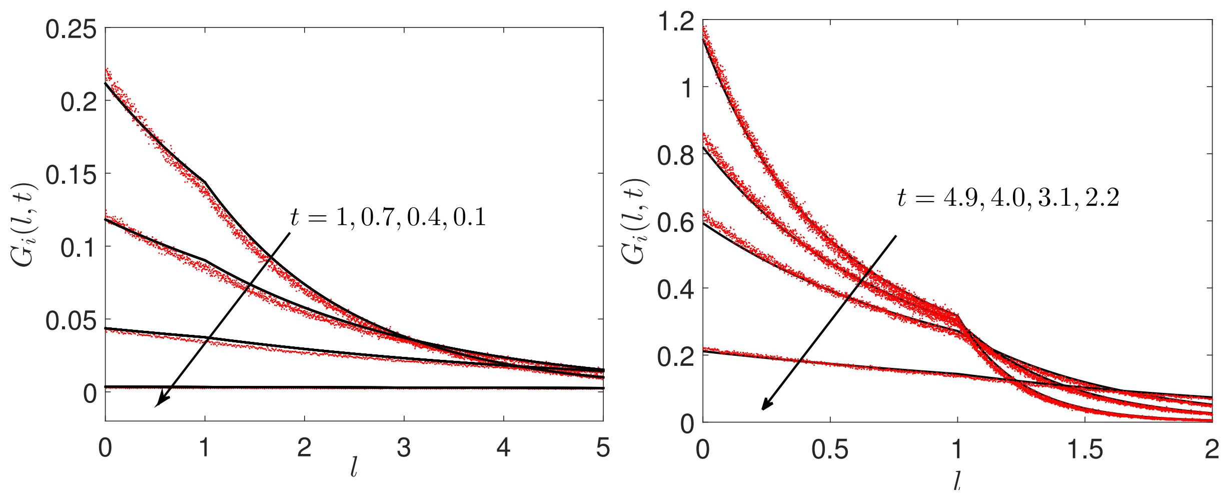

Figure 5.5: The evolution of gap density function for rods of a particular color as a function of gap length l for $\sigma = 1$. Solid lines and dotted markers represent theoretical approximation and simulations result, respectively.

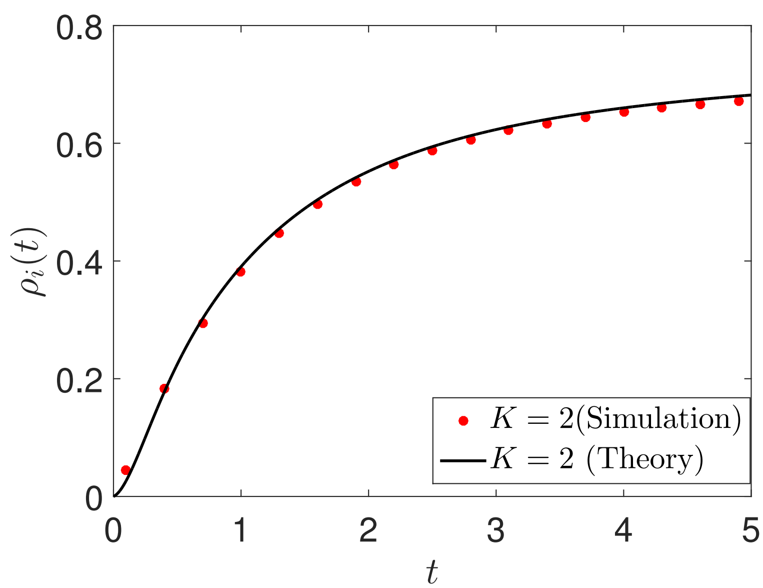

Figure 5.6: The evolution of density of rods of a particular color as a function of time t for $\sigma = 1$.

5.4.2 Results for generic K

Our next goal is to extend the previous approximation to $K \geq 2$ layers. However, capturing all the events mentioned in the previous subsection to characterize the rate equation for the gap density function becomes increasingly tedious as the number of layers increases. Therefore, to keep the numerical evaluation tractable, we make the following assumptions. The first assumption is the same as the approximation we have used for the previous approach that ignores the spatial dependence among prior arrivals beyond a certain range.

Assumption 5.1. *The admitted rods in the neighborhood $B_\sigma(x)$ of an arriving rod at x are assumed to be deposited uniformly at random and independent of arrivals beyond $B_\sigma(x)$. Hence, these prior arrivals are assumed to follow Poisson process in $B_\sigma(x)$.*

Further, if two prior arrivals in $B_\sigma(x)$ are separated by a distance σ, then there is non-zero probability that these two arrivals can be assigned the same color. However, considering this case exactly becomes cumbersome even for $K \geq 3$. Hence, we make the following assumption to make the rate equation for the gap density function tractable.

Assumption 5.2. *If there are $m < K$ admitted rods in $B_\sigma(x)$, then these are assigned m different colors irrespective of their relative distances.*

With these assumptions, we propose following approximation to characterize the evolution of density of the rods of color c_i.

Proposition 3. For a multilayer RSA process with K colors, the density of rods of a given color c_i is given as

$$\rho_i(t) = \int_{l \geq 0} G_i(l,t)\mathrm{d}l,$$

where the time evolution of $G_i(l,t)$ is given as

$$\frac{\partial G_i(l,t)}{\partial t} = \begin{cases} \left[-r_a(l-\sigma)G_i(l,t) + 2r_a \int\limits_{y=l+\sigma}^{\infty} G_i(y,t)\mathrm{d}y \right] \dfrac{\sum\limits_{n=0}^{K-1} \frac{(r_a 2\sigma t)^n}{n!}}{\sum\limits_{n=0}^{K-1} (K-n)\frac{(r_a 2\sigma t)^n}{n!}}, & l \geq \sigma \\ 2r_a \dfrac{\sum\limits_{n=0}^{K-1} \frac{(r_a 2\sigma t)^n}{n!}}{\sum\limits_{n=0}^{K-1} (K-n)\frac{(r_a 2\sigma t)^n}{n!}} \displaystyle\int_{y=l+\sigma}^{\infty} G_i(y,t)\mathrm{d}y, & l < \sigma. \end{cases} \tag{5.14}$$

Proof: The above proposition can be derived on the similar lines as the exposition of the $K = 2$ case in the previous subsection. First, the rate of change equation for gap density function is the same as (5.7). Now the conditional probability expression in (5.7) can be expanded as

$$\begin{aligned}&\frac{\mathbb{P}[\mathcal{I}_i(x,t),\mathcal{C}_i(x,t,l)]}{\mathbb{P}[\mathcal{C}_i(x,t,l)]}\\ =&\frac{\sum_{n\geq 0}\mathbb{P}[\mathcal{I}_i(x,t)|\mathcal{C}_i(x,t,l),\mathcal{E}_n(x,t)]\mathbb{P}[\mathcal{C}_i(x,t,l)|\mathcal{E}_n(x,t)]\mathbb{P}[\mathcal{E}_n(x,t)]}{\mathbb{P}[\mathcal{C}_i(x,t,l)]}.\end{aligned} \tag{5.15}$$

Using both the assumptions mentioned above, we write

$$\mathbb{P}[\mathcal{E}_n(x,t)] = e^{-r_a 2\sigma t}\sum_{n=0}^{K-1}\frac{(r_a 2\sigma t)^n}{n!}, \quad 0\leq n\leq K-1.$$

Further, on the similar lines as discussed in the previous section

$$\mathbb{P}[\mathcal{C}_i(x,t,l)|\mathcal{E}_n(x,t)] = \frac{(l-\sigma)G_i(l,t)\mathrm{d}l}{\Phi_i(t)}\frac{K-n}{K}, \quad 0\leq n\leq K-1.$$

Hence, using the law of total probability, we write

$$\mathbb{P}[\mathcal{C}_i(x,t,l)] = \sum_{n=0}^{K-1}\frac{(l-\sigma)G_i(l,t)\mathrm{d}l}{\Phi_i(t)}\frac{K-n}{K}\frac{(r_a 2\sigma t)^n}{n!}e^{-r_a 2\sigma t}.$$

Moreover, due to equi-probable assignment of colors

$$\mathbb{P}[\mathcal{I}_i(x,t)|\mathcal{C}_i(x,t,l),\mathcal{E}_n(x,t)] = \frac{1}{K-n}, \quad 0\leq n\leq K-1.$$

Using the above four equations in (5.15), we get

$$\mathbb{P}[\mathcal{I}_i(x,t)|\mathcal{C}_i(x,t,l)] = \frac{\sum\limits_{n=0}^{K-1}\frac{(r_a 2\sigma t)^n}{n!}}{\sum\limits_{n=0}^{K-1}(K-n)\frac{(r_a 2\sigma t)^n}{n!}}.$$

The final result is obtained using the relationship between the gap density function and the density of rods of a particular color. ■

The density result using the above proposition is presented in Fig. 5.7. From the figure we observe that the simulations and the approximate theoretical results are remarkably close. Further, as expected the time required to reach the jamming limit increases as the number of layers increases.

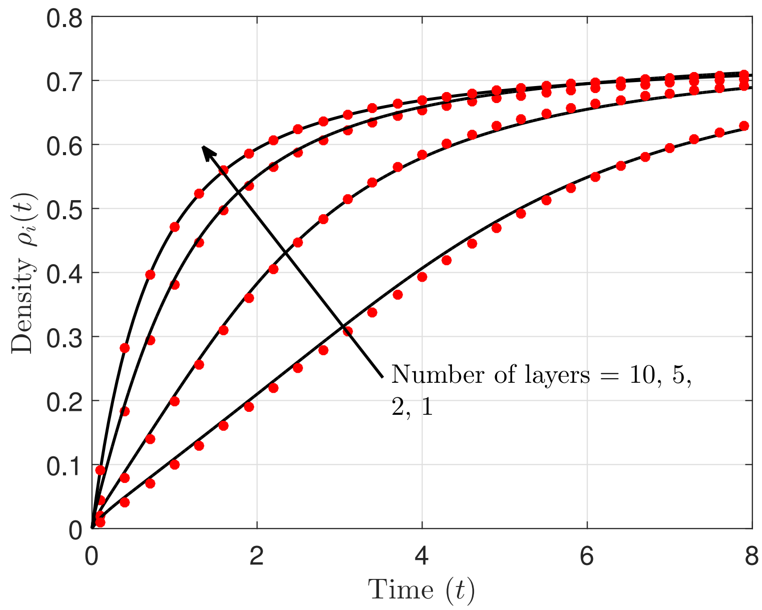

Figure 5.7: The evolution of density of rods of a particular color as a function of time t. The length of rods is $\sigma = 1$. Markers and solid lines represent simulations and theoretical results, respectively.

5.5 Extension to 2D Multilayer RSA

In this section, we present the 2D version of the proposed multilayer RSA problem. We consider that circles with diameter σ arrive uniformly at random in $\mathbb{R}^2$. Let there be K colors in the system $\mathcal{K} = \{c_1, c_2, \ldots, c_K\}$ that are assigned to these circles based on the following rules:

1. An arriving circle that does not overlap with any of the admitted circles is assigned a color uniformly at random from $\mathcal{K}$.
2. If the circle overlaps with $n < K$ colors, it is assigned a color uniformly at random from the rest of the colors.
3. If the circle overlaps with all the colors, it is not admitted into the system.

Based on the above rules, an illustrative example is given in Fig. 5.8 where we have considered $K = 2$. In the left figure, all the arrivals before a given time t are presented. From a communications network perspective, the centers represent communicating nodes, the range of each node is represented by a circle centered at the node. These nodes transmit to their respective receivers (not shown in the illustration) on an orthogonal frequency band out of the two available bands. In the right figure, nodes with the same color transmit on the same frequency band. Hence, interference is reduced among nodes that are within the communication range of each other.

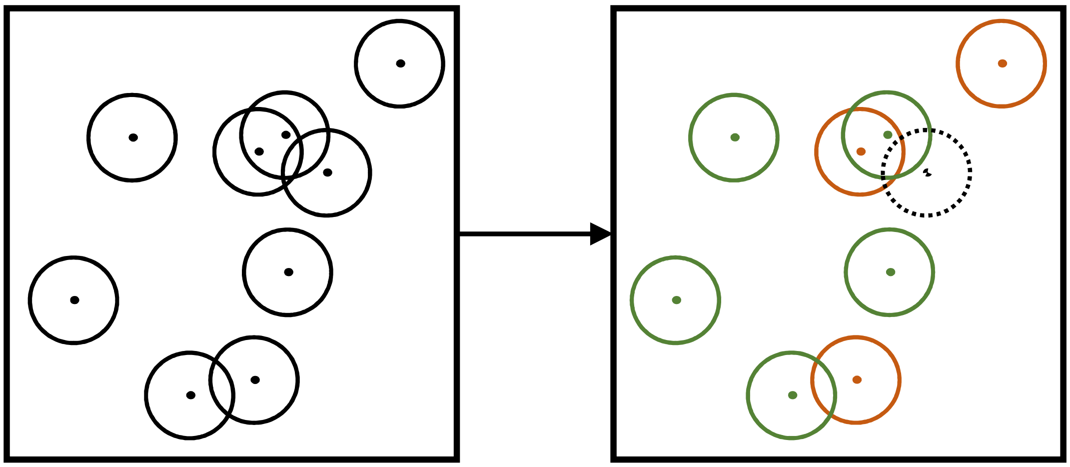

Figure 5.8: An illustration of the frequency band assignment process in a 2D wireless network. (Left) All the nodes that appear for transmission before a given time t. (Right) Nodes with the same color are assigned the same frequency band for transmission. Since there are two orthogonal frequency bands, only two out of three nodes with overlapping communication ranges are allowed to transmit. The node with a dotted circle remains silent.

Similar to the 1D case, our goal is to obtain the density of circles of a given color. Since the exact solution to the problem is extremely difficult to obtain even in the monolayer case [93, 94], we resort to an approximation. It is natural to consider an extension of either of the two approximation approaches developed for the 1D case. As mentioned in Section 5.3, the first approximation based on the iterative application of the monolayer RSA result is highly tractable, which makes it a promising candidate for extension to higher dimensions. Even though the second approximation based on the gap density function is slightly more accurate, its setup does not lend itself for a natural extension to higher dimensions. Therefore, to obtain the density of circles of a given color, we rely on extending the iterative approximation approach. In the sequel, we present this result for the 2D multilayer RSA case.

5.5.1 Approximate density characterization

Since this approach requires the known density result for monolayer RSA to be invoked repeatedly, for the sake of completeness, we first present this result from the literature [93]. Consider a 2D monolayer RSA process that is obtained from circles of diameter σ arriving uniformly at random at rate r_a per unit area per unit time. In the following lemma, we present $\rho(t)$, the density of the admitted circles at time t.

Lemma 5.3. *The density $\rho(t)$ is obtained by solving the following differential equation with the initial condition $\rho(0) = 0$:*

$$\int \frac{\mathrm{d}\rho(t)}{\phi(\kappa\rho(t))} = \frac{r_a}{\kappa} t + C, \tag{5.16}$$

where $\kappa = \frac{\pi\sigma^2}{4}$ is the area covered by a circle, $\kappa\rho(t)$ is the fraction of the area that is covered by the retained circles at time t, $\phi(\kappa\rho(t))$ is the probability that a circle arriving at an arbitrary location in $\mathbb{R}^2$ is retained at time t, and C is the integration constant. The series expansion of the retention probability in terms of density $\rho(t)$ is given as [93, Eq. 30]

$$\begin{aligned}\phi(\kappa\rho(t)) =& 1 - 4\pi\sigma^2\rho(t) + \frac{\rho(t)^2}{2}\int_{\sigma}^{2\sigma} 4\pi r A_2(r)\mathrm{d}r + \frac{\rho(t)^3}{3}\int_{\sigma}^{2\sigma} 2\pi r A_2^2(r)\mathrm{d}r \\ & - S_3^{\mathtt{eq}} + O(\rho(t)^4),\end{aligned} \tag{5.17}$$

where $S_3^{\mathtt{eq}} = \frac{\rho(t)^3}{8}\pi\left(\sqrt{3}\pi - \frac{14}{3}\right)\sigma^6 + O(\rho(t)^4)$, $A_2(r)$ is the area of intersection of two circles of radius σ whose centers are separated by distance r.

Proof: For the detailed proof of this lemma, please refer to [93]. We just present the proof sketch here. Note that $\kappa\rho(t)$ is the fraction of area covered by the retained circles at time t. Now, the rate of change of the fraction of the covered area depends on the number of arrivals $r_a\mathrm{d}t$ per unit area and the probability of an arrival being retained, which is given by $\phi\left(\kappa\rho(t)\right)$. Hence,

$$\frac{\mathrm{d}(\kappa\rho(t))}{\mathrm{d}t} = r_a\phi\left(\kappa\rho(t)\right). \tag{5.18}$$

The expression for $\phi\left(\kappa\rho(t)\right)$ is derived in [93]. ■

The result of the above lemma is accurate up to a coverage of about 35% by all the admitted circles. Using the knowledge of the asymptotic coverage of the 2D RSA process at the jamming limit, a unified equation for the retention probability is presented in [93] that is accurate for the entire coverage range. This equation is given as

$$\phi_{\mathtt{FIT}}(\rho(t)) = (1 + b_1x(t) + b_2x(t)^2 + b_3x(t)^3)(1 - x(t)^3), \tag{5.19}$$

where $x(t) = \rho(t)/\rho(\infty)$ and $\rho(\infty)\kappa = 0.5474$ is the fraction of the area that is covered at the jamming limit as $t \to \infty$. The coefficients $b_1 = 0.8120, b_2 = 0.4258$ and $b_3 = 0.0716$ are obtained by matching the order of $\rho(t)$ in equations (6.12) and (6.13). Now the expression for $\rho(t)$ can be obtained by numerically solving the differential equation (6.11) using (6.13).

As mentioned earlier, we use the same approach as the 1D multilayer RSA presented in Sec. 5.3 to approximate the density of circles of a given color. Let us extend the sequential color assignment process presented in Sec. 5.3 for 2D case, where an arriving circle is considered to be assigned c_1 before c_2 and so on. Let $\tilde{\rho}_i(t)$ be the density of circles of i-th color under this sequential assignment scheme. In the following proposition we present the approximate result to estimate the density of circles of a given color for 2D multilayer RSA with the original random color assignment scheme.

Proposition 4. The density of circles of a given color for 2D multilayer RSA with random color assignment scheme is given as

$$\rho_i(t) = \frac{\sum_{k=1}^{K} \tilde{\rho}_k(t)}{K},$$

where $\tilde{\rho}_k(t)$ is obtained by solving the monolayer RSA problem using Lemma 6.2 with adjusted rate of arrival per unit area for the k-th layer as $r_a - \sum_{i=1}^{k-1} \frac{\tilde{\rho}_i(t)}{t}$.

In Fig. 5.9, we present the fraction of the total area covered by circles of a given color as a function of time. From the figure, we see the approximated theoretical result are in close agreement with the Monte Carlo simulations result for different number of colors.

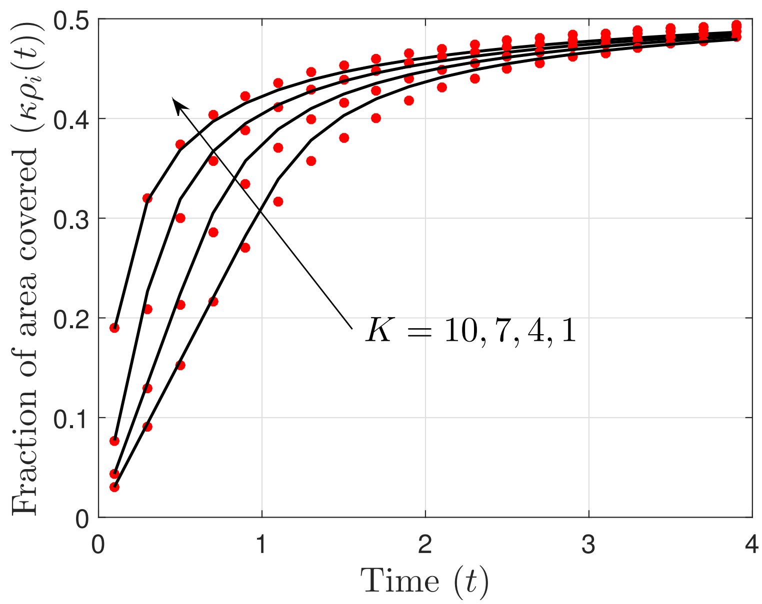

Figure 5.9: The fraction of the area covered by a circle of a particular color for a 2D multilayer RSA as a function of time t. Markers and solid lines represent simulations and theoretical results, respectively.

5.6 Conclusion

In this chapter, we introduced a new variant of the multilayer RSA process that is inspired by the orthogonal resource sharing in wireless networks. For the 1D version of this process, we presented two useful approximations to obtain the density of deposited rods for a given layer.

While our first approach is more amenable to numerical evaluation, the second approach is more accurate and provides useful information regarding the gap density function, which is an important statistical quantity to understand the kinetics of the RSA process. We have also extended the first approximation to obtain the density of a given layer for the 2D version of this multilayer RSA process. In the next chapter, using the results derived for the 2D version, we analyze the pilot assignment probability in a cell-free mMIMO network.

Chapter 6

Pilot Assignment Schemes for Cell-Free Massive MIMO Networks

6.1 Introduction

Similar to cellular mMIMO networks, the channel state information (CSI) acquisition in a cell-free mMIMO systems needs to be done through uplink (UL) pilot transmission due to its scalability. Not surprisingly, under the assumptions of independent Rayleigh fading and sub-optimal linear precoders, pilot contamination becomes one of the capacity limiting factor of cell-free mMIMO networks [2, 5, 95]. Hence, judicious pilot assignment is essential to reduce the effect of pilot contamination, which is the main focus of this chapter.

6.1.1 Related works

In general, the optimal pilot assignment problem for a cell-free mMIMO system is non-deterministic polynomial-time (NP)-hard in nature. As a consequence the computational resources required to obtain the optimal solution scales exponentially with the number of users. Therefore, almost all the works in the literature focus on providing heuristics-based algorithms to get an efficient solution. These algorithms can be broadly categorized into centralized and distributed schemes. In [5], a distributed random pilot allocation and a centralized greedy pilot allocation schemes are presented for a cell-free mMIMO network. In [20] and [96], a distributed random access type pilot assignment scheme is proposed, where a user is not served if its CSI cannot be estimated reliably. A centralized structured pilot allocation scheme with an iterative application of the K-means clustering algorithm is presented in [23]. A natural way to address the resource allocation problem is by framing it as a graph coloring problem. This idea has been explored in [21] and [22]. In [21], a centralized pilot sequence design scheme is proposed where the users in the neighborhood of an access point (AP) use orthogonal pilot sequences. The problem is posed as a vertex coloring problem and solved using the greedy DASTUR algorithm. [22] follows a similar theme, where authors construct the conflict graph by having an edge between users that are dominant interferer to each other. The graph coloring problem is solved using a greedy algorithm. In [97], a dynamic pilot allocation approach is presented where two users can be assigned the same pilot sequence if the signal to interference and noise ratios (SINRs) of both the users are above a certain threshold. While the aforementioned works, primarily focus on reducing the interference due to pilot contamination, authors in [24] and [98], solve pilot allocation optimization problems to maximize certain utility metric. Due to the NP-hard nature of the problem, authors in [24] use the Tabu search to solve the pilot allocation problem with the objective of maximizing sum-user spectral efficiency (SE). Further, in [98], system throughput maximization, and minimum user throughput maximization problems are solved using an iterative scheme based on the Hungarian algorithm. Most of these works rely on the common underlying principle that the same pilot can be assigned to the users that have sufficient geographical separation. This principle also motivates the main pilot assignment scheme proposed in this work along with the additional objective that it should be distributed as well as scalable in nature while providing competitive performance in terms of user SE. Our contributions are summarized next.

6.1.2 Contributions

RSA-based pilot assignment scheme

First, we propose a random pilot assignment algorithm with a minimum distance constraint among the co-pilot users to reduce the effect of pilot contamination. The algorithm is inspired by RSA process, which has been traditionally used across different scientific disciplines such as condensed matter physics, surface chemistry, and cellular biology, to name a few, to study the adsorption of large-particles such as colloids, proteins, and bacteria on a surface. Apart from proposing the algorithm with a potential distributed implementation in the network, we have used the results of the multilayer RSA scheme presented in Chapter 5 to analyze/predict the probability of a pilot assignment to a typical user in the network.

Two centralized pilot allocation schemes for benchmarking

To quantify the efficacy of the proposed RSA-based pilot allocation scheme, we also propose two centralized algorithms. The first algorithm, similar to the RSA scheme, is agnostic to AP locations and considers only the user locations. This algorithm, named the max-min distance-based algorithm, partitions the users into sets of co-pilot users to maximize the minimum Euclidean distance among the co-pilot users. This scheme is optimal from the perspective of geographical separation between a set of co-pilot users. In the proposed algorithm, the minimum distance is obtained through the bisection search subject to a set of feasibility constraints. The second algorithm, which takes into account both AP and user locations, maximizes the sum-user SE of the network subject to minimum user `SINR` constraint. First, leveraging tools from spectral graph theory, the algorithm partitions the users into a desired number of clusters based on similar path loss with respect to the APs. Next, using the branch and price (BnP) algorithm, sets of co-pilot users are obtained with the additional constraint that two users in the same cluster are not assigned the same pilot.

This approach provides us with a near-optimal solution in terms of sum-SE at the cost of a significant increase in computational complexity compared to the other two algorithms. Therefore, it is more suitable to use this algorithm for benchmarking other pilot allocation schemes than practical implementation.

Insights from numerical results

Through extensive system simulation, we conclude that the RSA-based pilot allocation scheme provides competitive performance compared to the max-min distance-based pilot allocation scheme, especially when the ratio of the number of users to the pilots is relatively high. Further, both the RSA and the max-min distance-based schemes achieve close to near-optimal performance with increasing AP density. In addition, we compare the performance of RSA and the max-min scheme to a centralized pilot allocation scheme based on iterative K-means algorithm available in the literature. While RSA performs as good as the K-means, max-min distance based scheme marginally outperforms it.

6.2 System Model

6.2.1 Network model

We limit our attention to the downlink (DL) of a cell-free mMIMO system. The locations of the APs form a Poisson point process (PPP) Φ_r of density λ_r. Similarly, the user point process Ψ_u is also modeled as an independent PPP of density λ_u. Each AP is equipped with N antennas and each user with a single antenna. The APs are connected to a BBU and collectively serve users in the network. The distance between a user at $\mathbf{u}_k \in \Psi_u$ and an AP at $\mathbf{r}_m \in \Phi_r$ is denoted by d_{mk}. In line with the mMIMO literature, where the number of antennas is assumed to be an order of magnitude more than the number of users, we consider that the antenna density $N\lambda_r \gg \lambda_u$. Further, invoking stationarity of this setup, we analyze the system performance for the typical user $\mathbf{u}_o$, which is located at the origin $\mathbf{o}$.

Channel estimation: Let $\mathbf{g}_{mk} = \sqrt{\beta_{mk}}\mathbf{h}_{mk}$ be the channel gain between the m-th AP and the k-th user, where β_{mk} captures the large-scale channel gain and $\mathbf{h}_{mk} \sim \mathcal{CN}(0, \mathbf{I}_N)$ captures the small-scale channel fluctuations. We consider that the large-scale channel gain β_{mk} is only due to the distance dependent path-loss, i.e. $\beta_{mk} = l(d_{mk})^{-1}$, where $l(\cdot)$ is a non-decreasing path-loss function. While the analysis presented in this paper is agnostic to the choice of $l(\cdot)$, we will need to choose a specific $l(\cdot)$ for the numerical results, which is presented in Section 6.6.

In order to obtain the channel estimates, each user uses a pilot from a set of P orthogonal pilot sequences $\mathcal{P} = [\mathbf{p}_1, \mathbf{p}_2, \ldots, \mathbf{p}_P]^T$, where $\mathbf{p}_i$ denotes the i-th sequence. The length of each pilot is τ_p symbol durations, which is less than the coherence interval. Since we assume that the P sequences are orthogonal to each other, $P \leq \tau_p$ and $\mathbf{p}_i^H \mathbf{p}_j = \tau_p \mathbf{1}(i = j)$, where $\mathbf{1}(\cdot)$ denotes the indicator function. Due to finite number of pilots, the pilot set needs to be reused across the network. Let the pilot used by the k-th user be $\mathbf{p}(k)$. During the pilot transmission phase, the received signal matrix $Y_m \in \mathbb{C}^{N \times \tau_p}$ at the m-th AP is

$$Y_m = \tau_p \sum_{\mathbf{u}_k \in \Psi_u} \mathbf{g}_{mk} \mathbf{p}(k)^T + W_m,$$

where ρ_p is the normalized transmit signal-to-noise ratio (SNR) of each pilot symbol and W_m is an additive white Gaussian noise matrix whose elements follow $\mathcal{CN}(0, 1)$. At the m-th AP, the least-square estimate, $\mathbf{y}_{ml} \in \mathbb{C}^{N \times 1}$, of the channel of the users that use the l-th sequence is

$$\mathbf{y}_{ml} = Y_m \mathbf{p}_l^* = \tau_p \rho_p \sum_{\mathbf{u}_k \in \Phi_{ul}} \mathbf{g}_{mk} + W_m \mathbf{p}_l^*,$$

where Φ_{ul} is the set of users that use the l-th sequence. Further, the set of users that are assigned a pilot is defined as $\Phi_u = \cup_{k=1}^{P} \Phi_{uk}$. Assuming $\mathbf{u}_o \in \Phi_{ul}$, the minimum-mean-squared-error (MMSE) estimate of the channel of the typical user at the m-th AP is given as

$$\hat{\mathbf{g}}_{mo} = \mathbb{E}[\mathbf{y}_{ml} \mathbf{g}_{mo}^H](\mathbb{E}[\mathbf{y}_{ml} \mathbf{y}_{ml}^H])^{-1} \mathbf{y}_{ml} = \frac{\beta_{mo}}{\sum\limits_{\mathbf{u}_k \in \Phi_{ul}} \beta_{mk} + \frac{1}{\tau_p \rho_p}} \mathbf{y}_{ml} = \alpha_{mo} \mathbf{y}_{ml}. \tag{6.1}$$

In this case, the error vector $\tilde{\mathbf{g}}_{mk} = \mathbf{g}_{mk} - \hat{\mathbf{g}}_{mk}$ is uncorrelated to the estimated vector. Now the estimate and the error vectors are distributed as follows [6]:

$$\hat{\mathbf{g}}_{mo} \sim \mathcal{CN}\left(\mathbf{0}, \gamma_{mo} \mathbf{I}_N\right), \ \tilde{\mathbf{g}}_{mo} \sim \mathcal{CN}\left(\mathbf{0}, \left(\beta_{mo} - \gamma_{mo}\right) \mathbf{I}_N\right),$$

where $\gamma_{mo} = \frac{\tau_p \rho_p \beta_{mo}^2}{1 + \sum_{\mathbf{u}_k \in \Phi_{ul}} \tau_p \rho_p \beta_{mk}}$. From the expression of γ_{mo}, it is clear that the quality of channel estimates depend on the locations of the co-pilot users in Φ_{ul}.

DL user SINR*:* Using the channel estimates, each AP precodes the data for all the users in the network. In this work, we consider conjugate beamforming precoding scheme. Since the m-th AP cannot distinguish among the channels of the users that use the l-th pilot, it uses the normalized direction of $\mathbf{y}_{ml}$ for beamforming, i.e. the precoding vector used to transmit data to the users that use l-th pilot is given as

$$\mathbf{w}_{ml} = \mathbf{y}_{ml} / \sqrt{\mathbb{E}[\|\mathbf{y}_{ml}\|^2]} = \hat{\mathbf{g}}_{mo} / \sqrt{\mathbb{E}[\|\hat{\mathbf{g}}_{mo}\|^2]}.$$

Now the data transmitted by the m-th AP is given as

$$\mathbf{x}_m = \sqrt{\rho_d} \sum_{p=1}^{P} \mathbf{w}_{mp}^* \sum_{\mathbf{u}_k \in \Phi_{up}} \sqrt{\eta_{mk}} q_k,$$

where η_{mk} is the transmission power used by the m-th AP for the k-th user and $q_k \sim \mathcal{CN}(0,1)$ is the transmit symbol of the k-th user. For each AP, we assume the following power constraint: $\mathbb{E}[\|\mathbf{x}_m\|^2] \leq \rho_d$. The symbol received at $\mathbf{o}$ (that uses the l-th pilot) is given as

$$
\begin{aligned}
r_o = \sum_{\mathbf{r}_m \in \Phi_r} \mathbf{g}_{mo}^T \mathbf{x}_m + n_o = &\sqrt{\rho_d} \sum_{\mathbf{r}_m \in \Phi_r} (\hat{\mathbf{g}}_{mo}^T + \tilde{\mathbf{g}}_{mo}^T) \frac{\hat{\mathbf{g}}_{mo}^*}{\sqrt{N\gamma_{mo}}} \sqrt{\eta_{mo}} q_o \\
&+ \sqrt{\rho_d} \sum_{p=1, p\neq l}^{P} \sum_{\mathbf{u}_k \in \Phi_{up}} \sum_{\mathbf{r}_m \in \Phi_r} \mathbf{g}_{mo}^T \frac{\hat{\mathbf{g}}_{mp}^*}{\sqrt{N\gamma_{mp}}} \sqrt{\eta_{mk}} q_k \\
&+ \sqrt{\rho_d} \sum_{\mathbf{u}_{k'} \in \Phi'_{ul}} \sum_{\mathbf{r}_m \in \Phi_r} (\hat{\mathbf{g}}_{mo}^T + \tilde{\mathbf{g}}_{mo}^T) \frac{\hat{\mathbf{g}}_{mo}^*}{\sqrt{N\gamma_{mo}}} \sqrt{\eta_{mk'}} q_{k'} + n_o,
\end{aligned}
$$

where $\Phi'_{ul} = \Phi_{ul} \setminus \mathbf{u}_o$, the first term on the right hand side is the desired term, the second term corresponds to multi-user interference due to non-copilot users, and the third term is the source of interference due to pilot contamination.

6.2.2 Metrics for system performance analysis

DL power control and SINR of an arbitrary user

Since our objective is to propose a scheme to reduce pilot contamination, we focus on the operational regime where pilot contamination dominates rest of the interference terms. In the following lemma, we present the SINR expression of the typical user under the assumption that the APs are equipped with $N \to \infty$ antennas.

Lemma 6.1. *Conditioned on Φ_r and Φ_u, the asymptotic* SINR *of the typical user is given as*

$$
\mathtt{SINR}_{o,\infty} = \frac{\left(\sum_{\mathbf{r}_m \in \Phi_r} \sqrt{\eta_{mo}\gamma_{mo}}\right)^2}{\sum_{\mathbf{u}_k \in \Phi'_{ul}} \left(\sum_{\mathbf{r}_m \in \Phi_r} \sqrt{\eta_{mk}\gamma_{mo}}\right)^2}. \tag{6.2}
$$

Proof: The estimated symbol at the typical user can be obtained as $\hat{q}_o = r_o/\sqrt{N}$. Now, using the law of large numbers, as $N \to \infty$, $\frac{\hat{\mathbf{g}}_{mo}^T \hat{\mathbf{g}}_{mo}^*}{N} \to \gamma_{mo}$, $\frac{\tilde{\mathbf{g}}_{mo}^T \hat{\mathbf{g}}_{mo}^*}{N} \to 0$, and $\frac{\mathbf{g}_{mo}^T \hat{\mathbf{g}}_{mp}^*}{N} \to 0$. Hence, the limiting SINR converges to (6.2). ■

In this work, we consider a distributed power control scheme [23] where the transmission power used by the the m-th AP for the typical user at $\mathbf{o}$ is given as

$$
\eta_{mo} = \frac{\gamma_{mo}}{P \sum_{\mathbf{u}_k \in \Phi_{ul}} \gamma_{mk}}, \tag{6.3}
$$

such that $\sum_{\mathbf{u}_k \in \Phi_{ul}} \eta_{mk} = 1/P$. We assume that the APs allocate equal power $1/P$ to serve each set of co-pilot users. Now, we define the following metrics for the performance analysis:

i. Pilot assignment probability of the typical user: Since the RSA-based pilot assignment is stochastic in nature, for a given realization of user locations, a few of the users may not be assigned a pilot. Hence, pilot assignment probability to the typical user is an important metric to analyze for this scheme. Let $\{\mathcal{I}_o = 1\}$ be the event that the user at $\mathbf{o}$ is assigned a pilot. Then the aforementioned probability is given as

$$\mathcal{M}_o = \mathbb{P}[\mathcal{I}_o = 1] = \mathbb{E}[\mathbf{1}(\mathcal{I}_o = 1)], \tag{6.4}$$

where the expectation is taken over Ψ_u. In Section 6.3.1, we present our proposed approach to characterize the above quantity along with the RSA-based pilot assignment scheme. This quantity can be used to get an estimate of the number of pilots necessary to satisfy target pilot assignment probability for a given user density. Note that $\mathcal{M}_o = 1$ for the max-min distance-based and the BnP-based schemes proposed in this work.

ii. Average user spectral efficiency: It is defined as

$$\overline{\mathtt{SE}}_o = \mathbb{E}\left[\mathcal{I}_o \log_2(1 + \mathtt{SINR}_o)\right] = \mathbb{E}\left[\log_2(1 + \mathtt{SINR}_o) \middle| \mathcal{I}_o = 1\right] \mathbb{P}[\mathcal{I}_o = 1], \tag{6.5}$$

where the expectation is taken over Φ_r, Ψ_u.

iii. Sum-user spectral efficiency: In contrast to the above two quantities, sum-user SE is defined for a given realization of Φ_r and Ψ_u over a finite observation window $W \subset \mathbb{R}^2$ and given as

$$\Sigma_{\mathtt{SE}} = \sum_{\mathbf{u}_j \in \Psi_u \cap W} \mathcal{I}_j \log_2(1 + \mathtt{SINR}_j), \tag{6.6}$$

where $\mathcal{I}_j = 1$ for the max-min and BnP-based schemes and $\mathcal{I}_j \in \{0, 1\}$ for the RSA-based scheme.

6.3 RSA-based Pilot Allocation Scheme

Before delving into the proposed RSA-based pilot assignment scheme, we find it pertinent to mention the complexity associated with pilot assignment problem that serves as a motivation to propose a heuristic algorithm. The objective of any resource allocation algorithm is to maximize a cost (reward) function subject to certain constraints due to a limited availability of resources. In our case, we choose the cost function to be the sum SE. Hence, for a given realization of the locations of APs and users, our objective is to maximize the sum SE by judiciously selecting the set of co-pilot users. Inspired by the column generation approach prevalent in the linear programming literature, the problem can be formulated in the following way. We consider each potential set of co-pilot users as a column. In order to have a finite dimension for the set of feasible solutions, it is imperative to consider a finite observation window with N_u users $\mathcal{S} = \{\mathbf{u}_1, \mathbf{u}_2, \ldots, \mathbf{u}_{N_u}\}$ and N_r APs. Let $\mathcal{A}$ denotes the set of all the potential co-pilot user sets avoiding the null and singleton sets. Hence, the cardinality of $\mathcal{A}$, which is also the total number of columns, is $2^{N_u} - N_u - 1$. As an example, consider a set of users $\mathcal{A}_k = \{\mathbf{u}_1, \mathbf{u}_2, \mathbf{u}_3\}$. The corresponding column for these co-channel users is given as $\mathbf{x}_k = \begin{bmatrix}1 & 1 & 1 & 0 & \dots & 0\end{bmatrix}^T \in \{0,1\}^{N_u}$. We define the matrix A, where each column corresponds to a set in $\mathcal{A}$. Further, the cost of a set $\mathcal{A}_j$ (equivalently, the cost of the j-th column $\mathbf{x}_j$) is given as

$$c(\mathbf{x}_j) = \begin{cases} \sum_{\mathbf{u}_i \in \mathcal{A}_j} \log_2(1 + \Gamma_{ij}), & \text{if } \Gamma_{ij} \geq \Gamma_{\min} \ \forall \mathbf{u}_i \in \mathcal{A}_j \\ -M, & \text{if } \Gamma_{ij} < \Gamma_{\min} \text{ for any } \mathbf{u}_i \in \mathcal{A}_j \end{cases} \tag{6.7}$$

where the SINR of the i-th user in the j-th set is $\Gamma_{ij} = \frac{\left(\sum_{\mathbf{r}_m \in \Phi_r} \sqrt{\eta_{mi}\gamma_{mi}}\right)^2}{\sum_{\mathbf{u}_k \in \{\mathcal{A}_j \setminus \mathbf{u}_i\}} \left(\sum_{\mathbf{r}_m \in \Phi_r} \sqrt{\eta_{mk}\gamma_{mi}}\right)^2}$, $\Gamma_{\min}$ is the minimum SINR threshold, and M is a large positive number. With this definition the set of co-pilot users not satisfying the minimum SINR threshold even for a single user is (almost) never selected. Now, we express the optimization problem as

$$\max_{\Lambda} \quad \sum_{s=1}^{|\mathcal{A}|} c(\mathbf{x}_s)\lambda_s \tag{6.8a}$$

$$\text{s.t.} \quad A\Lambda = \mathbf{1} \tag{6.8b}$$

$$\|\Lambda\|_1 = P \tag{6.8c}$$

$$\Lambda \in \{0,1\}^{|\mathcal{A}|}, \tag{6.8d}$$

where $\Lambda = \left[\lambda_1, \lambda_2, \dots, \lambda_{|\mathcal{A}|}\right]^T$, (6.8b) ensures that each user is assigned exactly one pilot, (6.8c) ensures that P columns are selected each representing a set of co-pilot users. Above problem is NP-hard. Further, the feasible solution space of the problem is $\binom{|\mathcal{A}|}{P}$. Hence, if we wish to obtain the optimal solution even for a moderately small system of 24 users with 6 pilots, we need to search over a feasible set of size approximately 3.1×10^{40}.

Owing to the complexity of the problem, it is natural to consider heuristic solutions, *albeit* sub-optimal, that can be implemented efficiently in the network. In the following subsection, we present a sub-optimal pilot allocation algorithm that only considers user locations to select the set of co-pilot users such that the pilot contamination-based interference is mitigated thereby implicitly improving the user SE as well as the sum SE. This algorithm, which is inspired by the RSA process, can be implemented both in a centralized or distributed manner and is easily scalable as the network size grows.

6.3.1 RSA-based pilot assignment algorithm

Our goal is to select the sets of co-pilot users among all the users in the network such that a minimum distance $R_{\texttt{inh}}$ is maintained between two co-pilot users. This can be achieved by dependent selection of the users from the original user point process Ψ_u as outlined in

Algorithm 1. The algorithm assigns a random mark t_k, which is uniformly distributed in $[0,1]$, to each point $\mathbf{u}_k \in \Psi_u$. Let $\mathcal{B}_{R_{\mathtt{inh}}}(\mathbf{u}_k)$, a circle of radius $R_{\mathtt{inh}}$ centered at $\mathbf{u}_k$, be defined as the contention domain of the point at $\mathbf{u}_k$. For pilot assignment, the algorithm considers each user in increasing order of their marks, i.e. the lowest mark is considered first. From the available set of pilots, a pilot is randomly assigned to a user at $\mathbf{u}_k$, where the set of available pilots are those which have not been assigned to the users in $\mathcal{B}_{R_{\mathtt{inh}}}(\mathbf{u}_k)$. Note that to implement this algorithm, the BBU requires only the location information of the users, which does not require any additional signaling overhead as this information is typically present at a centralized node in the network such as the BBU. At the end of this subsection, we also discuss a protocol for potential distributed implementation of the algorithm.

```
Input: User locations Ψ_u, the set of pilots P, inhibition distance R_inh
Result: Pilot assignment table T
Initialization: T = ∅, a random mark t_i ~ U(0,1) for each u_i ∈ Ψ_u;
Let Ψ̃_u be the set of users in the increasing order of marks;
for User u ∈ Ψ̃_u do
    Set: P' = P;
    while User u is not assigned a pilot do
        if P' == ∅ then
            No pilot can be assigned: T = T ∪ ∅;
            Break;
        else
            Select a pilot sequence p_k randomly from the set P';
        end
        if No other users in B_{R_inh}(u) are using p_k then
            Assign the pilot: T = T ∪ p_k;
            Break;
        else
            Remove p_k from list of potential pilots: P' = P' \ p_k;
        end
    end
end
```

Algorithm 1: The RSA-based pilot assignment algorithm in for a cell-free mMIMO system.

For the system designers, it is useful to know the probability that a user will be scheduled as a function of the density of users and the number of pilots in the system. Following subsections present an approximate theoretical result that answers the aforementioned question eliminating the need for a system simulation. It is worth-mentioning that the approximate result is a new contribution to the RSA literature as the exact solution for counterpart of this problem even in the case of 1D is unknown.

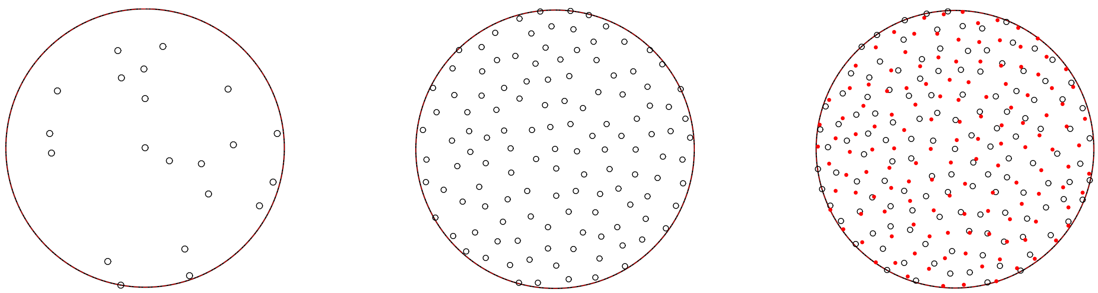

Figure 6.1: Realizations of co-pilot user locations using Algorithm 1. Parameters: $R_{\texttt{inh}} = 200$, $\lambda_u = 2 \times 10^{-6}$ (left), $\lambda_u = 10^{-3}$ (center, right). Left and center figures represent realizations of co-pilot users for $P = 1$. Right figure represents a realization of co-pilot users for $P = 2$.

Analysis of the pilot assignment probability

Recall that Φ_u is the set of users that are assigned a pilot (in this case by Algorithm 1), i.e. $\Phi_u = \cup_{p=1}^{P} \Phi_{up}$. Let t_o be the mark associated with the typical user. Now, the user at $\mathbf{o}$ is assigned a pilot if $|\Phi_u \cap \mathcal{B}_{R_{\texttt{inh}}}(\mathbf{o})| \leq P - 1$. This is ensured by the following two events:

- $\mathcal{E}_1$: there are at most $P - 1$ points in $\mathcal{B}_{R_{\texttt{inh}}}(\mathbf{o}) \cap \Psi_u$ that have marks less than t_o,
- $\mathcal{E}_2$: there are more than $P - 1$ points in $\mathcal{B}_{R_{\texttt{inh}}}(\mathbf{o}) \cap \Psi_u$ that have marks less than t_o. However, some of these points are not assigned a pilot as their contention domains have more than P points with marks smaller than their respective marks.

While obtaining the probability of $\mathcal{E}_1$ is straightforward, characterizing $\mathcal{E}_2$ is highly non-trivial even for $P = 1$. Note that for $P = 1$, the above formulation has been used to model the CSMA-CA networks. However, due to the intractability of $\mathcal{E}_2$, Matérn hardcore process of type-II (MHPP-II) has been used for approximate characterization for Φ_u [43]. Hence, one may be inclined to extend the MHPP-II process for $P \geq 2$. However, one of the limitations of the MHPP-II process is that it underestimates the number of points in Φ_u [99]. Hence, the extension of the MHPP-II model for $P \geq 2$ will not result in an accurate estimation. On the other hand, for $P = 1$, Φ_u is exactly modeled by the simple sequential inhibition (SSI) process [99] or the RSA process [100]. Using this fact, in the sequel, we present an efficient heuristic to estimate the pilot assignment probability.

Consider a finite observation window $\mathcal{B}_{R_s}(\mathbf{o}) \subset \mathbb{R}^2$, where $R_s \gg R_{\texttt{inh}}$. Let $N_u = |\Psi_u \cap \mathcal{B}_{R_s}(\mathbf{o})|$ be the total number of users and $N_s = |\Phi_u \cap \mathcal{B}_{R_s}(\mathbf{o})|$ be the number of users that are assigned a pilot. Note that for a given N_u, N_s is a random variable as it depends on the realization of Ψ_u as well as random marks associated with these points. Now, for a given $N_u > P$, $\mathbb{E}[N_s|N_u]$ is the average number of users that are assigned a pilot. Hence, the probability that the typical user out of the N_u users is assigned a pilot is $\mathbb{E}[N_s|N_u]/N_u$. On the other hand, for $N_u \leq P$, the typical user is assigned a pilot with probability 1.

Combining these two events, we write the pilot assignment probability as

$$\begin{aligned}\mathbb{P}[\mathcal{I}_o = 1] =& \mathbb{P}\left[N_u \leq P\right] + \mathbb{E}_{N_u}[\mathbb{E}[N_s|N_u]N_u^{-1}\big|N_u > P]\mathbb{P}\left[N_u > P\right] \\ \approx& \mathbb{P}\left[N_u \leq P\right] + \mathbb{E}\left[N_s|N_u = \pi R_s^2\lambda_u\right]\mathbb{E}[N_u^{-1}\big|N_u > P]\mathbb{P}\left[N_u > P\right],\end{aligned} \tag{6.9}$$

where the second step is an approximation as instead of $\mathbb{E}_{N_u}[\mathbb{E}[N_s|N_u]|N_u > P]$, we determine $\mathbb{E}[N_s]$ by considering $N_u = \pi R_s^2\lambda_u$, which is its expected value. Since N_u is Poisson distributed with mean $\lambda_u\pi R_s^2$,

$$\mathbb{E}\left[N_u^{-1}|N_u > P\right] = \frac{\lambda_u\pi R_s^2 - \sum_{n=0}^{P}\mathrm{Poi}(\lambda_u\pi R_s^2, n)}{1 - \sum_{n=0}^{P}\mathrm{Poi}(\lambda_u\pi R_s^2, n)}, \tag{6.10}$$

where $\mathrm{Poi}(\lambda_u\pi R_s^2, n) = e^{-\lambda_u\pi R_s^2}\frac{(\lambda_u\pi R_s^2)^n}{n!}$.

Next, we discuss our approach to analytically estimate $\mathbb{E}\left[N_s|N_u = \pi R_s^2\lambda_u\right]$ leveraging the rich theory of the RSA process. For convenience, we use the notation $\mathbb{E}\left[N_s\right]$ to represent the above expectation. We first present the analysis for the special case of $P = 1$ followed by its extension to the general case of $P \geq 2$.

Pilot assignment probability for $P = 1$

Traditionally, the RSA process has been used across different disciplines, such as condensed matter physics, surface chemistry, and cellular biology, to study the adsorption of different substances, such as colloids, proteins, and bacteria, on a surface [100]. Next, we present a brief overview of the RSA process before analyzing pilot assignment probability.

Random sequential adsorption process: An RSA process is defined as a stochastic space-time process, where n-dimensional hard spheres sequentially arrive at random locations in $\mathbb{R}^n$ such that any arriving sphere cannot overlap with already existing sphere. More formally, for 2D case, let Ψ be a homogeneous space-time point process on $\mathbb{R}^2 \times \mathbb{R}^+$. The circles with radii $R_{\mathtt{inh}}/2$ are arriving at a rate of λ_Ψ per unit area. Let $\Psi(t)$ be the point process on $\mathbb{R}^2$ when Ψ is observed at an arbitrary time t. Observe that the density of $\Psi(t)$ is $\lambda_\Psi t$. At time t, an arriving point at $\mathbf{x} \in \mathbb{R}^2$ is retained if there are no other points within $\mathcal{B}_{R_{\mathtt{inh}}}(\mathbf{x})$. Let $\varphi(t|\Psi)$ be a realization of the set of the retained points at time t. Clearly, $\varphi(t_1|\Psi) \subseteq \varphi(t_2|\Psi)$ for $t_1 \leq t_2$. Moreover, there exists a time $c \in R^+$ such that $\varphi(t_i|\Psi) = \varphi(t_j|\Psi)$ for $t_i, t_j > c$, i.e. no more points can be added to the system. This is known as the *jamming limit*. Observe that the random marks assigned by Algorithm 1 can be thought of as the arrival times of the points in Ψ_u. In this interpretation, the points that arrive early (have smaller marks) are more likely to get an assignment.

Let $\Phi(t)$ be the point process of the retained points at time t and $\rho(t)$ be the corresponding density. In order to obtain the density of retained point process for a given density of original point process, we need to observe the system at a specific time. For example, if we want to obtain the density of retained points for an original point density of $2\lambda_\Psi$, then we need to observe the system at $t = 2$. Fig. 6.1 illustrates the realizations of co-pilot users for different λ_u and P. In the left figure, the system does not reach the jamming limit due to lower density of the original user point process Ψ_u. On the other hand, the center figure (almost) reaches the jamming limit and there cannot be more co-pilot users in the system. Notice the regular, almost grid-type, realization of points. The right figure illustrates the jamming state for $P = 2$. In the following lemma, we present the density of $\Phi(t)$.

Lemma 6.2. *The density $\rho(t)$ of the point process $\Phi(t)$ is obtained by solving the following differential equation [93] with the initial condition $\rho(0) = 0$:*

$$\int \frac{\mathrm{d}\rho(t)}{\phi(\kappa\rho(t))} = \frac{\lambda_\Psi}{\kappa} t + C, \tag{6.11}$$

where $\kappa = \frac{\pi R_{\mathtt{inh}}^2}{4}$ is the area covered by a circle, $\kappa\rho(t)$ is the fraction of the area that is covered by the retained circles at time t, $\phi(\kappa\rho(t))$ is the probability that a circle arriving at an arbitrary location in $\mathbb{R}^2$ is retained at time t, and C is the integration constant. The retention probability is given as [93, Eq. 19] $\phi(\kappa\rho(t)) =$

$$1 - 4\pi R_{\mathtt{inh}}^2 \rho(t) + \frac{\rho(t)^2}{2} \int_{R_{\mathtt{inh}}}^{2R_{\mathtt{inh}}} 4\pi r A_2(r)\mathrm{d}r + \frac{\rho(t)^3}{3} \int_{R_{\mathtt{inh}}}^{2R_{\mathtt{inh}}} 2\pi r A_2^2(r)\mathrm{d}r - S_3^{\mathtt{eq}} + O(\rho(t)^4), \tag{6.12}$$

where $S_3^{\mathtt{eq}} = \frac{\rho(t)^3}{8}\pi\left(\sqrt{3}\pi - \frac{14}{3}\right) R_{\mathtt{inh}}^6$, $A_2(r)$ is the area of intersection of two circles of radius $R_{\mathtt{inh}}$ whose centers are separated by distance r.

Since the function (6.12) is difficult to work with, a fitting function is analytically presented in [93] as $\phi_{\mathtt{FIT}}(\rho(t)) =$

$$(1 + b_1 x(t) + b_2 x(t)^2 + b_3 x(t)^3)(1 - x(t)^3), \tag{6.13}$$

where $x(t) = \rho(t)/\rho(\infty)$ and $\rho(\infty)\kappa = 0.5474$ is the fraction of the area that is covered at the jamming limit as $t \to \infty$. The coefficients b_1, b_2 and b_3 are obtained by matching the order of $\rho(t)$ in equations (6.12) and (6.13). Now the expression for $\rho(t)$ is obtained by solving the differential equation (6.11). While the closed form solution of the equation is difficult, the problem can be efficiently solved using standard numerical softwares. Now, with the help of Lemma 6.2, we present pilot assignment probability to a user for $P = 1$.

Lemma 6.3. *For a system with $P = 1$, the probability that the typical user is assigned a pilot is*

$$\mathbb{P}[\mathcal{I}_o = 1] \approx (1 + \pi R_s^2 \lambda_u) e^{-\pi R_s^2 \lambda_u} + (1 - (1 + \pi R_s^2 \lambda_u) e^{-\pi R_s^2 \lambda_u})(\rho(1)\pi R_s^2)\mathbb{E}\left[N_u^{-1} | N_u > 1\right],$$

where $\rho(1)$ is determined using Lemma 6.2 and $\mathbb{E}\left[N_u^{-1} | N_u > 1\right]$ using (6.10).

Proof: Since the density of user process Ψ_u is λ_u users per unit area, as per the RSA process definition, we can construct an equivalent space-time process where the arrivals occur at λ_u users per unit area per unit time. Now, to obtain the density of Φ_u, we observe this space-time system at time $t = 1$. Hence, the density of Φ_u is $\rho(1)$. The final expression is obtained by replacing $\mathbb{E}[N_s] = \pi R_s^2 \rho(1)$ in (6.9). ■

Pilot assignment probability for $P \geq 2$

For the general case of $P \geq 2$, consider that $\Phi_{u1}, \Phi_{u2}, \ldots, \Phi_{uP}$ contain the locations of the users that are assigned the pilots $\mathbf{p}_1, \mathbf{p}_2, \ldots, \mathbf{p}_P$, respectively, by Algorithm 1. Since Algorithm 1 has no preference regarding the pilots, the densities of $\Phi_{u1}, \Phi_{u2}, \ldots, \Phi_{uP}$ are the same. Let $\lambda_{\Phi_{uo}}$ be this density. In order to determine $\lambda_{\Phi_{uo}}$, modifications in Lemma 6.2 are necessary. To be specific, for (6.12), the knowledge of virial coefficients for a mixture of non-interacting hard spheres, and subsequently derivation of $S_3^{\mathtt{eq}}$ is necessary [93]. Since the above steps appear extremely difficult for this case, we provide an approximate yet accurate way to estimate the pilot assignment probability for $P \geq 2$.

Input: User locations Ψ_u, the set of pilots $\mathcal{P}$, inhibition distance $R_{\mathtt{inh}}$;
Result: Pilot assignment table $\mathcal{T}$;
Initialization: $\Psi'_u = \Psi_u$, $\mathcal{T} = \emptyset$;
for *Each pilot* $\mathbf{p}_k \in \mathcal{P}$ **do**
  for *Each user* $\mathbf{u} \in \Psi'_u$ **do**
    if *No other users in* $\mathcal{B}_{R_{\mathtt{inh}}}(\mathbf{u})$ *are using* $\mathbf{p}_k$ **then**
      Assign the pilot: $\mathcal{T} = \mathcal{T} \cup \mathbf{p}_k$;
      Remove $\mathbf{u}$ from list of users: $\Psi'_u = \Psi'_u \setminus \mathbf{u}$;
    end
  end
end

Algorithm 2: The regenerative algorithm for pilot assignment.

First, we present the regenerative pilot assignment algorithm (Algorithm 2) that is essential for our approximate analysis. Different from Algorithm 1, in Algorithm 2, the pilots are assigned to users sequentially, i.e. for the typical user the second pilot sequence is considered if the first pilot has already been assigned to a user in its contention domain, the third pilot sequence is considered if both the first and the second pilots have been used in its contention domain, and so on. In order to proceed with our analysis, we make the following remark:

Remark 6.4. *The total number of pilot reuses required in* $\mathcal{B}_{R_s}(\mathbf{o})$ *to obtain a target pilot assignment probability is the same for both Algorithms 1 and 2. In other words, the density of users that are assigned a pilot is the same for both the algorithms.*

Let $\tilde{\Phi}_{u1}, \tilde{\Phi}_{u2}, \ldots, \tilde{\Phi}_{uP}$ contain the locations of the users that are assigned pilots $\mathbf{p}_1, \mathbf{p}_2, \ldots, \mathbf{p}_P$, respectively, by Algorithm 2. Let $\lambda_{\tilde{\Phi}_{u1}}, \lambda_{\tilde{\Phi}_{u2}}, \ldots, \lambda_{\tilde{\Phi}_{uP}}$ be the densities of $\tilde{\Phi}_{u1}, \tilde{\Phi}_{u2}, \ldots, \tilde{\Phi}_{uP}$, respectively. We obtain these densities by sequentially using Lemma 6.2. First, the density $\lambda_{\tilde{\Phi}_{u1}}$ of the users that are assigned the pilot $\mathbf{p}_1$ is directly obtained from Lemma 6.2 where the initial density of the process is λ_u. Now, to obtain the density $\lambda_{\tilde{\Phi}_{u2}}$ of the users that are assigned the pilot $\mathbf{p}_2$, we approximate the initial density of users as $\lambda_u - \lambda_{\tilde{\Phi}_{u1}}$. Also note that the points in $\Psi_u \setminus \tilde{\Phi}_{u1}$ do not form a PPP. However, for simplicity we approximate $\Psi_u \setminus \tilde{\Phi}_{u1}$ as a PPP. Similarly, to obtain $\lambda_{\tilde{\Phi}_{u3}}$, we approximate $\Psi_u \setminus \{\tilde{\Phi}_{u1} \cup \tilde{\Phi}_{u2}\}$ as a PPP of density $\lambda_u - \lambda_{\tilde{\Phi}_{u1}} - \lambda_{\tilde{\Phi}_{u2}}$ and use Lemma 2. The same approximation is made to get the rest of the densities. In the next section, we will demonstrate that these approximations do not compromise the accuracy of our results. Based on Remark 6.4, with the knowledge of $\lambda_{\tilde{\Phi}_{u1}}, \lambda_{\tilde{\Phi}_{u2}}, \ldots, \lambda_{\tilde{\Phi}_{uP}}$, we can obtain

$$\lambda_{\Phi_{uo}} = \sum_{l=1}^{P} \lambda_{\tilde{\Phi}_{ul}}/P. \tag{6.14}$$

In the next lemma, we present the pilot assignment probability for the general case of $P \geq 1$.

Lemma 6.5. *For a system with $P \geq 1$, the pilot assignment probability for the typical user is*

$$\mathbb{P}[\mathcal{I}_o = 1] \approx \mathbb{P}[N_u \leq P] + \mathbb{P}[N_u > P](P\lambda_{\Phi_{uo}}\pi R_s^2)\mathbb{E}[N_u^{-1}|N_u > P], \tag{6.15}$$

where $\lambda_{\Phi_{uo}}$ is determined from (6.14) and Lemma 6.2, $\mathbb{E}[N_u^{-1}|N_u > P]$ is determined using (6.10), and N_u is Poisson distributed with mean $\lambda_u \pi R_s^2$.

Proof: The proof follows on the similar lines as that of Lemma 6.3. ∎

6.3.2 Distributed implementation of the RSA-based pilot allocation scheme

The RSA based pilot allocation scheme can also be implemented in a distributed manner. Consider the moment when a user $\mathbf{u}_o$ enters the network. During the initial access phase, the user senses the environment to get an estimate of active pilot transmission in the vicinity. Let $\mathbf{r}_o \in \mathbb{C}^{1\times\tau_{\mathtt{IA}}}$ be the received signal obtained through sensing. Note that $\tau_{\mathtt{IA}}$ should span over multiple coherence time intervals τ_c to average out the effect of small scale fading. Assuming synchronization has been established between the network and the user, the received signal strength on k-th pilot can be estimated as

$$P_k = \frac{1}{\tau_{\mathtt{IA}}/\tau_c} \sum_{m=1}^{\tau_{\mathtt{IA}}/\tau_c} \mathbf{r}_o[(m-1)\tau_c + 1 : (m-1)\tau_c + \tau_p]^H \mathbf{p}_k, \tag{6.16}$$

where τ_p is the duration of the pilot sequence. Once the received signal powers on all the pilots are calculated, they are compared with a threshold power $P_{\texttt{inh}}$, which is a function of $R_{\texttt{inh}}$. A pilot is randomly selected from the set of candidate pilots $\{\mathbf{p}_k : P_k \leq P_{\texttt{inh}}\}$. If this set is empty, then the user is not assigned a pilot. Algorithm 3 presents the above-mentioned procedure.

Input: Power threshold $P_{\texttt{inh}}$, Received signal $\mathbf{r}_o$;
Result: Pilot for user $\mathbf{u}_o$;
Initialization: Candidate set of pilots $\mathcal{P}_c = \emptyset$;
for *Each pilot* $\mathbf{p}_k \in \mathcal{P}$ **do**
  Obtain P_k using (6.16) ;
  if $P_k \leq P_{\texttt{inh}}$ **then**
    $\mathcal{P}_c = \mathcal{P}_c \cup \mathbf{p}_k$;
  end
end
if $\mathcal{P}_c \neq \emptyset$ **then**
  Select a pilot randomly from $\mathcal{P}_c$.
end

Algorithm 3: The algorithm for an arriving user to select a pilot during initial access phase.

6.4 Max-min Distance-based Pilot Allocation Scheme

While the proposed RSA-based scheme is a computationally efficient scheme with possible distributed implementation, a natural question is how good is the quality of the solution. In this section, we propose an algorithm that has the objective of maximizing the minimum distance between the set of co-pilot users similar to the RSA-based scheme. However, in contrast to the RSA scheme that can be implemented in a distributed manner, this algorithm can only be implemented in a centralized way and does not have the scalability property of the RSA-based scheme.

To have a meaningful problem formulation, we restrict our attention to a finite spatial observation window $W \subset \mathbb{R}^2$. Let the set of users in this observation window be given as $\mathcal{S} = \{\mathbf{u}_1, \mathbf{u}_2, \ldots, \mathbf{u}_{N_u}\}$. Our objective is to partition $\mathcal{S}$ into P sets $\mathcal{S}_1, \mathcal{S}_2, \ldots, \mathcal{S}_P$ such that the minimum distance between any two users in a partition is maximized. For a user $\mathbf{u}_n$, the binary variable $y_{nk} = 1$ if the user belongs to $\mathcal{S}_k$ and 0 otherwise. We define the metric $d_{\min}(\mathcal{S}_k) := \min\{\|\mathbf{u}_i - \mathbf{u}_j\| : \mathbf{u}_i \neq \mathbf{u}_j, y_{ik} = y_{jk} = 1\}$ as the minimum distance between two elements in $\mathcal{S}_k$. The problem of maximizing the minimum distance between users belonging to the same set can be written as

$$\max_{\{y_{nk}\}} \min_{k=1,\dots,P} \quad d_{\min}(\mathcal{S}_k) \tag{6.17a}$$

$$\text{s.t.} \quad \sum_{k=1}^{P} y_{nk} = 1, \quad \forall n = 1, 2, \dots, N_u, \tag{6.17b}$$

$$\sum_{n=1}^{N_u} y_{nk} > 1, \quad \forall k = 1, 2, \dots, P, \tag{6.17c}$$

$$y_{nk} \in \{0, 1\}, \quad \forall n, \forall k, \tag{6.17d}$$

where (6.17b) ensures that each point belongs to exactly one partition, (6.17c) ensures that each partition has more than two points, (6.17d) imposes the integrality constraint. Note that (6.17c) can be modified to ensure more balanced partitioning. For example, if we need each partition to have more than $x \leq N_u/P$ users then we can set the constraint as $\sum_{n=1}^{N} y_{nk} > x, \quad \forall k$. This problem can be reformulated as

$$\max_{t, y_{nk}} \quad t \tag{6.18a}$$

$$\text{s.t.} \quad \|\mathbf{u}_i - \mathbf{u}_j\| > t y_{ik} y_{jk} \quad \mathbf{u}_i \in \mathcal{S}, \mathbf{u}_j \in \mathcal{S}, i \neq j, k = 1, 2, \dots P, \tag{6.18b}$$

$$\sum_{k=1}^{P} y_{nk} = 1, \quad \forall n = 1, 2, \dots, N_u, \tag{6.18c}$$

$$\sum_{n=1}^{N_u} y_{nk} > 1, \quad \forall k = 1, 2, \dots, P, \tag{6.18d}$$

$$y_{nk} \in \{0, 1\}, \quad \forall n, \forall k, \tag{6.18e}$$

where (6.18b) ensures that two points belonging to the same partition are separated by distance t and rest of the constraints are the same as the previous formulation. The aforementioned problem can be solved in two steps. In the first step, a bisection search is used to improve the objective function, and in the second step for a given t, a feasibility problem is solved. The optimization routine to solve the problem is presented in Algorithm 4.

Both the algorithms mentioned so far do not take into account the distances among the users and the APs. As a consequence, two users that are separated by a reasonable distance, but have a common set of dominant APs may be assigned the same pilot. In such a scenario, both the users will experience performance degradation. This scenario is more likely to occur when the density of APs is low. In order to overcome this performance degradation, in the following section we propose a centralized AP location aware pilot allocation algorithm.

Input: The values of $t_{\min}$ and $t_{\max}$ that defines the solution space for the bisection search, tolerance parameter ϵ;
Result: Max-min separation distance;
Set $t = \frac{t_{\min}+t_{\max}}{2}$. Solve the following feasibility problem: ;

$$\sum_{k=1}^{K} y_{nk} = 1 \quad \forall n = 1, 2, \ldots, N \tag{6.19a}$$

$$\sum_{n=1}^{N} y_{nk} > 1 \quad \forall k = 1, 2, \ldots, P \tag{6.19b}$$

$$y_{ik} + y_{jk} \leq 1 \quad \forall \|\mathbf{x}_i - \mathbf{x}_j\| < t, \tag{6.19c}$$

$$y_{nk} \in \{0, 1\} \quad \forall n, \forall k. \tag{6.19d}$$

while $|t_{\max} - t_{\min}| < \epsilon$ **do**
  if (6.19) *is feasible* **then**
    Set $t_{\min} = t$;
  else
    Set $t_{\max} = t$;
  end
end

Algorithm 4: Solving the max-min distance partitioning problem

6.5 AP Location Aware Pilot Allocation Scheme

In this section, we present a heuristic algorithm to solve the original pilot allocation problem (6.8) presented in Sec. 6.3. Despite a few useful constraints that we introduce to the problem to limit the size of the feasible solution space, the complexity of the problem still remains high. Hence, the practical utility of the algorithm is somewhat questionable in a large network (hundreds of users), but it provides an excellent opportunity for benchmarking any pilot allocation algorithms for a smaller network with tens of users. Further, we use this scheme to benchmark the RSA-based and max-min distance-based algorithms proposed in the previous sections.

In order to reduce the space of good quality feasible solutions, we first use a clustering algorithm to group the users that have a similar path-loss with respect to the set of APs. Once the clusters of users are obtained, we use BnP algorithm to solve the sum SE maximization problem with the additional constraint that users in the same cluster cannot be assigned the same pilot. In the following two subsections, we discuss the clustering algorithm followed by a brief overview of the BnP algorithm with application to the problem at hand.

6.5.1 AP location-aware user clustering based on spectral graph theory

We use a spectral graph theory-based algorithm to cluster users with similar propagation characteristics. Before proceeding further, we present a few graph theoretic notations and definitions that are required for a rigorous exposition.

Graph definitions

Consider the weighted undirected graph $G = (\mathcal{V}, \mathcal{E}, \mathcal{W})$, where $\mathcal{V} = \{v_1, v_2, \ldots, v_n\}$ is known as the vertex set, $\mathcal{E} = \{e_{ij}\}_{i,j=1,\ldots,n}$ is the edge set that contains the edges connecting these vertices, and $\mathcal{W} = \{w_{ij}\}_{i,j=1,\ldots,n}$ is a set of non-negative weights assigned to each edge. If two vertices i, j are connected then $e_{ij} = 1$ and $w_{ij} > 0$. Otherwise, $e_{ij} = w_{ij} = 0$. The adjacency matrix of the graph G is denoted by $A \in \{0,1\}^{n\times n}$ and defined as $A(i,j) = e_{ij}$. Further, the *weighted* adjacency matrix is given as $W \in \mathbb{R}^{n\times n}$ and defined as $W(i,j) = w_{ij}$. The degree matrix of a weighted graph G, denoted by $D \in \mathbb{R}^{n\times n}$, is a diagonal matrix whose i-th diagonal element is given as $D(i,i) = \sum_{j=1}^{n} w_{ij}$. The Laplacian matrix of the graph G is defined as $L = D - W$. The K-cut of the graph G is defined as

$$\mathrm{cut}(\mathcal{V}_1, \mathcal{V}_2, \ldots, \mathcal{V}_K) = \frac{1}{2}\sum_{i=1}^{K} \sum_{v_l \in \mathcal{V}_i, v_m \in \mathcal{V}_i^C} w_{lm},$$

where $\mathcal{V}_i$ is the i-th partition of $\mathcal{V}$. Further, $\cup_{i=1}^{K}\mathcal{V}_i = \mathcal{V}$ and $\mathcal{V}_i \cap \mathcal{V}_j = \emptyset$ for $i \neq j$. The volume of a partition $\mathcal{V}_i$ is defined as

$$\mathrm{Vol}(\mathcal{V}_i) = \sum_{v_j \in \mathcal{V}_i} D(j,j).$$

The graph G is bipartite, if the vertex set can be partitioned into two sets $\mathcal{X}, \mathcal{Y} \subset \mathcal{V}$ such that the edges in $\mathcal{E}$ have one end point in $\mathcal{X}$ and another end point in $\mathcal{Y}$. Further, the graph G is a connected graph, if there is at least one path between any two vertices. Next, we formulate the problem of clustering users with similar propagation characteristic, namely the path-loss.

Graph theoretic formulation of the clustering problem

We consider a weighted bipartite graph where the vertices are the sets of users $\tilde{\Psi}_u = \Psi_u \cap W$ and APs $\tilde{\Phi}_r = \Phi_r \cap W$ over the finite spatial observation window W. An edge exists between each AP and each user, but no edge exists among the APs or the users. The weight of an edge is the path-loss between a user and an AP. In terms of the notations introduced earlier, $\mathcal{V} = \tilde{\Psi}_u \cup \tilde{\Phi}_r$, $\mathcal{E} = \{e_{mk} = 1 : \mathbf{u}_k \in \tilde{\Psi}_u, \mathbf{r}_m \in \tilde{\Phi}_u\}$, and $\mathcal{W} = \{w_{mk} = \beta_{mk} : \mathbf{u}_k \in \tilde{\Psi}_u, \mathbf{r}_m \in \tilde{\Phi}_r\}$. As mentioned earlier, $|\tilde{\Psi}_u| = N_u$ and $|\tilde{\Phi}| = N_r$. The degree matrix is given as

$$D = \begin{bmatrix} D_u & \mathbf{0}_{N_u \times N_r} \\ \mathbf{0}^T_{N_u \times N_r} & D_r \end{bmatrix} \in \mathbb{R}^{(N_u+N_r)\times(N_u+N_r)},$$

where $D_u \in \mathbb{R}^{N_u \times N_u}$ is the degree matrix for the users and $D_r \in \mathbb{R}^{N_r \times N_r}$ is the degree matrix for the APs. Further, the weighted adjacency matrix for the considered bipartite graph is

$$W = \begin{bmatrix} \mathbf{0}_{N_u \times N_u} & W_{UR} \\ W_{UR}^T & \mathbf{0}_{N_r \times N_r} \end{bmatrix} \in \mathbb{R}^{(N_u+N_r)\times(N_u+N_r)},$$

where the rows of $W_{UR} \in \mathbb{R}^{N_u \times N_r}$ represent the weights associated with a user with respect to all the APs. The problem of user clustering is based on the idea of partitioning the graph into desired number of groups such that edges across the groups have the lowest weights. In the current case, the output of the partitioning algorithm should be the clusters of users along with corresponding set of dominant APs such that the sum of edge weights between a set of clustered users and corresponding set of non-dominant APs should be minimum. The problem can be formally stated as a *min-cut* problem presented below:

$$\begin{aligned} &\underset{\mathcal{V}_1,\mathcal{V}_2,\ldots,\mathcal{V}_K}{\text{minimize}} \quad \mathrm{cut}(\mathcal{V}_1,\mathcal{V}_2,\ldots,\mathcal{V}_K) = \underset{\mathcal{V}_1,\mathcal{V}_2,\ldots,\mathcal{V}_K}{\text{minimize}} \quad \sum_{k=1}^{K} \frac{1}{2} \sum_{v_l \in \mathcal{V}_k, v_m \in \mathcal{V}_k^C} w_{lm} \\ &\text{subject to} \quad \bigcup_{k=1}^{K} \mathcal{V}_k = \mathcal{V}, \quad \bigcap_{k=1}^{K} \mathcal{V}_k = \emptyset, \end{aligned} \tag{6.20}$$

where $\mathcal{V}_k = \tilde{\Psi}_k \cup \tilde{\Phi}_k$ contains the nodes (both users and APs) corresponding to the k-th cluster. Different algorithms exist to solve the above min-cut problem. However, one major drawback of these algorithms is that they partition the vertices into unequal groups. To circumvent this problem, normalized ratio cut (`Ncut`) is considered as the objective instead of the cut presented in (6.20) [101]. Hence, the modified optimization problem can be written as

$$\begin{aligned} &\underset{\mathcal{V}_1,\mathcal{V}_2,\ldots,\mathcal{V}_K}{\text{minimize}} \quad \texttt{Ncut}(\mathcal{V}_1,\mathcal{V}_2,\ldots,\mathcal{V}_K) = \underset{\mathcal{V}_1,\mathcal{V}_2,\ldots,\mathcal{V}_K}{\text{minimize}} \quad \sum_{k=1}^{K} \frac{1}{2} \frac{\sum_{v_l\in\mathcal{V}_k, v_m\in\mathcal{V}_k^C} w_{lm}}{\text{Vol}(\mathcal{V}_k)}, \\ &\text{subject to} \quad \bigcup_{k=1}^{K} \mathcal{V}_k = \mathcal{V}, \quad \bigcap_{k=1}^{K} \mathcal{V}_k = \emptyset. \end{aligned} \tag{6.21}$$

The aforementioned problem is NP-hard in nature. However, an efficient approximate solution can be obtained by relaxing the above problem that is presented next.

Spectral graph theory to solve the `Ncut` problem

The general idea of the algorithm is composed of two steps. In the first step, user locations are transformed into a space that captures the propagation characteristics between the set of users and the set of APs. In the second step, user clustering is performed by K-means algorithm to the transformed user and AP locations.

For the i-th cluster $\mathcal{V}_i$, let us define the vector $\mathbf{f}_i \in R^{N_t\times 1}$ whose j-th element is given as

$$f_{ij} = \begin{cases} \frac{1}{\sqrt{\text{Vol}(\mathcal{V}_i)}}, & \text{if } v_j \in \mathcal{V}_i \\ 0, & \text{if } v_j \in \mathcal{V}_i^C, \end{cases}$$

where $N_t = N_u + N_r$. Note that based on the definition of the degree matrix, $\mathbf{f}_i^T D\mathbf{f}_i = 1$. Further, in case of the Laplacian matrix of the graph, $\mathbf{f}_i^T L\mathbf{f}_i = \text{cut}(\mathcal{V}_i, \mathcal{V}_i^C)/\text{Vol}(\mathcal{V}_i)$. Verifying these statements is straightforward and we refer the reader to [101] (and the references therein) for further insights on the graph Laplacian.

Let the matrix $F = [\mathbf{f}_1, \mathbf{f}_2, \ldots, \mathbf{f}_K]$. Now, the optimization problem in (6.21), can be written as

$$\underset{F}{\text{minimize}} \quad \text{Tr}\left(F^T L F\right), \qquad \text{subject to} \quad F^T D F = \mathbf{I}_K. \tag{6.22}$$

The optimal solution for the columns of F should only take discrete binary values. However, due to the NP-hard nature of the problem, a relaxed version of the above problem is solved, which is given as

$$\underset{F\in\mathbb{R}^{N_t\times K}}{\text{minimize}} \quad \text{Tr}\left(F^T L F\right), \qquad \text{subject to} \quad F^T D F = \mathbf{I}_K. \tag{6.23}$$

Substituting $Z = D^{1/2}F$, we get

$$\underset{Z\in\mathbb{R}^{N_t\times K}}{\text{minimize}} \quad \text{Tr}\left(Z^T D^{-1/2} L D^{-1/2} Z\right), \qquad \text{subject to} \quad Z^T Z = \mathbf{I}_K. \tag{6.24}$$

Note that the above problem is convex and can be solved by reducing it to an unconstrained optimization problem using Lagrange multiplier [102]. In the following lemma, the solution to the (6.24) is presented.

Lemma 6.6. *The solution to (6.24) consists of K eigenvectors corresponding to the K smallest non-zero eigenvalues of $D^{-1/2}LD^{-1/2}$.*

Proof: The Lagrangian of (6.24) is given as [102]

$$\mathcal{L}(Z, \Sigma) = \text{Tr}\left(Z^T D^{-1/2} L D^{-1/2} Z\right) + \text{Tr}\left(\Sigma^T (Z^T Z - \mathbf{I}_K)\right).$$

Now, taking the derivative of $\mathcal{L}$ with respect to Z and equating it to zero we get

$$\frac{\partial \mathcal{L}(Z, \Sigma)}{\partial Z} = 2D^{-1/2}LD^{-1/2}Z - 2Z\Sigma = 0 \implies D^{-1/2}LD^{-1/2}Z = \Sigma Z. \tag{6.25}$$

Above problem is the eigenvalue problem of $D^{-1/2}LD^{-1/2}$. Let Q contains the eigenvectors of $D^{-1/2}LD^{-1/2}$ and Σ is a diagonal matrix consisting of the corresponding eigenvalues. For our solution, Z contains the K columns of Q corresponding to the smallest K eigenvalues. ∎

Let $\tilde{Z}_n \in \mathbb{R}^{N_t\times K}$ be the row normalized version of Z. The transformed locations of the APs and users are the rows of $\tilde{Z}_n$ [103, 104]. We perform K-means clustering algorithm on the rows of $\tilde{Z}_n$ to group the users and their dominant set of APs. Once the cluster of users are obtained, we invoke the additional constraint of not assigning the same pilot to two users in the same cluster. With this additional constraint, we solve the problem (6.8) using BnP algorithm that is presented next.

6.5.2 Branch and price (BnP) algorithm

BnP is an efficient method to solve large integer programming problems and has been successfully applied to many discrete optimization problems, such as generalized assignment problem [105], graph coloring [106], and also to communication network problems of link scheduling [107], [108]. The core idea of BnP algorithm is to traverse through a branch and bound (BnB) tree. At each node of the tree, a smaller version of the original problem (by optimizing over a reduced feasible space) and a pricing problem are iteratively solved. The objective of the pricing problem is to add good quality feasible columns to the feasible space of the smaller problem. The process is repeated until no good quality columns are found. As a consequence of this iterative approach, a large number of (useless) columns are never considered in the entire process saving significant amount of computational resources. Depending on the nature of the problem, some branching constraint is used to traverse through the tree. Similar to any BnB-based algorithm, the BnP algorithm terminates once there is no improvement in the objective value in the remaining nodes of the tree compared to the incumbent solution. An illustration of the BnP algorithm and flow of the column generation process (using the pricing problem) is presented in Fig. 6.2.

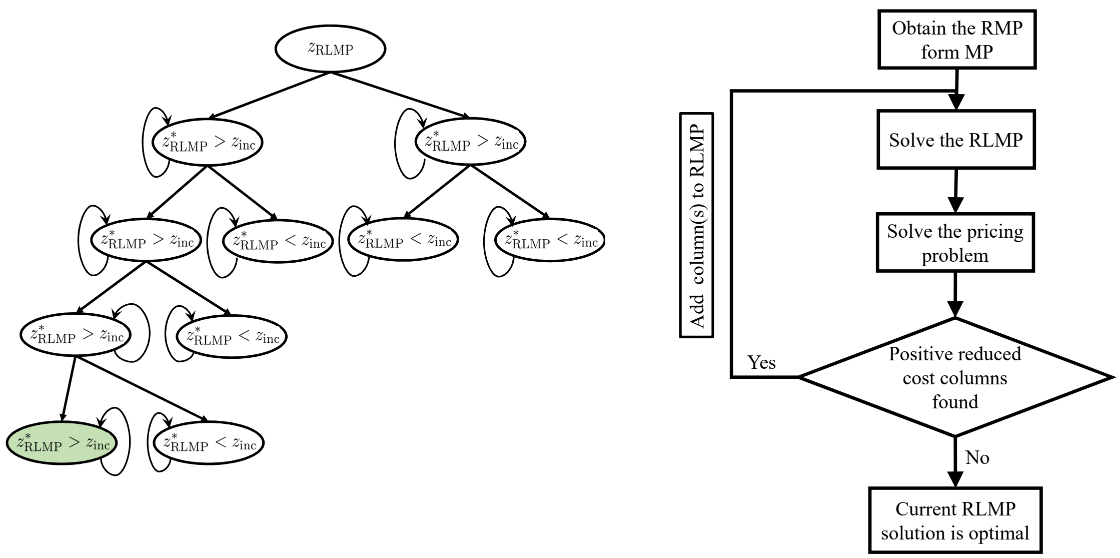

Figure 6.2: The branch and bound tree (left). The column generation algorithm flow chart (right).

Modified cost function and reduced linear master problem

Using the clustering algorithm presented in the previous section, we get K sets of clustered user partitions given by $\{\mathcal{V}_1, \mathcal{V}_2, \ldots, \mathcal{V}_K\}$. To ensure that users in the same cluster are not assigned the same pilot, we modify the cost function (6.7) as

$$c(\mathbf{x}_j) = \begin{cases} \sum_{\mathbf{u}_i \in \mathcal{A}_j} \log_2 (1 + \Gamma_{ij}), & \text{if } \Gamma_{ij} \geq \Gamma_{\min} \ \forall \mathbf{u}_i \in \mathcal{A}_j \\ -M, & \text{if } \Gamma_{ij} < \Gamma_{\min} \text{ for any } \mathbf{u}_i \in \mathcal{A}_j \\ -M, & \text{if } |\mathcal{V}_k \cap \mathcal{A}_j| > 1 \text{ for any } k = 1, 2, \ldots K, \end{cases} \tag{6.26}$$

where the last row ensures that the columns that have users from the same cluster are (almost) never considered as good columns in the pricing problem. Based on the above definition of the cost function, to make sure that the original problem remains feasible, number of users in a cluster should be less than the number of pilots. Hence, we choose $K = \max\{P, N_u/P\}$. We call (6.8) with the modified cost function definition as the *master* *problem (MP)*. Further, we refer to the problem with relaxed integer constraint (6.8d) of the MP as linear master problem (LMP), which is expressed as

$$\max_{\Lambda} \quad \sum_{s=1}^{|\mathcal{A}|} c(\mathbf{x}_s)\lambda_s \tag{6.27a}$$
$$\text{s.t.} \quad A\Lambda = \mathbf{1} \tag{6.27b}$$
$$\|\Lambda\|_1 = P \tag{6.27c}$$
$$\Lambda \in [0,1]^{|\mathcal{A}|}. \tag{6.27d}$$

As mentioned earlier, at each node of the BnB tree, we solve the problem with a subset of all potential columns in A, and gradually keep adding good columns determined by the pricing algorithm. We define the set $\mathcal{H} \subset \mathcal{A}$ and the corresponding matrix as H, which contains a few of the columns of A. We refer to this problem as the reduced linear master problem (RLMP), which is given as

$$\max_{\Lambda} \quad \sum_{s=1}^{|\mathcal{H}|} c(\mathbf{x}_s)\lambda_s \tag{6.28a}$$
$$\text{s.t.} \quad H\Lambda = \mathbf{1} \tag{6.28b}$$
$$\|\Lambda\|_1 = P \tag{6.28c}$$
$$\Lambda \in [0,1]^{|\mathcal{H}|}. \tag{6.28d}$$

Let $\Pi = [\pi_1, \pi_2, \ldots, \pi_{N_u}]$ be the set of dual variables that correspond to the constraint (6.28c) and β be the dual variable for the constraint (6.28d). Note that the optimal set of dual variable for LMP is also the optimal set of dual variables for RLMP.

Pricing problem

At each node of the BnB tree, the RLMP is solved to optimality using any linear programming method, such as the simplex, and the corresponding dual variables are used to obtain new columns that can improve the objective of RLMP by solving a pricing problem. The idea behind the pricing problem can be better understood from the Lagrange function of LMP, which is given as

$$\mathcal{L}(\Pi, \beta, \Lambda) = \sum_{s=1}^{|\mathcal{A}|} c(\mathbf{x}_s)\lambda_s - \Pi^T(A\Lambda - \mathbf{1}) - \beta(\|\Lambda\|_1 - P). \tag{6.29}$$

Note that if a given set of solutions Λ^* is optimal for the LMP, then the first derivative of $\mathcal{L}$ with respect to each variable is zero. On the other hand, for a given set of dual variables, if we can improve the value of $\mathcal{L}$ by increasing the value of λ_j, then it must be the case that

$$\frac{\partial \mathcal{L}(\Pi, \beta, \Lambda)}{\partial \lambda_j} = c(\mathbf{x}_j) - \Pi^T \mathbf{x}_j - \beta > 0. \tag{6.30}$$

The quantity $c(\mathbf{x}_j) - \Pi^T \mathbf{x}_j - \beta$ is known as the *positive reduced cost* of the column $\mathbf{x}_j$. This provides us a direct way to add new columns to an RLMP that can improve its objective function value. To be specific, for a given set of dual variables (Π, β) corresponding to a RLMP, the pricing problem is given as

$$\arg\max_{\mathbf{x} \in A} \quad c(\mathbf{x}) - \Pi^T \mathbf{x} - \beta, \tag{6.31}$$

and the optimal column is added to the RLMP, thus obtaining an augmented matrix $\tilde{H}$. The RLMP is solved again using $\tilde{H}$ and the new set of dual variables are used in the pricing problem to get better columns. The procedure is repeated until there is no column in A with positive reduced cost, i.e. $c(\mathbf{x}) - \Pi^T \mathbf{x} - \beta \leq 0$ for all the columns in $\mathcal{A} \setminus \tilde{\mathcal{H}}$. The flow of the column generation process is given in Fig. 6.2 (right). Note that even with the linear relaxation (6.31) is a non-convex non-linear problem. Hence, solving it to optimality in polynomial time is not possible. However, meta-heuristic algorithms such as the genetic algorithm, or tabu search, can be used to get efficient solutions. In this work, we focus on solving (6.31) with exhaustive enumeration over the set of feasible columns. This process is significantly more efficient compared to solving the original problem through exhaustive enumeration.

Note that the optimal solution of the RLMP, i.e. Λ^*, is not guaranteed to be an integral solution. The following branching rule in the BnB tree ensures that the optimal solution to the RLMP is an integer vector, thereby making Λ^* an optimal solution to the original RMP problem that has the integrality constraint.

Branching rule

The objective of the branching rule is to progressively introduce branching constraints such that eventually the solution to the RLMP becomes integral [105]. The branching rule is derived from a relatively well-known result in the linear programming literature that is stated in the following lemma.

Lemma 6.7. *Consider the linear maximization problem* $\{\max \mathbf{c}^T \mathbf{x} : A\mathbf{x} = \mathbf{1}, \mathbf{x} > \mathbf{0}\}$. *If* A *is a totally balanced matrix, then the optimal solution* $\mathbf{x}^*$ *is integer valued.*

For the proof along with detailed discussion of the result stated in the lemma, please refer to [109]. After solving the RLMP and pricing problem to (near) optimality, the objective is to introduce the branching constraints such that the augmented matrix of the RLMP $\tilde{H}$ eventually becomes a *totally balanced matrix* as we traverse through the BnB tree. As mentioned in [105], this can be achieved by the constraints $\tilde{h}_{pk} = \tilde{h}_{rk}$ on one branch and $\tilde{h}_{pk} = \tilde{h}_{rk} = 0$ or $\tilde{h}_{pk} \neq \tilde{h}_{rk}$ on the other branch, where $\tilde{h}_{pk}$ is the element corresponding to the p-th row and k-th column of $\tilde{H}$. The branching constraint implicitly ensures that on one branch two users belong to the same column, while on the other branch the users belong to two different columns. These branching constraints are introduced in the RLMP and also used in the column generation process.

Node pruning and termination criterion for the BnB tree

The backbone of the BnP algorithm is the BnB algorithm. To harvest full benefits of the BnB tree, it is essential to introduce efficient node pruning criteria so that unnecessary nodes are never visited. Let $z^*_{\rm MP}$, $z^*_{\rm LMP}$ are the optimal values of the MP and LMP, respectively. Further, $z^*_{\rm LMP} \leq z_{\rm RLMP} + Pc$, where c is the maximum positive reduced cost of columns for a given RLMP. When the RLMP along with pricing problem is solved to optimality, $z^*_{\rm LMP} = z^*_{\rm RLMP}$, since there exists no column that can improve the value of $z^*_{\rm RLMP}$. Let $z_{\rm inc}$ be the incumbent solution, which is always integral in nature. If at a node of BnB tree, we have $z^*_{\rm RLMP} < z_{\rm inc}$, subsequent nodes in the branch will not provide any better solution. Hence, the pruning occurs at this node of the branch, i.e., subsequent nodes on the same branch are not explored and the nodes on the other branches are explored. Once no nodes with $z^*_{\rm RLMP} > z_{\rm inc}$ are found, $z_{\rm inc}$ is the optimal solution.

6.6 Results

In this section, through Monte Carlo simulations, we validate the theoretical analysis on pilot assignment probability and assess the performance of the RSA-inspired pilot allocation compared to other schemes presented in this work. The simulations environment for each scenario is presented in the specific subsection.

6.6.1 Performance of the RSA-based pilot allocation scheme

In this case, for the simulations, we consider a network of radius 1500 m. In order to avoid edge effects, points within 600 m are considered. The average user spectral efficiency is reported for the typical user located at the center. We use the following non-line-of-sight path-loss function [110]:

$$\begin{aligned} l(d) =& 161.04 - 7.1\log_{10}(W) + 7.5\log_{10}(h) - [24.37 - 3.7(h/h_{\rm AP})^2]\log_{10}(h_{\rm AP}) \\ &+ [43.42 - 3.1\log_{10}(h_{\rm AP})][\log_{10}(d) - 3] + 20\log_{10}(f_c) - (3.2[\log_{10}(11.75h_{\rm AT})^2] - 4.97), \end{aligned}$$

where $W = 20, h_{\rm AP} = 40, h_{\rm AT} = 1.5, h = 5, f_c = 0.45$ GHz.

In Fig. 6.3 (left), the co-pilot user density as a function of number of pilots is presented. As expected, the co-pilot user density decreases with increasing number of pilots. In Fig. 6.3 (center), we present the pilot assignment probability as a function of the number of pilots. This result is useful in determining the number of pilots that is required to achieve a certain assignment probability. Finally, in Fig. 6.3 (right), we present the average user SE as a function of $R_{\tt inh}$. To generate this result, we set the uplink pilot SNR $\rho_p = 80$ dB, length of pilot sequence $\tau_p = P = 16$. We observe that with increasing λ_u, the optimal $R_{\tt inh}$ that maximizes user SE becomes smaller. Further, there exists a range of $R_{\tt inh}$ that provides higher user SE compared to the random pilot assignment scheme [5]. However, this range shrinks as λ_u increases.

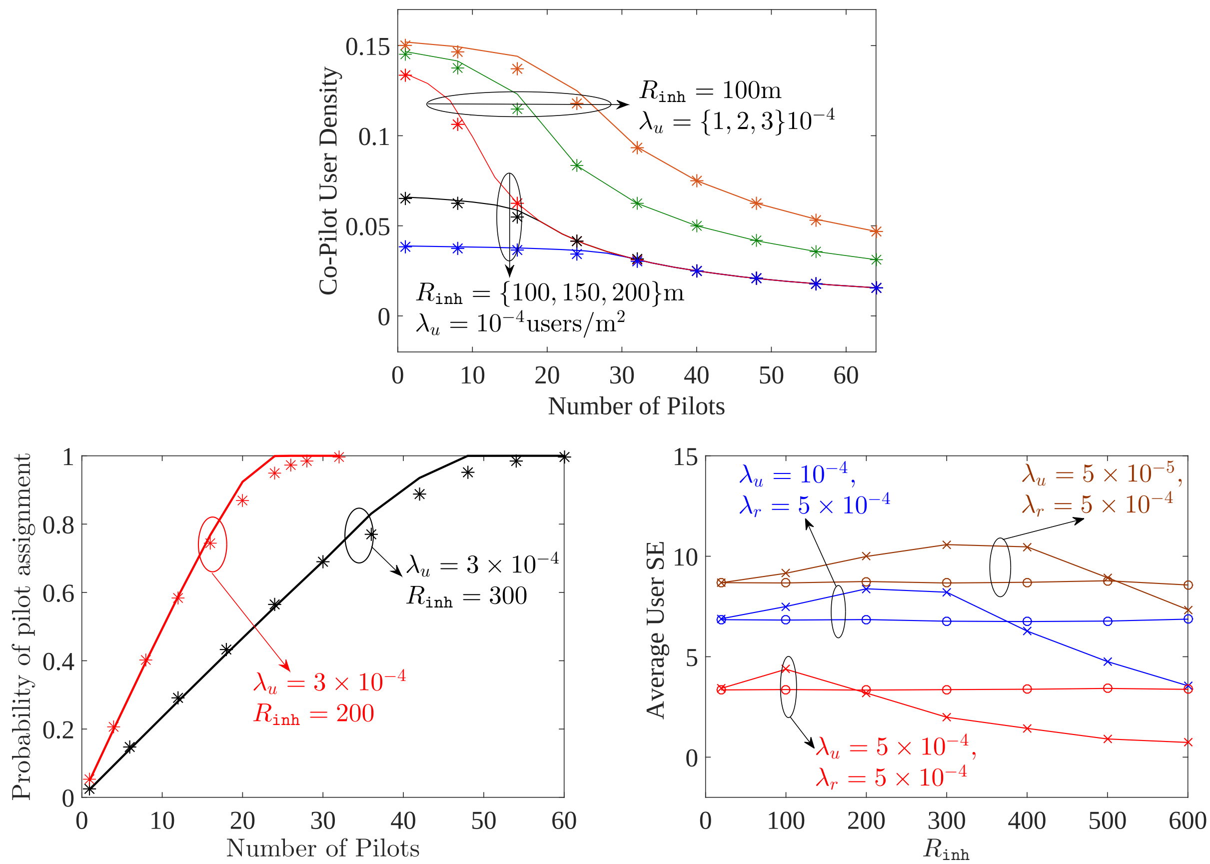

Figure 6.3: The co-pilot user density as a function of P (top), Probability of pilot assignment as a function P (bottom-left), and Average user SE as a function of $R_{\texttt{inh}}$ (bottom-right). In the first two figure, markers and solid lines represent simulations and theoretical results, respectively.

6.6.2 Performance comparison of RSA-based scheme to the max-min distance-based scheme

In this subsection, we compare the performance of the RSA scheme to the max-min distance-based scheme. Further, we also provide the relative performance between RSA and the following two existing schemes in the literature: iterative K-means-based algorithm [97] and the random pilot allocation algorithm [5]. In the case of the RSA-based scheme, for a given λ_r and λ_u, the $R_{\texttt{inh}}$ that maximizes the average user SE is selected. The simulation environment remains the same as that of the previous subsection. In Fig. 6.4, we present the ratio of the average user SEs of different schemes with respect to the average user SE of the RSA scheme. From the results, we conclude that the system performance is primarily affected by (i) the average number of users per pilot and (ii) AP density. When the average number of users per pilot is relatively low, the RSA scheme marginally outperforms the max-min as well as the iterative K-means algorithms, especially at the low AP density. On the other hand, with a relatively high average number of users per pilot, the max-min scheme performs marginally better compared to both the RSA and iterative K-means algorithm. In the case of the RSA, this slightly inferior performance can be attributed to the reduced pilot assignment probability in a dense environment. All the three schemes provide significant average user SE improvement over the random pilot allocation scheme.

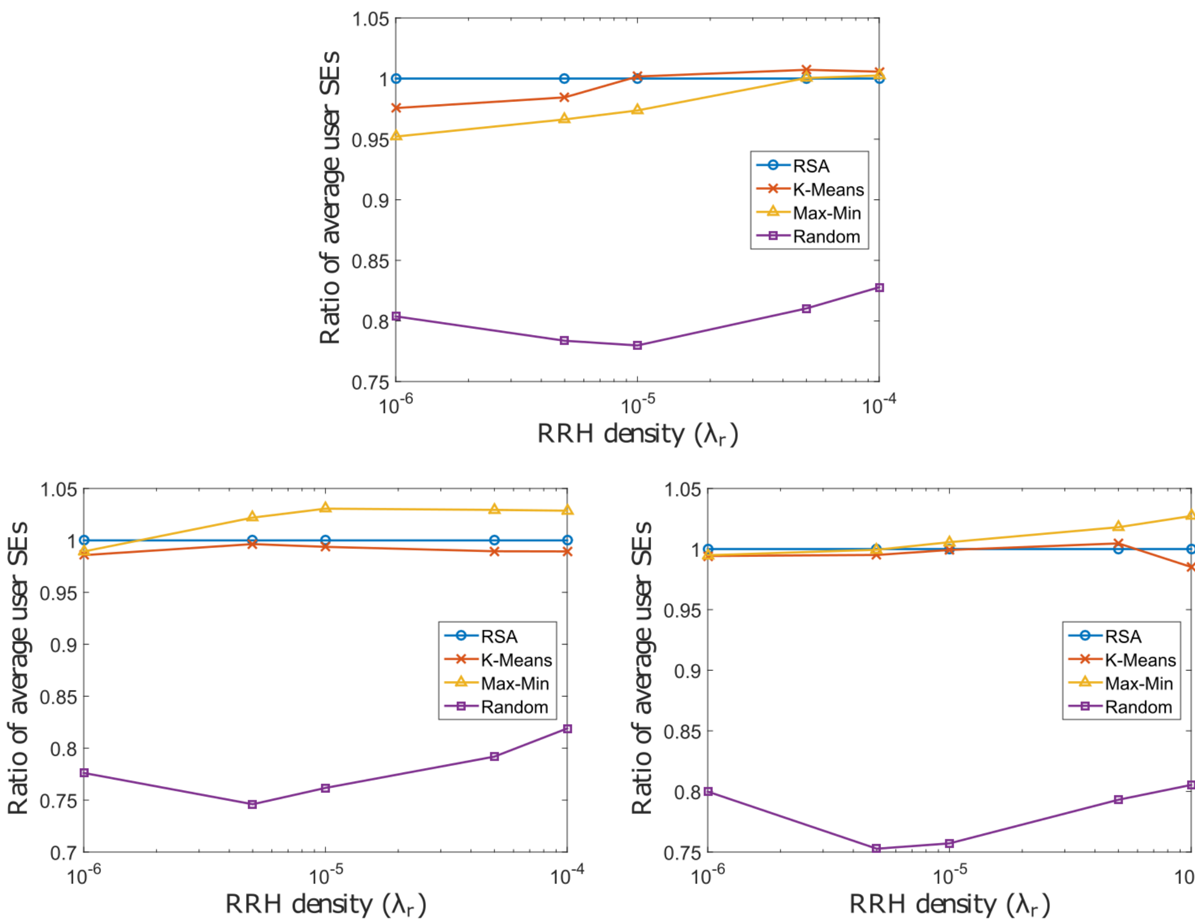

Figure 6.4: The ratio of average user SEs of different schemes with respect to the RSA-based scheme for different system configurations: (top) $\lambda_u = 10^{-5}, P = 16$; (bottom-left) $\lambda_u = 10^{-4}, P = 16$; (bottom-right) $\lambda_u = 10^{-5}, P = 8$.

6.6.3 Performance comparison of the RSA-based scheme to the BnP scheme

Since the AP location-aware heuristic scheme based on BnP algorithm exhibits significant computational complexity for a large system (hundreds of users), we compare the performance for a relatively small system with 48 users uniformly distributed over a circular area of radius 400 m. Further, these users are simultaneously served by N_r APs distributed uniformly over the same area. The path-loss function remains the same as given in the previous subsection. In Fig. 6.5, we present the cumulative distribution function (CDF) of the ratio of sum user SEs for the RSA to BnP scheme. As observed from Fig. 6.5 (left), the performance of the RSA scheme improves with the increasing number of APs in the system. However, the effect of number of pilots on the relative performance of RSA compared to the BnP scheme is negligible as evident from Fig. 6.5 (right), where RSA gives similar performance for different number of pilots.

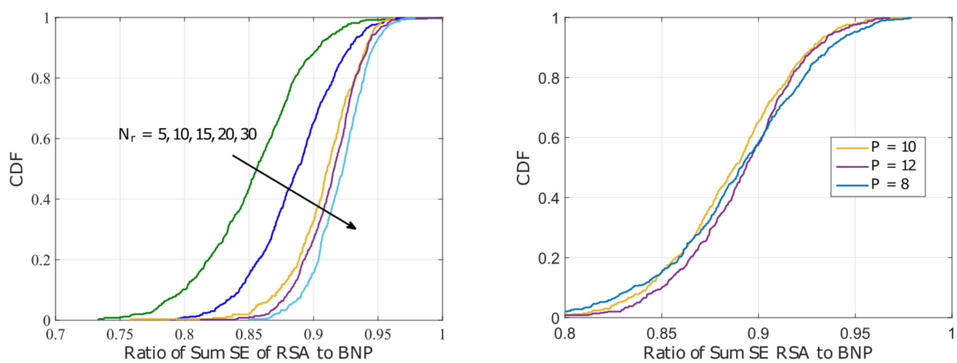

Figure 6.5: The CDF of the ratio of sum user SE of RSA to BnP scheme for different system configuration: (left) $N_u = 48, P = 10$; (right) $N_u = 48, N_r = 10$.

6.7 Conclusions

In this chapter, we propose a pilot assignment algorithm to mitigate the effect of pilot contamination for a cell-free mMIMO system. Our algorithm is inspired by RSA process, which has been used to study the adsorptions of hard particles on a surface across different scientific fields. Using the results derived in Chapter 5, we present an accurate analytical expression for average pilot assignment probability for a typical user in the network. Further, the performance of the proposed algorithm is compared to two centralized pilot allocation schemes. With respect to the first centralized scheme, which partitions the users in the network in such a way that minimum distance among the sets of co-pilot users is maximized, the RSA-based scheme provides competitive average user SE performance. The second centralized pilot allocation scheme, which is based on BnP algorithm, provides near optimal solution in terms of sum user SE for a relatively small system with tens of users. The performance of the RSA-based scheme, despite its distributed implementation, is appreciable with respect to the near-optimal BnP scheme. Owing to its competitive performance and scalable distributed implementation, the RSA-based scheme is an attractive algorithm for pilot allocation in a pilot contamination limited distributed mMIMO network. A promising future direction of this work is to investigate efficient solution for the pricing problem used in the column generation process so that the BnP-based scheme can used to benchmark the performance of relatively large systems with hundreds of users.

Chapter 7

Downlink Performance Analysis of Cell-Free Massive MIMO with Finite Fronthaul Capacity

7.1 Introduction

In cell-free mMIMO networks, the APs perform a limited set of signal processing operations such as precoding/filtering using the local channel state information (CSI) while most of the baseband processing operations are carried out at centralized baseband units (BBUs). The communication between the APs and BBUs is done through fronthaul links. In the previous chapter, we presented the system performance assuming that the fronthaul links are ideal, i.e., they have infinite capacity. However, in reality these links, such as optical cables, have limited capacity. One of the direct consequences of having finite fronthaul links is that the compression/quantization error gets introduced into the system and directly affects the system performance. Hence, analyzing the network-wide performance of cell-free mMIMO with finite fronthaul capacity is an important requirement for the successful integration of this technology to the fifth generation (5G) networks. In this work, our goal is to model and analyze such a system using tools from stochastic geometry and provide a few useful system design guidelines.

7.1.1 Related works

We first discuss a few prior works that focus on devising compression algorithms while taking into account the limited fronthaul capacity for other variants of cooperative cellular networks such as coordinated multipoint (CoMP) and cloud radio access networks (C-RAN). In [111, 112], authors provide information-theoretic insights regarding the capacity of a backhaul-constrained distributed MIMO system. Extending the insights obtained from information-theoretic analyses, in other notable works, authors use optimization-based frameworks to devise compression algorithms that efficiently utilize the fronthaul capacity constraints while maximizing a certain performance metric (e.g., sum-rate) (cf. [113], [114]). A comprehensive overview of such works can be found in [115, 116]. While the insights obtained from these works are useful, some of the inferences may not hold true for a cell-free mMIMO system owing to its practical aspects such as beamforming based on local imperfect CSI at the APs, time division duplex (TDD) mode of operation. This motivated a different set of system analyses [30, 31, 32, 33, 34, 35, 36, 37] for cell-free mMIMO with finite fronthaul capacity. In [30], the authors analyze the uplink performance using Bussgang decomposition to capture the effect of quantization error introduced due to finite fronthaul capacity. The authors present the effect of the number of quantization bits on the uplink outage probability. In [31], the authors extend the framework of [30] and compare the uplink performance of the scheme where both the quantized version of the received signal and quantized channel estimates are available at the BBU to the scheme where the BBU has the quantized weighted signal from each AP. In addition, an uplink max-min power allocation algorithm and an AP-user assignment scheme to reduce the fronthaul load are also proposed. In [34], the authors compare the uplink performances of perfect fronthaul links, the case when the quantized version of the estimated channel and signal available at the BBU, and the case when only quantized weighted signal is available at the BBU. The uplink energy efficiency analysis of cell-free network with finite fronthaul capacity is studied in [32]. In [35], the authors study the performance of a cell-free network with hardware impairments where the authors compare the performance of three transmission strategies between the BBU and the APs through finite capacity links. The uplink and downlink performances of fronthaul constrained cell-free network with low resolutions analog to digital converters (ADCs) are presented in [36]. Note that most of these works focus on *traditional* cell-free architecture where all the APs serve each user in the network. Since the user performance degrades with quantization/compression error, which depends on the number of users (load) per AP, each AP should serve a subset of users in the network. A network-centric approach that achieves the goal is proposed [31, 34]. However, from the scalability perspective, a *user-centric* architecture is preferred [38, 39, 40, 20, 41, 42, 37] where a user selects its set of serving APs. Further, a user-centric approach can also be implemented in a distributed manner. However, in the literature, there are few works on the downlink performance of the user-centric cell-free architecture with finite fronthaul capacity.

From the perspective of system analysis, a complementary approach to simulations-based studies is theoretical analyses using tools from stochastic geometry. To this end, there has been a lot of work that analyzes the performance of cooperative cellular networks, such as CoMP and C-RAN (cf. [117, 118, 119, 120, 121, 122]). However, the system architecture of cell-free mMIMO along with the practical constraints, such as imperfect CSI, local beamforming, finite fronthaul capacity, makes the signal-to-interference-noise ($\mathtt{SINR}$) expression different from the above-mentioned works. Hence, the analyses developed in these works cannot be directly extended to performance analysis of cell-free mMIMO system. Further, the performance of traditional cell-free architecture has been carried out in [20, 123, 124] using tools from stochastic geometry. However, to the best of our knowledge, there is no work in the literature, that presents the theoretical performance analysis of cell-free systems with finite fronthaul capacity using tools from stochastic geometry. With this discussion on prior works, our contributions are outlined next.

7.1.2 Contributions

System modeling

In this work, we consider the downlink of a cell-free mMIMO system with finite capacity fronthaul links. To capture the effect of finite fronthaul, we consider a point-to-point compression scheme between an AP and the BBU. Further, we focus on both the traditional cell-free mMIMO architecture where each AP serves each user in the network and a variant of the user-centric cell-free architecture. Since the compression error is a function of the number of users, to limit the effect of compression error, the traditional cell-free network has to be of finite size. Hence, for this architecture, we model the AP and user locations as two independent Binomial point processes (BPPs). On the other hand, for the user-centric architecture, we model the AP and user locations as two independent homogeneous Poisson point processes (PPPs) and assume that each user is served by a specified number of its nearest APs. We restrict our attention to conjugate beamforming. Conditioned on the AP and user locations, we derive an achievable rate expression for a randomly selected user that is valid for both the architecture and captures the effect of finite fronthaul capacity.

Load characterization of user-centric architecture

Due to the dependence of compression error on the number of users served by an AP, the statistics of the load in terms of the number of users is important for system analysis. While for the traditional architecture this number of fixed, for the user-centric architecture the load is a function of user and AP densities as well as the number of APs that serve a user in the network. Hence, for the user-centric architecture, we first determine the load distribution for the set of tagged APs that serve the typical user. Since an exact determination of the probability mass function (`PMF`) of the number of users associated with each tagged AP is intractable, we derive the first two moments of the load and then approximate load for each of the tagged AP as a negative binomial random variable through the moment matching method. This result is later used to derive the rate coverage of the typical user in the user-centric architecture. Further, we use a similar methodology to derive the load result for the typical AP in the network. This result is useful in network dimensioning, especially determining the desired capacity of the fronthaul link between the typical AP and the BBU to satisfy a certain signal to compression noise ratio `SCNR`. It is worth mentioning that this result has a direct equivalence to the degree distribution in an *AB random geometric graph*.

Performance analysis of the traditional architecture

We first focus on deriving the downlink user rate coverage result for the traditional architecture. Leveraging the relevant distance distributions for a BPP, we provide an approximate expression to analytically evaluate the rate coverage averaged over the AP and user locations. From our analyses, we infer that the average system sum-rate is a strictly quasi-concave function of the number of users, and the optimal number of users to achieve the maximum system sum-rate increases with increasing fronthaul capacity. Further, in contrast to the established notion that fully distributed MIMO is superior to the collocated MIMO, our results suggest that in the presence of high-quality CSI at the APs, a less distributed form of cell-free mMIMO is better, i.e. for an equal number of antennas in the system, it is better to deploy a fewer APs with more antennas per AP.

Performance analysis of the cell-free architecture

Using the load distribution result of the typical AP, we highlight the interplay between different system parameters such as fronthaul capacity, the SCNR, the number of serving APs. Further, exploiting the statistical properties associated with a PPP along with a few subtle approximations, we derive the rate coverage result for the typical user when it gets scheduled. In this process, we use the load distribution results for the tagged APs. All the theoretical results are validated through extensive Monte Carlo simulations.

7.2 System Model

We limit our attention to the downlink of a cell-free mMIMO system. The sets of AP and user locations are given by Φ_r and Φ_u, respectively. To capture the spatial randomness in the AP and user locations, we model Φ_r and Φ_u by appropriate point processes. The corresponding discussions on the point processes are relegated to the following sections as it is not necessary for the results derived in this section. We assume that each AP is equipped with N antennas. The distance between a user at $\mathbf{u}_k \in \Phi_u$ and an AP at $\mathbf{r}_m \in \Phi_r$ is denoted by d_{mk}. All the APs are connected to a BBU through a fronthaul network, where the capacity of each link is C_f bits/s/Hz. As mentioned earlier, in the case of the traditional cell-free architecture, all the APs serve all the users in the network. In contrast, in case of the user-centric network architecture, we consider that each user is served by its nearest N_s APs. Both type of architectures are illustrated in Fig. 7.1.

7.2.1 Compression at the BBU

Due to the limited fronthaul capacity, the BBU employs a lossy compression scheme to forward user symbols to the APs. Consider an AP located at $\mathbf{r}_o$ serves a set of K_o users $\Phi_{uo} \subseteq \Phi_u$. Note that in the case of traditional architecture, $\Phi_{uo} = \Phi_u$. Let $\mathbf{q}_o = [q_{1_o}, q_{2_o}, \ldots, q_{K_o}]^T$ be the signal vector consisting of the symbols to be transmitted to the users in Φ_{uo}. We consider that $\mathbf{q}_o$ is a circularly symmetric complex Gaussian random vector and $\mathbf{q}_o \sim \mathcal{CN}(\mathbf{0}_{K_o}, \rho_{q_o}\mathbf{I}_{K_o})$, where $\rho_{q_o} = \mathbb{E}\left[|q_{1_o}|^2\right] = \mathbb{E}\left[|q_{2_o}|^2\right] = \ldots = \mathbb{E}\left[|q_{K_o}|^2\right]$. Using a lossy compres-

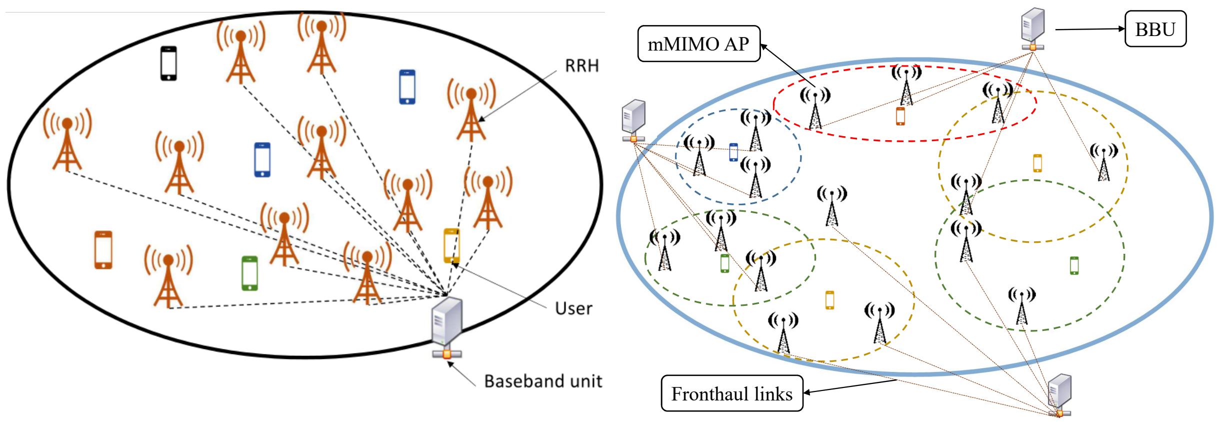

Figure 7.1: (Left) A representative network diagram of the traditional architecture, where each AP serves all the user in the network. (Right) A representative diagram for the user-centric architecture over a finite observation window. In this case, each user is served by its nearest three APs as marked by dotted circles.

sion scheme, the BBU transmits $\hat{\mathbf{q}}_o = [\hat{q}_{1_o}, \hat{q}_{2_o}, \ldots, \hat{q}_{K_o}]^T$ over the fronthaul links to the AP. Similar to [111], we consider $\hat{\mathbf{q}}_o = \mathbf{q}_o + \tilde{\mathbf{q}}_o$, where $\tilde{\mathbf{q}}_o \sim \mathcal{CN}(\mathbf{0}_{K_o}, \rho_{\tilde{q}_o}\mathbf{I}_{K_o})$ is the compression error vector and $\rho_{\tilde{q}_o} = \mathbb{E}\left[|\tilde{q}_{1_o}|^2\right] = \mathbb{E}\left[|\tilde{q}_{2_o}|^2\right] = \ldots = \mathbb{E}\left[|\tilde{q}_{K_o}|^2\right]$. Further, we assume that $\mathbf{q}_o$ and $\tilde{\mathbf{q}}_o$ are uncorrelated. Since both are Gaussian random vectors, they are independent as well. From the above exposition, it is clear that $\hat{\mathbf{q}} \sim \mathcal{CN}(\mathbf{0}_{K_o}, (\rho_{\tilde{q}_o} + \rho_{q_o})\mathbf{I}_{K_o})$. If $\mathbb{E}\left[|\hat{q}_{k_o}|^2\right]$ is the same for all $k = 1, 2, \ldots K_o$, then both $\rho_{\tilde{q}_o}, \rho_{q_o}$ depend on the fronthaul capacity C_f, as discussed in the following lemma.

Lemma 7.1. *For a fronthaul capacity C_f and number of users K_o served by the typical AP, $\rho_{q_o} = \left(1 - 2^{-C_f/K_o}\right)\mathbb{E}\left[|\hat{q}_{k_o}|^2\right]$ and $\rho_{\tilde{q}_o} = 2^{-C_f/K_o}\mathbb{E}\left[|\hat{q}_{k_o}|^2\right]$.*

Proof: The amount of information that can be transmitted from the BBU to each AP is upper limited by the fronthaul capacity C_f. Hence, we write

$$I(\hat{\mathbf{q}}_o; \mathbf{q}_o) \leq C_f \implies \mathrm{h}(\hat{\mathbf{q}}_o) - \mathrm{h}(\hat{\mathbf{q}}_o|\mathbf{q}_o) \leq C_f \implies \sum_{i=1}^{K_o} \mathrm{h}(\hat{q}_{i_o}) - \sum_{i=1}^{K_o} \mathrm{h}(\hat{q}_{i_o}|q_{i_o}) \leq C_f$$
$$\implies \log_2(\pi e(\rho_{q_o} + \rho_{\tilde{q}_o})) - \log_2(\pi e \rho_{\tilde{q}_o}) \leq \frac{C_f}{K_o},$$

where $I(x;y)$ denotes the mutual information between two random variables x and y, $\mathrm{h}(x)$ denotes the differential entropy of a random variable x, and the last step follows from the fact that $\hat{q}_i$s and $\tilde{q}_i$s are complex Gaussian random variables. Ideally, the BBU would like to transmit the maximum information. Hence, we write

$$\log_2\left(1 + \frac{\rho_{q_o}}{\rho_{\tilde{q}_o}}\right) = \frac{C_f}{K_o} \implies \frac{\rho_{q_o}}{\rho_{\tilde{q}_o}} = 2^{C_f/K_o} - 1.$$

The expression in the lemma follows directly using the fact that $\rho_{q_o} + \rho_{\tilde{q}_o} = \mathbb{E}\left[|\hat{q}_{k_o}|^2\right]$. If we consider that $\mathbb{E}\left[|\hat{q}_{k_o}|^2\right] = 1$, then $\rho_{q_o} = \left(1 - 2^{-C_f/K_o}\right)$ and $\rho_{\tilde{q}_o} = 2^{-C_f/K_o}$. ∎

Remark 7.2. *The* SCNR*, defined as* $\frac{\rho_{q_o}}{\rho_{\tilde{q}_o}} = 2^{C_f/K_o} - 1$*, is a decreasing function of the number of users served by the AP. While in the case of the traditional cell-free mMIMO, the* SCNR *can only be improved by increasing* C_f*, in the case of user-centric architecture,* SCNR *can also be improved by limiting the maximum number of users that should be scheduled by the typical AP. Hence, for a given* C_f *and target* SCNR *threshold* T_s*, the maximum number of scheduled users* $K_{\mathtt{max}}$ *should satisfy* $K_{\mathtt{max}} \log_2(1 + T_s) \le C_f$*.*

7.2.2 Uplink channel estimation

Let $\mathbf{g}_{mk} = \sqrt{\beta_{mk}}\mathbf{h}_{mk}$ be the channel gain between the AP at $\mathbf{r}_m$ and the user at $\mathbf{u}_k$, where β_{mk} captures the large-scale channel gain and $\mathbf{h}_{mk} \sim \mathcal{CN}(\mathbf{0}_N, \mathbf{I}_N)$ captures the small-scale channel fluctuation. We consider that the large-scale channel gain β_{mk} is only due to the distance dependent pathloss, i.e. $\beta_{mk} = l(d_{mk})^{-1}$, where d_{mk} is the distance between the m-th AP and the k-th user, and $l(\cdot)$ is a non-decreasing pathloss function presented in Section 7.6.

In order to obtain the channel estimates, we consider that each user uses a pilot from a set of P orthogonal pilot sequences of τ_p symbol duration, which is assumed to be less than the coherence interval. Further, the transmit signal-to-noise ratio (SNR) of each symbol in a pilot is ρ_p. Since we assume that these P sequences are orthogonal to each other, $\tau_p \ge P$ and $\boldsymbol{\psi}_i^H \boldsymbol{\psi}_j = \mathbf{1}(i = j)$, where $\mathbf{1}(\cdot)$ denotes the indicator function. Let the pilot used by the user at $\mathbf{u}_k$ be $\boldsymbol{\psi}(k)$. During the pilot transmission phase, the received signal matrix $\mathbf{R}_o \in \mathbb{C}^{N \times \tau_p}$ at the typical AP is

$$\mathbf{R}_o = \sqrt{\tau_p \rho_p} \sum_{\mathbf{u}_k \in \Phi_u} \mathbf{g}_{ok} \boldsymbol{\psi}(k)^T + \mathbf{W}_o,$$

where each element of $\mathbf{W}_m$ is $\mathcal{CN}(0,1)$. Let $\hat{\mathbf{g}}_{ok}$ be the estimated channel vector at the AP $\mathbf{r}_o$ for the user $\mathbf{u}_k \in \Phi_{uo}$ that is obtained after performing minimum-mean-squared-error (MMSE) channel estimation. Further, $\tilde{\mathbf{g}}_{ok}$ be the estimation error vector. Using the properties of MMSE estimation, we write [6]

$$\hat{\mathbf{g}}_{ok} \sim \mathcal{CN}\left(\mathbf{0}_N, \gamma_{ok}\mathbf{I}_N\right), \quad \tilde{\mathbf{g}}_{ok} \sim \mathcal{CN}\left(\mathbf{0}_N, \left(\beta_{ok} - \gamma_{ok}\right)\mathbf{I}_N\right), \tag{7.1}$$

where

$$\gamma_{ok} = \frac{\tau_p \rho_p \beta_{ok}^2}{1 + \tau_p \rho_p \sum_{\mathbf{u}_j \in \Phi_u} \boldsymbol{\psi}(k)^H \boldsymbol{\psi}(j) \beta_{oj}}. \tag{7.2}$$

7.2.3 Downlink data transmission

In this work, we consider that each AP employs CB based on the local CSI. Hence, the precoded symbol transmitted by the AP at $\mathbf{r}_o$ is given as

$$\mathbf{x}_o = \sum_{\mathbf{u}_i \in \Psi_{uo}} \sqrt{\rho_d \eta_{oi}} \frac{\hat{\mathbf{g}}_{oi}^*}{\sqrt{\mathbb{E}[\|\hat{\mathbf{g}}_{oi}\|^2]}} \hat{q}_{i_o} = \sum_{\mathbf{u}_i \in \Psi_{uo}} \sqrt{\rho_d \eta_{oi}} \mathbf{w}_{oi} \hat{q}_{i_o},$$

where ρ_d is the DL transmit $\mathtt{SNR}$, η_{oi} is normalization coefficient used by the typical AP for the user at $\mathbf{u}_i$ to satisfy the average power constraint $\mathrm{Tr}(\mathbb{E}\left[\mathbf{x}_o \mathbf{x}_o^H\right]) \leq \rho_d$, and $\Psi_{uo} \subseteq \Phi_{uo}$ is the set of scheduled users associated with the AP at $\mathbf{r}_o$ such that $|\Psi_{uo}| \leq K_{\mathtt{max}}$ for the user-centric architecture. Note that for the traditional architecture, $\Psi_{uo} = \Phi_{uo} = \Phi_u$ and $K_{\mathtt{max}} = K_o$. We observe that by setting $\eta_{mk} = 1/K_{\mathtt{max}}$ and $\rho_{\hat{q}_o} = \mathbb{E}[|\hat{q}_{i_o}|^2] = 1$ above constraint is satisfied. More sophisticated power allocation algorithms, such as max-min power allocation, can be considered. However, the advantages of the above mentioned equal power allocation scheme are its minimal complexity and distributed implementation. Furthermore, this scheme also provides certain degree of tractability in the coverage analysis as we will see in the sequel.

7.2.4 An achievable rate for a randomly selected user

Now, we present an achievable rate for a randomly selected user in the network that is applicable for both type of architectures. Consider that a randomly selected user is located at $\mathbf{u}_o$ and is served by the set of APs $\Phi_{ro} \subseteq \Phi_r$. The received signal at this user is given as

$$\begin{aligned} y_o^{\mathtt{dl}} &= \sum_{\mathbf{r}_l \in \Phi_{ro}} \mathbf{g}_{lo}^T \mathbf{x}_l + \sum_{\mathbf{r}_j \in \Phi_{ro}^C} \mathbf{g}_{jo}^T \mathbf{x}_j + \mathbf{n}_o \\ &= \sum_{\mathbf{r}_l \in \Phi_{ro}} \sqrt{\rho_d \eta_{lo}} \frac{\mathbf{g}_{lo}^T \hat{\mathbf{g}}_{lo}^*}{\sqrt{N \gamma_{lo}}} \hat{q}_{lo} + \sum_{\mathbf{r}_l \in \Phi_{ro}} \sum_{\mathbf{u}_i \in \tilde{\Psi}_{ul}} \frac{\sqrt{\rho_d \eta_{li}} \mathbf{g}_{lo}^T \hat{\mathbf{g}}_{li}^*}{\sqrt{N \gamma_{li}}} \hat{q}_{li} + \sum_{\mathbf{r}_l \in \Phi_{ro}^C} \sum_{\mathbf{u}_i \in \Phi_{ul}} \frac{\sqrt{\rho_d \eta_{li}} \mathbf{g}_{lo}^T \hat{\mathbf{g}}_{li}^*}{\sqrt{N \gamma_{li}}} \hat{q}_{li} + n_o, \end{aligned} \tag{7.3}$$

where $\Phi_{ro}^C = \Phi_r \setminus \Phi_{ro}$. In the following lemma, we provide an expression for an achievable rate (a lower bound on capacity). Note that in favor of simpler exposition, we ignore the constant pre-log factors such as bandwidth and fraction of DL transmission duration in a TDD setup as we do not study the corresponding trade offs in this work.

Lemma 7.3. *Conditioned on Φ_r and Φ_u, an achievable rate of the typical user at $\mathbf{u}_o$ is given as*

$$\mathtt{SE}_o = \log_2\left(1 + \mathtt{SINR}_o\right) \quad \textit{bits/s/Hz}, \tag{7.4}$$

where

$$\mathtt{SINR}_o = \frac{\rho_d N \left(\sum\limits_{\mathbf{r}_l \in \Phi_{ro}} \sqrt{\frac{\gamma_{lo}(1-2^{-C_f/k_l})}{K_{\max}}} \right)^2}{\rho_d N \sum\limits_{\mathbf{r}_l \in \Phi_{ro}} \gamma_{lo} \frac{2^{-C_f/k_l}}{K_{\max}} + \rho_d \sum\limits_{\mathbf{r}_l \in \Phi_r} \beta_{lo} + \rho_d N \sum\limits_{\mathbf{u}_i \in \{\mathcal{P}_o \setminus \mathbf{u}_o\}} \left(\sum\limits_{\mathbf{r}_l \in \Phi_{ri}} \sqrt{\frac{\gamma_{lo}}{K_{\max}}} \right)^2 + 1}, \tag{7.5}$$

where $\mathcal{P}_o$ is the set of users that use the same pilot sequence as the typical user $\mathbf{u}_o$.

Proof: Please refer to Appendix C.1. ∎

7.3 Rate Coverage for traditional cell-free mMIMO

In this section, we derive the rate coverage result for the traditional cell-free mMIMO system where each AP serves all the users in the network. If we consider an infinite network on $\mathbb{R}^2$, then as per the result of Lemma 1, the $\mathtt{SCNR} \to 0$ as $K_o \to \infty$ and subsequently $\mathtt{SINR}_o \to 0$ as given in Lemma 7.3. Hence, for a meaningful analyses of the traditional architecture, we need to consider a finite network, e.g., a shopping mall. Therefore, we assume the system is limited to $\mathcal{B}_{R_s}(\mathbf{o})$, a finite circular region of radius R_s centered at $\mathbf{o}$, where the set of APs $\Phi_r = \{\mathbf{r}_1, \mathbf{r}_2, \ldots, \mathbf{r}_M\}$ are randomly and uniformly distributed. Further, $\Phi_u = \{\mathbf{u}_1, \mathbf{u}_2, \ldots, \mathbf{u}_{K_o}\}$ contains the set of user locations that are uniformly and randomly distributed in $\mathcal{B}_{R_s}(\mathbf{o})$ and are independent of AP locations. Note that by construction, Φ_r and Φ_u form two independent BPPs. Alternatively, one can consider modeling Φ_r and Φ_u as two independent PPPs over a finite region. However, in that case K_o becomes a Poisson random variable that theoretically has an infinite support. Hence, in certain cases when K_o is high, $\mathtt{SINR}_o$ becomes undesirably low for a fixed C_f. Therefore, we consider a fixed number of users and APs in the network by modeling them as BPPs. Moreover, most of the studies in the cell-free mMIMO literature consider a fixed number of users and APs in the network. As assumed in the cell-free mMIMO literature, we consider that $MN \gg K_o$. Further, we assume that the coherence block is sufficiently long to ensure that $\tau_p \geq K_o$. As a consequence, pilots are not reused in the network eliminating the effect of pilot contamination. Under these assumptions, using the result of Lemma 7.3, the achievable rate of a user at $\mathbf{u}_o$ is given as $\mathtt{SE}_{o,f} = \log_2(1 + \mathtt{SINR}_{o,f})$, where

$$\mathtt{SINR}_{o,f} = \frac{\rho_d \frac{N}{K_o}(1 - 2^{-C_f/K_o}) \left(\sum\limits_{m=1}^{M} \sqrt{\gamma_{mo}} \right)^2}{\rho_d \frac{N}{K_o} 2^{-C_f/K_o} \sum\limits_{m=1}^{M} \gamma_{mo} + \rho_d \sum\limits_{m=1}^{M} \beta_{mo} + 1}. \tag{7.6}$$

Our goal is to determine the rate coverage $R_{c_f}(T_r) = \mathbb{P}[\log_2(1 + \mathtt{SINR}_{o,f}) \geq T_r]$ for a randomly selected user in this finite network that requires averaging over the distances of the APs from the user. Next, we present a few important distance distributions for a BPP.

7.3.1 Relevant distance distributions in a BPP

Let R_o be the distance of the user at $\mathbf{u}_o$ from the center of the circle $\mathcal{B}_{R_s}(\mathbf{o})$. Since $\mathbf{u}_o$ is uniformly and randomly distributed in $\mathcal{B}_{R_s}(\mathbf{o})$, the cumulative distribution function (CDF) and probability density function (PDF) of R_o is given as

$$F_{R_o}(r) = \frac{r^2}{R_s^2}, \qquad f_{R_o}(r) = \frac{2r}{R_s^2} \quad 0 \leq r \leq R_s. \tag{7.7}$$

Next, we present the distance distribution between $\mathbf{u}_o$ to a randomly distributed AP in $\mathcal{B}_{R_s}(\mathbf{o})$.

Lemma 7.4. *Conditioned on the distance R_o, the* CDF *of the distance between the user at $\mathbf{u}_o$ and the AP at $\mathbf{r}_m$ is given as*

$$\begin{aligned} F_{D_{mo}}(d|r_o) =& \frac{d^2}{R_s^2}\mathbf{1}(0 \leq d < R_s - r_o) \\ &+ \mathbf{1}(R_s - r_o \leq d \leq R_s + r_o)\left(\frac{d^2}{\pi R_s^2}\left(\theta^* - \frac{\sin(2\theta^*)}{2}\right) + \frac{1}{\pi}\left(\phi^* - \frac{\sin(2\phi^*)}{2}\right)\right), \end{aligned}$$

and corresponding PDF *is given as*

$$f_{D_{mo}}(d|r_o) = \frac{2d}{R_s^2}\ \mathbf{1}(0 \leq d < R_s - r_o) + \mathbf{1}(R_s - r_o \leq d \leq R_s + r_o)\frac{2d}{\pi R_s^2}\theta^*$$

where $\theta^* = \arccos\left(\frac{d^2 + r_o^2 - R_s^2}{2 r_o d}\right), \phi^* = \arccos\left(\frac{R_s^2 + r_o^2 - d^2}{2 r_o R_s}\right)$.

Proof: We provide the sketch of the proof of this lemma. Please refer to [125, Lemma 1] for the detail proof. Without loss of generality, consider that $\mathbf{u}_o = (r_o, 0)$. Then, conditioned on $\mathbf{u}_o$ (equivalently r_o), a uniformly distributed point in $\mathcal{B}_{R_s}(\mathbf{o})$ can lie either in the circle $\mathcal{B}_{R_s - r_o}(\mathbf{u}_o)$ or in the region $\mathcal{B}_{R_s}(\mathbf{o}) \backslash \mathcal{B}_{R_s - r_o}(\mathbf{u}_o)$. In the CDF expression of the lemma both this conditions are captured by the indicator function and corresponding conditional CDFs are presented. The expression for the PDF is obtained by taking the derivative of the CDF with respect to d along with some algebraic manipulation. ■

Now, using the results from order statistics, we present the conditional distance distribution between $\mathbf{u}_o$ and its nearest AP.

Lemma 7.5. *Conditioned on the distance R_o, the* CDF *of the distance D_{oo} between the $\mathbf{u}_o$ and its nearest AP is given as $F_{D_{oo}}(d_{oo}|r_o) =$*

$$\mathbb{P}\left[D_{oo} \leq d_{oo}|r_o\right] = 1 - (1 - F_{D_{mo}}(d_{oo}|r_o))^M,$$

and the corresponding PDF *is given as*

$$f_{D_{oo}}(d_{oo}|r_o) = M f_{D_{mo}}(d_{oo}|r_o)(1 - F_{D_{mo}}(d_{oo}|r_o))^{M-1},$$

where $f_{D_{mo}}, F_{D_{mo}}$ are presented in Lemma 7.4.

Note that conditioned on the distance D_{oo}, rest of the APs in $\mathcal{B}_{R_s}(\mathbf{o})$ are uniformly and randomly located in $\mathcal{B}_{R_s}(\mathbf{o}) \setminus \mathcal{B}_{d_{oo}}(\mathbf{u}_o)$, where d_{oo} is a realization of D_{oo}. In the following lemma, we present the distribution of the distance between a randomly located AP in the above region and $\mathbf{u}_o$.

Lemma 7.6. *Conditioned D_{oo} and R_o, the* PDF *of the distance $\hat{D}_{mo}$ between a randomly located AP in $\mathcal{B}_{R_s}(\mathbf{o}) \setminus \mathcal{B}_{d_{oo}}(\mathbf{u}_o)$ and $\mathbf{u}_o$ is given as*

$$f_{\hat{D}_{mo}}(d|d_{oo}, r_o) = \frac{f_{D_{mo}}(d|r_o)}{1 - F_{D_{mo}}(d_{oo}|r_o)}, \quad d_{oo} \leq d \leq r_o + R_s.$$

Proof: We provide the sketch of the proof for this lemma. For the detailed proof, please refer to [125, Lemma 3]. Conditioned on D_{oo}, rest of the APs are uniformly distributed in $\mathcal{B}_{R_s}(\mathbf{o}) \setminus \mathcal{B}_{d_{oo}}(\mathbf{u}_o)$. Hence, the distribution of the distance $\hat{D}_{mo}$ follows the lower truncated distribution of D_{mo}, which is captured in the above expression. ■

Next, using the above distance distributions, we present the approximate expression for rate coverage.

7.3.2 Approximate evaluation of average achievable user rate

The exact evaluation of rate coverage R_{c_f} is challenging as it requires an $(M+1)$-fold integration to average it over the locations of all the M APs and the user at $\mathbf{u}_o$. Notice that the $\mathtt{SINR}_{o,f}$ in (7.6) has the following terms:

$$I_1 = \sum_{m=1}^{M} \sqrt{\gamma_{mo}}, \quad I_2 = \sum_{m=1}^{M} \gamma_{mo}, \quad I_3 = \sum_{m=1}^{M} \beta_{mo}. \tag{7.8}$$

Since there is no pilot contamination, $\gamma_{mk}(d_{mk}) = \frac{\tau_p \rho_p l(d_{mk})^{-2}}{1+\tau_p \rho_p l(d_{mk})^{-1}}$. Further, γ_{mk} is a decreasing function of d_{mk}. Due to path loss these terms are likely to be dominated by contributions from a few nearest APs. Hence, we approximate I_1, I_2, and I_3 as the sum of exact contribution from the nearest AP and the mean contribution from the rest of the APs conditioned on the distance d_{oo} between $\mathbf{u}_o$ and its nearest AP. Hence, we write

$$\begin{aligned} I_1(d_{oo}, r_o) &= \sum_{m=1}^{M} \sqrt{\gamma_{mo}} \approx \sqrt{\gamma_{oo}} + \mathbb{E}\Big[\sum_{m=1, m\neq o}^{M} \sqrt{\gamma_{mo}} \Big| d_{oo}, r_o \Big], \\ I_2(d_{oo}, r_o) &= \sum_{m=1}^{M} \gamma_{mo} \approx \gamma_{oo} + \mathbb{E}\Big[\sum_{m=1, m\neq o}^{M} \gamma_{mo} \Big| d_{oo}, r_o \Big], \\ I_3(d_{oo}, r_o) &= \sum_{m=1}^{M} \beta_{mo} \approx \beta_{oo} + \mathbb{E}\Big[\sum_{m=1, m\neq o}^{M} \beta_{mo} \Big| d_{oo}, r_o \Big]. \end{aligned} \tag{7.9}$$

It is worth mentioning that this approach has been used for DL coverage probability analysis in cellular systems (cf. [84]). Note that conditioned on D_{oo}, distances between $\mathbf{u}_o$ and rest of the APs in the network are i.i.d. Hence, using Campbell's theorem, (7.9) can be written as

$$\begin{aligned} \hat{I}_1(d_{oo}, r_o) &= \sqrt{\gamma_{oo}} + (M-1) \int_{r=d_{oo}}^{r_o+R_s} \frac{\sqrt{\tau_p \rho_p} l(r)^{-1}}{\sqrt{1+\tau_p \rho_p l(r)^{-1}}} f_{\hat{D}_{mo}}(r | d_{oo}, r_o) \mathrm{d}r, \\ \hat{I}_2(d_{oo}, r_o) &= \gamma_{oo} + (M-1) \int_{r=d_{oo}}^{r_o+R_s} \frac{\tau_p \rho_p l(r)^{-1}}{1+\tau_p \rho_p l(r)^{-1}} f_{\hat{D}_{mo}}(r | d_{oo}, r_o) \mathrm{d}r, \\ \hat{I}_3(d_{oo}, r_o) &= \beta_{oo} + (M-1) \int_{r=d_{oo}}^{r_o+R_s} l(r)^{-1} f_{\hat{D}_{mo}}(r | d_{oo}, r_o) \mathrm{d}r. \end{aligned} \tag{7.10}$$

With the above approximation, in the next Proposition, we present an expression to evaluate the rate coverage of the typical user in this finite cell-free mMIMO network.

Proposition 5. For a given threshold T_r, the rate coverage of a randomly selected user in the network is given as

$$R_{c_f}(T_r) = \int_{r_o=0}^{R_s} \int_{d_{oo}=0}^{R_s} \mathbf{1}\left(\mathtt{SINR}_o^{\mathrm{Apx}}(d_{oo}, r_o) > 2^{T_r} - 1 \right) f_{D_{oo}}(d_{oo} | r_o) f_{R_o}(r_o) \mathrm{d}d_{oo} \mathrm{d}r_o,$$

where

$$\mathtt{SINR}_o^{\mathrm{Apx}}(d_{oo}, r_o) = \frac{\rho_d \frac{N}{K_o}(1-2^{-C_f/K_o})(\hat{I}_1(d_{oo}, r_o))^2}{\rho_d \frac{N}{K_o}(\hat{I}_2(d_{oo}, r_o)) 2^{-C_f/K_o} + \rho_d \hat{I}_3(d_{oo}, r_o) + 1}, \tag{7.11}$$

the $\mathtt{PDFs}$ of D_{oo} and R_o are presented in Lemma 7.5 and (7.7), respectively.

Proof: The result follows by first replacing different terms in the $\mathtt{SINR}_{o,f}$ by their approximations given in (7.10) to obtain $\mathtt{SINR}_o^{\mathrm{Apx}}(d_{oo}, r_o)$. In the next step, we decondition over D_{oo} and R_o to obtain $R_{c_f}(T_r)$. ■

The result of the above proposition concludes the rate coverage derivation for a traditional cell-free mMIMO system with finite fronthaul capacity. Next, we focus on the user-centric cell-free mMIMO. In this case, we model Φ_r and Φ_u as two independent homogeneous PPP. Further, each user is served by its nearest N_s APs. Observe that the SINR expression of Lemma 2 is a function of the number of users served by each AP in the network. Owing to the spatial randomness of both user and AP locations, the number of users served by each AP is a random variable. Therefore, to derive the rate coverage expression, we need the statistical properties of the load of associated with an AP in the network that is presented in the next section.

7.4 Load Characterization in User-Centric Architecture

Before proceeding further, we need to provide the distinction between the typical AP and the set of tagged APs in the network. The typical AP is by definition a randomly selected AP in Φ_r. On the other hand the set of tagged APs are the serving APs of the typical user that is selected randomly from Φ_u. This random selection of the typical user makes it more likely to be served by APs that have larger service regions. This effect is reminiscent of the *waiting time* paradox in queuing system and the difference between 0-cell and the typical cell in a Poisson-Voronoi tessellation [126, 127]. Since we are focusing on the performance analysis of the typical user, we need the load distribution result associated with the set of tagged APs. On the other hand, from network dimensioning perspective, such as provisioning of fronthaul capacity, we need statistical information on the load associated with the typical AP. In the next subsection, we derive the load distribution results associated with the set of tagged APs.

7.4.1 The load of a tagged AP

The statistical metric that we are interested in is the PMF. The exact derivation of PMF is intractable. Hence, we first derive the exact result for the first two moments of the number of users for a tagged AP. Then we approximate the load though an appropriate random variable using the moment matching method.

Determination of the first two moments

Since Φ_u is homogeneous PPP, it is translation invariant. Hence, we assume that the typical user is located at the origin $\mathbf{o}$. It is worth mentioning that the load associated with each of the tagged APs are not identical. Hence, we need to present a generic result that is a function of the serving AP rank in terms of the distance from the typical user. Next, we derive the first two moments of the load for the N-th nearest tagged AP.

Lemma 7.7. *The first moment of the number of users (excluding the typical user) served by the N-th nearest AP to the typical user at the origin is given as*

$$\mathbb{E}[K_N] = 2\pi\lambda_r\lambda_u \int_{r_o=0}^{\infty} \mathrm{d}r_o \int_{d_x=0}^{\infty} \mathrm{d}d_x \int_{v_x=0}^{2\pi} \mathrm{d}v_x \; h_{\mathtt{tag,m_1}}(r_o, d_x, v_x) d_x r_o, \quad \textit{where}$$

$$h_{\mathtt{tag,m_1}}(r_o, d_x, v_x) = \sum_{n=0}^{N_s-1} \mathtt{Pos}_{\mathtt{PMF}}(n, \lambda_r \mathtt{AoI}_2(r_o, d_x, v_x)) \mathtt{Pos}_{\mathtt{PMF}}(N_s - n - 1, \lambda_r(\pi r_o^2 - \mathtt{AoI}_2(r_o, d_x, v_x)))$$
$$\mathtt{Pos}_{\mathtt{CMF}}(N_s - n - 1, \lambda_r(\pi r_x^2 - \mathtt{AoI}_2(r_o, d_x, v_x))).$$

In the above expression $r_x(r_o, d_x, v_x) = \sqrt{r_o^2 + d_x^2 - 2r_o d_x \cos(v_x)}$ *and* $\mathtt{AoI}_2(r_o, d_x, v_x)$ *is the area of intersection of two circles is given as*

$$\mathtt{AoI}_2(r_o, d_x, v_x) = r_o^2 \left(v_x - \frac{\sin(2v_x)}{2} \right) + r_x^2 \left(u(r_o, d_x, v_x) - \frac{\sin(2u(r_o, d_x, v_x))}{2} \right), \tag{7.12}$$

where

$$u(r_1, r_2, v) = \arccos\left(\frac{r_2 - r_1 \cos(v)}{\sqrt{r_1^2 + r_2^2 - 2r_1 r_2 \cos(v)}} \right). \tag{7.13}$$

The corresponding second moment is given as

$$\mathbb{E}[K_N^2] = 2\pi\lambda_r\lambda_u^2 \int\limits_{r_o=0}^{\infty} \int\limits_{d_x=0}^{\infty} \int\limits_{d_y=0}^{\infty} \int\limits_{v_x=0}^{2\pi} \int\limits_{v_y=0}^{2\pi} h_{\mathtt{tag,m_2}}(r_o, d_x, d_y, v_x, v_y) \mathrm{d}v_y \mathrm{d}v_x d_y \mathrm{d}d_y d_x \mathrm{d}d_x r_o \mathrm{d}r_o,$$

where $h_{\mathtt{tag,m_2}}(r_o, d_x, d_y, v_x, v_y)$ *is given by* (C.4) *in Appendix C.2.*

Proof: Please refer to Appendix C.2. ■

Remark 7.8. *The load on a tagged AP depends on its distance from the typical user at the origin. Using the results of the above lemma, we conclude that* $\mathbb{E}[K_1] > \mathbb{E}[K_2] > \mathbb{E}[K_3] > \ldots$, *and* $\mathbb{E}[|K_1|^2] > \mathbb{E}[|K_2|^2] > \mathbb{E}[|K_3|^2] > \ldots$ *and so on.*

Approximation of the load PMF

With the knowledge of the first two moments of the load, we approximate it as a negative binomial random variable. The PMF of this random variable with parameters r and p is given as

$$\mathbb{P}[K_N = k] = \frac{\Gamma(k + r)}{k!\Gamma(r)} p^r (1 - p)^k,$$

where $\mathbb{E}[K_N] = (1-p)r/p$ and $\mathbb{E}[K_N^2] = (1-p)r(1+(1-p)r)/p^2$. Using the results of Lemma 7.7, we solve the aforementioned two equations to obtain the values of r and p. The intuition behind consideration of negative binomial stems from the following fact: if we consider that each user is served by its nearest AP, then the serving region of each AP is its corresponding Poisson-Voronoi cell. The area of this cell is well approximated as a gamma random variable [128]. Now, conditioned on the area of a cell, the number of users that fall in this area follows Poisson distribution. This leads to a Poisson-gamma mixture distribution for the number of users served by a tagged AP once we decondition over the serving area. Since negative binomial distribution is a consequence of Poisson-gamma mixture distribution, our choice to approximate the load with this distribution is justified. The results validating the approximation is presented in Sec. 7.6.

7.4.2 The load of the typical AP

In this section, we derive the approximate PMF of the number of users served by the typical AP in the network. Similar to the previous case, since exact characterization of the PMF is intractable, we first derive the exact expression for the first two moments of the load for the typical AP. Next, using moment-matching method, we approximate the PMF as a negative binomial PMF. The derivation of the first two moments now becomes the special case of the tagged AP result. In the following lemma, we present the first two moments.

Lemma 7.9. *The first two moments of the number of users K_o served by the typical AP at $\mathbf{r}_o \in \Phi_r$ is given as*

$$\mathbb{E}[K_o] = N_s \frac{\lambda_u}{\lambda_r}$$
$$\mathbb{E}[K_o^2] = 2\pi\lambda_u^2 \int_{r_x=0}^{\infty}\int_{r_y=0}^{\infty}\int_{u=0}^{2\pi} h_{\mathtt{typ,m2}}(r_1, r_2, u)\mathrm{d}u r_2 \mathrm{d}r_2 r_1 \mathrm{d}r_1 + N_s\frac{\lambda_u}{\lambda_r},$$

where

$$h_{\mathtt{typ,m2}}(r_x, r_y, u) = \sum_{l=0}^{N_s-1}\Big[\mathtt{Pos}_{\mathtt{PMF}}(l, \lambda_r \mathtt{AoI}_2(r_x, r_y, v_{xy}))\mathtt{Pos}_{\mathtt{CMF}}(N_s - l - 1, \lambda_r(\pi r_x^2 - \mathtt{AoI}_2(r_x, r_y, v_{xy}))$$
$$\times \mathtt{Pos}_{\mathtt{CMF}}(N_s - l - 1, \lambda_r(\pi r_y^2 - \mathtt{AoI}_2(r_x, r_y, v_{xy}))\Big]. \tag{7.14}$$

In the above equation, $v_{xy} = \arccos\left(\frac{r_x - r_y\cos(u)}{\sqrt{r_x^2+r_y^2-2r_xr_y\cos(u)}}\right)$, and $\mathtt{AoI}_2$ is given in (7.12).

Proof: Please refer to Appendix C.3. ■

Similar to the tagged AP case, we approximate the load of the typical AP by negative binomial random variable.

Remark 7.10. *We observe that $\mathbb{E}[K_o^2] \approx \mathbb{E}[K_o]^2 + 1.2802N_s$. This result is exact for $N_s = 1$ [129].*

Remark 7.11. *The load distribution result of the typical AP also characterizes the degree distribution in a AB random geometric graph (AB-RGG). An AB-RGG is a bipartite random graph between two sets of vertices A and B, where a point in A is connected to a few points in B based on certain distance criteria [130, 131]. In our case, $A = \Phi_r, B = \Phi_u$ and an edge exists if $\mathbf{x} \in \Phi_u$ is served by $\mathbf{y} \in \Phi_r$. It is worth mentioning that a simulation-based approximation result for the degree distribution of this type of AB-RGG is recently proposed in [132].*

7.5 Rate Coverage for user-centric cell-free mMIMO

The achievable rate result derived in Lemma 7.3 is directly applicable to the user-centric cell-free architecture. Recall that Φ_r and Φ_u are two independent homogeneous PPP. Further, we consider that the typical user at the origin and its set of serving APs Φ_{ro} consists of the nearest N_s APs. Determining the distribution of the rate or $\mathtt{SINR}$ of the typical user is intractable as each term in the expression are functions of a set of common distances. However, a degree of tractability can be achieved for theoretical analysis by assuming that the network is operating in a regime where pilot contamination is negligible. There are two consequences of this assumption. First, we can ignore the pilot contamination interference term in (7.6). Second, the variance of the channel estimate between AP at $\mathbf{r}_m$ and user at $\mathbf{u}_k$ can be approximated as

$$\gamma_{mk} = \frac{\tau_p \rho_p \beta_{mk}^2}{1 + \tau_p \rho_p \sum_{\mathbf{u}_j \in \Phi_u} \boldsymbol{\psi}(k)^H \boldsymbol{\psi}(j) \beta_{mj}} \approx \frac{\tau_p \rho_p \beta_{mk}^2}{1 + \tau_p \rho_p \beta_{mk}}.$$

Remark 7.12. *A system with a pilot allocation scheme that ensures that each AP serves only one user per pilot is likely to operate in the regime where the above assumption holds, especially, for the set of serving (dominant) APs. This pilot assignment is realizable in a low mobility scenario, where the coherence block is sufficiently large. For example, if we consider a coherence bandwith of 200 kHz and a coherence time of 2 ms, then the TDD coherence block has 400 samples. Let us assume that each AP is served by the nearest $N_s = 5$ APs. In such a scenario, the probability that the set of tagged APs, which serve the typical user, collectively serve more than 30 users is less than 0.002. Hence, by reserving more than 30 symbols for pilot estimation in the coherence block above criteria is met.*

With this assumption, we present the probability of coverage for the typical user.

Proposition 6. Conditioned on the links associated with the typical user is active, the rate coverage of the user is given as $R_c = \mathbb{P}[R_o > T_r] =$

$$\int\limits_{d_{oN_s}=0}^{\infty} \int\limits_{d_{oN_s-1}=0}^{d_{oN_s}} \cdots \int\limits_{d_{oN_s-1}=0}^{d_{o1}} \sum_{k_1=0}^{\infty} \mathbf{1}\left(2\pi\lambda_r \int\limits_{d_{oN_s}}^{\infty} l(r) r \mathrm{d}r \leq h_{\texttt{cov}}(k_1, d_{o1}, d_{o2}, \ldots, d_{oN_s})\right)$$
$$\times \mathbb{P}[K_1 = k_1] \prod_{i=1}^{N_s-1} \frac{2d_{oi}}{d_{oN_s}} f_{D_{oN_s}}(d_{oN_s}) \mathrm{d}d_{o1} \ldots \mathrm{d}d_{oN_s},$$

where $h_{\texttt{cov}}\left(k_1, d_{o1}, d_{o2}, \ldots, d_{oN_s}\right)) =$

$$\frac{N}{(2^{T_r}-1)K_{\texttt{max}}}\left(\sqrt{\gamma_{o1}(1-2^{-\frac{C_f}{\min\{k_1+1, K_{\texttt{max}}\}}})} + \sum_{l=2}^{N_s}\sqrt{\gamma_{ol}(1-2^{-C_f/\bar{K}_l})}\right)$$
$$- \frac{N}{K_{\texttt{max}}}\left(\gamma_{o1} 2^{-\frac{C_f}{\min\{k_1+1, K_{\texttt{max}}\}}} + \sum_{l=2}^{N_s} \gamma_{ol} 2^{-C_f/\bar{K}_l}\right) - \sum_{l=1}^{N_s} l(d_{ol}) - \frac{1}{\rho_d}. \tag{7.15}$$

In the above expression, $d_{o1} \leq d_{o2} \leq \ldots \leq d_{oN_s}$, where d_{oi} is the distance between the typical user and its i-th closest AP. The load of the closest AP is K_1 and the mean load of the i-th closest AP is $\bar{K}_i$, which is given as $\bar{K}_i = 1 + \sum_{k_i=0}^{\infty} \min\{k_i, K_{\texttt{max}}\}\mathbb{P}[K_i = k_i]$.

Proof: Please refer to Appendix C.5. ■

7.6 Results and Discussion

In this section, we validate the theoretical rate coverage result through extensive Monte Carlo simulations. Further, we provide a few useful system design insights from our analyses.

7.6.1 Performance of traditional cell-free mMIMO

First, we validate the theoretical results derived for the traditional architecture in Sec. 7.3. We have considered a finite circular region of radius $R_s = 500$ m. The path loss function between any two nodes at a distance r is

$$l(r) = r^{3.7}\mathbf{1}(r > 1) + \mathbf{1}(r \leq 1). \tag{7.16}$$

We consider the transmit $\texttt{SNR}$ $\rho_d = 100$ dB[1], transmit pilot $\texttt{SNR}$ $\rho_p = 100$ dB. We consider the TDD coherence block consists of 400 samples that corresponds to a coherence bandwidth

[1]The received SNR at the edge of the system from the center with the considered path loss model is 0.1381 dB.

of 200 kHz and a coherence time of 2 ms. Further, the pilot sequence is of length $\tau_p = 80$ samples unless stated otherwise. We consider that the users are assigned orthogonal pilot sequences that is number of users in this finite system $K \leq \tau_p$. Note that as stated before Lemma 7.3, we only present the user or system SE (in terms of bits/s/Hz). These values will scale depending on the system bandwidth and the fraction of coherence block dedicated for the downlink transmission. The choice of other system parameters are indicated at necessary places. Using the rate coverage result of Proposition 5, the average user rate is expressed as

$$\bar{\mathtt{SE}}_{o,f} = \int_{t=o}^{\infty} t R_{c_f}(t) \mathrm{d}t \quad \text{bits/s/Hz},$$

and corresponding average system sum-rate is $K\bar{\mathtt{SE}}_{o,f}$ bits/s/Hz.

The effect of fronthaul capacity

In Fig. 7.2 (left), we have presented the rate coverage of the system for $K = 20$ users in the system. As expected, the rate coverage improves with increasing SCNR threshold T_s as it directly corresponds to higher fronthaul capacity C_f. Further, in Fig. 7.2 (right), the average system sum-rate is presented as a function of the number of users K for different fronthaul capacities. We have kept a high pilot transmission SNR $\rho_p = 100$ dB corresponding to an almost perfect CSI scenario to highlight the effect of fronthaul capacity on the system performance. As evident from the figure, the average system sum-rate is quasi-concave function of the number of users. Further, for a given number of APs, the optimum number of users that should be multiplexed to maximize the average rate increases with the increasing fronthaul capacity. From the trend, we infer that when C_f has unlimited capacity, the maximum average system sum-rate is obtained by serving all the users simultaneously.

Distributed vs. collocated

In Fig. 7.3 (left), we present the rate coverage of the system for different number of antennas at the AP while keeping the total number of antennas in the system fixed, i.e. $MN = 128$. We observe that conjugate beamforming along with the equal power allocation scheme results in a more centralized architecture to be better than a distributed architecture. In Fig. 7.3 (right), we present the average user rate for different number of antennas at each AP while keeping the total number of antennas in the service region fixed. We consider the SCNR threshold $T_s = 15$ dB. We observe that for high ρ_p (i.e. high-quality CSI) as we move towards a more collocated setup, average user rate increases. On the other hand, with low ρ_p (i.e. low-quality CSI), the average user SE is a concave function of the number of antennas per AP. This behavior is in contrast to the conventional MIMO results where a distributed implementation is always preferred. The justification to this counter-intuitive trend can be explained by the fact that due to ConjBF, we get a self-interference term from all the APs as evident from the SINR expression in (7.6). Hence, with a distributed implementation, the desired signal power from the nearest AP increases and so does the self interference term. Therefore, a more collated set up is preferred.

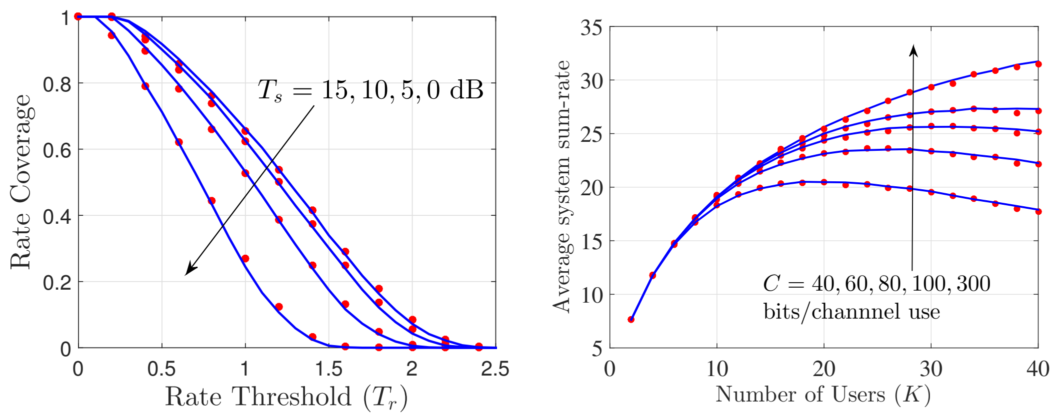

Figure 7.2: The effect of fronthaul capacity on system performance. The solid lines are obtained using the analytical results presented in Sec 7.3 and markers are Monte Carlo simulation results. The system parameters are $M = 32, N = 4, \tau_p = 80, \rho_p = \rho_d = 100$ dB.

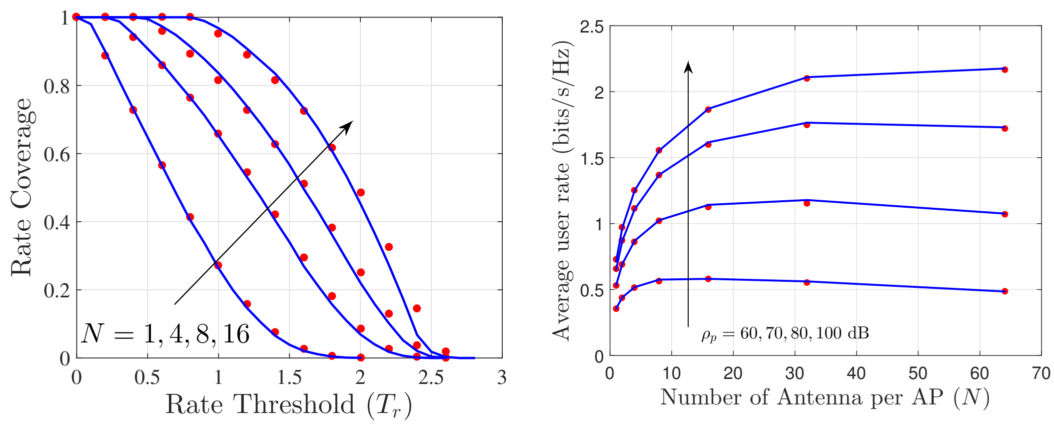

Figure 7.3: The effect of number of antennas per AP on rate coverage (left) and average user rate (right). Solid lines and markers represent analytical and simulation results, respectively. We have considered $MN = 128, \tau_p = 80, K = 20, \rho_d = 100$ dB, $\texttt{SCNR} = 15$ dB.

7.6.2 Performance of user-centric cell-free mMIMO

Now, we verify the theoretical results derived in Secs. 7.4 and 7.5 through extensive Monte Carlo simulations. Further, we provide a few useful network dimensioning guidelines. For the simulations, we consider the system radius to be 2000 m. The path loss is the same as (7.16). Further, we consider the $\rho_d = \rho_p = 100$ dB and $\tau_p = 80$. The choice of other system parameters are indicated at necessary places.

The load distribution result and insights

In Fig. 7.4, we validate the approximate theoretical PMFs obtained from Secs. 7.4.1 and 7.4.2, respectively, by Monte Carlo simulations. In both the cases, theoretical and simulation results are in remarkably close. In Fig. 7.5 (left), using the typical AP load distribution result, we present the probability that SCNR for a user symbol is above a predefined threshold T_s as a function of number of serving APs N_s for a given fronthaul capacity C_f. Formally, we write

$$\mathbb{P}[\texttt{SCNR} \geq T_s] = \mathbb{P}[2^{C/K_o} - 1 \geq T_s] = \mathbb{P}[K_o \leq C_f/\log_2(1+T_s)],$$

which is the cumulative mass function (CMF) of the typical AP load. As expected, the more stringent the T_s, the lower the probability of having a SCNR more than T_s for a given number of serving APs. Note that in this result we assume that all the users attached to the typical AP are scheduled on the same resource while using different pilots. In Fig. 7.5 (right), we present the required fronthaul capacity as a function of number of serving APs. As expected, we observe a linear growth in C_f with increasing N_s. However, the rate of growth depends on the stringency of the SCNR constraint.

The rate coverage result and insights

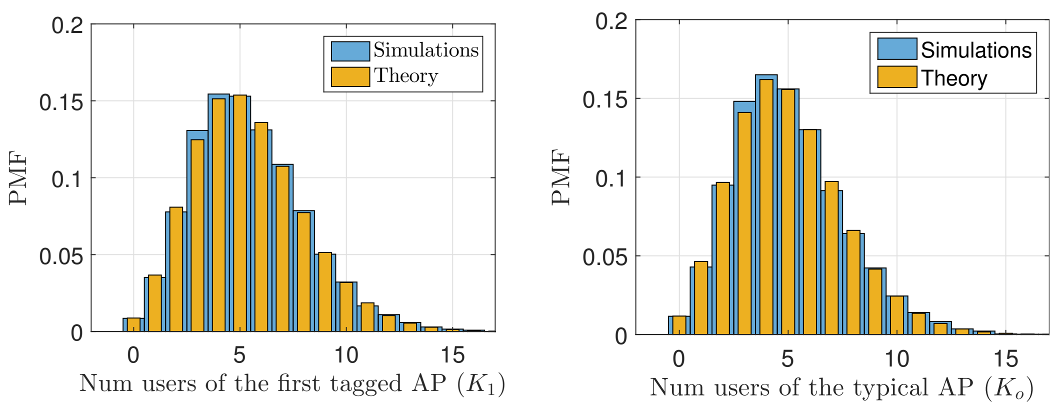

Figure 7.4: The PMF of the number of users served by the nearest tagged AP (left) and the typical AP (right) in the network. $\lambda_r = \lambda_u = 10^{-4}, N_s = 5$.

In Fig. 7.6 (left), we present the rate coverage for the typical user for different SQNR thresholds when it gets scheduled. As observed from the figure, for a fixed C_f, with increasing T_s the rate coverage improves. Note that as per Remark 7.2, for a fixed C_f, maximum scheduled user per resource unit increasing with decreasing T_s. As a result, the power is equally divided among more users that results in the poorer coverage. In Fig. 7.6 (right), we plot the rate coverage of the typical user for different N_s. The corresponding C_f is selected using the result of Fig. 7.5 such that $\mathbb{P}[\texttt{SCNR} \geq T_s] \approx 0.95$. From the figure, we observe that

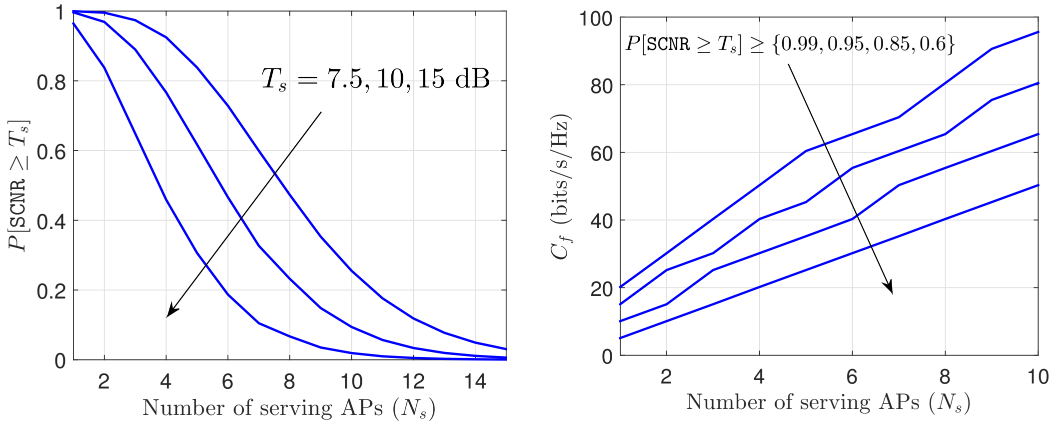

Figure 7.5: (Left) The number of serving APs to ensure a certain minimum SCNR for different T_s. Other parameters: $\lambda_u = \lambda_r = 10^{-4}, C_f = 20$ bits/s/Hz. (Right) The required fronthaul capacity as a function of N_s to satisfy $\mathbb{P}[\texttt{SCNR} \geq T_s]$ is above a certain threshold. Other parameters: $\lambda_u = \lambda_r = 10^{-4}, T_s = 15$ dB.

service by more number of APs is not always advantageous. Hence, system should operate at the optimum N_s for a given set of parameters.

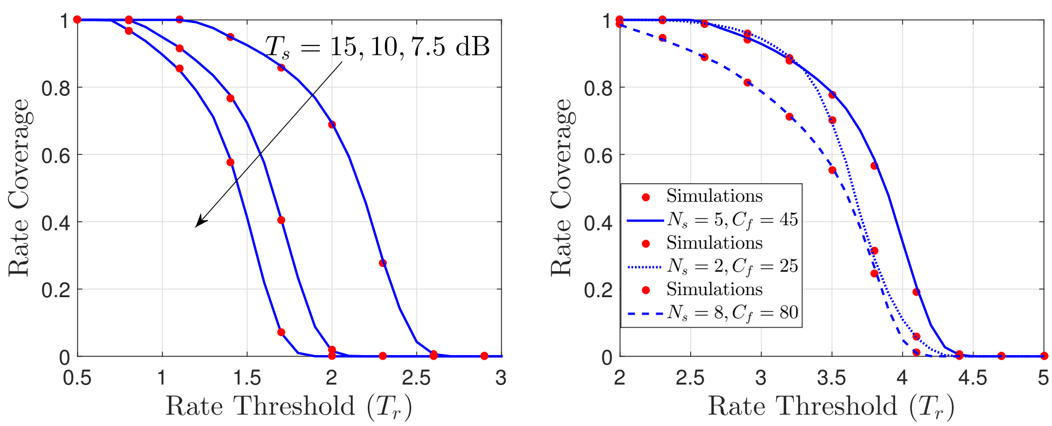

Figure 7.6: (Left) The rate coverage when the typical user for different T_s and fixed $C_f = 45$ bits/s/Hz. Solid lines and markers represent theory and simulations, respectively. Other system parameters:$\lambda_u = \lambda_r = 10^{-4}, N = 10, N_s = 5, \tau_p = 80, \rho_p = \rho_d = 100$ dB. (Right) The rate coverage for different number of serving APs (N_s). Other system parameters: $\lambda_u = \lambda_r = 10^{-4}, N = 40, \tau_p = 120, \rho_p = \rho_d = 100, T_s = 15$ dB.

7.7 Conclusion

In this chapter, we modeled and analyzed a cell-free mMIMO network with finite fronthaul capacity using tools from stochastic geometry. We considered two different architectures of cell-free mMIMO, namely, the traditional architecture where each AP serves all the users in the network and the user-centric architecture where the typical user is served by a few nearest APs. For the traditional architecture, we provided the user rate coverage result using the relevant statistics of BPPs. For the user-centric architecture, we characterized the load distribution result for the typical AP as well as the set of tagged APs that serve the typical user in the network. Further, using the statistical properties of PPPs, we presented the rate coverage result for the typical user in the network. From our analyses, we conclude that for the traditional architecture, in the presence of low-quality CSI at the APs, a more collocated implementation of cell-free mMIMO is preferred over the fully distributed implementation. Further, for the cell-free architecture, increasing the number of serving APs does not necessarily improve the rate coverage. Hence, there exists an optimal number of serving APs that depends on different system parameters. Promising future extensions of this work include the determination of the scheduling probability of the typical user for the user-centric architecture. This requires knowledge of the total number of users served by the set of tagged APs. Further, the system behavior in presence of pilot contamination is also a promising direction that can lead to useful guidelines for the pilot allocation.

Chapter 8

Stochastic Geometry-based Modeling and Analysis of Citizens Broadband Radio Service System

8.1 Introduction

In this dissertation, we have focused on the mMIMO system that operates in the sub-6 GHz of the electromagnetic spectrum. Owing to the limited availability of frequency bands, in this frequency range spectrum sharing is often encouraged by regulatory bodies. An example of sub-6 GHz spectrum sharing is the recent proposal by the FCC to foster co-existence of commercial cellular networks alongside the defense communication systems [133] in the 3.5 GHz band, a.k.a. CBRS band. One of the main advantages of the CBRS band is the mature hardware technology in the sub-6 GHz spectrum, which is suitable for near-future system deployment. For successful co-existence, the CBRS ecosystem is divided into three-tiered access systems: (1) incumbent access (IA) tier that consists of defense systems, (2) priority access licensed (PAL) tier for the licensed networks, and (3) general authorized access (GAA) tier for the unlicensed networks. Under key guidelines mentioned in [133], recent studies have shown that the co-existence between IA tier and PAL tier can be successfully achieved without violating the security and interference protection constraints of the defense systems while achieving appreciable data rates for the licensed communication networks [134, 135, 136]. However, from the commercial application perspective, the study on successful co-existence of PAL and GAA networks (operators) is of prime importance, which has not been addressed in the literature and is the main focus of this work.

8.1.1 Motivation and related works

One of the key elements of the FCC guidelines is that the communication links of the licensed operator are to be protected from unlicensed BSs' interference by creating protection zones (PZs) around each licensed BS. Within these PZs, none of the unlicensed BSs are allowed to operate. The overall system is controlled by a centralized node known as the spectrum access system (SAS). While it is possible to centrally manage network operations such as spectrum access and transmission power control for the unlicensed BSs, doing so may result in increased signaling overhead due to potentially large number of unlicensed BSs. Hence, a preferable option is to perform some of the tasks, such as contention-based channel access among the unlicensed BSs, in a distributed manner. Consideration of contention-based channel access is also important since wireless LAN systems are likely to co-exist in this band. While one can, in principle, study the performance of this system through extensive simulations, simulators do not usually scale well with the growing number of nodes. As a result, it is highly desirable to develop a tractable approach capable of exposing fundamental performance trends of such large-scale systems.

One such approach that has received significant attention over the past few years is to compute network-wide metrics by spatially averaging over all possible topologies using powerful tools from stochastic geometry [7, 8, 9, 10, 11, 12, 13]. While it is natural to think that the existing approaches for wireless network analysis may be directly applicable to the analysis of the CBRS system, it is not quite true. In particular, there are two CBRS-specific challenges that need to be overcome first: (1) the presence of PZs around licensed BSs creates correlation among the locations of licensed and unlicensed BSs that ultimately results in correlation among aggregate interference powers generated by the both sets of BSs; (2) presence of PZs, as well as the consideration of contention-based channel access mechanism, makes the statistical characterization of interference from unlicensed BSs a difficult task.

To the best of our knowledge, there exists no work in the literature that studies co-existence of licensed and unlicensed networks considering both PZs around licensed BSs and contention-based channel access mechanism among unlicensed BSs from the perspective of stochastic geometry. However, the performance of wireless systems considering either one of the above-mentioned key elements can be found in the literature. The performance of IEEE 802.11 network that considers carrier sense multiple access with collision avoidance (CSMA-CA) based contention access mechanism is presented in [43]. In the above work, the active node locations are modeled as a Matérn hardcore process of type-II (MHPP-II), and the performance analysis is presented in terms of the medium access probability (`MAP`) and the signal to interference ratio (`SIR`) coverage probability. The extension of the above approach to the performance analysis of cellular networks can be found in [46]. From the perspective of co-existence between licensed and unlicensed networks, in [44] and [45], MHPP-II is used to model contention-based channel access mechanism among primary and secondary transmitters. However, the performance analysis is limited to a bipolar ad hoc network. The extension of the above approach to a cellular setup for co-existence study between LTE and Wi-Fi systems is presented in [137]. However, in these works, the key system consideration regarding the node locations is in contrast to the FCC proposed model, where the spatial separation between licensed and unlicensed BSs is strictly enforced through PZs.

On the other hand, in order to capture the strict spatial separation among primary (licensed) and secondary (unlicensed) transmitters (BSs), in [138] authors have introduced Poisson hole process (PHP) and presented the performance analysis for a cognitive ad hoc network. However, in the system model, the distance between a transmitter and receiver pair is considered to be fixed, and contention-based channel access among secondary transmitters is not considered, which can degrade their performance considerably. To overcome the later limitation of [138], in [139] performance analysis of a cognitive network is presented considering Aloha protocol for channel access for the secondary transmitters, and in [140] considering exclusions zones around secondary transmitters so that two nearby secondary transmitters can not access the channel simultaneously. The extension of [138] to the performance analysis of heterogeneous cellular can be found in [141]. However, in all the above-mentioned works, the presence of holes (PZs) in the network is usually modeled by either thinning the unlicensed (secondary) transmitter density or by approximating the PHP with a cluster process. As a result, these approaches do not accurately model the correlation among the node locations. A more refined approach to the performance analysis of a PHP network in terms of coverage probability is presented in [142]. In particular, authors have provided useful bounds for the Laplace transform (LT) of interference that help in accurate coverage probability evaluation of a PHP network.

Unlike the prior art, where the effect of one of the two aspects of the FCC proposed system model is handled in isolation, we propose a unified analytic approach that takes into account the joint effect of both PZs and contention mechanisms. As we will see in following sections, this *joint* analysis is significantly challenging and requires a careful handling of several types of dependencies in the interference field to obtain accurate results for different performance metrics. Therefore, in addition to the contributions summarized below, one indirect consequence of our analysis is the detailed exposition of several key open problems that appear in the performance analysis of a CBRS system.

8.1.2 Contributions

System modeling

We propose a stochastic geometry-based framework to analyze the performance of a network that operates in the licensed band of the CBRS spectrum and consists of a licensed and an unlicensed operator. To be specific, we model the locations of the licensed BSs as a PPP and the locations of the unlicensed BSs as a PHP that takes into account the PZs around each licensed BS. In addition, a CSMA-CA type contention-based mechanism is also considered for medium access by the unlicensed BSs. This model captures the essential elements of the FCC envisioned system, whose key goal is to facilitate the symbiotic co-existence of the licensed and unlicensed operators.

System analysis

For the system analysis of the licensed operator, the performance metrics that we consider are the SIR and the link rate coverage probability, as well as area spectral efficiency (ASE).

Since `ASE` of the unlicensed operators depend on the `MAP` of their BSs, we derive an approximate expression and useful lower bounds for the `MAP`. Further, exact evaluation of coverage probabilities is difficult due to correlation in interference induced by the dependency in the licensed and unlicensed BS locations, as well as the presence of PZs. Hence, we provide approximate but fairly accurate results for coverage probabilities by carefully capturing the interference correlation and the effect of PZs in the vicinity of the typical user. In the process of evaluating the `MAP` and the coverage probability, we also provide approximate expressions for two useful distance distributions specific to the PHP network.

System design insights

Using the expressions for the `MAP` and the coverage probabilities, we study the impact of PZ radius and unlicensed BS transmission power on the network performance in terms of `ASE`. One important observation is that there exists an optimal operating point that maximizes the `ASE`s of the unlicensed operator and the overall network with respect to unlicensed BS transmission power. Another important observation is that the `ASE` of the unlicensed operator saturates beyond a certain carrier sense threshold.

8.2 System model

8.2.1 Network geometry

We consider the DL of a cellular network that has two operators, namely Operator A (OpA) and Operator B (OpB), operating in the licensed band of the CBRS spectrum. This band of the spectrum is divided into multiple frequency bands (FBs) of smaller bandwidth. Without loss of generality, we present our analysis for an arbitrarily selected FB (from amongst the smaller frequency bands) that we call the *representative FB.* We assume that OpA has the license to operate in PAL mode of operation, while OpB, as an unlicensed operator, can only operate in GAA mode of operation. Each operator is assumed to have deployed a set of citizens broadband service devices (CBSDs) (referred as BSs hereafter) in the region of consideration. The locations of the OpA BSs follow a homogeneous PPP Ψ_A of density λ_A. As per the FCC regulations, interference protection is provided to each OpA BS by considering a PZ around it, where operation of OpB BSs is prohibited. One reasonable way of modeling these interference protection zones is to assume that the OpB BSs form a PHP with the hole centers being the locations of the OpA BSs. In this case, the locations of OpB BSs in the PHP Φ_B are obtained by considering a baseline PPP Ψ_B of intensity λ_B and retaining only those points in Ψ_B that lie outside all the PZs, i.e.

$$\Phi_B = \left\{ \mathbf{x} \in \Psi_B : \prod_{\mathbf{y} \in \Psi_A} \mathbf{1} \left(\|\mathbf{y} - \mathbf{x}\| > R_{pz} \right) = 1 \right\}, \tag{8.1}$$

Table 8.1: Summary of notations used in this chapter

Notation	**Description**
Ψ_A, λ_A	Homogeneous PPP modeling the locations OpA BSs, density of Ψ_A
Φ_B	PHP modeling the locations of OpB BSs
Ψ_B, λ_B	Parent homogeneous PPP for Φ_B, density of Ψ_B
R_{pz}	Protection zone radius
$\mathbf{u}_o^A, \mathbf{u}_o^B$	Locations of the typical OpA and OpB users
$\mathbf{x}_o^A, \mathbf{x}_o^B$	Locations of the tagged OpA and OpB BSs
R_o^A	Distance between a typical user and its nearest OpA BS
R_o^B	Distance between the typical OpB user and tagged OpA BS
D_o^B	Distance between the typical OpA user and its nearest active OpB BS
$R_{o,AB}$	Distance between the tagged OpB BS and its nearest OpA BS
P_A, P_B	Transmission power per unit bandwidth of OpA and OpB BSs
$P_r(\mathbf{y}, \mathbf{x}_i)$	Received power per unit bandwidth at a location $\mathbf{y}$ from a location $\mathbf{x}_i$
$\mathcal{I}_o^B$	Medium access indicator of the tagged OpB BS
$\mathcal{M}_o^B$	Medium access probability of the tagged OpB BS
τ_{cs}	Carrier sense threshold
$\mathtt{SIR}_o^A, \mathtt{SIR}_o^B$	The $\mathtt{SIR}$ for the typical OpA and OpB user
$\mathtt{P}_\mathtt{c}^{(\mathtt{X})}(T)$	Coverage probability of typical typical OpX user for a $\mathtt{SIR}$ threshold T
$\mathcal{B}_r(\mathbf{x})$	A circle of radius r centered at $\mathbf{x}$.
$N_\Psi(\mathcal{C})$	Number of points of the point process Ψ that lie in the region $\mathcal{C}$
$\lvert\mathcal{C}\rvert$	The area of the region $\mathcal{C}$

and the density of OpB BSs in Φ_B is given as

$$\hat{\lambda}_B = \lambda_B \exp(-\pi\lambda_A R_{pz}^2). \tag{8.2}$$

Above density follows from the null probability of PPP applied to Ψ_A that stems from the fact that for a typical point $\mathbf{x} \in \Psi_B$ to be in Φ_B, there should be no OpA BS within $\mathcal{B}_{R_{pz}}(\mathbf{x})$, i.e. a circle of radius R_{pz} centered at $\mathbf{x}$. Please refer [142, Lemma 2] for a formal proof.

We consider a closed-access system, where the OpA serves a set of *end users* (referred as users hereafter) whose locations form a homogeneous PPP ϑ_A and OpB serves another set of users whose locations form a homogeneous PPP ϑ_B. For simplicity, we assume that ϑ_A and ϑ_B are independent of each other as well as Ψ_A and Ψ_B. A user of an operator gets attached to its nearest BS belonging to that particular operator. In this work, we analyze the performance of a typical user of OpA (OpB) whose location is denoted by $\mathbf{u}_o^A$ ($\mathbf{u}_o^B$). Without loss of generality, we present the performance analysis considering $\mathbf{u}_o^A$ ($\mathbf{u}_o^B$) is placed at the origin. The serving BS of the typical user is termed as the *tagged* BS and its location is denoted as $\mathbf{x}_o^A$ ($\mathbf{x}_o^B$). In case of OpA, the distance $R_o^A = \|\mathbf{x}_o^A - \mathbf{u}_o^A\|$ between the typical user and the tagged BS follows Rayleigh distribution, which is given as

$$f_{R_o^A}(r_o^A) = 2\pi\lambda_A r_o^A \exp(-\pi\lambda_A (r_o^A)^2). \tag{8.3}$$

Above expression is the probability density function (PDF) of the contact distance for a homogeneous PPP [12]. On the other hand, for the OpB, the distribution of the distance $R_o^B = \|\mathbf{x}_o^B - \mathbf{u}_o^B\|$, between the typical user and the serving BS corresponds to the contact distance distribution for PHP. Accurate characterization of this distance distribution requires the consideration of the relative overlaps among the PZs, as well as the probability of the PZs deleting the points of Ψ_B in a given region. Owing to its analytical complexity, characterization of the contact distance distribution of PHP remains an open problem. Having said that, in the literature, the PDF of R_o^B is approximated as Weibull distribution (cf. [141]) and is given as

$$f_{R_o^B}(r_o^B; \alpha, \beta) \approx \frac{\beta}{\alpha}\left(\frac{r_o^B}{\alpha}\right)^{\beta-1} \exp\left(-\frac{r_o^B}{\alpha}\right)^{\beta}, \tag{8.4}$$

where α is the shape parameter and β is the scale parameter of the function. Corresponding CDF is given as

$$F_{R_o^B}(r_o^B; \alpha, \beta) \approx 1 - \exp\left(-\frac{r_o^B}{\alpha}\right)^{\beta}. \tag{8.5}$$

The values of these parameters depend on λ_A, λ_B, and R_{pz} and are determined through curve-fitting for a given set of system parameters.

An illustration of the CBRS network studied in this chapter is presented in Fig 8.1. Further, a representative network diagram where a typical user of OpA (OpB) is served by

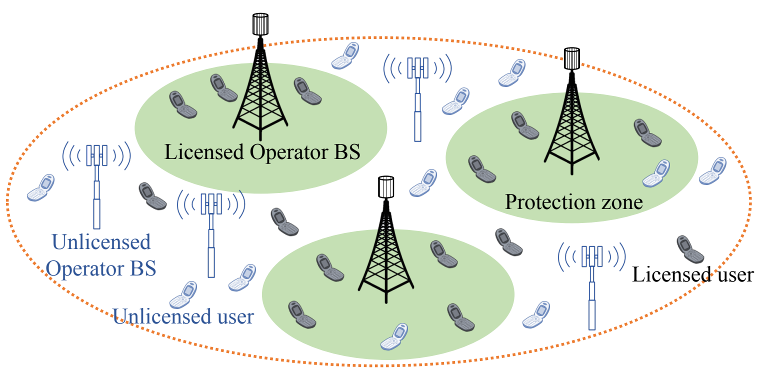

Figure 8.1: As illustration of the CBRS network studied in this chapter.

the tagged OpA (OpB) BS is presented in Fig. 8.2a (Fig. 8.2b).

8.2.2 Propagation model

The representative FB is divided into a certain number of orthogonal time-frequency resources known as resource blocks. We assume that the channel gain on each resource block is affected by path loss and multi-path fading. Multi-path fading is assumed to be Rayleigh distributed and independent across resource blocks. For simplicity, we ignore the effect of

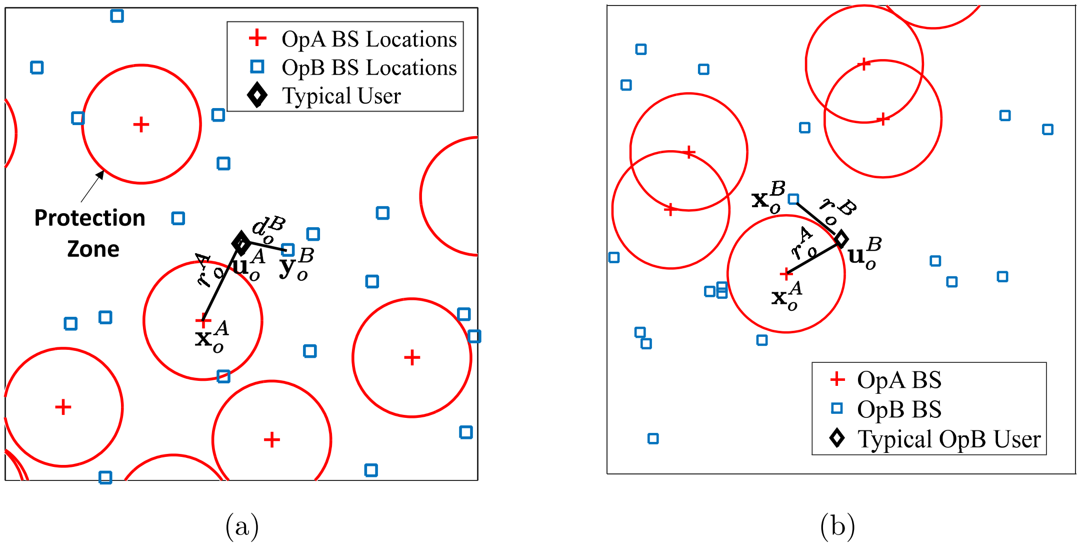

Figure 8.2: (a) Typical OpA user located at $\mathbf{u}_o^A$ served by the tagged OpA BS at $\mathbf{x}_o^A$. (b) Typical OpB user located at $\mathbf{u}_o^B$ is served by the tagged OpB BS located at $\mathbf{x}_o^B$.

shadowing. Without loss of generality, we present our analysis for a *representative resource block*. The transmission power spectral density, i.e. transmission power per unit bandwidth of OpA (OpB) is P_A (P_B). Now, on the representative resource block, the received power per unit bandwidth at a generic location $\mathbf{y}$ from a BS located at $\mathbf{x}_i \in \Psi_A$ or Φ_B is given as

$$P_r(\mathbf{y}, \mathbf{x}_i) = \frac{P_T h(\mathbf{y}, \mathbf{x}_i)}{l(\|\mathbf{y} - \mathbf{x}_i\|)}, \tag{8.6}$$

where P_T can be P_A or P_B, $l(\|\mathbf{y} - \mathbf{x}_i\|)$ is the path loss in linear scale, and $h(\mathbf{y}, \mathbf{x}_i)$ is the multi-path gain of the channel between the BS at $\mathbf{x}_i$ and the receiver node at $\mathbf{y}$. We assume that the multi-path fading gains are i.i.d. among links between different nodes. Since the amplitude of multi-path fading is assumed to be Rayleigh distributed, the multi-path gain $h(\mathbf{y}, \mathbf{x}_i) \sim \exp(1)$. In this work, we consider Urban Micro non-line-of-sight path loss model [143], which is characterized as

$$10 \log_{10}(l(d)) = 36.7 \log_{10}(d) + 22.7 + 26 \log_{10}(f_c), \tag{8.7}$$

where d is the distance between the two nodes in meters and $f_c = 3.5$ GHz is the carrier frequency.

8.2.3 Contention-based medium access mechanism

For successful co-existence of OpB BSs in GAA mode of operation, a contention-based channel access mechanism is necessary. In this work, we consider CSMA-CA based channel access mechanism that is prevalent in Wireless LAN (WLAN) systems. This access mechanism is divided into two phases, namely *listen before talk* (LBT) and *contention*. In the LBT phase, a potential BS tries to detect the presence of other active BSs, where the detection is successful if the potential BS is able to decode one of the received preambles from active BSs. Successful decoding of a preamble requires the received signal strength to be above certain threshold known as carrier sense threshold (τ_{cs}). If the received signal strength is more than the carrier sense threshold, the potential BS waits till the end of the transmission followed by contention phase. In contention phase, the potential BS does a random back-off, where the back-off timer depends on the contention window size, which is a system implementation parameter. On the other hand, if the potential BS observes the channel to be idle during LBT phase (i.e. received signal strength from each of the active BSs is less than τ_{cs}), then it reduces its back-off timer. This process continues until the back-off timer is zero after which the BS transmits its data immediately. In case the back-off timers of two BSs are the same, advanced protocols are used to avoid the packet collision. A flow chart of the above procedure is presented in Fig. 8.3.

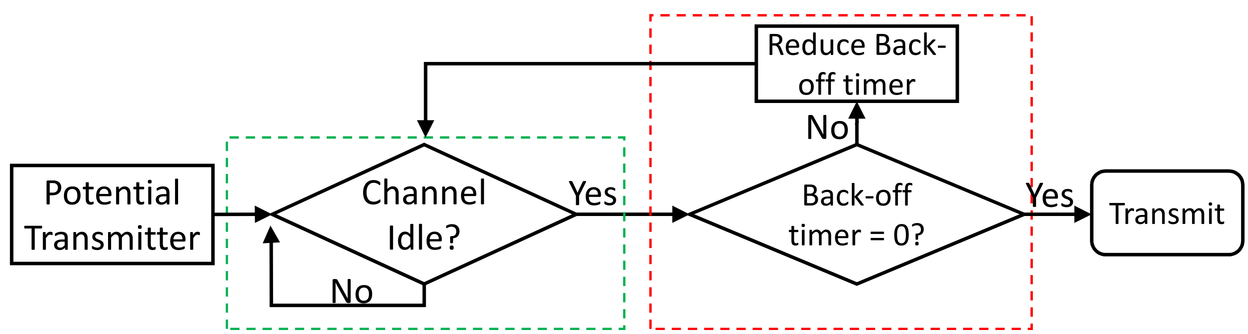

Figure 8.3: A simplified flow chart of CSMA-CA. The green dotted rectangle corresponds to the LBT phase and the red dotted rectangle corresponds to the contention phase.

Based on the above-mentioned channel access mechanism, to model the *active* OpB BSs that access the channel simultaneously, we follow the same formulation as presented in [43]. We briefly describe this for the tagged OpB BS located at $\mathbf{x}_o^B \in \Phi_B$. The tagged BS wins contention w.r.t. a BS at $\mathbf{x}_j^B$ if either of the following events takes place:

1. The received signal strength from a BS at $\mathbf{x}_j^B$ is less than τ_{cs}, i.e. the BS at $\mathbf{x}_j^B$ does not lie in the *contention domain* of the BS at $\mathbf{x}_o^B$.

2. The received signal strength from the BS at $\mathbf{x}_j^B$ is more than the threshold τ_{cs}, but its back-off timer $t_{x_j^B}$ is larger than the back-off timer $t_{x_o^B}$ of the tagged BS. Similar to [43], we assume that the back-off timers are uniformly distributed between $[0, 1]$.

Now if the BS at $\mathbf{x}_o^B$ wins contention w.r.t. all other BSs in Φ_B, then it gets access to the channel. Based on the above discussion, the medium access indicator of the BS $\mathbf{x}_o^B$ is given as $\mathcal{I}_o^B =$

$$\prod_{\mathbf{x}_j^B \in \Phi_B \setminus \mathbf{x}_o^B} \left(\mathbf{1}_{P_r(\mathbf{x}_o^B, \mathbf{x}_j^B) \leq \tau_{cs}} + \mathbf{1}_{P_r(\mathbf{x}_o^B, \mathbf{x}_j^B) > \tau_{cs}} \mathbf{1}_{t^B_{x_j} > t^B_{x_o}} \right). \tag{8.8}$$

where $P_r(\cdot, \cdot)$ is defined in (8.6). Now, the MAP of the tagged OpB BS is given as $\mathcal{M}_o^B = \mathbb{P}\left[\mathcal{I}_o^B = 1\right] =$

$$\mathbb{E}\left[\prod_{\mathbf{x}_j^B \in \Phi_B \setminus \mathbf{x}_o^B} \left(\mathbf{1}_{P_r(\mathbf{x}_o^B, \mathbf{x}_j^B) \leq \tau_{cs}} + \mathbf{1}_{P_r(\mathbf{x}_o^B, \mathbf{x}_j^B) > \tau_{cs}} \mathbf{1}_{t^B_{x_j} > t^B_{x_o}} \right) \right]. \tag{8.9}$$

8.2.4 Performance metrics

We evaluate the performance of OpA and OpB networks, using the following metrics:

1. *Coverage Probability:* Under the assumption of an interference limited network, the SIR of a typical OpB user is defined as

$$\mathtt{SIR}_o^B = \frac{\mathcal{I}_o^B P_r(\mathbf{u}_o^B, \mathbf{x}_o^B)}{I_{agg}^{BB} + I_{agg}^{BA}}, \tag{8.10}$$

where $I_{agg}^{BB} = \sum_{\mathbf{x}_j^B \in \Phi_B \setminus \mathbf{x}_o^B} \mathcal{I}_j^B P_r(\mathbf{u}_o^B, \mathbf{x}_j^B)$, and $I_{agg}^{BA} = \sum_{\mathbf{y}_j^A \in \Psi_A} P_r(\mathbf{u}_o^B, \mathbf{y}_j^A)$ are the aggregate interference powers received at the typical OpB user from the OpB and OpA BSs, respectively. Now, the SIR coverage probability is defined as the probability that the SIR at the typical user is greater than a target threshold T. In this work, we present the SIR coverage probability for the typical OpB user when the tagged BS is active, i.e. $\mathcal{I}_o^B = 1$. Hence, for a target SIR threshold T, this is formally expressed as

$$\mathtt{P}_\mathtt{c}^{(\mathtt{B})}(T) = \mathbb{P}\left[\mathtt{SIR}_o^B > T | \mathcal{I}_o^B = 1\right]. \tag{8.11}$$

Similarly, the link rate coverage probability of the typical OpB user for a target threshold T is defined as

$$\begin{aligned} \mathtt{R}_\mathtt{c}^{(\mathtt{B})}(T) =& \mathbb{P}\left[B_w \log_2(1 + \mathtt{SIR}_o^B) > T | \mathcal{I}_o^B = 1\right] \\ =& \mathbb{P}\left[\mathtt{SIR}_o^B > 2^{T/B_w} - 1 | \mathcal{I}_o^B = 1\right], \end{aligned} \tag{8.12}$$

where B_w denotes bandwidth.

On the other hand, for the typical OpA user, the coverage probability can be expressed as

$$\mathtt{P}_\mathtt{c}^{(\mathtt{A})}(T) = \mathbb{P}\left[\mathtt{SIR}_o^A > T\right] = \mathbb{P}\left[\frac{P_r(\mathbf{u}_o^A, \mathbf{x}_o^A)}{I_{agg}^{AB} + I_{agg}^{AA}} > T\right], \tag{8.13}$$

where $I_{agg}^{AB} = \sum_{\mathbf{x}_j^B \in \Phi_B} \mathcal{I}_j^B P_r(\mathbf{u}_o^B, \mathbf{x}_j^B)$ is the interference received at the typical OpA user from OpB BSs, and $I_{agg}^{AA} = \sum_{\mathbf{x}_j^A \in \Psi_A \setminus \mathbf{x}_o^A} P_r(\mathbf{u}_o^B, \mathbf{x}_j^A)$ is the interference received from OpA BSs. Similar to the previous case, for a target threshold T, the link rate coverage probability for the typical OpA user is defined as

$$\begin{aligned}\mathtt{R}_{\mathtt{c}}^{(\mathtt{A})}(T) =& \mathbb{P}\left[B_w \log_2(1+\mathtt{SIR}_o^A) > T\right]\\ =& \mathbb{P}\left[\mathtt{SIR}_o^A > 2^{T/B_w} - 1\right].\end{aligned} \quad (8.14)$$

2. *Area Spectral Efficiency (*ASE*):* In this chapter, we define the ASE of the network for a target SIR threshold T as

$$\mathcal{A}(T) = \left(\hat{\lambda}_B \mathcal{M}_o^B \mathtt{P}_{\mathtt{c}}^{(\mathtt{B})}(T) + \lambda_A \mathtt{P}_{\mathtt{c}}^{(\mathtt{A})}(T)\right) \log_2(1+T). \quad (8.15)$$

Note that it is more precise to use the coverage probabilities and MAP computed from the typical BS perspective in the above expression. However, in order to maintain tractability, we use the ones computed for the tagged BS (equivalently the typical user), which provides a reasonable approximation. While there is a subtle difference in the two viewpoints, either is sufficient to expose macroscopic system-level trends, which is the main purpose of our analysis.

From the definition of performance metrics it is clear that theoretical expressions for following metrics are necessary: (1) MAP of the tagged OpB BSs, and (2) SIR coverage probability of a typical OpA (OpB) user. In the next section, we characterize these quantities.

8.3 Medium access probability for the tagged OpB BS

Before deriving the main results, we present the following Lemma that is going to be useful in the derivation of several relevant distance distributions and conditional density functions of Ψ_A and Φ_B in the subsequent sections.

Lemma 8.1 (Presence of a hole in a homogeneous PPP)**.** *Consider a homogeneous PPP Ψ of density λ and a hole of radius R located at an arbitrary point $\mathbf{y} \in \mathbb{R}^2$. Conditioned on the distance $\|\mathbf{y}\|$ between the hole center and the origin, the intensity measure of Ψ is given as* $\Lambda_\Psi(\mathcal{B}_x(\mathbf{o}) | \|\mathbf{y}\|) = \mathcal{G}(x, \lambda, R, \|\mathbf{y}\|) =$

$$\begin{cases} 0 & \|\mathbf{y}\| \le R, 0 \le x \le R - \|\mathbf{y}\| \\ \pi\lambda x^2 & \|\mathbf{y}\| > R, 0 \le x \le \|\mathbf{y}\| - R \\ \lambda(\pi x^2 - A(x, R, \|\mathbf{y}\|)) & |\|\mathbf{y}\| - R| < x \le \|\mathbf{y}\| + R \\ \pi\lambda x^2 - \pi\lambda R^2 & x > \|\mathbf{y}\| + R, \end{cases} \quad (8.16)$$

where $\mathbf{o} = (0,0)$ *is the origin, and* $A(r, R, d) =$

$$\begin{aligned} & r^2 \cos^{-1}\left(\frac{r^2 + d^2 - R^2}{2rd}\right) + R^2 \cos^{-1}\left(\frac{R^2 + d^2 - r^2}{2Rd}\right) \\ & - \frac{1}{2}\sqrt{(r + R - d)(r + R + d)(d + r - R)(d - r + R)}, \end{aligned} \quad (8.17)$$

$$\frac{\mathrm{d}A(r,R,d)}{\mathrm{d}r} = -\frac{r^2\left(\frac{1}{d}-\frac{r^2+d^2-R^2}{2r^2d}\right)}{\sqrt{1-\frac{(r^2+d^2-R^2)^2}{4r^2d^2}}} + 2r\arccos\left(\frac{r^2+d^2-R^2}{2rd}\right) + \frac{Rr}{d\sqrt{1-\frac{(R^2-r^2+d^2)^2}{4R^2d^2}}}$$
$$-\frac{(r+R-d)(R-r+d)(r-R+d)+(R+r-d)(R-r+d)(R+r+d)}{4\sqrt{(r+R-d)(r+R+d)(r-R+d)(R-r+d)}}$$
$$+\frac{(R+r-d)(-R+r+d)(R+r+d)-(R-r+d)(r-R+d)(R+r+d)}{4\sqrt{(r+R-d)(r+R+d)(r-R+d)(R-r+d)}}. \tag{8.19}$$

---

which represents the area of intersection of two circles with radii r and R, and their centers are separated by a distance d. Corresponding conditional density function is given as

$$\lambda_\Psi(x|\|\mathbf{y}\|) = \frac{1}{2\pi x}\frac{\mathrm{d}\Lambda_\Psi(\mathcal{B}_x(\mathbf{o})|\|\mathbf{y}\|)}{\mathrm{d}x} \equiv \mathcal{E}(x,\lambda,R,\|\mathbf{y}\|). \tag{8.18}$$

The derivative of $A(r,R,d)$ with respect to r is given in (8.19) at the top of the next page.

Proof: The intensity measure of a point process is defined as the average number of points that lie within a given area [10]. In this case, we are interested in finding the average number of points of Ψ that lie in $\mathcal{B}_x(\mathbf{o}) \setminus \{\mathcal{B}_x(\mathbf{o}) \cap \mathcal{B}_R(\mathbf{y})\}$. Depending on the location of the hole from the origin, the average number of points that lie in $\mathcal{B}_x(\mathbf{o}) \cap \mathcal{B}_R(\mathbf{y})$ would be different, which is captured in (8.16). Fig. 8.4a represents the third case of (8.16). The other cases of interest involve either complete overlap or no overlap between the circles $\mathcal{B}_x(\mathbf{o})$ and $\mathcal{B}_R(\mathbf{y})$, and illustrations are omitted to avoid repetition. ■

8.3.1 MAP of the Tagged OpB BS

In this section, we present the MAP of the tagged OpB BS, which is an important intermediate metric as it is useful in obtaining the ASE of the OpB network. In (8.9), MAP is expressed as the product of the indicator functions that represent the contention winning event of the tagged BS w.r.t. the rest of the BSs in Φ_B. In point process theory, this product is evaluated using probability generating functional (PGFL) of the underlying point process [10, Chapter 4]. However, the PGFL for a PHP is not known [138], and any attempt to characterizing it involves exact consideration of relative overlaps among PZs, which is not straightforward. The approach that is usually followed in the literature to circumvent this problem is to approximate the PHP by a PPP. The density of the approximated PPP is either set to the density of baseline PPP Ψ_B (by completely ignoring the PZs) or to $\hat{\lambda}_B$ defined in (8.2) (cf. [138]). However, it has been shown recently in [142] that the interference field of a PHP can be accurately bounded by simply considering the exact effect of the closest

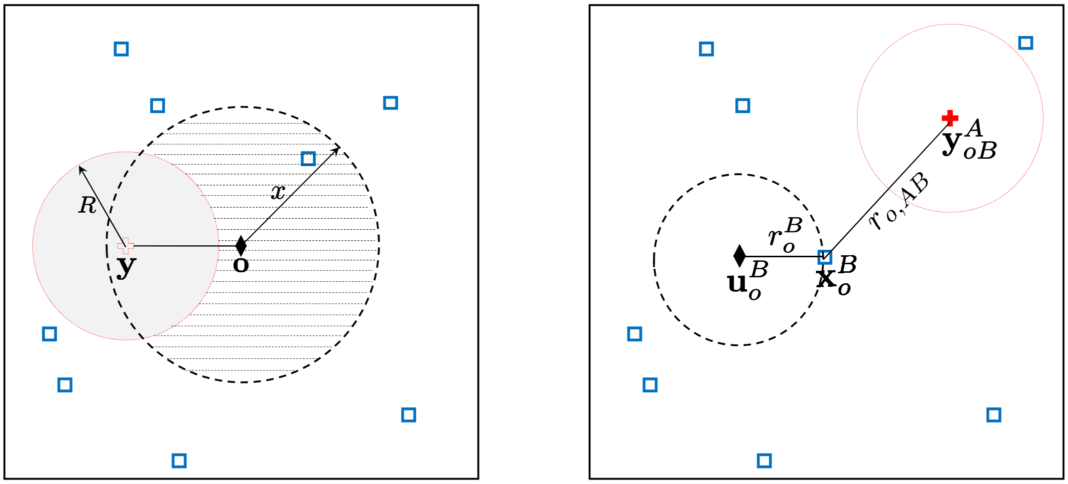

(a) (b)

Figure 8.4: (a) Illustration of a PPP with a hole for Lemma 8.1. The blue squares represent the set of points in Ψ. The red cross is the center of a hole with radius R. (b) A representative network diagram for Lemma 8.2.

hole while ignoring the rest of the holes. In the context of our work, this means that we can bound Φ_B with the baseline process Ψ_B from where the points lying in the PZ nearest to the tagged BS are removed. Clearly, the consideration of only the nearest PZ gives a lower bound on the `MAP` as more number of points are taken into consideration for the contention process than the actual number of BSs in Φ_B.

Conditional `MAP` of the tagged OpB BS

In this subsection, we derive a lower bound on the `MAP` of the tagged BS conditioned on its distance from the typical user and the nearest OpA BS, which is the center of its nearest PZ.

Lemma 8.2. *The* `MAP` *of the tagged OpB BS at* $\mathbf{x}_o^B \in \Phi_B$ *conditioned on its distances* $R_{o,AB}$ *from the nearest OpA BS and* R_o^B *from the typical user is given as*

$$\mathbb{P}\left[\mathcal{I}_o^B = 1 \middle| r_{o,AB}, r_o^B\right] \geq \frac{1-\exp(-f_1(r_{o,AB}, r_o^B))}{f_1(r_{o,AB}, r_o^B)}, \tag{8.20}$$

where

$$f_1(r_{o,AB}, r_o^B) = 2\Big(\pi \int_0^\infty \lambda_{\Psi_B}(y|r_o^B) e^{\frac{-\tau_{cs} l(y)}{P_B}} y \mathrm{d}y - \int_{r_{o,AB}-R_{pz}}^{r_{o,AB}+R_{pz}} \lambda_{\Psi_B}(y|r_o^B) e^{\frac{-\tau_{cs} l(y)}{P_B}} \varphi_{pz}(y|r_{o,AB}) y \mathrm{d}y\Big), \tag{8.21}$$

$\varphi_{pz}(y|x) = \arccos\left(\frac{y^2+x^2-R_{pz}^2}{2xy}\right)$, *and* $\lambda_{\Psi_B}(y|r_o^B) = \mathcal{E}(y, \lambda_B, r_o^B, r_o^B)$ *as given in* (8.18).

Proof: Please refer to Appendix D.1. ■

In order to obtain the final expression for MAP, we need to decondition the conditional MAP result derived above w.r.t. the distributions of R_o^B and $R_{o,AB}$. While R_o^B is approximated to follow Weibull distribution and given in (8.4), the distance distribution for $R_{o,AB}$ is not known. Further, as we discuss later in this section, R_o^B and $R_{o,AB}$ are dependent random variables. Hence, the above deconditioning needs to be performed using the joint distribution of R_o^B and $R_{o,AB}$. In the following two subsections, we present an approximate expression and useful lower bounds for the CDF of $R_{o,AB}$ conditioned on R_o^B, as well as lower bound and approximate expressions for the MAP of the tagged BS considering the joint distribution of $R_{o,AB}$ and R_o^B.

Lower bounds and approximate expression for CDF of $R_{o,AB}$

Since the tagged BS is a point in the PHP Φ_B, there are no OpA BSs inside the circle $\mathcal{B}_{R_{pz}}(\mathbf{x}_o^B)$. Now, for a given realization of R_o^B (i.e. r_o^B) between the typical user and the tagged BS, the density of OpA BSs in the vicinity of the tagged BS beyond $\mathcal{B}_{R_{pz}}(\mathbf{x}_o^B)$ depends on the following two events:

- Event-1 (Illustrated in Fig. 8.5a): The tagged BS at $\mathbf{x}_o^B$ is not the nearest point to the typical user in the baseline PPP Ψ_B, i.e. points in Ψ_B closer to the typical user than $\mathbf{x}_o^B$ are deleted by the PZ(s). This event indicates that there is at least one OpA BS in $\mathcal{B}_{r_o^B+R_{pz}}(\mathbf{u}_o^B) \setminus \mathcal{B}_{R_{pz}}(\mathbf{x}_o^B)$ (hence in the vicinity of the tagged OpB BS) that has deleted the points in Ψ_B. Therefore, in this case, the density of OpA BSs in the vicinity of the typical user is likely to be higher than λ_A as the probability of having no OpA BS in $\mathcal{B}_{r_o^B+R_{pz}}(\mathbf{u}_o^B)$ is zero. Further, the higher density is also intuitively justified by the argument that to ensure all the points of Ψ_B in $\mathcal{B}_{r_o^B}(\mathbf{u}_o^B)$ are deleted, the density of OpA BSs in $\mathcal{B}_{r_o^B+R_{pz}}(\mathbf{u}_o^B) \setminus \mathcal{B}_{R_{pz}}(\mathbf{x}_o^B)$ is likely to be larger than λ_A.

- Event-2 (Illustrated in Fig. 8.5b): The location of the tagged BS $\mathbf{x}_o^B \in \Phi_B$ is the nearest point to the typical user in the baseline PPP Ψ_B. In this case, the locations of OpA BSs follow a homogeneous PPP of density λ_A beyond the circle $\mathcal{B}_{R_{pz}}(\mathbf{x}_o^B)$. Further, in contrast to Event-1, in this case, the knowledge of r_o^B does not convey any information regarding the distribution of $R_{o,AB}$. Hence, R_o^B is independent of $R_{o,AB}$.

Taking both the events into account, the CDF of $R_{o,AB}$ conditioned on the distance to

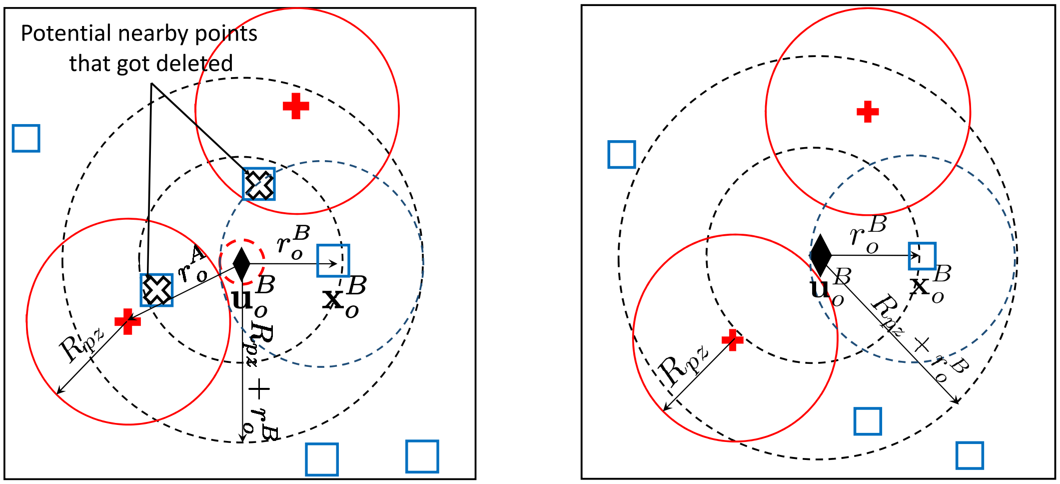

(a) An Illustration of Event-1 (b) An Illustration of Event-2

Figure 8.5: The diamond, crosses, and squares represent the locations of the typical OpB user, OpA BSs, and OpB BSs, respectively. The location of the typical user is $\mathbf{u}_o^B = (0,0)$ and the tagged OpB BS is $\mathbf{x}_o^B = (r_o^B, 0)$.

the tagged BS R_o^B is given in (8.22) is given as

$$
\begin{aligned}
F_{R_{o,AB}}(r_{o,AB}|r_o^B) =& \mathbb{P}\left[R_{o,AB} \leq r_{o,AB} | r_o^B, N_{\Phi_B}(\mathcal{B}_{r_o^B}(\mathbf{u}_o^B)) = 0\right] \\
=& \mathbb{P}\left[R_{o,AB} \leq r_{o,AB} \middle| r_o^B, N_{\Phi_B}(\mathcal{B}_{r_o^B}(\mathbf{u}_o^B)) = 0, N_{\Psi_B}(\mathcal{B}_{r_o^B}(\mathbf{u}_o^B)) \neq 0\right] \times \\
& \mathbb{P}\left[N_{\Psi_B}(\mathcal{B}_{r_o^B}(\mathbf{u}_o^B)) \neq 0 \middle| N_{\Phi_B}(\mathcal{B}_{r_o^B}(\mathbf{u}_o^B)) = 0, r_o^B\right] \\
& + \mathbb{P}\left[R_{o,AB} \leq r_{o,AB} \middle| r_o^B, N_{\Phi_B}(\mathcal{B}_{r_o^B}(\mathbf{u}_o^B)) = 0, N_{\Psi_B}(\mathcal{B}_{r_o^B}(\mathbf{u}_o^B)) = 0\right] \times \\
& \mathbb{P}\left[N_{\Psi_B}(\mathcal{B}_{r_o^B}(\mathbf{u}_o^B)) = 0 \middle| N_{\Phi_B}(\mathcal{B}_{r_o^B}(\mathbf{u}_o^B)) = 0, r_o^B\right] \\
=& \mathbb{P}\left[R_{o,AB} \leq r_{o,AB} \middle| r_o^B, E_1(r_o^B)\right] \mathbb{P}\left[N_{\Psi_B}(\mathcal{B}_{r_o^B}(\mathbf{u}_o^B)) \neq 0 \middle| N_{\Phi_B}(\mathcal{B}_{r_o^B}(\mathbf{u}_o^B)) = 0, r_o^B\right] \\
& + \mathbb{P}\left[R_{o,AB} \leq r_{o,AB} \middle| r_o^B, E_2(r_o^B)\right] \mathbb{P}\left[N_{\Psi_B}(\mathcal{B}_{r_o^B}(\mathbf{u}_o^B)) = 0 \middle| N_{\Phi_B}(\mathcal{B}_{r_o^B}(\mathbf{u}_o^B)) = 0, r_o^B\right],
\end{aligned}
\tag{8.22}
$$

where $N_{\Phi_B}(\mathcal{B}_{r_o^B}(\mathbf{u}_o^B))$ and $N_{\Psi_B}(\mathcal{B}_{r_o^B}(\mathbf{u}_o^B))$ represent the number of points of Φ_B and Ψ_B in $\mathcal{B}_{r_o^B}(\mathbf{u}_o^B)$, respectively. Further, $E_1(r_o^B)$ represents $\{N_{\Phi_B}(\mathcal{B}_{r_o^B}(\mathbf{u}_o^B)) = 0, N_{\Psi_B}(\mathcal{B}_{r_o^B}(\mathbf{u}_o^B)) \neq 0\}$ and $E_2(r_o^B)$ represents $\{N_{\Phi_B}(\mathcal{B}_{r_o^B}(\mathbf{u}_o^B)) = 0, N_{\Psi_B}(\mathcal{B}_{r_o^B}(\mathbf{u}_o^B)) = 0\}$.

While the CDF of $R_{o,AB}$ conditioned on Event-1 and Event-2, can be obtained in different ways, in our case, we first condition on the distance R_o^A between the typical user to its nearest

OpA BS and then obtain the CDF expression. Hence, (8.22) can be further expanded as

$$\begin{aligned}
&\mathbb{P}\left[R_{o,AB} \leq r_{o,AB} | r_o^B, N_{\Phi_B}(\mathcal{B}_{r_o^B}(\mathbf{u}_o^B)) = 0\right] \\
&= \int_{r_o^A=0}^{\infty} \underbrace{\mathbb{P}\left[R_{o,AB} \leq r_{o,AB} | r_o^A, r_o^B, E_1(r_o^B)\right]}_{K_1} f_{R_o^A}(r_o^A | r_o^B, E_1(r_o^B)) \mathrm{d}r_o^A \\
&\mathbb{P}\left[N_{\Psi_B}(\mathcal{B}_{r_o^B}(\mathbf{u}_o^B)) \neq 0 \middle| N_{\Phi_B}(\mathcal{B}_{r_o^B}(\mathbf{u}_o^B)) = 0, r_o^B\right] + \\
&\int_{r_o^A=0}^{\infty} \underbrace{\mathbb{P}\left[R_{o,AB} \leq r_{o,AB} | r_o^A, r_o^B, E_2(r_o^B)\right]}_{K_2} f_{R_o^A}(r_o^A | r_o^B, E_2(r_o^B)) \mathrm{d}r_o^A \\
&\mathbb{P}\left[N_{\Psi_B}(\mathcal{B}_{r_o^B}(\mathbf{u}_o^B)) = 0 \middle| N_{\Phi_B}(\mathcal{B}_{r_o^B}(\mathbf{u}_o^B)) = 0, r_o^B\right].
\end{aligned} \tag{8.23}$$

From the above expression it is clear that to obtain the CDF of $R_{o,AB}$ conditioned on R_o^B, we need to compute the expressions for K_1, K_2 and the PDF of R_o^A conditioned on Event-1 and Event-2. It is relatively simple to obtain the expression for K_2 as Ψ_A is a homogeneous PPP of density λ_A beyond $\mathcal{B}_{R_{pz}}(\mathbf{x}_o^B)$. On the other hand, as explained earlier, the conditional CDF of $R_{o,AB}$ given by K_1 is not trivial to obtain as the conditional density of Ψ_A in $\mathcal{B}_{r_o^B+R_{pz}}(\mathbf{u}_o^B) \setminus \mathcal{B}_{R_{pz}}(\mathbf{x}_o^B)$ is difficult to characterize. Hence, for Event-1, we assume Ψ_A to follow homogeneous PPP of density λ_A in $\mathcal{B}_{r_o^B+R_{pz}}(\mathbf{u}_o^B) \setminus \mathcal{B}_{R_{pz}}(\mathbf{x}_o^B)$. In other words, we approximate K_1 by K_2. Therefore, we are now left with the task to obtain the expression for K_2. To do so, consider the following two events:

1. The nearest OpA BS to the typical user is also the nearest OpA BS for the tagged OpB BS. Let $\hat{R}_{o,AB}$ denotes the distance between the OpB tagged BS and the nearest OpA BS to the typical user. An illustration is provided in Fig. 8.6a. Note that the nearest OpA BS to the typical user is located at $\mathbf{x}_o^A$ and there are no BSs in the circle $\mathcal{B}_{\hat{R}_{o,AB}}(\mathbf{x}_o^B)$, where

$$\hat{R}_{o,AB} = \sqrt{(r_o^A)^2 + (r_o^B)^2 - 2r_o^A r_o^B \cos(\Theta_A)}, \tag{8.24}$$

   where Θ_A is the angle between the lines joining the points $\mathbf{x}_o^B, \mathbf{u}_o^B$ and $\mathbf{x}_o^A, \mathbf{u}_o^B$ (refer to Fig. 8.6a for an illustration). Further, the randomness in $\hat{R}_{o,AB}$ is due to Θ_A.

2. The other event of interest is the scenario where the nearest PZ to the tagged BS is different from the nearest PZ to the typical user, i.e. there is at least one BS in $\mathcal{B}_{\hat{R}_{o,AB}}(\mathbf{x}_o^B)$ as illustrated Fig. 8.6b.

Taking into account both the events, we can write

$$R_{o,AB} = \begin{cases} \hat{R}_{o,AB} & N_{\Psi_A}\left(\mathcal{C}_1(\hat{R}_{o,AB})\right) = 0 \\ \tilde{R}_{o,AB} & N_{\Psi_A}\left(\mathcal{C}_1(\hat{R}_{o,AB})\right) \neq 0, \end{cases} \tag{8.25}$$

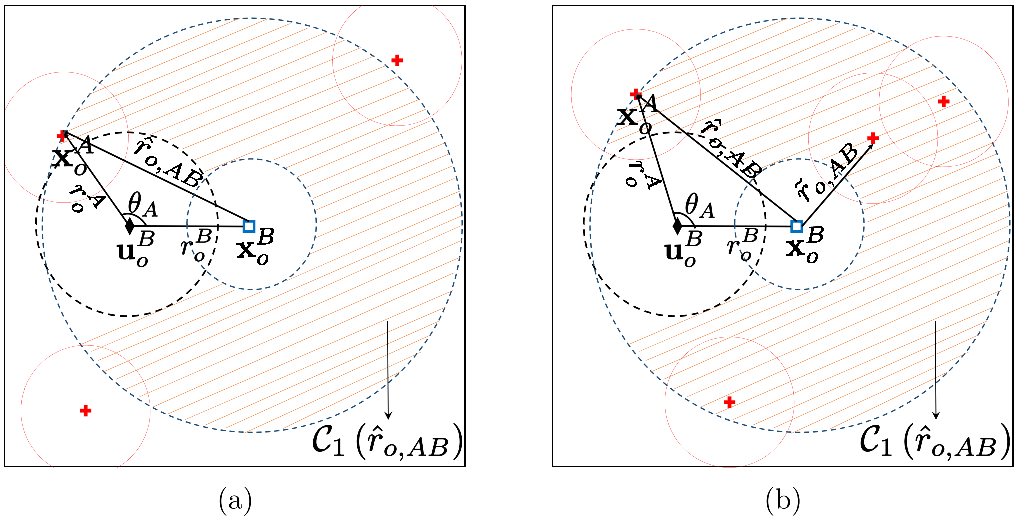

Figure 8.6: The diamond, crosses, and squares represent the locations of the typical OpB user, OpA BSs, and OpB BSs, respectively. The location of the typical user is $\mathbf{u}_o^B = (0,0)$ and the tagged OpB BS is $\mathbf{x}_o^B = (r_o^B, 0)$.

where

$$\mathcal{C}_1(x) = \mathcal{B}_x(\mathbf{x}_o^B) \setminus \left\{\mathcal{B}_{r_o^A}(\mathbf{u}_o^B) \cup \mathcal{B}_{R_{pz}}(\mathbf{x}_o^B)\right\}, \tag{8.26}$$

$\tilde{R}_{o,AB}$ is the distance to the nearest OpA BS that lies in $\mathcal{C}_1(\hat{R}_{o,AB})$, and $N_{\Psi_A}(\mathcal{C})$ denotes the number of points of Ψ_A in the region $\mathcal{C}$. Based on the above discussion, in the following Lemma, we present the expression for K_2, which is the CDF of $R_{o,AB}$ conditioned on the distances R_o^A, R_o^B, and Event-2.

Lemma 8.3. *The CDF of the distance $R_{o,AB}$ conditioned on distances R_o^A, R_o^B, and Event-2 is given as $F_{R_{o,AB}}(r_{o,AB}|r_o^A, r_o^B, E_2(r_o^B)) =$*

$$\mathbb{P}\left[R_{o,AB} \leq r_{o,AB}\middle| r_o^A, r_o^B, E_2(r_o^B)\right] = 1 - \mathbb{E}_{\Theta_A}\left[\mathbf{1}(\hat{R}_{o,AB} > r_{o,AB}) \exp(-\lambda_A|\mathcal{C}_1(\hat{R}_{o,AB})|)\right], \tag{8.27}$$

where

$$f_{\Theta_A}(\theta_A|r_o^A, r_o^B, E_2(r_o^B)) = \frac{1}{2\varphi_{AB}(r_o^A, r_o^B, R_{pz})}, \quad |\theta_A| \leq \varphi_{AB}(r_o^A, r_o^B, R_{pz}), \tag{8.28}$$

and

$$\varphi_{AB}(r_o^A, r_o^B, R_{pz}) = \begin{cases} \pi & r_o^B - R_{pz} \leq r_o^A, r_o^B \geq R_{pz}, \\ \arccos\left(\frac{R_{pz}^2 - (r_o^A)^2 - (r_o^B)^2}{2r_o^A r_o^B}\right) & r_o^B - R_{pz} < r_o^A \leq r_o^B + R_{pz}, \\ \pi & r_o^B + R_{pz} \leq r_o^A. \end{cases} \tag{8.29}$$

Proof: Please refer to Appendix D.2. ■

Our next objective is to get the conditional density functions of R_o^A presented in (8.23). Hence, in the following Lemma, taking both the events discussed in Section 8.3.1 into account, we derive a lower bound on the CDF of R_o^A conditioned on R_o^B.

Lemma 8.4. *Conditioned on the distance R_o^B between the tagged OpB BS and the typical user, the* CDF *of the distance R_o^A between the typical user and its nearest OpA BS is*

$$F_{R_o^A}(r_o^A|r_o^B) \geq F_{R_o^A}^{\mathtt{LB}}(r_o^A|r_o^B) = \left(1-\exp(-\mathcal{G}(r_o^A,\lambda_A,R_{pz},r_o^B))\right)\frac{\exp(-\pi\lambda_B(r_o^B)^2)}{1-F_{R_o^B}(r_o^B)} + F_{R_o^A}^{\mathtt{LB}}(r_o^A|r_o^B,E_1(r_o^B))\left(1-\frac{\exp(-\pi\lambda_B(r_o^B)^2)}{1-F_{R_o^B}(r_o^B)}\right). \quad (8.30)$$

In the above equation

$$F_{R_o^A}^{\mathtt{LB}}(r_o^A|r_o^B,E_1(r_o^B)) = \begin{cases} 0 & r_o^A+r_o^B \leq R_{pz} \\ \frac{1-\exp(-\lambda_A|\mathcal{C}_2(r_o^A,r_o^B,R_{pz})|)}{1-\exp(-\lambda_A|\mathcal{C}_2(r_o^B+R_{pz},r_o^B,R_{pz})|)} & r_o^A+r_o^B > R_{pz}, \end{cases} \quad (8.31)$$

where $\mathcal{C}_2(r_o^A,r_o^B,R_{pz}) = \mathcal{B}_{r_o^A}(\mathbf{u}_o^B)\setminus\{\mathcal{B}_{r_o^A}(\mathbf{u}_o^B)\cap\mathcal{B}_{R_{pz}}(\mathbf{x}_o^B)\}$. Corresponding PDF *$f_{R_o^A}^{\mathtt{LB}}(r_o^A|r_o^B)$ is obtained by differentiating $F_{R_o^A}^{\mathtt{LB}}(r_o^A|r_o^B)$ w.r.t. r_o^A. $F_{R_o^B}(r_o^B)$ is the* CDF *of the contact distance of PHP.*

Proof: Please refer to Appendix D.3. ■

While above lower bound captures the effect of both Event-1 and Event-2, as we will see later this bound on the CDF of R_o^A results in a relatively loose bound for the CDF of $R_{o,AB}$. Hence, our next objective is to present an accurate approximate expression for R_o^A conditioned on R_o^B. Observe that when the typical user is farther from tagged BS, the average area of overlap between a protection zone (whose center is uniformly distributed over the region $\mathcal{B}_{R_o^B+R_{pz}}(\mathbf{u}_o^B)\setminus\mathcal{B}_{R_{pz}}(\mathbf{x}_o^B))$ and the the circle $\mathcal{B}_{R_o^B}(\mathbf{u}_o^B)$ is relatively small. Hence, the average number of OpA BSs required in $\mathcal{B}_{R_o^B+R_{pz}}(\mathbf{u}_o^B)$ to ensure that all the points of Ψ_B in $\mathcal{B}_{R_o^B}(\mathbf{u}_o^B)$ are deleted is likely to be larger than one. Considering the above observation, in the following Lemma, we present an approximate expression for the CDF of R_o^A conditioned on the distance R_o^B.

Lemma 8.5. *Conditioned on the distance R_o^B between the tagged OpB BS and the typical user, the approximate* CDF *of the distance R_o^A between the typical user and its nearest OpA BS is given as $F_{R_o^A}(r_o^A|r_o^B) =$*

$$\mathbb{P}\left[R_o^A \leq r_o^A | N_{\Phi_B}(\mathcal{B}_{r_o^B}(\mathbf{u}_o^B))=0, r_o^B\right] = 1-\exp(-\mathcal{G}(r_o^A,\lambda_A,R_{pz},r_o^B))\frac{\exp(-\pi\lambda_B(r_o^B)^2)}{1-F_{R_o^B}(r_o^B)} + F_{R_o^A}(r_o^A|r_o^B,E_1(r_o^B))\left(1-\frac{\exp(-\pi\lambda_B(r_o^B)^2)}{1-F_{R_o^B}(r_o^B)}\right), \quad (8.32)$$

where approximate expression is obtained by replacing $F_{R_o^A}(r_o^A|r_o^B, E_1(r_o^B))$ by

$$F_{R_o^A}(r_o^A|r_o^B, E_1(r_o^B)) \approx \begin{cases} 0 & r_o^A + r_o^B \leq R_{pz} \\ \frac{1-\exp(-\lambda_A\pi((r_o^A)^2-(R_{pz}-r_o^B)^2))}{1-\exp(-\lambda_A\pi((R_{pz}+r_o^B)^2-(R_{pz}-r_o^B)^2))} & r_o^B \leq R_{pz}/2, R_{pz}-r_o^B < r_o^A \leq R_{pz}+r_o^B \\ \frac{1-\exp\left(-\lambda_A\pi\left((r_o^A)^2-\max(0,R_{pz}-r_o^B)^2\right)\right)}{1-\exp(-\lambda_A\pi((r_o^B)^2-\max(0,R_{pz}-r_o^B)^2))} & R_{pz}/2 < r_o^B, \max(0, R_{pz}-r_o^B) < r_o^A \leq r_o^B. \end{cases} \tag{8.33}$$

Corresponding conditional PDF *of R_o^A is*

$$f_{R_o^A}(r_o^A|r_o^B) = f_{R_o^A}(r_o^A|r_o^B, E_2(r_o^B))\frac{\exp(-\pi\lambda_B(r_o^B)^2)}{1-F_{R_o^B}(r_o^B)} + f_{R_o^A}(r_o^A|r_o^B, E_1(r_o^B))\left(1 - \frac{\exp(-\pi\lambda_B(r_o^B)^2)}{1-F_{R_o^B}(r_o^B)}\right), \tag{8.34}$$

where

$$f_{R_o^A}(r_o^A|r_o^B, E_2(r_o^B)) = 2\pi\mathcal{E}(r_o^A, \lambda_A, R_{pz}, r_o^B)r_o^A\exp(-\mathcal{G}(r_o^A, \lambda_A, R_{pz}, r_o^B)). \tag{8.35}$$

The approximate expression for the PDF *is obtained by replacing $f_{R_o^A}(r_o^A|r_o^B, E_1(r_o^B))$ by the derivative of $F_{R_o^A}(r_o^A|r_o^B, E_1(r_o^B))$ in (8.33). Further, the complementary* CDF *of R_o^B in the denominator is replaced by the approximate expression in (D.12). The expressions for $\mathcal{E}(r_o^A, \lambda_A, R_{pz}, r_o^B)$ and $\mathcal{G}(r_o^A, \lambda_A, R_{pz}, r_o^B)$ were presented in Lemma 8.1.*

Proof: Please refer to Appendix D.4. ■

In the following Lemma, using Lemmas 8.3 and 8.4, we derive a lower bound for the CDF of $R_{o,AB}$.

Lemma 8.6. *The* CDF *of the distance $R_{o,AB}$ between the tagged BS and its nearest OpA BS is lower bounded by*

$$F_{R_{o,AB}}(r_{o,AB}) \geq F^{(\mathtt{LB},1)}_{R_{o,AB}}(r_{o,AB}) = \int_0^\infty\int_0^\infty F_{R_{o,AB}}(r_{o,AB}|r_o^A, r_o^B, E_2(r_o^B))f^{\mathtt{LB}}_{R_o^A}(r_o^A|r_o^B)f_{R_o^B}(r_o^B)\mathrm{d}r_o^A\,\mathrm{d}r_o^B, \tag{8.36}$$

where $F_{R_{o,AB}}(r_{o,AB}|r_o^A, r_o^B, E_2(r_o^B))$ is given by (8.27), $f^{\mathtt{LB}}_{R_o^A}(r_o^A|r_o^B)$ is obtained by differentiating $F^{\mathtt{LB}}_{R_o^A}(r_o^A|r_o^B)$ w.r.t. r_o^A presented in Lemma 8.4, and $f_{R_o^B}(r_o^B)$ is the PDF *of the contact distance distribution of PHP.*

Note that accurate evaluation of the above lower bound requires the exact expression for the CDF of R_o^B. Now, using Lemmas 8.3, and 8.5, we derive an approximate expression for the CDF of $R_{o,AB}$, which is presented next.

Lemma 8.7. *The* CDF *of the distance* $R_{o,AB}$ *conditioned on* R_o^B *is given as*

$$F_{R_{o,AB}}(r_{o,AB}|r_o^B) \approx \int_{r_o^A=0}^{\infty} F_{R_{o,AB}}(r_{o,AB}|r_o^A, r_o^B, E_2(r_o^B)) f_{R_o^A}(r_o^A|r_o^B)\, \mathrm{d}r_o^A, \tag{8.37}$$

where $F_{R_{o,AB}}(r_{o,AB}|r_o^A, r_o^B, E_2(r_o^B))$ *is given by* (8.27) *and* $f_{R_o^A}(r_o^A|r_o^B)$ *is given by* (8.34).

The marginal distribution of $R_{o,AB}$ can be obtained by deconditioning the above expression w.r.t. R_o^B whose PDF can be approximated as Weibull distribution (Refer to Section 2.2).

The expressions for lower bound and approximate CDF presented in (8.36) and (8.37) are not in closed form and require a fair amount of computational resource for evaluation. In the following Lemma, considering only Event-2 discussed in Section 8.3.1, we present another lower bound on the CDF of $R_{o,AB}$ that assumes a closed form expression.

Lemma 8.8. *The lower bound on the* CDF *of the distance* $R_{o,AB}$ *between the tagged OpB BS and its nearest OpA BS is*

$$F_{R_{o,AB}}(r_{o,AB}) \geq F^{(\mathtt{LB},2)}_{R_{o,AB}}(r_{o,AB}) = 1 - \exp\left(-\pi\lambda_A((r_{o,AB})^2 - R_{pz}^2)\right),$$

which is a truncated Rayleigh distribution.

Proof: Please refer to Appendix D.5. ∎

Approximate and lower bound expressions for the MAP of the tagged BS

Based on the distance distributions of $R_{o,AB}$ presented in the previous subsection, in this subsection, we present lower bound and approximated expressions for the MAP of the tagged BS.

First, using the approximate conditional CDF of $R_{o,AB}$ presented in Lemma 8.7, we derive an approximate expression for the MAP of the tagged BS, which is presented in the following Lemma.

Lemma 8.9. *The* MAP *of the tagged OpB BS located at* $\mathbf{x}_o^B \in \Phi_B$ *is given as*

$$\mathcal{M}_o^B = \mathbb{P}\left[\mathcal{I}_o^B = 1\right] \approx \int_{r_o^B=0}^{\infty} \mathrm{d}r_o^B \int_{r_o^A=0}^{\infty} \mathrm{d}r_o^A \int_{r_{o,AB}=R_{pz}}^{\infty} \frac{1 - e^{-f_1(r_{o,AB}, r_o^B)}}{f_1(r_{o,AB}, r_o^B)} \times \mathrm{d}F_{R_{o,AB}}(r_{o,AB}|r_o^A, r_o^B, E_2(r_o^B)) f_{R_o^A}(r_o^A|r_o^B) f_{R_o^B}(r_o^B), \tag{8.38}$$

where $F_{R_{o,AB}}(r_{o,AB}|r_o^A, r_o^B, E_2(r_o^B))$ *is given by* (8.27), $f_{R_o^A}(r_o^A|r_o^B)$ *is given by* (8.34), *and* $f_{R_o^B}(r_o^B)$ *is given in* (8.4).

Proof: The proof follows from deconditioning (8.20) in Lemma 8.2 w.r.t. $R_{o,AB}$ and R_o^B. Above expression for the MAP can be evaluated using numerical integration technique such as Monte-Carlo integration. ∎

Now, instead of the approximate expression, if we consider any of the lower bound expressions on the CDF to decondition the MAP in (8.20), then we obtain a lower bound on the MAP of the tagged BS. Intuitively this is justified as follows: considering a lower bound on the CDF of the distance implies that on an average, the distance to the nearest PZ center is relatively larger than the actual distance. As a result, in the contention domain of the tagged BS, relatively closer points in Ψ_B are considered during the evaluation of MAP. Based on this observation, in the following Lemma, we present a lower bound expression for the MAP of the tagged BS.

Lemma 8.10. *A lower bound on the* MAP *of the tagged OpB BS located at* $\mathbf{x}_0^B \in \Phi_B$ *is given as*

$$\mathcal{M}_o^B = \mathbb{P}\left[\mathcal{I}_o^B = 1\right] \geq \int\limits_{r_o^B=0}^{\infty} \int\limits_{r_{o,AB}=R_{pz}}^{\infty} \frac{1-\exp(-f_1(r_{o,AB}, r_o^B))}{f_1(r_{o,AB}, r_o^B)} \mathrm{d}F_{R_{o,AB}}^{(\mathtt{LB,x})}(r_{o,AB}) f_{R_o^B}(r_o^B) \mathrm{d}r_o^B, \tag{8.39}$$

where $f_{R_o^B}$ *is the* PDF *of the contact distance of PHP. Above expression can be evaluated using either of the lower bound expressions for the* CDF *of* $R_{o,AB}$ *presented in Lemmas 8.6 and 8.8.*

Proof: Please refer to Appendix D.6. ∎

In Fig. 8.7, the CDFs of $R_{o,AB}$ obtained from Lemmas 8.6, 8.8, and 8.7 are compared with simulation results for two different combinations of λ_A and λ_B. Note that to obtain the lower bound on the CDF of $R_{o,AB}$ using Lemma 8.6, we need the exact CDF of R_o^B in (8.30). As mentioned earlier, due to unavailability the exact expression for the CDF, we have used the approximated cumulative CDF of R_o^B given in (D.12). On the other hand, since the density of OpA BS λ_A is fixed in both the cases, the lower bounds obtained using Lemma 8.8 are the same irrespective of the value of λ_B. The results on the tightness of the lower bounds and accuracy of the approximated MAP expression are presented in Section 8.6.

8.4 Coverage probability for a typical OpB user

Due to the consideration of Rayleigh fading, the small-scale channel gain in the desired link follows exponential distribution. Hence, the coverage probability of the typical user can be readily expressed in terms of the LT of aggregate interference [12]. However, in this case, *exact* characterization of the LT of aggregate interference is not trivial because of the following reasons:

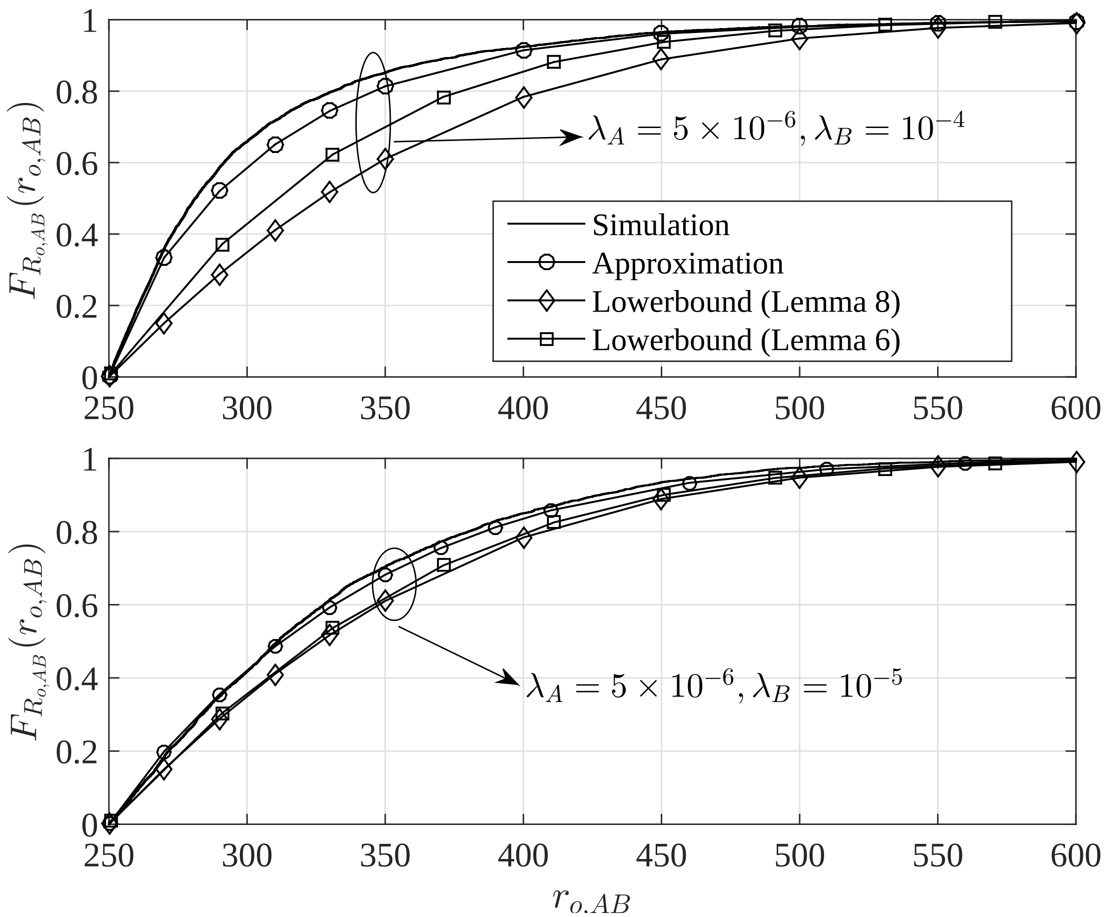

Figure 8.7: CDF of the distance between the tagged BS and its nearest OpA BS.

1. Based on our discussion in Section 8.3.1, conditioned on the distance between the tagged BS and the typical user, characterizing the distance distribution between the typical user and its nearest OpA interfering BS is not trivial.

2. Due to the presence of PZs around each OpA BS, there is dependency in the locations of OpA and OpB BSs. This dependency leads to correlation in the interference power perceived at the typical user from both sets of BSs. In addition, characterizing the interference contribution from OpB BSs while taking the PZs into account is not trivial.

3. Conditioned on the event that the tagged BS is always active, the MAP of the interfering OpB BSs in Φ_B gets affected, i.e. any OpB BS in the contention domain of the tagged OpB BS remains inactive, which affects the interference field.

Circumventing the above problems, we provide fairly accurate expression for the LT of interference using the following steps:

1. Note that in the previous section, we have already addressed the first problem. In Lemma 8.5, we have presented an approximate expression for the CDF of the R_o^A conditioned on R_o^B.

2. To capture the correlation in the interference powers from the BSs in the vicinity of the typical user, we determine the density of interfering OpA BSs conditioned on R_o^B and R_o^A (Refer to Lemma 8.11). Further, we approximate the PHP Φ_B by a non-homogeneous PPP conditioned on R_o^A and R_o^B (Refer to Lemma 8.12).

3. We obtain the MAP of an interfering OpB BS conditioned on the event that the tagged OpB BS is active (Refer to Lemma 8.13). This conditional MAP provides the retention probability of an interfering BS in Φ_B.

A flow diagram of the above sequence of steps is presented in Fig. 8.8.

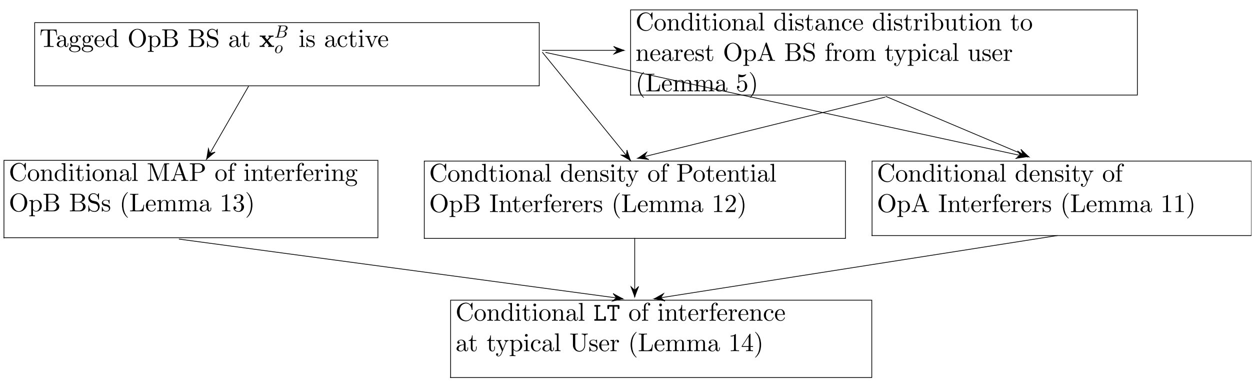

Figure 8.8: Sequence of steps to obtain the LT of aggregate interference at the typical OpB user conditioned on the distance to the tagged BS and the nearest OpA interfering user.

Conditional density of interfering OpA BSs

As per the assumption made in the system model, the locations of the interfering OpA BSs follow a homogeneous PPP of density λ_A. However, due to the presence of exclusion zone $\mathcal{B}_{R_{pz}}(\mathbf{x}_o^B)$, the density of OpA BS is zero in $\mathcal{B}_{R_{pz}}(\mathbf{x}_o^B)$. As mentioned in Section 8.3.1, conditioned on the distance R_o^B, the density of OpA BSs in the vicinity of the typical user is dictated by both Event-1 and Event-2. Since characterizing the density of Ψ_A conditioned on Event-1 is difficult, we only take into account Event-2 to obtain the density of Ψ_A. In the following Lemma, we present this conditional density of interfering OpA BSs.

Lemma 8.11. *Conditioned on the distances R_o^B and R_o^A, Ψ_A is characterized as a non-homogeneous PPP with the density function*

$$\tilde{\lambda}_{\Psi_A}(x|r_o^B, r_o^A) = \mathcal{E}(x, \lambda_A, R_{pz}, r_o^B)\mathbf{1}(x > r_o^A) \tag{8.40}$$

where $\mathcal{E}$ is given by (8.18) in Lemma 8.1.

Proof: Let $\mathbf{x}_o^B$ be the location of the tagged BS and $r_o^B = \|\mathbf{x}_o^B\|$. Since the tagged OpB BS is active, there are no interfering OpA BSs in $\mathcal{B}_{R_{pz}}(\mathbf{x}_o^B)$, i.e. $\mathcal{B}_{R_{pz}}(\mathbf{x}_o^B)$ is a hole in the PPP Ψ_A (See Fig. 8.9a). Hence, the density function given in (8.40) follows directly from the application of Lemma 8.1 and the fact that all the interfering BSs are at a distance greater than r_o^A from the typical user. ■

In Section 8.6, we verify through Monte Carlo simulations that the effect of above approximation is negligible on the coverage probability result. Note that the aggregate interference is dictated by the most dominant interference term (cf. [137] for a simulation based verification). In this case, the interference contribution from the nearest OpA BS, which is likely to be the most dominant interferer, is captured reasonably accurately. This leads to fairly accurate approximation of total interference from the OpA BSs.

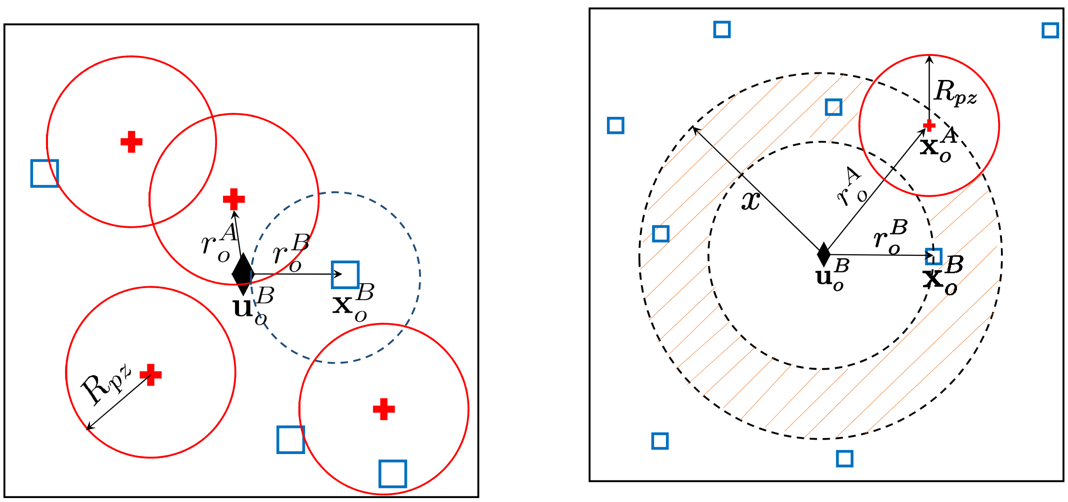

(a) An illustration for Lemma 8.11.

(b) A representative diagram for Lemma 8.12.

Figure 8.9: The diamond, crosses, and squares represent the locations of the typical OpB user, OpA BSs, and OpB BSs, respectively. The location of the typical user is $\mathbf{u}_o^B = (0, 0)$ and the tagged OpB BS is $\mathbf{x}_o^B = (r_o^B, 0)$.

Approximation of Φ_B as a non-homogeneous PPP

As discussed earlier, since the `PGFL` of a PHP is not known, characterizing the `LT` of aggregate interference from the BSs in Φ_B is not trivial. Hence, we approximate the PHP Φ_B by a non-homogeneous PPP. First, we consider the parent PPP Ψ_B and determine its density function taking into account the nearest PZ to the typical user [142]. Then, to capture the effect of rest of the PZs in the network, we introduce independent thinning of points in Ψ_B beyond the nearest OpA BS. Based on the above discussion, conditioned on R_o^A and R_o^B, we characterize the density of Φ_B, which is presented next.

Lemma 8.12. *Conditioned on the distances R_o^A and R_o^B, we approximate Φ_B as a non-homogeneous PPP with piece-wise density function given as*

$$\tilde{\lambda}_{\Psi_B}(x|r_o^A, r_o^B)\frac{1}{2\pi x}\frac{\mathrm{d}\Lambda_{\Psi_B}\left(\mathcal{B}_x(\mathbf{o})|r_o^A, r_o^B\right)}{\mathrm{d}x}\exp(-\pi\lambda_A R_{pz}^2\mathbf{1}(x \geq r_o^A)), \tag{8.41}$$

where $\Lambda_{\Psi_B}\left(\mathcal{B}_x(\mathbf{o})|r_o^A, r_o^B\right) = \mathcal{H}(x, r_o^A, r_o^B, R_{pz})$ is the conditional intensity measure of the PPP Ψ_B and $\mathcal{H}(x, r_o^A, r_o^B, R_{pz}) =$

$$\begin{cases} \lambda_B\pi(x^2 - (r_o^B)^2) & r_o^A + R_{pz} < r_o^B \\ \lambda_B(\pi(x^2 - (r_o^B)^2) - A(x, R_{pz}, r_o^A) + A(r_o^B, R_{pz}, r_o^A)) & r_o^B - R_{pz} < r_o^A < r_o^B + R_{pz}, r_o^B \leq x \leq r_o^A + R_{pz} \\ \lambda_B\pi(x^2 - (r_o^B)^2 - R_{pz}^2 + \frac{A(r_o^B, R_{pz}, r_o^A)}{\pi}) & r_o^B - R_{pz} < r_o^A < r_o^B + R_{pz}, x \geq r_o^A + R_{pz} \\ \lambda_B\pi(x^2 - (r_o^B)^2) & r_o^A > r_o^B + R_{pz}, x < r_o^A - R_{pz} \\ \lambda_B\pi(x^2 - ((r_o^B)^2 + \frac{A(x, R_{pz}, r_o^A)}{\pi})) & r_o^A > r_o^B + R_{pz}, r_o^A - R_{pz} \leq x \leq r_o^A + R_{pz} \\ \lambda_B\pi(x^2 - (r_o^B)^2 - R_{pz}^2) & r_o^A > r_o^B + R_{pz}, x > r_o^A + R_{pz}, \end{cases} \tag{8.42}$$

where $A(r, R, d)$ is defined in (8.17) and $x > r_o^B$.

Proof: Let $\mathbf{x}_o^A \in \Psi_A$ and $\mathbf{x}_o^B \in \Phi_B$ be the locations of the nearest OpA BS to the typical user and the tagged OpB BS, respectively. Further, $r_o^A = \|\mathbf{x}_o^A\|$ and $r_o^B = \|\mathbf{x}_o^B\|$. This Lemma can be proved in two steps. In the first step, we consider the baseline PPP Ψ_B from which Φ_B is obtained. Considering only the nearest PZ and the distance to the tagged BS, the conditional intensity measure of Ψ_B is the average number of points in the region

$$\mathcal{C}_3(x, \mathbf{x}_o^B, \mathbf{x}_o^A, R_{pz}) = \mathcal{B}_x(\mathbf{u}_o^B) \setminus \{\mathcal{B}_{r_o^B}(\mathbf{u}_o^B) \cup \mathcal{B}_{R_{pz}}(\mathbf{x}_o^A), \tag{8.43}$$

which is illustrated as the shaded region in Fig. 8.9b. Hence, the conditional intensity measure of Ψ_B is given as

$$\Lambda_{\Psi_B}\left(\mathcal{B}_x(\mathbf{o})|r_o^A, r_o^B\right) = \lambda_B|\mathcal{C}_3(x, \mathbf{x}_o^B, \mathbf{x}_o^A, R_{pz})|, \tag{8.44}$$

where $|\mathcal{C}|$ denotes the area of the region $\mathcal{C}$. $\mathbf{u}_o^B$ and $\mathbf{o}$ are interchangeably used as it is assumed that the typical user is located at the origin. Depending on the relative distances r_o^A, r_o^B, and x, the conditional intensity measure is a piece-wise function given in (8.42). Now, the corresponding conditional density function of Ψ_B is

$$\lambda_{\Psi_B}(x|r_o^A, r_o^B) = \frac{1}{2\pi x}\frac{\mathrm{d}\Lambda_{\Psi_B}\left(\mathcal{B}_x(\mathbf{o})|r_o^A, r_o^B\right)}{\mathrm{d}x}. \tag{8.45}$$

In the second step, to account for the rest of the PZs in the network, independent thinning of the BS locations in Ψ_A beyond the nearest OpA BS is performed. Combining both the steps, we get the conditional density function of Φ_B in (8.41). ∎

Conditional MAP of the interfering OpB BSs

Except the tagged BS, each BS in Φ_B acts as a potential interfering BS, but only those BSs who win contention w.r.t. other OpB BSs in Φ_B will actually interfere. However, this contention process is conditioned on the event that the tagged OpB BS is always active. In the following Lemma, we derive the conditional MAP of an interfering BS located at $\mathbf{x}_i^B \in \Phi_B$.

Lemma 8.13. *Conditioned on the events that the tagged OpB BS at $\mathbf{x}_o^B = (r_o^B, 0)$ is active, the conditional MAP of an interfering OpB BS located at $\mathbf{x}_i^B = (\|\mathbf{x}_i^B\| \cos(\theta_{x_i^B}), \|\mathbf{x}_i^B\| \sin(\theta_{x_i^B})) \in \Phi_B$ is given as $M(\mathbf{x}_i^B | r_o^B) =$*

$$\frac{f_3(r_o^B, \mathbf{x}_o^B)}{1 - e^{-f_3(r_o^B, \mathbf{x}_o^B)}} \left[\frac{1 - e^{-f_3(r_o^B, \mathbf{x}_i^B)}}{f_3(r_o^B, \mathbf{x}_i^B)} - \frac{1 - e^{-f_4(r_o^B, \mathbf{x}_i^B)}}{f_4(r_o^B, \mathbf{x}_i^B)}\right] \frac{2\left(1 - \exp\left(-\frac{\tau_{cs} l(\|\mathbf{x}_o^B - \mathbf{x}_i^B\|)}{P_B}\right)\right)}{(f_4(r_o^B, \mathbf{x}_i^B) - f_3(r_o^B, \mathbf{x}_i^B))}, \tag{8.46}$$

where

$$f_3(r_o^B, \mathbf{x}_i^B) = \int_{x=r_0^B}^{\infty} \int_{\theta_x=0}^{2\pi} \lambda_B e^{-\frac{\tau_{cs} l\left(\sqrt{x^2 + \|\mathbf{x}_i^B\|^2 - 2x\|\mathbf{x}_i^B\| \cos(\theta_x - \theta_{x_i^B})}\right)}{P_B}} x \mathrm{d}x, \tag{8.47}$$

and

$$\begin{aligned} f_4(r_o^B, \mathbf{x}_i^B) = \int_{x=r_o^B}^{\infty} \int_{\theta_x=0}^{2\pi} \lambda_B \Bigg(1 - \Bigg(1 - e^{-\frac{\tau_{cs} l\left(\sqrt{x^2 + (r_o^B)^2 - 2x r_o^B \cos(\theta_x)}\right)}{P_B}}\Bigg) \\ \times \Bigg(1 - e^{-\frac{\tau_{cs} l\left(\sqrt{x^2 + \|\mathbf{x}_i^B\|^2 - 2x\|\mathbf{x}_i^B\| \cos(\theta_x - \theta_{x_i^B})}\right)}{P_B}}\Bigg)\Bigg) x \mathrm{d}x. \end{aligned} \tag{8.48}$$

Proof: This proof follows on the same lines as that of [43, Proposition 2]. Here, we provide a brief sketch. The main assumption that we have made in this case is to ignore the effect of all the PZs. Let $\mathcal{I}_o^B$ and $\mathcal{I}_j^B$ be the medium access indicators of the tagged BS and the OpB BS located at $\mathbf{x}_j^B$. Now,

$$\mathbb{P}\left[\mathcal{I}_j^B = 1 \middle| \mathcal{I}_o^B = 1, r_o^B\right] = \frac{\mathbb{P}\left[\mathcal{I}_j^B = 1, \mathcal{I}_o^B = 1 \middle| r_o^B\right]}{\mathbb{P}\left[\mathcal{I}_o^B = 1 \middle| r_o^B\right]}. \tag{8.49}$$

From [43, Proposition 2], $\mathbb{P}\left[\mathcal{I}_j^B = 1, \mathcal{I}_o^B = 1 \middle| r_o^B\right] =$

$$\left[\frac{1 - \exp(-f_3(r_o^B, \mathbf{x}_i^B))}{f_3(r_o^B, \mathbf{x}_i^B)} - \frac{1 - \exp(-f_4(r_o^B, \mathbf{x}_i^B))}{f_4(r_o^B, \mathbf{x}_i^B)}\right] \frac{2\left(1 - \exp\left(-\frac{\tau_{cs} l(\|\mathbf{x}_o^B - \mathbf{x}_i^B\|)}{P_B}\right)\right)}{(f_4(r_o^B, \mathbf{x}_i^B) - f_3(r_o^B, \mathbf{x}_i^B))}, \tag{8.50}$$

and

$$\mathbb{P}\left[\mathcal{I}_o^B = 1 \middle| r_o^B\right] = \frac{1 - \exp(-f_3(r_o^B, \mathbf{x}_o^B))}{f_3(r_o^B, \mathbf{x}_o^B)}. \tag{8.51}$$

Replacing (8.50) and (8.51) in (8.49), we obtain $M(\mathbf{x}_i^B | r_o^B)$ presented in the Lemma. ■

8.4.1 LT of interference and coverage probability

Using Lemmas 8.11, 8.12, and 8.13, we derive the LT of interference at the typical OpB user conditioned on its distance to the tagged OpB BS and the nearest OpA BS.

Lemma 8.14. *The approximate* LT *of aggregate interference at the typical user conditioned on the distances R_o^A and R_o^B is given as*

$$\mathcal{L}_{I_{agg}^B}(s|r_o^A, r_o^B, \mathcal{I}_o^B = 1) = \mathcal{L}_{I_{agg}^{BA}}(s|r_o^A, r_o^B)\mathcal{L}_{I_{agg}^{BB}}(s|r_o^A, r_o^B, \mathcal{I}_o^B = 1), \tag{8.52}$$

where I_{agg}^{BA} and I_{agg}^{BB} represent the total interference at the OpB typical user from the OpA and OpB BSs, respectively. In the above equation,

$$\mathcal{L}_{I_{agg}^{BB}}(s|r_o^A, r_o^B, \mathcal{I}_o^B = 1) = \exp\Bigg(-\int_{x=r_o^B}^{\infty}\int_{\theta=0}^{2\pi}\frac{\tilde{\lambda}_{\Psi_B}(x|r_o^A, r_o^B)M(\mathbf{x}(x,\theta)|r_o^B)}{l(x)(sP_B)^{-1}+1}\mathrm{d}\theta x\mathrm{d}x\Bigg), \tag{8.53}$$

and

$$\mathcal{L}_{I_{agg}^{BA}}(s|r_o^A, r_o^B) = \frac{1}{1+\frac{sP_A}{l(r_o^A)}}\exp\Bigg(-2\pi\int_{y=r_o^A}^{\infty}\frac{\tilde{\lambda}_{\Psi_A}(y|r_o^A, r_o^B)}{l(y)(sP_A)^{-1}+1}y\mathrm{d}y\Bigg). \tag{8.54}$$

Proof: Please refer to Appendix D.7. ■

Next, using the LT of interference, we derive the SIR coverage probability for a typical OpB user in the following Proposition.

Proposition 8.15. *The* SIR *coverage probability for a typical OpB user at the origin is given as*

$$\mathtt{P}_{\mathtt{c}}^{(\mathtt{B})}(T) = \int_{r_o^B=0}^{\infty}\int_{r_o^A=0}^{\infty}\mathcal{L}_{I_{agg}^B}\left(\frac{Tl(r_o^B)}{P_B}\Bigg|r_o^A, r_o^B, \mathcal{I}_o^B = 1\right)f_{R_o^A}(r_o^A|r_o^B)f_{R_o^B}(r_o^B)\mathrm{d}r_o^A\mathrm{d}r_o^B, \tag{8.55}$$

where the $f_{R_o^B}(r_o^B)$ and $f_{R_o^A}(r_o^A|r_o^B)$ are given by (8.4) and (8.34), respectively.

Proof: Conditioned on the distances R_o^A and R_o^B, the SIR coverage probability is given as

$$\begin{aligned}
&\mathbb{P}\left[\frac{P_B h}{l(r_o^B) I_{agg}^B} > T \middle| r_o^A, r_o^B, \mathcal{I}_o^B = 1\right] \\
=&\mathbb{P}\left[h > \frac{T l(r_o^B) I_{agg}^B}{P_B} \middle| r_o^A, r_o^B, \mathcal{I}_o^B = 1\right] \\
=&\mathbb{E}\left[\exp\left(-\frac{T l(r_o^B) I_{agg}^B}{P_B}\right) \middle| r_o^A, r_o^B, \mathcal{I}_o^B = 1\right] \\
=&\mathcal{L}_{I_{agg}^B}\left(\frac{T l(r_o^B)}{P_B} \middle| r_o^A, r_o^B, \mathcal{I}_o^B = 1\right),
\end{aligned} \tag{8.56}$$

where the last step follows from the definition of the LT. The expression for the LT is presented in Lemma 8.14. Since the expression only depends on the distances R_o^B and R_o^A, the final coverage probability expression is obtained by deconditioning the LT using joint distribution of R_o^A and R_o^B. ■

8.5 Coverage probability for a typical OpA user

In this section, we present the coverage probability expression for a typical OpA user, who is served by the nearest OpA BS (the tagged OpA BS). Similar to the approach followed in the previous section, we capture the correlation in the interference powers from OpA and OpB BSs in the vicinity of the typical user. In addition, we evaluate the LT of interference from OpB BSs following the similar method as described in the previous section. Most of the theoretical expressions presented in this section such as conditional density of interferers can be proved on the similar lines of the proofs presented in the previous section. Hence, to avoid repetitions, instead of providing detailed proofs we just present proof sketches.

Approximation of Φ_B as a non-homogeneous PPP

To begin with, in the following Lemma, we approximate the PHP Φ_B by a non-homogeneous PPP and derive its density function conditioned on the distance between the typical OpA user and the tagged OpA BS.

Lemma 8.16. *Conditioned on the serving distance R_o^A between the typical user and the tagged OpA BS, Φ_B is approximated as a non-homogeneous PPP with density function*

$$\tilde{\lambda}_{\Psi_B}(x|r_o^A) = \frac{1}{2\pi x}\frac{\mathrm{d}\Lambda_{\Psi_B}\left(\mathcal{B}_x(\mathbf{o})|r_o^A\right)}{\mathrm{d}x}\exp(-\pi\lambda_A R_{pz}^2 \mathbf{1}(x \geq r_o^A)), \tag{8.57}$$

where $\Lambda_{\Psi_B}\left(\mathcal{B}_x(\mathbf{o})|r_o^A\right) = \mathcal{G}(x, \lambda_B, R_{pz}, r_o^A)$ is the conditional intensity measure of the PPP Ψ_B and $\mathcal{G}$ is defined in Lemma 8.1.

Proof: Proof of this Lemma can be done on the similar lines as that of Lemma 8.12. Let the tagged OpA BS is located at $\mathbf{x}_o^A$ and $r_o^A = \|\mathbf{x}_o^A\|$. In the first step, we obtain the intensity measure of Ψ_B conditioned on the location of the nearest PZ $\mathcal{B}_{R_{pz}}(\mathbf{x}_o^A)$ to the typical user (Refer Fig. 8.2a). Since we are considering only the nearest PZ, i.e. $\mathcal{B}_{R_{pz}}(\mathbf{x}_o^A)$, the conditional intensity measure is obtained directly by applying Lemma 8.1 and is given as

$$\Lambda_{\Psi_B}\left(\mathcal{B}_x(\mathbf{o})|r_o^A\right) = \mathcal{G}(x, \lambda_B, R_{pz}, r_o^A). \tag{8.58}$$

Corresponding conditional density function is given as

$$\lambda_{\Psi_B}(x|r_o^A) = \frac{1}{2\pi x}\frac{\mathrm{d}\Lambda_{\Psi_B}\left(\mathcal{B}_x(\mathbf{o})|r_o^A\right)}{\mathrm{d}x} = \mathcal{E}(x, \lambda_B, R_{pz}, r_o^A), \tag{8.59}$$

where $\mathcal{E}$ is defined in Lemma 8.1. In the next step, to account for the rest of the PZs, independent thinning of the points in Ψ_B is performed with retention probability $\exp(-\pi\lambda_A R_{pz}^2)$ beyond the tagged OpA BS, which is at a distance r_o^A from the typical user. ■

Distribution of distance to the nearest active OpB BS

Conditioned on distance R_o^A, we are interested in the statistical characterization of the distance between the typical user and the nearest interfering OpB BS. In Fig. 8.2a, this distance is denoted by d_o^B, which is a realization of the random variable D_o^B. However, obtaining the distribution of D_o^B is not straightforward due to the following reasons:

1. the OpB BSs form a PHP process whose contact distribution is not known, and
2. due to contention based channel access, the nearest OpB BS in the PHP Φ_B to the typical user may not be the nearest active interfering BS.

To derive the distance distribution by exactly considering both the things mentioned above is left as a promising direction for future work. Instead, in the following Lemma, we derive an approximate distance distribution leveraging the conditional density function of Φ_B (in Lemma 8.16) and following the result presented in [144]. Note that, in contrast to our scenario, in [144] the locations of the contending BSs follow a homogeneous PPP.

Lemma 8.17. *Conditioned on the serving distance R_o^A between the typical user and the tagged OpA BS, the* PDF *of the distance D_o^B between the typical user and the nearest active OpB BS is given as*

$$f_{D_o^B}(d_o^B|r_o^A) = 2\pi\tilde{\lambda}_{\Psi_B}(d_o^B|r_o^A)\eta(d_o^B|r_o^A)d_o^B \exp\left(-2\pi\int_{y=0}^{d_o^B}\tilde{\lambda}_{\Psi_B}(y|r_o^A)\eta(y|r_o^A)y\mathrm{d}y\right), \tag{8.60}$$

where $\tilde{\lambda}_{\Psi_B}(y|r_o^A)$ *is defined in Lemma 8.16,* $\eta(y|r_o^A)$ *is the probability that a point located at a distance* y *from the typical user wins contention, which is given as*

$$\eta(y|r_o^A) = \frac{1 - \exp(-f_5(y, r_o^A))}{f_5(y, r_o^A)}, \tag{8.61}$$

and

$$f_5(y, r_o^A) = \int_{z=y}^{\infty} \int_{\theta=0}^{2\pi} \tilde{\lambda}_{\Psi_B}(z|r_o^A) \exp\left(\frac{-P_B \tau_{cs}}{l(z^2 + y^2 - 2zy\cos(\theta))}\right) \mathrm{d}\theta y \mathrm{d}y. \tag{8.62}$$

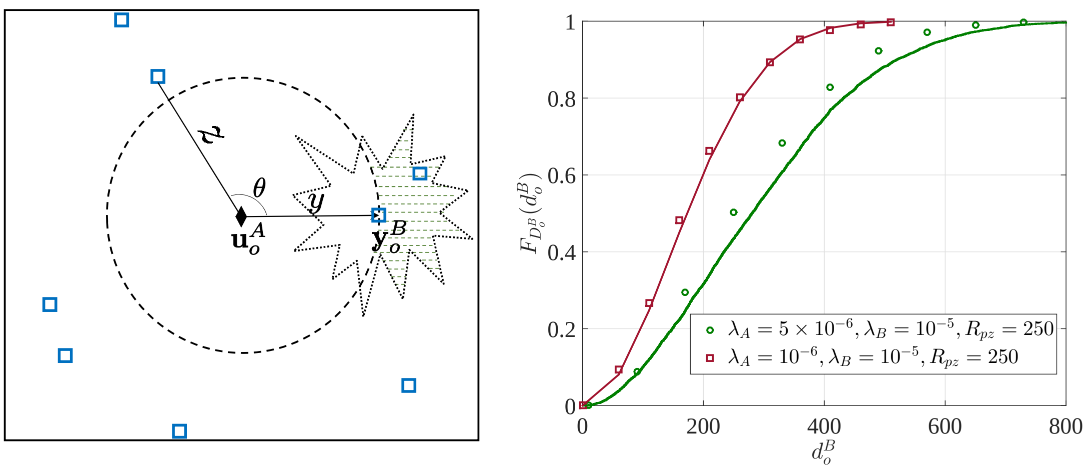

(a) (b)

Figure 8.10: (a) An illustration for Lemma 8.17. The dotted region represents the hypothetical contention domain of the OpB BS at $\mathbf{y}_o^B$. The contention shape is illustrated as irregular due to channel fading. (b) CDF of the distance between the nearest active OpB interferer and the typical user. $R_{pz} = 250$ m, $\tau_{cs} = -80$ dBm/10 MHz. Solid lines and markers represent the simulation and theoretical results, respectively.

Proof: Please refer to Appendix D.8. ■

Although an approximation, above distance distribution is valid for a useful range of system parameters. In Fig. 8.10b, the theoretical CDF of D_o^B is compared with simulation results. The theoretical expression for $F_{D_o^B}(d_o^B)$ is given as

$$F_{D_o^B}(d_o^B) = \int_{r_o^A=0}^{\infty} \int_{z=0}^{d_o^B} f_{D_o^B}(z|r_o^A) f_{R_o^A}(r_o^A) \, \mathrm{d}z \, \mathrm{d}r_o^A. \tag{8.63}$$

The density of interfering OpA BSs

In order to get the LT of the aggregate interference from OpA BSs, we need to take into account the distance to the nearest active OpB BS. In the following Lemma, we derive the density function for the interfering OpA BSs conditioned on R_o^A and D_o^B.

Lemma 8.18. *Conditioned on the distances R_o^A and D_o^B, the piece-wise density function of Ψ_A is given as*

$$\lambda_{\Psi_A}(x|r_o^A, d_o^B) = \frac{1}{2\pi x}\frac{\mathrm{d}\Lambda_{\Psi_A}\left(\mathcal{B}_x(\mathbf{o})|r_o^A, d_o^B\right)}{\mathrm{d}x}, \tag{8.64}$$

where $\Lambda_{\Psi_A}\left(\mathcal{B}_x(\mathbf{o})|r_o^A, d_o^B\right) = \mathcal{H}(x, d_o^B, r_o^A, R_{pz})$ is the conditional intensity measure of the PPP Ψ_A and $\mathcal{H}$ is given by (8.42).

Proof: The proof of this Lemma can be done on the similar lines as that of Lemma 8.12, and is hence skipped. ■

Using the conditional density functions of OpA and OpB BSs, and the distance to the nearest active interfering OpB BS, we present the coverage probability of a typical user served by OpA BS in the following proposition.

Proposition 8.19. *The* SIR *coverage probability for a typical OpA user at the origin is given as*

$$\mathtt{P}_{\mathtt{c}}^{(\mathtt{A})}(T) = \int\limits_{r_o^A=0}^{\infty}\int\limits_{d_o^B=0}^{\infty} \mathcal{L}_{I_{agg}^A}\left(\frac{Tl(r_o^A)}{P_A}\bigg| r_o^A, d_o^B\right) f_{D_o^B}(d_o^B|r_o^A)\mathrm{d}d_o^B f_{R_o^A}(r_o^A)\mathrm{d}r_o^A, \tag{8.65}$$

where the PDF*s $f_{R_o^A}(r_o^A)$ and $f_{D_o^B}(d_o^B|r_o^A)$ are given by (8.3) and (8.60), respectively, and the conditional* LT *of interference at the typical user is given as*

$$\mathcal{L}_{I_{agg}^A}\left(s|r_o^A, d_o^B\right) = \mathcal{L}_{I_{agg}^{AA}}\left(s|r_o^A, d_o^B\right)\mathcal{L}_{I_{agg}^{AB}}\left(s|r_o^A, d_o^B\right). \tag{8.66}$$

In the above equation

$$\mathcal{L}_{I_{agg}^{AA}}\left(s|r_o^A, d_o^B\right) = \exp\left(-2\pi\int_{x=r_o^A}^{\infty}\frac{\lambda_{\Psi_A}(x|r_o^A, d_o^B)}{l(x)(sP_A)^{-1}+1}x\mathrm{d}x\right), \tag{8.67}$$

where $\lambda_{\Psi_A}(x|r_o^A, d_o^B)$ is given in (8.64). Further,

$$\mathcal{L}_{I_{agg}^{AB}}(s|r_o^A, d_o^B) = \frac{1}{1+\frac{sP_B}{l(d_o^B)}}\exp\left(-\int_{x=d_o^B}^{\infty}\int_{\theta=0}^{2\pi}\frac{\tilde{\lambda}_{\Psi_B}(x|r_o^A)M(\mathbf{x}(x,\theta)|d_o^B)}{l(x)(sP_B)^{-1}+1}\mathrm{d}\theta x\mathrm{d}x\right), \tag{8.68}$$

where $\tilde{\lambda}_{\Psi_B}(x|r_o^A)$ is given in (8.57). The expression for $M(\mathbf{x}(x,\theta)|d_o^B)$ is provided in Lemma 8.13.

Proof: This Proposition can be proved on similar line with Lemma 8.14 and Proposition 1. ■

8.6 Results and discussion

In this section, the approximations made in the theoretical results are validated by simulations. Further, the performance analysis of both OpA and OpB network is also presented in terms of metrics discussed in the system model. The path loss model given in (8.7) is used for the system evaluation. Other system parameters are specified at appropriate places.

8.6.1 Performance analysis of OpB network

1. `MAP` *of the tagged OpB BS:* The effect of carrier sense threshold and protection zone radius on the `MAP` of the tagged OpB BS is presented in Figs. 8.11a and 8.11b. Note that to evaluate the lower bound of `MAP` presented in Lemma 8.10, the `PDF` of the contact distance of PHP is necessary. However, as mentioned in the system model, the contact distance distribution of PHP is an open problem, and for a given set of system parameters it is approximated as Weibull distribution. Hence, the results presented in Figs. 8.11a and 8.11b are not lower bounds in a true sense. However, as evident from the figures, the `MAP` evaluated using Lemma 8.10 and the approximated Weibull distribution acts as a tight bound with respect to different system parameters. In this case, the lower bound on the distribution of $R_{o,AB}$ presented in Lemma 8.8 is used. Further, the approximate result for `MAP` obtained from Lemma 8.9 matches closely with simulations. In Fig 8.11a, in accordance with intuition, as τ_{cs} increases, the `MAP` also increases since lesser number of BSs lie in the contention domain of the tagged BS. In addition, `MAP` of the tagged OpB BS for varying protection zone radii R_{pz} is presented in Fig. 8.11b. The effect of R_{pz} on `MAP` is less prominent compared to the carrier sense threshold, especially for lower density of OpA BSs. Further, from Fig. 8.11b, we observe that as λ_B increases, `MAP` reduces since more BSs contend for the channel. On the other hand, by increasing λ_A, the average number of OpB BSs decreases in the network, which improves the `MAP` of the tagged OpB BS.

2. *Coverage probability for a typical OpB user:* The `SIR` and the link rate coverage probabilities for a typical OpB user are presented in Figs. 8.12a and 8.12b. A close match between simulation and theoretical results is observed. Further, in both the cases, the coverage probability decreases with increasing λ_A. This can be justified by the fact that by increasing λ_A more interference is introduced into the network by the OpA BSs. Further, the serving distance between the typical user and the tagged OpB BS gets larger as the average number of OpB BSs reduces. On the other hand, increasing λ_B results in coverage probability improvement as the distance between the typical user and the tagged BS reduces, which improves the desired signal power.

3. *Normalized* `ASE` *for OpB network:* The effect of different system parameters on normalized `ASE` of the OpB is presented in Figs. 8.13a and 8.13b. The `ASE` is normalized w.r.t. $\hat{\lambda}_B$. From Fig. 8.13a, we observe that by increasing λ_B or reducing λ_A, the normalized `ASE` improves. From Fig. 8.13b, it is clear that the impact of τ_{cs} on `ASE` is negligible beyond

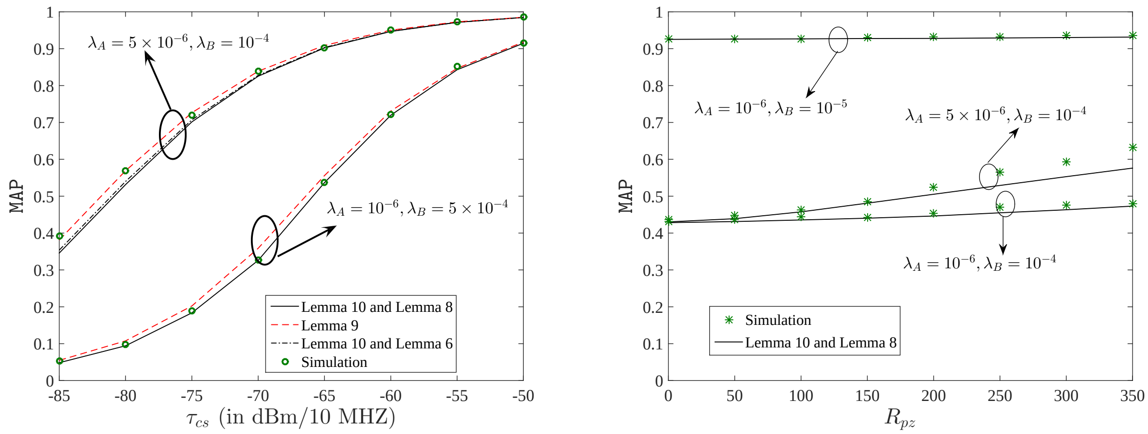

(a) MAP of the tagged BS vs carrier sense threshold.

(b) MAP of the tagged BS vs PZ radius.

Figure 8.11: MAP of the tagged BS. (a) $R_{pz} = 250$ m, and (b) $\tau_{cs} = -80$ dbm/10 MHz.

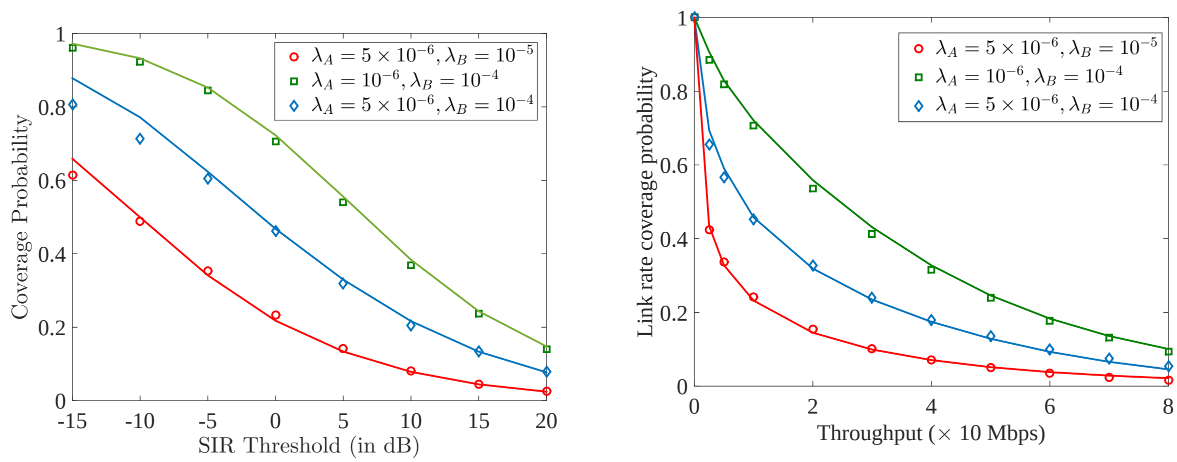

(a) SIR coverage probability for the typical OpB user.

(b) Link rate coverage probability for the typical OpB user.

Figure 8.12: Markers represent simulation results and solid lines represent the theoretical results obtained from Proposition 8.15. $R_{pz} = 250$ m, $\tau_{cs} = -80$ dBm/10 MHz, $P_A = P_B = 30$ dBm/10 Mhz.

a certain threshold. The reason behind this behavior can be explained by the fact that by increasing τ_{cs}, the MAP of interfering BSs becomes unity, and the average interference contribution from the OpB BSs saturates. Hence, the overall coverage probability does not change with τ_{cs}.

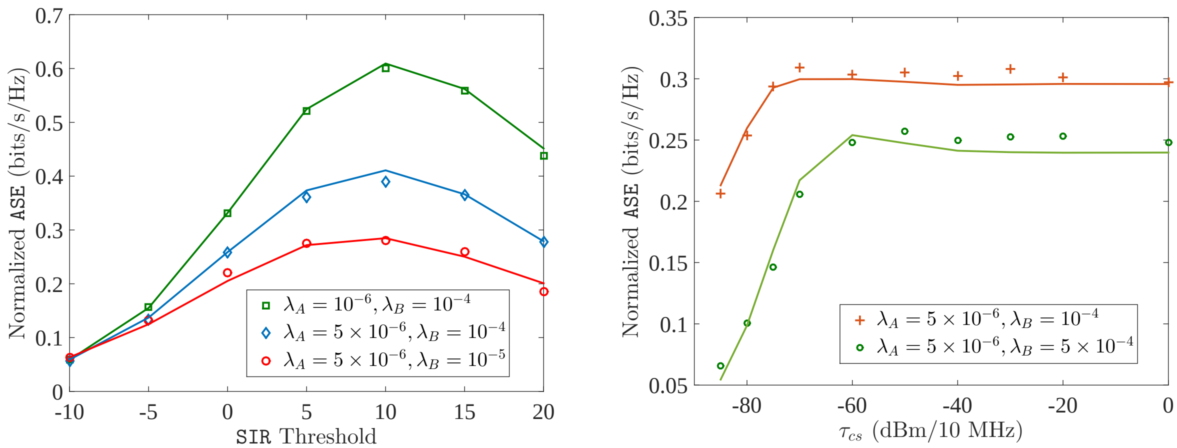

(a) (b)

Figure 8.13: (a) Normalized `ASE` for different target `SIR` thresholds. $\tau_{cs} = -80$ dBm/10 MHz, $R_{pz} = 250$ m. (b) Normalized `ASE` for different carrier sense thresholds. Target `SIR` threshold is 0 dB, $R_{pz} = 250$ m. Lines and markers represent theoretical and simulation results, respectively. The `MAP` of the tagged BS is evaluated using Lemma 8.9.

8.6.2 Performance analysis of OpA network

The `SIR` and the link rate coverage probabilities of the typical OpA user are presented in Figs. 8.14a and 8.14b. A close match between the simulation and theoretical results is observed. As expected, by increasing λ_A, the coverage probability improves in both the cases.

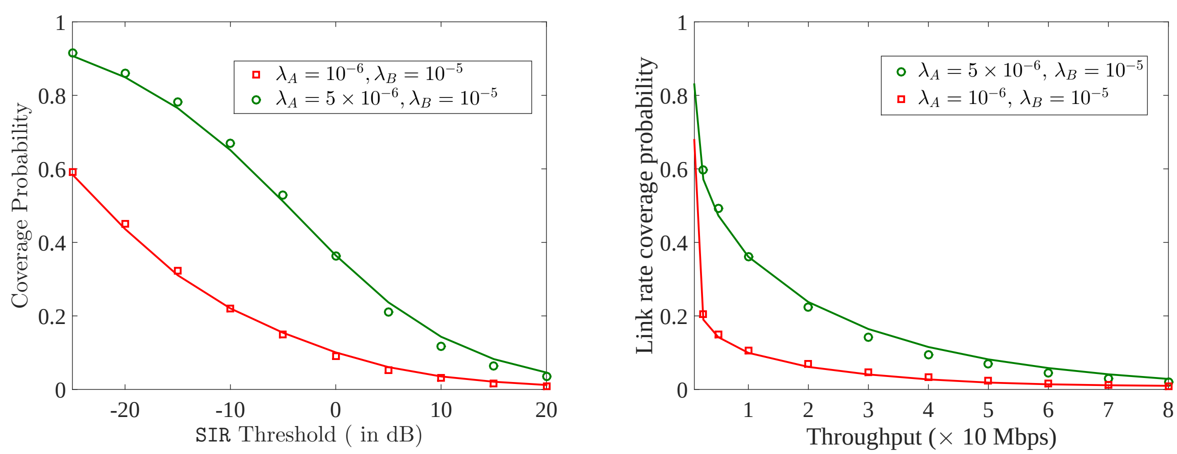

(a) `SIR` coverage probability for the typical OpA user. (b) Link rate Coverage for a typical OpA user.

Figure 8.14: Markers represent simulation results and solid lines represent the theoretical results obtained from Proposition 8.19. $R_{pz} = 250$ m, $\tau_{cs} = -80$ dBm/10 MHz, $P_A = P_B = 30$ dBm/10 Mhz.

8.6.3 Network ASE analysis

The effect of PZ radius on the ASE of both the operators as well as the overall network ASE is presented in Fig. 8.15a. From the figure, it is clear that by increasing R_{pz}, overall ASE of the network goes down as a lesser number of OpB BSs are present in the network. The effect of OpB transmission power on the ASE is presented in Fig. 8.15b. In this figure, in order to evaluate coverage probability using Proposition 8.19, the joint PDF $f_{D_o^B, R_o^A}$ is obtained from Monte-Carlo simulations. From the figure, it is clear that OpB ASE is a concave function of P_B. Hence, proper optimization of P_B is necessary to maximize both network and OpB ASEs.

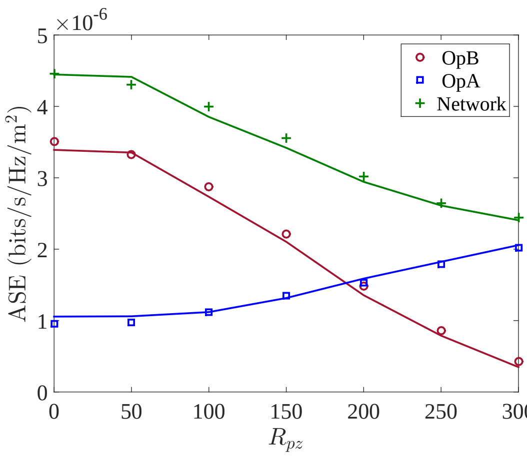

(a)

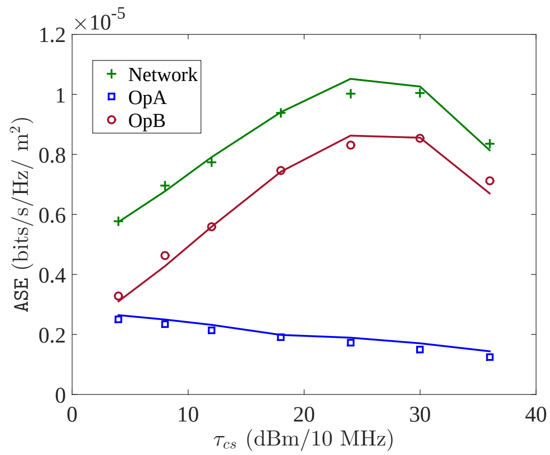

(b)

Figure 8.15: (a) Effect of R_{pz} on ASE. $T = 0$ dB, $P_A = P_B = 30$ dBm/10 MHz, $\tau_{cs} = -80$ dBm/10 MHz, $\lambda_A = 5 \times 10^{-6}$, $\lambda_B = 10^{-5}$. The MAP of the OpB tagged BS is evaluated using Lemmas 8.10 and 8.8. (b) Effect of P_B on ASE. $T = 0$ dB, $P_A = 36$ dBm/10 MHz, $\tau_{cs} = -80$ dBm/10 MHz, $\lambda_A = 5 \times 10^{-6}$, $\lambda_B = 10^{-4}$. The MAP of the OpB tagged BS is evaluated using Lemma 8.9.

8.6.4 Performance in presence of MIMO-enabled GAA BSs

The effect of the presence of multiple antennas at the GAA BS on average GAA user SE is presented in Fig. 8.16. In the system model, we consider that in presence of multiple antennas, the typical GAA BS at $\mathbf{o}_g$ is allowed to operate in a PZ, if it can successfully nullify the interference for the PAL users that lie in $\mathcal{B}_{R_{pz}}(\mathbf{o}_g)$. We assume that each GAA BS has the perfect knowledge of the channels of the PAL users in its vicinity and employs partial zero-forcing precoding scheme. Under these assumptions, for the typical GAA BS, if the number of PAL users in $\mathcal{B}_{R_{pz}}(\mathbf{o}_g)$ is equal to or more than the number of available antennas then it will not be able to successfully cancel the interference to all the users. In such scenarios, if the GAA BS lies in one of the PZs, then it stays silent. As observed from the figure, with increasing number of antennas the average user SE improves owing to the increase in the beamforming gain.

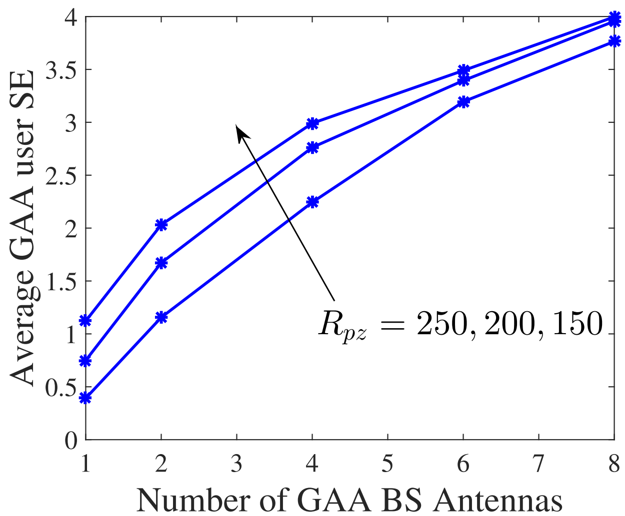

Figure 8.16: Effect of number of GAA BS antennas on average GAA user SE. $P_A = P_B = 30$ dBm/10 MHz, $\tau_{cs} = -80$ dBm/10 MHz, $\lambda_A = 10^{-5}$, $\lambda_B = 5 \times 10^{-5}$.

8.7 Conclusions and future extension

In this work, we have presented the first comprehensive analysis of the co-existence between a licensed and unlicensed operator in the licensed band of the CBRS spectrum. Using tools from stochastic geometry, we have modeled the network as per the key recommendations from the FCC. Further, we have presented useful lower bound for the MAP of a serving unlicensed BS and fairly accurate coverage probability expressions for typical users of the licensed operator and unlicensed operator. The key technical novelty of this work lies in the way the correlation in the interference powers from licensed and unlicensed users is captured by accurately considering the local neighbourhood around the typical user. Using the derived expressions, we have studied the effect of PZ radius and transmission power of the unlicensed BSs on the area spectral efficiency of the network. One of the natural extensions of this work is network performance analysis considering an open access policy, and cooperation between the licensed and unlicensed operators. Further analysis is also possible in this direction by considering the presence of a large number of antennas at the licensed and unlicensed BSs. Other fundamental extensions include handling distance dependent power control by the unlicensed BSs, and consideration of directional CSMA-CA protocol [145], which can be used to study mmWave systems.

Chapter 9

Conclusion and Outlook

In this chapter, we summarize the main contributions of this dissertation and discuss a few potential future directions.

9.1 Summary

Massive MIMO (mMIMO) is at the forefront of different technologies to meet the variegated and often conflicting quality of service requirements of the 5G and beyond networks. There are two different architectures to implement mMIMO: (1) the cellular architecture and (2) the cell-free architecture. In both these architectures, due to the reuse of a finite number of pilot sequences throughout the network, pilot contamination becomes one of the performance-limiting factors. Hence, efficient techniques to mitigate pilot contamination are necessary, which was one of the main objectives of this dissertation. Further, the performance of the cell-free architecture is also limited by the finite capacity of the fronthaul links among the BBU and the APs. Understanding the impact of the finite capacity fronthaul links on system performance is necessary to provide useful system design guidelines. One can, in principle, model and answer the relevant questions through a simulation-based framework. However, the success of stochastic geometry over the last decade to model and analyze wireless networks makes it an appealing alternative to study the mMIMO systems as well. Hence, in this dissertation using appropriate statistical constructs from the stochastic geometry literature we modeled, analyzed, and provided design insights for both the architectures of mMIMO. In addition, we also have provided a stochastic geometry-inspired pilot allocation algorithm that highlights the versatility of these statistical tools to optimize wireless networks.

In Chapter 2, we considered a cellular mMIMO system with an asymptotically large number of antennas at each BS such that the network operates at the pilot contamination-induced interference regime. Further, to reduce the effect of pilot contamination, we considered the fractional pilot reuse (FPR) scheme, which is a low complexity and distributed pilot allocation scheme. The optimal partition of the total number of available pilots for the cell-center and cell-edge users is essential for the successful implementation of the FPR scheme. To answer this question, we first modeled the network using a stochastic geometric construct, namely the Johnson-Mehl (JM) cell, which results in a distance-based partition of each Poisson-Voronoi cell in the network into cell-edge and cell-center regions. Further, we derived key properties, such as area distribution of the typical JM cell and the pair correlation function (PCF) of interfering users in the network, that were useful in analytical characterization of SINR coverage probability and average spectral efficiency (SE) of a randomly selected cell-center/cell-edge user in the typical cell. From our system analyses, we presented a pilot partitioning guideline that ensures that the cell-edge user performance can be improved with negligible performance degradation for the-cell center users compared to the unity pilot reuse.

The concept of JM cells presented in Chapter. 2, can be used to model a variety of wireless networks such as fractional frequency reuse, soft pilot reuse (SPR). In Chapter 3, we used JM cells to model a cellular network where the user and BS locations are spatially coupled, i.e., the user locations are in the vicinity of its serving BS. Further, using the theory developed in Chapter. 2, we derived the uplink SIR coverage probability and average SE of the typical user in the network. One of the key conclusions of the work is that compared to the proposed model the MCP-based model, which is popular for modeling clustered BS-user location, underestimates the coverage probability.

As mentioned above, JM cells can also be used to model and analyze an mMIMO system with SPR. The first step to do so is to capture the uplink power control in the analysis, which was carried out in Chapter. 4. We considered a network with unity pilot reuse and fractional power control (FPC) scheme. With the application of the displacement theorem, we presented the coverage probability and average user SE for the typical user in the network.

In the next part of the dissertation, we focused on the performance analysis of cell-free mMIMO systems. Similar to the cellular architecture, pilot contamination becomes one of the performance-limiting factors of the cell-free network as well. One useful approach to reduce the effect of pilot contamination is to ensure a minimum distance among the set of co-pilot users. A direct consequence of this pilot allocation scheme is the formation of a new point process, namely the multilayer random sequential adsorption (RSA) process, which constitutes the locations of the users that are assigned a pilot. To facilitate theoretical analyses, we need information regarding the density and the pair correlation function of this new point process. In Chapter 5, we formally defined the multilayer RSA point process as a space-time process. For the 1D version of this process, we presented two useful approximations to obtain the density of deposited rods for a given layer. While our first approach is more amenable to numerical evaluation, the second approach is more accurate and provides useful information regarding the gap density function. We also extended the first approximation to obtain the density of circles in a given layer for the 2D version of this multilayer RSA process.

Based on the multilayer RSA process of Chatper 5, in Chapter 6, we proposed a distributed pilot allocation scheme to reduce the effect of pilot contamination in a cell-free network. Further, using the analytical result for the 2D version of the problem derived in Chatper 5, we also presented an accurate analytical expression for the typical user pilot assignment probability that is useful from the perspective of network dimensioning. To benchmark the performance of the RSA-based scheme, we also proposed two optimization-based centralized pilot allocation schemes. With respect to the first centralized scheme, which partitions the users in the network in such a way that minimum distance among the sets of co-pilot users is maximized, the RSA-based scheme provides competitive average user SE performance. The second centralized pilot allocation scheme, which is based on the branch-and-price algorithm, provides a near-optimal solution in terms of sum user SE for a relatively small system with tens of users. The performance of the RSA-based scheme, despite its distributed implementation, is appreciable with respect to the near-optimal branch-and-price scheme. Owing to its competitive performance and scalable distributed implementation, the RSA-based scheme is an attractive algorithm for pilot allocation in a cell-free mMIMO network where the performance is limited by pilot contamination.

In Chapter 7, we modeled and analyzed a cell-free mMIMO network with finite fronthaul capacity. Due to the finite capacities of the links, compression error gets introduced into the system that results in user SINR degradation. Taking into account the compression error, we derived an achievable user rate conditioned on the user and access point (AP) locations. Further, using tools from stochastic geometry, we derived rate coverage expressions for a randomly selected user in the network for the following two different architectures: the traditional finite architecture where each AP serves all the users in the network and the user-centric architecture where each user is served by a few nearest APs. An intermediate useful result is the derivation of the load distribution results for the typical AP and the tagged AP in the user-centric architecture. These results can also be used to study the degree distribution in a bipartite random geometric graph.

The flavors of mMIMO that are discussed in this dissertation has already been and will be implemented in the Sub-6 GHz frequency range. Owing to the sparsity of frequency resources in this spectrum range, spectrum sharing is encouraged. In the final chapter of the dissertation, we modeled and analyzed the performance of a spectrum sharing network that operates in the CBRS band. Our key results were the derivation of useful lower bound for the medium access probability of a serving unlicensed BS and coverage probability expressions for the typical users of the licensed and unlicensed operators. Using the derived expressions, we have studied the effect of protection zone radius and transmission power of the unlicensed BSs on the area spectral efficiency of the network. Further, we also highlight the usefulness of MIMO-enabled BSs over omni-directional transmission.

9.2 Outlook

9.2.1 Performance analysis of soft pilot reuse scheme

In Chapter 2, we analyzed the performance of an mMIMO system that employs FPR to reduce the effect of pilot contamination. A more promising method to reduce the effect of pilot contamination for the cell-edge users is SPR, where instead of following a reuse pattern for the set of cell-edge pilots, all the cell-edge pilots are used in each cell of the network. However, the pilot transmission powers in adjacent cells are controlled using a certain reuse pattern [146]. This scheme is reminiscent of the soft frequency reuse (SFR) scheme in the LTE networks. One of the potential future works is to develop suitable theoretical results to analyze the performance of the SPR scheme in an mMIMO network. The derived theoretical results can also be applied to analyze other co-channel interference mitigation schemes such as SFR. The result derived in Chapters 2 and 4 can be leveraged with suitable modifications to achieve this objective.

9.2.2 Extension of the multilayer RSA process to three-dimension

In Chapter 5, we derived the density results for the 1D and 2D versions of the multilayer RSA process. A promising future direction is to extend the results to the three-dimension. Another promising direction is to derive the PCF results. The new set of results can be applied to model contention-based channel access in an unmanned area vehicle (UAV) network. Further, these results will also be useful in modeling and analyzing UAV-empowered cell-free networks where the distributed pilot assignment scheme proposed in Chapter 6 is used.

9.2.3 Impact of fronthaul topology and compression method on cell-free network

In Chapter 7, we considered a star topology for the fronthaul network where each AP is connected to a central BBU. However, in most practical scenarios, laying out fiber to all the AP from the BBU is not feasible. Therefore, a multihop topology is usually preferred [147]. It would be interesting to analyze the benefits of the multihop topology over the star topology in terms of capital expenditure. Further, system analysis is more interesting as there are more degrees of freedom in fronthaul capacity dimensioning compared to the star topology. In addition, in this dissertation, we focused on a point-to-point compression scheme. However, there are many sophisticated compression algorithms available in the literature. Understanding the impact of these algorithms on cell-free mMIMO system performance is also another promising research direction.

9.2.4 Comprehensive analysis of mMIMO-enabled CBRS systems

In Chapter 8, we laid the foundation for modeling and analysis of the CBRS system that takes into account the FCC guidelines. Further, we also provided the initial promising results on the application of MIMO to improve the average SE of the users of the unlicensed network. However, there lie many possible extensions of this work. First, in the presence of a large number of antennas at unlicensed BSs, the contention-based channel access mechanism needs modification so that the hidden node and exposed node problems can be mitigated. Further, the impact of modified contention-based channel access on the unlicensed BS medium access probability also needs to be analyzed. These new results can be used to gain insights on the possibility of relaxing a few of the FCC recommendations leading to more opportunities for spectrum sharing. Second, in Chapter 8, we have limited our focus to deriving the area spectral efficiency result. In the future extension, the load distribution for the typical unlicensed BS can be derived that will subsequently be used to obtain the average user SE.

Appendices

Appendix A

Proofs of Lemmas and Remarks of Chapter 2

A.1 Proof of Lemma 2.1

The mean area of the CE region can be expresses as

$$\begin{aligned}\mathbb{E}\left[|\mathcal{X}_E(\mathbf{o},R_c,\Psi_b)|\right] =&\mathbb{E}\left[\int\limits_{\mathbf{x}\in\mathbb{R}^2}\mathbf{1}_{(\mathbf{x}\in\mathcal{V}_{\Psi_b}(\mathbf{o})\cap\mathcal{B}^C_{R_c}(\mathbf{o}))}\mathrm{d}\mathbf{x}\right]\\ \overset{(a)}{=}&\int_{\mathbf{x}\in\mathbb{R}^2\cap\mathcal{B}^C_{R_c}(\mathbf{o})}\exp(-\pi\lambda_0\|\mathbf{x}\|^2)\mathrm{d}\mathbf{x}\\ =&2\pi\int_{r=R_c}^{\infty}\exp(-\pi\lambda_0 r^2)r\mathrm{d}r,\end{aligned}$$

where (a) follows from that fact that a point located at a distance $\|\mathbf{x}\|$ from the origin belongs to $\mathcal{V}_{\Psi_b}(\mathbf{o})$, if there are no other BSs in $\mathcal{B}_{\|\mathbf{x}\|}(\mathbf{x})$. Solving the final integral gives us the expression for the mean in (2.22). Similarly, the second moment of the CE area can be expressed as

$$\begin{aligned}\mathbb{E}\left[|\mathcal{X}_E(\mathbf{o},R_c,\Psi_b)|^2\right] =&\mathbb{E}\left[\int\limits_{\mathbf{x}\in\mathbb{R}^2}\mathbf{1}_{(\mathbf{x}\in\mathcal{V}_{\Psi_b}(\mathbf{o})\cap\mathcal{B}^C_{R_c}(\mathbf{o}))}\mathrm{d}\mathbf{x}\int\limits_{\mathbf{y}\in\mathbb{R}^2}\mathbf{1}_{(\mathbf{y}\in\mathcal{V}_{\Psi_b}(\mathbf{o})\cap\mathcal{B}^C_{R_c}(\mathbf{o}))}\mathrm{d}\mathbf{y}\right]\\ =&\int_{\mathbf{x}\in\mathbb{R}^2}\int_{\mathbf{y}\in\mathbb{R}^2}\mathbb{E}\left[\mathbf{1}_{(\mathbf{x}\in\mathcal{V}_{\Psi_b}(\mathbf{o})\cap\mathcal{B}^C_{R_c}(\mathbf{o}),\mathbf{y}\in\mathcal{V}_{\Psi_b}(\mathbf{o})\cap\mathcal{B}^C_{R_c}(\mathbf{o}))}\right]\mathrm{d}\mathbf{x}\mathrm{d}\mathbf{y}\\ \overset{(b)}{=}&\int\limits_{(\mathbf{x},\mathbf{y})\in\mathbb{R}^2\cap\mathcal{B}^C_{R_c}(\mathbf{o})\times\mathbb{R}^2\cap\mathcal{B}^C_{R_c}(\mathbf{o})}e^{-\lambda_0|\mathcal{B}_{\|\mathbf{x}\|}(\mathbf{x})\cup\mathcal{B}_{\|\mathbf{y}\|}(\mathbf{y})|}\mathrm{d}\mathbf{x}\mathrm{d}\mathbf{y}\\ =&2\pi\int\limits_{r_1=R_c}^{\infty}\int\limits_{r_2=R_c}^{\infty}\int\limits_{u=0}^{2\pi}e^{-\lambda_0 V(r_1,r_2,u)}\mathrm{d}ur_2\mathrm{d}r_2r_1\mathrm{d}r_1,\end{aligned}$$

where (b) follows from the fact that if points $\mathbf{x}$ and $\mathbf{y}$ belong to $\mathcal{V}_{\Psi_b}(\mathbf{o})$, then there are no other BSs in the region $\mathcal{B}_{\|\mathbf{x}\|}(\mathbf{x})\cup\mathcal{B}_{\|\mathbf{y}\|}(\mathbf{y})$, and the last step follows from changing the integration limits from Cartesian to polar coordinates.

A.2 Proof of Lemma 2.8

One approach to deriving $g_1^{\mathrm{CC}}(r,\kappa)$ is to first determine the Ripley's K-function $K_1^{\mathrm{CC}}(r,\kappa)$ and then use the following relationship: $g_1^{\mathrm{CC}}(r,\kappa) = \frac{\mathrm{d}K_1^{\mathrm{CC}}(r,\kappa)/\mathrm{d}r}{2\pi r}$. Note that points in $\Phi_{\mathtt{u,CC}}$ are likely to exhibit repulsion w.r.t. $\mathbf{o}$ as these points do not lie in $\mathcal{V}_{\Psi_b}(\mathbf{o})$. Since the total interference is likely to be dominated by the nearby users, our main interest lies in characterizing $g_1^{\mathrm{CC}}(r,\kappa)$ for small r. Note that $g_1^{\mathrm{CC}}(r,\kappa) \to 1$ as $r \gg 0$. Recall that for a point process Φ of density λ the Ripley's K-function is defined as $K_\lambda(r) = \mathbb{E}\left[N_\Phi(\mathcal{B}_r(\mathbf{o}))\right]/\lambda$ [10], where $N_\Phi(\mathcal{B}_r(\mathbf{o}))$ denotes the number of points of Φ that lie in $\mathcal{B}_r(\mathbf{o})$. In this case, the K-function is given as $K_1^{\mathrm{CC}}(r,\kappa) = \mathbb{E}\left[N_{\Phi_{\mathtt{u,CC}}}\left(\cup_{\mathbf{x}\in\Phi_b}(\mathcal{B}_r(\mathbf{o}) \cap \mathcal{X}_C(\mathbf{x},\kappa/\sqrt{\pi c_2},\Psi_b))\right)\right]$. Now,

$$K_1^{\mathrm{CC}}(r,\kappa) \simeq \mathbb{E}\left[N_{\Phi_{\mathtt{u,CC}}}\left(\mathcal{B}_r(\mathbf{o}) \cap \mathcal{X}_C(\mathbf{y},\kappa/\sqrt{\pi c_2},\Psi_b)\right)\right], \quad r \to 0, \tag{A.1}$$

where $\simeq$ denotes approximation that becomes better asymptotically, $\mathbf{y}$ is the nearest BS to the typical BS at $\mathbf{o}$. Without loss of generality, we assume that $\mathbf{y} = (\|\mathbf{y}\|, 0)$. As per our construction of $\Phi_{\mathtt{u,CC}}$, we are concerned with only one uniformly distributed point in $\mathcal{X}_C(\mathbf{y},\kappa/\sqrt{\pi c_2},\Psi_b)$ lying in the region $\mathcal{B}_r(\mathbf{o}) \cap \mathcal{X}_C(\mathbf{y},\kappa/\sqrt{\pi c_2},\Psi_b)$. Hence, we write (A.1) as

$$\begin{aligned}
K_1^{\mathrm{CC}}(r,\kappa) \simeq & \mathbb{E}\left[\frac{|\mathcal{B}_r(\mathbf{o}) \cap \mathcal{X}_C(\mathbf{y},\frac{\kappa}{\sqrt{\pi c_2}},\Psi_b)|}{|\mathcal{X}_C(\mathbf{y},\frac{\kappa}{\sqrt{\pi c_2}},\Psi_b)|}\right] = \mathbb{E}\left[\frac{S_C(r_m,r,\kappa)}{X_{C0}(1,\frac{\kappa}{\sqrt{\pi c_2}})}\right] \\
\approx & \mathbb{E}_{R_m}\left[S_C(r_m,r,\kappa)\right]\mathbb{E}\left[X_{C0}(1,\frac{\kappa}{\sqrt{\pi c_2}})^{-1}\right],
\end{aligned}$$

where $S_C(r_m,r,\kappa)$ denotes the area of the region $\mathcal{B}_r(\mathbf{o}) \cap \mathcal{B}_{R_c}(\mathbf{y}) \cap ((\mathbb{R}-r_m)^+ \times \mathbb{R})$, and the last approximation follows from independence assumption between $S_C(r_m,r,\kappa)$ and $X_{C0}(1,\kappa/\sqrt{\pi c_2})^{-1}$. Now, using the result presented in Appendix A.3, we write

$$\mathbb{E}_{R_m}\left[S_C(r_m,r,\kappa)\right] \simeq \mathbf{1}(R_c > r)\frac{\pi^2 r^4}{2} + \mathbf{1}(R_c \le r)\pi^2 R_c^2 r^2 - \frac{\pi^2 R_c^4}{2}, r \to 0, \tag{A.2}$$

where $R_c = \kappa/\sqrt{\pi c_2}$. The first inverse moment of $X_{C0}(1,\kappa/\sqrt{\pi c_2})$ can be evaluated numerically using the approximated distribution presented in Sec. 2.3. Now, the K-function is given as

$$K_1^{\mathrm{CC}}(r,\kappa) \simeq \begin{cases} \dfrac{\pi^2 r^4}{2}\mathbb{E}\left[X_{C0}(1,\dfrac{\kappa}{\sqrt{\pi c_2}})^{-1}\right] & R_c > r, r \to 0 \\ (\pi^2 R_c^2 r^2 - \dfrac{\pi^2 R_c^4}{2})\mathbb{E}\left[X_{C0}(1,\dfrac{\kappa}{\sqrt{\pi c_2}})^{-1}\right] & R_c \le r, r \to 0, \end{cases}$$

and the PCF is given as

$$g_1^{\mathrm{CC}}(r,\kappa) = \frac{\mathrm{d}K_1^{\mathrm{CC}}(r,\kappa)}{2\pi r \mathrm{d}r} \simeq \begin{cases} \pi r^2 \mathbb{E}\left[X_{C0}(1, \frac{\kappa}{\sqrt{\pi c_2}})^{-1}\right] & R_c > r, r \to 0 \\ \pi R_c^2 \mathbb{E}\left[X_{C0}(1, \frac{\kappa}{\sqrt{\pi c_2}})^{-1}\right] & R_c \leq r, r \to 0. \end{cases}$$

Note that as $R_c \to 0$, the 0-th BSs observes user locations that are almost identical to BS locations, which is a homogeneous PPP. In this case, when $R_c \to 0$, $\mathbb{E}\left[X_{C0}(1, \kappa/\sqrt{\pi c_2})^{-1}\right] \simeq \frac{1}{\pi R_c^2}$. Hence, $g_1^{\mathrm{CC}}(r,\kappa) \to 1$ as expected for a homogeneous PPP.

Using the asymptotic result that $1 - \exp(-u) \simeq u$ as $u \to 0$, we write

$$g_1^{\mathrm{CC}}(r,\kappa) \simeq \left(1 - e^{-\pi r^2 \mathbb{E}\left[X_{C0}\left(1, \frac{\kappa}{\sqrt{\pi c_2}}\right)^{-1}\right]}\right)\mathbf{1}(r < R_c) + \mathbf{1}(r \geq R_c),$$

as $r \to 0$. Accordinng to the simulation based observation mentioned in [61], due to the condition $r \to 0$, the Voronoi cell $\mathcal{V}_{\Psi_b}(\mathbf{y})$ is skewed whose area is likely to be half of the area of a typical Voronoi cell. Similar argument can be made for the area of the CC region as well. Hence, a factor of 2 needs to be introduced for the first condition. Using this fact, for any value of r, a reasonable approximation for the PCF is $g_1^{\mathrm{CC}}(r,\kappa) \approx 1 - \exp(-2\pi r^2 \mathbb{E}\left[X_{C0}(1, \kappa/\sqrt{\pi c_2})^{-1}\right])$.

A.3 Proof of (A.2)

Depending on the value of R_c and r we have the following two cases of interest:
Case 1: $r < R_c$: The result for this case is obtained from [61, Lemma 2], and is given as

$$\mathbb{E}_{R_m}\left[S_C(r_m, r, \kappa)\right] \simeq \frac{\pi^2 r^4}{2}, \quad r \to 0.$$

Case 2: $r \geq R_c$: In this case, the area of the region $\mathcal{B}_r(\mathbf{o}) \cap \mathcal{X}_C(\mathbf{y}, \kappa/\sqrt{\pi c_2}, \Psi_b)$ is given as

$$S_C(r_m, r, \kappa) = \begin{cases} r^2\left(u - \frac{\sin 2u}{2}\right) + R_c^2\left(v - \frac{\sin 2v}{2}\right) \\ \quad -(wR_c^2 - r_m\sqrt{R_c^2 - r_m^2}), & R_c \geq r_m \\ r^2 u - \frac{r^2}{2}\sin 2u + R_c^2 v - \frac{R_c^2}{2}\sin 2v, & R_c < r_m, \end{cases}$$

where $R_c = \kappa/\sqrt{\pi c_2}$, $u = \cos^{-1}\left(\frac{r^2+4r_m^2-R_c^2}{4rr_m}\right)$, $v = \cos^{-1}\left(\frac{R_c^2+4r_m^2-r^2}{4R_cr_m}\right)$, and $w = \cos^{-1}\left(\frac{r_m}{R_c}\right)$. Averaging over the random variable R_m, we get

$$\mathbb{E}\left[S_C(r_m, r, \kappa)\right] = \pi R_c^2 \int_0^{(r-R_c)/2} f_{R_m}(r_m)\mathrm{d}r_m + \int_{(r-R_c)/2}^{(r+Rc)/2} S_C(r_m, r, \kappa) f_{R_m}(r_m)\mathrm{d}r_m,$$

where we have used the fact that for $r > 2r_m + R_c$, $S_C(r_m, r, \kappa) = \pi R_c^2$. Further, note that for $2r_m > r+R_c$, $S_C(r_m, r, \kappa) = 0$. Hence, the upper limit is introduced to consider the values of R_m for which $S_C(r_m, r, \kappa) \neq 0$. In addition, we use the asymptotic approximation $f_{R_m}(r_m) = 8\pi r_m \exp(-4\pi r_m^2) \simeq 8\pi r_m(1-4\pi r_m^2)$, as $r_m \to 0$. After performing the integration, we obtain

$$\begin{aligned}\mathbb{E}\left[S_C(r_m, r, \kappa)\right] \simeq &\frac{\pi^2 R_c^2 r^4}{2} - \frac{\pi^2 R_c^4 r^2}{2} + \pi^2 R_c^2 r^2 - \left(\frac{\pi^3 R_c^2 r^4}{2} + \frac{\pi^2 R_c^4}{2} + \frac{\pi^3 R_c^6}{2}\right)\\ &\simeq \pi^2 R_c^2 r^2 - \frac{\pi^2 R_c^4}{2}, \quad r \to 0.\end{aligned}$$

This completes the proof of (A.2).

A.4 Derivation of Lemma 2.14

The proof can be done on the similar lines as that of Appendices A.2 and A.3. In this case, the Ripley's K-function is given as

$$K_1^{\mathrm{CE}}(r, \kappa) \approx \mathbb{E}_{R_m}\left[S_E(r_m, r, \kappa)|\mathcal{E}_3^C\right]\mathbb{E}\left[X_{E0}\left(1, \frac{\kappa}{\sqrt{\pi c_2}}\right)^{-1}\middle|\mathcal{E}_3^C\right], \quad r \to 0, r > R_c.$$

Asymptotically, conditioned on $\mathcal{E}_3^C$, the distribution of R_m is given as

$$F_{R_m}(r_m|R_M > R_c) = \frac{\mathbb{P}\left[R_m \leq r_m, R_M > R_c\right]}{\mathbb{P}\left[R_M > R_c\right]} \simeq \mathbb{P}\left[R_m \leq r_m\right], \quad R_c \to 0.$$

The condition $R_c \to 0$ is of interest to us as our goal is to find the `PCF` for $r \to 0$, and $r > R_c$. Now, the following expectation

$$\begin{aligned}\mathbb{E}_{R_m}\left[S_E(r_m, r, R_c)|\mathcal{E}_3^C\right] \simeq &\int_0^r A_1(r, r_m, R_c)\mathrm{d}F_{R_m}(r_m) - \int_0^{(r-R_c)/2} A_2(r, r_m, R_c)\mathrm{d}F_{R_m}(r_m)\\ &- \int_{(r-R_c)/2}^{(r+R_c)/2} A_2(r, r_m, R_c)\mathrm{d}F_{R_m}(r_m) - \int_0^{R_c} A_3(r, r_m, R_c)\mathrm{d}F_{R_m}(r_m)\end{aligned}$$

$$
\begin{aligned}
=&\frac{\pi^2 r^4}{2} + \frac{\pi^3 r^6}{2} - \frac{\pi^2 R_c^2 r^4}{2} + \frac{\pi^2 R_c^4 r^2}{2} \\
&- \pi^2 R_c^2 r^2 + \frac{\pi^3 R_c^2 r^4}{2} + \frac{\pi^2 R_c^4}{2} + \frac{\pi^3 R_c^6}{2} \\
\simeq&\frac{\pi^2 (r^4 + R^4 - 2R_c^2 r^2)}{2},
\end{aligned}
$$

where the last step follows from neglecting the 6-th order terms. In the previous expression

$$
\begin{aligned}
A_1(r, r_m, R_c) =& r^2 \arccos \frac{r_m}{r} - r_m \sqrt{r^2 - r_m^2}, \\
A_2(r, r_m, R_c) =& \left(r^2 u - \frac{r^2 \sin(2u)}{2} + R_c^2 v - \frac{R_c^2 \sin(2v)}{2} \right) \\
& \mathbf{1}\big(|2r_m - r| \leq R_c\big) + \pi R_c^2 \mathbf{1}\big(r_m < \frac{r - R_c}{2}\big), \\
A_3(r, r_m, R_c) =& \left(R_c^2 \arccos \left(\frac{r_m}{R_c} \right) - r_m \sqrt{R_c^2 - r_m^2} \right) \times \\
& \mathbf{1}\left(r_m \leq R_c \right).
\end{aligned}
$$

Using the above result, the Ripley's K-function is given as

$$
K_1^{\mathrm{CE}}(r, \kappa) \simeq \frac{\pi^2 \left(r^2 - R_c^2\right)^2}{2} \mathbb{E}\left[X_{E0}(1, \frac{\kappa}{\sqrt{\pi c_2}})^{-1} \middle| \mathcal{E}_3^C \right], \; r > R_c, r \to 0. \tag{A.3}
$$

Hence, the PCF is given as

$$
\begin{aligned}
g_1^{\mathrm{CE}}(r, \kappa) =& \frac{\mathrm{d}K_1^{\mathrm{CE}}(r, \kappa)}{2\pi r \; \mathrm{d}r} \\
\simeq& \pi \left(r^2 - R_c^2\right) \mathbb{E}\left[X_{E0}\left(1, \frac{\kappa}{\sqrt{\pi c_2}})\right)^{-1} \middle| \mathcal{E}_3^C \right] \\
\approx& \frac{14\pi \left(r^2 - R_c^2\right) \mathbb{P}\left[\mathcal{E}_3^C\right]}{5 \exp(-\pi R_c^2)},
\end{aligned}
$$

where the intuition for the approximation in the last step follows from Jensen's inequality

$$
\mathbb{E}\left[X_{E0}\left(1, \frac{\kappa}{\sqrt{\pi c_2}}\right)^{-1} \middle| \mathcal{E}_3^C \right] \geq \frac{1}{\mathbb{E}\left[X_{E0}\left(1, \frac{\kappa}{\sqrt{\pi c_2}}\right) \middle| \mathcal{E}_3^C \right]} = \exp(\pi R_c^2) \mathbb{P}\left[\mathcal{E}_3^C\right].
$$

From [61], when $R_c = 0, \mathbb{E}\left[X_{E0}(1, \frac{\kappa}{\sqrt{\pi c_2}})^{-1}\right] \approx 14/5$. Hence, for $R_c \to 0$, we approximate

$$
\mathbb{E}\left[X_{E0}(1, \frac{\kappa}{\sqrt{\pi c_2}})^{-1} | \mathcal{E}_3^C \right] \approx 14/5 \exp(\pi R_c^2) \mathbb{P}\left[\mathcal{E}_3^C\right] = 14/5 \exp(\kappa^2 / c_2) \mathbb{P}\left[\mathcal{E}_3^C\right].
$$

This completes the proof of the Lemma.

Appendix B

Proofs of Lemmas and Remarks of Chapter 4

B.1 Proof of Lemma 4.5

Proof: The intensity measure of the PPP is defined as $\Lambda_\mu\left(\mathcal{B}(\mathbf{0},t)\right) = \mathbb{E}\left[\boldsymbol{\mu}_u\left(\mathcal{B}(\mathbf{0},t)\right)\right]$

$$
\begin{aligned}
&= 2\pi\lambda_0 \int_0^\infty \mathbb{P}\left[r/d_{jj}^\epsilon \le t, r > d_{jj}\right] r\mathrm{d}r \\
&= 2\pi\lambda_0 \int_0^\infty \mathbb{E}_{d_{jj}}\left[\mathbf{1}\left(d_{jj} < r \le t d_{jj}^\epsilon\right)\right] r\mathrm{d}r \\
&\overset{(a)}{=} 2\pi\lambda_0 \int\limits_{y=0}^{t^{\frac{1}{1-\epsilon}}} f_{d_{jj}}(y)\left[\int_y^{ty^\epsilon} r\mathrm{d}r\right]\mathrm{d}y \\
&\overset{(b)}{=} (\pi\lambda_0)^{1-\epsilon} t^2 \int\limits_0^{\pi\lambda_0 t^{2/(1-\epsilon)}} u^\epsilon e^{-u}\mathrm{d}u - \int\limits_0^{\pi\lambda_0 t^{2/(1-\epsilon)}} u e^{-u}\mathrm{d}u \\
&\overset{(c)}{=} (\pi\lambda_0)^{1-\epsilon} t^2 \Gamma_{\mathtt{L}}\left(1+\epsilon, \pi\lambda_0 t^{\frac{2}{(1-\epsilon)}}\right) - \Gamma_{\mathtt{L}}\left(2, \pi\lambda_0 t^{\frac{2}{(1-\epsilon)}}\right),
\end{aligned}
\tag{B.1}
$$

where the (a) follows from interchanging integration and expectation, and taking the limits of y to make sure that $y \le ty^\epsilon$; (b) follows from solving the inner integral and replacing $\pi\lambda_0 y^2 = u$; and (c) follows from the definition of lower incomplete gamma function. Note that the intensity function and intensity measure are related by

$$2\pi \int_0^t \lambda_\mu(r) r\mathrm{d}r = \lambda_\mu\left(\mathcal{B}(\mathbf{0},t)\right).$$

Hence, the intensity function is given as

$$\lambda_\mu(t) = \frac{\mathrm{d}}{\mathrm{dt}}\frac{\Lambda_\mu\left(\mathcal{B}(\mathbf{0},t)\right)}{2\pi t} = \frac{(\pi\lambda_0)^{1-\epsilon}}{c^\epsilon \pi}\Gamma_L(1+\epsilon, \pi c\lambda_0 t^{2/(1-\epsilon)}). \tag{B.2}$$

This completes the proof of Lemma 4.5. ∎

B.2 Proof of Lemma 4.7

Proof: The expected interference conditioned on the distance of the most dominant interferer is given as $\mathbb{E}\left[\sum_{\hat{\mathbf{u}}_j \in \boldsymbol{\mu}_u \setminus \hat{\mathbf{u}}_1} \hat{d}_{0j}^{-2\alpha} | \hat{d}_{01}\right]$

$$
\begin{aligned}
&\overset{(a)}{=} 2\pi \int_{\hat{d}_{01}}^{\infty} r^{-2\alpha} \lambda_\mu(r) r \mathrm{d}r = 2\pi \int_{\hat{d}_{01}}^{\infty} r^{-2\alpha+1} \frac{(\pi\lambda_0)^{1-\epsilon}}{\pi} \Gamma_L(1+\epsilon, \pi\lambda_0 r^{2/(1-\epsilon)}) \mathrm{d}r \\
&= 2(\pi\lambda_0)^{1-\epsilon} \int_{r=\hat{d}_{01}}^{\infty} r^{-2\alpha+1} \left[\int_{u=0}^{\pi\lambda_0 r^{2/(1-\epsilon)}} u^{\epsilon} \exp(-u) \mathrm{d}u \right] \mathrm{d}r \\
&\overset{(b)}{=} 2(\pi\lambda_0)^{1-\epsilon} \Bigg(\int_{u=0}^{\pi\lambda_0 \hat{d}_{01}^{2/(1-\epsilon)}} u^{\epsilon} \exp(-u) \int_{r=\hat{d}_{01}}^{\infty} r^{-2\alpha+1} \mathrm{d}r \mathrm{d}u \\
&\quad + \int_{u=\pi\lambda_0 \hat{d}_{01}^{2/(1-\epsilon)}}^{\infty} u^{\epsilon} \exp(-u) \int_{r=(u/(\pi\lambda_0))^{(1-\epsilon)/2}}^{\infty} r^{-2\alpha+1} \mathrm{d}r \mathrm{d}u \Bigg)
\end{aligned}
$$

where (a) follows from the application of Campbell's formula, (b) follows from the change in order of integration, and the expression (4.15) in the Lemma follows from solving the inner integral and using definition of lower and upper incomplete gamma functions in the last step. ■

B.3 Proof of Lemma 4.3

Proof: Following the standard definition the characteristic function of aggregate interference is given as

$$
\begin{aligned}
\varphi_{I_{agg}}(w) &= \mathbb{E}\left[e^{jwI_{agg}}\right] \\
&= \mathbb{E}\left[e^{jw \sum_{\mathbf{u}_j \in \Psi_u} d_{0j}^{-2\alpha} d_{jj}^{2\alpha\epsilon} \mathbf{1}(d_{0j} > d_{jj})}\right] \\
&= \mathbb{E}\Big[\prod_{\mathbf{u}_j \in \Psi_u} e^{jw d_{0j}^{-2\alpha} d_{jj}^{2\alpha\epsilon} \mathbf{1}(d_{0j} > d_{jj})}\Big] \\
&\overset{(a)}{=} e^{-2\pi\lambda_0 \int_0^\infty (1 - \mathbb{E}_{d_{jj}}\left[\exp(jw d_{jj}^{2\alpha\epsilon} r^{-2\alpha} \mathbb{1}(d_{jj} < r)\right]) r \mathrm{d}r} \qquad \text{(B.3)} \\
&= e^{-2\pi\lambda_0 \int\limits_{r=0}^{\infty} \left(1 - \int\limits_{y=0}^{r} f_{d_{jj}}(y) \exp\left(jw \frac{r^{-2\alpha}}{y^{-2\alpha\epsilon}}\right) \mathrm{d}y - \int\limits_{y=r}^{\infty} f_{d_{jj}}(y) \mathrm{d}y\right) r \mathrm{d}r}, \qquad \text{(B.4)}
\end{aligned}
$$

where (a) follows from the application of probability generating functional of PPP. The expression in Lemma 4.3 follows from substituting the expression for the PDF of $f_{d_{jj}}(y)$ in the above expression. ∎

Appendix C

Proof of Lemma of Chapter 7

C.1 Proof of Lemma 7.3

The proof of this lemma is based on a lower bound that is well known in the mMIMO literature (cf. [148, Lemma 2], [149]). From (7.3), we write $y_o^{\mathtt{dl}}$ as $y_o^{\mathtt{dl}} =$

$$\underbrace{\sqrt{\rho_d}\sum_{\mathbf{r}_l\in\Phi_{ro}}\sqrt{\eta_{lo}}\frac{\mathbb{E}\left[\|\hat{\mathbf{g}}_{lo}\|^2\right]}{\sqrt{N\gamma_{lo}}}q_{o_l}}_{T_1\text{: Desired signal}}+\underbrace{\sqrt{\rho_d}\sum_{\mathbf{r}_l\in\Phi_{ro}}\sqrt{\eta_{lo}}\frac{\left(\|\hat{\mathbf{g}}_{lo}\|^2-\mathbb{E}\left[\|\hat{\mathbf{g}}_{lo}\|^2\right]\right)}{\sqrt{N\gamma_{lo}}}q_{o_l}}_{T_2\text{: Beamforming uncertainity}}+\underbrace{\sum_{\mathbf{r}_l\in\Phi_{ro}}\frac{\|\hat{\mathbf{g}}_{lo}\|^2}{\sqrt{N\gamma_{lo}}}\sqrt{\rho_d\eta_{lo}}\tilde{q}_{o_l}}_{T_3\text{: compression error}}$$
$$+\underbrace{\sum_{\mathbf{r}_l\in\Phi_{ro}}\sqrt{\rho_d\eta_{lo}}\frac{\tilde{\mathbf{g}}_{lo}^T\hat{\mathbf{g}}_{lo}^*}{\sqrt{N\gamma_{lo}}}\hat{q}_{o_l}}_{T_4\text{: chanenel estimation error}}+\underbrace{\sum_{\mathbf{r}_l\in\Phi_{ro}}\sum_{\mathbf{u}_i\in\Psi_{ul}\setminus\{\mathbf{u}_o\}}\sqrt{\rho_d\eta_{li}}\frac{\mathbf{g}_{lo}^T\hat{\mathbf{g}}_{li}^*}{\sqrt{N\gamma_{li}}}\hat{q}_{i_l}}_{T_5\text{: inter user interference}}+\underbrace{\sum_{\mathbf{r}_l\in\Phi_{ro}^C}\sum_{\mathbf{u}_i\in\Psi_{ul}\setminus\mathcal{P}_o}\sqrt{\rho_d\eta_{li}}\frac{\mathbf{g}_{lo}^T\hat{\mathbf{g}}_{li}^*}{\sqrt{N\gamma_{li}}}\hat{q}_{i_l}}_{T_6\text{: interfering AP signal}}$$
$$+\underbrace{\sum_{\mathbf{u}_i\in\{\mathcal{P}_o\setminus\{\mathbf{u}_o\}\}}\sum_{\mathbf{r}_l\in\Phi_{ri}}\sqrt{\rho_d\eta_{li}}\frac{\mathbf{g}_{lo}^T\hat{\mathbf{g}}_{li}^*}{\sqrt{N\gamma_{li}}}\hat{q}_{i_l}}_{T_7\text{: pilot contamination}}+n_o, \tag{C.1}$$

where we assume that the user $\mathbf{u}_o$ has the average channel statistics with respect its serving APs, $\mathcal{P}_o$ contains the user locations that use the same pilot sequence as $\mathbf{u}_o$. From (C.1), it can be shown that the desired signal term is uncorrelated to the rest of the terms. An achievable rate is obtained by using the fact that mutual information is minimized when the uncorrelated signals to the desired signal is replaced by independent Gaussian noise [149] with variance equal to the sum of variances of undesired signals. Hence, the SINR corresponding to this lower bound on capacity is given as

$$\mathtt{SINR}_o=\frac{\mathbb{E}\left[|T_1|^2\right]}{\sum_{i=2}^{7}\mathbb{E}\left[|T_i|^2\right]+1}.$$

In this case, note that $\mathbb{E}\left[T_i\right]=0$ for all i. Further,

$$\mathbb{E}\left[|T_1|^2\right]=\rho_dN\left(\sum_{\mathbf{r}_l\in\Phi_{ro}}\sqrt{\frac{\gamma_{lo}(1-2^{-C_f/k_l})}{K_{\mathtt{max}}}}\right)^2,\mathbb{E}\left[|T_2|^2\right]=\rho_d\sum_{\mathbf{r}_l\in\Phi_{ro}}\frac{\gamma_{lo}(1-2^{-C_f/k_l})}{K_{\mathtt{max}}},$$
$$\mathbb{E}\left[|T_3|^2\right]=\rho_d(N+1)\sum_{\mathbf{r}_l\in\Phi_{ro}}\frac{\gamma_{lo}}{K_{\mathtt{max}}}2^{-C_f/k_l},\mathbb{E}\left[|T_4|^2\right]=\rho_d\sum_{\mathbf{r}_l\in\Phi_{ro}}\frac{(\beta_{lo}-\gamma_{lo})}{K_{\mathtt{max}}},$$

$$\mathbb{E}\left[|T_5|^2\right] = \rho_d \sum_{\mathbf{r}_l \in \Phi_{ro}} \frac{k_l - 1}{K_{\tt max}} \beta_{lo} \leq \rho_d \sum_{\mathbf{r}_l \in \Phi_{ro}} \frac{K_{\tt max} - 1}{K_{\tt max}} \beta_{lo}, \quad \mathbb{E}\left[|T_6|^2\right] = \rho_d \sum_{\mathbf{r}_l \in \Phi_{ro}^c} \leq \frac{K_{\tt max} - 1}{K_{\tt max}} \beta_{lo},$$

$$\mathbb{E}\left[|T_7|^2\right] = \rho_d \sum_{\mathbf{u}_i \in \{\mathcal{P}_o \setminus \mathbf{u}_o\}} \left(\sum_{\mathbf{r}_l \in \Phi_{ri}} \frac{\beta_{lo}}{K_{\tt max}} + N \left(\sum_{\mathbf{r}_l \in \Phi_{ri}} \sqrt{\frac{\gamma_{lo}}{K_{\tt max}}} \right)^2 \right).$$

Substituting these values, we obtain the expression presented in the lemma. ■

C.2 Proof of Lemma 7.7

The mean load of the N-th closest serving AP to the typical user at $\mathbf{o}$ is given as

$$\begin{aligned}
\mathbb{E}[K_N] &= \mathbb{E}\left[\sum_{\mathbf{x} \in \Phi_u} \mathbf{1}\left(|\Phi_r \cap \mathcal{B}_{r_x}(\mathbf{x})| \leq N_s - 1\right) \mathbf{1}\left(|\Phi_r \cap \mathcal{B}_{r_o}(\mathbf{o})| = N - 1\right)\right] \\
&= \mathbb{E}_{\Phi_u}\left[\sum_{\mathbf{x} \in \Phi_u} \mathbb{E}_{\Phi_r}\left[\mathbf{1}\left(|\Phi_r \cap \mathcal{B}_{r_x}(\mathbf{x})| \leq N_s - 1\right) \mathbf{1}\left(|\Phi_r \cap \mathcal{B}_{r_o}(\mathbf{o})| = N - 1\right)\right]\right],
\end{aligned}$$

where $r_o = \|\mathbf{r} - \mathbf{o}\|$, $r_x = \|\mathbf{r} - \mathbf{x}\| = \sqrt{r_o^2 + d_x^2 - 2r_o d_x \cos(v_x)}$, $d_x = \|\mathbf{x} - \mathbf{o}\|$ (please refer to Fig. C.1 (left)). Conditioned on the location of the AP at $\mathbf{r}$, we expand the inner expectation as

$$\begin{aligned}
&\mathbb{E}_{\{\Phi_r \setminus \mathbf{r}\}}\left[\sum_{n=0}^{N-1} \mathbf{1}_{(|\Phi_r \cap \mathcal{B}_{r_o}(\mathbf{o}) \cap \mathcal{B}_{r_x}(\mathbf{x})| = n)} \mathbf{1}_{(|\Phi_r \cap \{\mathcal{B}_{r_o}(\mathbf{o}) \setminus \mathcal{B}_{r_x}(\mathbf{x})\}| = N-n-1)} \mathbf{1}_{(|\Phi_r \cap \{\mathcal{B}_{r_x}(\mathbf{x}) \setminus \mathcal{B}_{r_o}(\mathbf{o})\}| \leq N_s - n - 1)}\right] \\
&= \sum_{n=0}^{N-1} \frac{(\lambda_r |\mathcal{B}_{r_o}(\mathbf{o}) \cap \mathcal{B}_{r_x}(\mathbf{x})|)^n}{n!} e^{-\lambda_r |\mathcal{B}_{r_o}(\mathbf{o}) \cap \mathcal{B}_{r_x}(\mathbf{x})|} \frac{(\lambda_r |\mathcal{B}_{r_o}(\mathbf{o}) \setminus \mathcal{B}_{r_x}(\mathbf{x})|)^{N-n-1}}{n!} e^{-\lambda_r |\mathcal{B}_{r_o}(\mathbf{o}) \setminus \mathcal{B}_{r_x}(\mathbf{x})|} \\
&\quad \sum_{l=0}^{N_s-n-1} \frac{(\lambda_r |\mathcal{B}_{r_x}(\mathbf{x}) \setminus \mathcal{B}_{r_o}(\mathbf{o})|)^{N_s-n-1}}{l!} e^{-\lambda_r |\mathcal{B}_{r_x}(\mathbf{x}) \setminus \mathcal{B}_{r_o}(\mathbf{o})|} \\
&= \sum_{n=0}^{N-1} \texttt{Pos}_{\texttt{PMF}}(n, \lambda_r \texttt{AoI}_2(r_o, d_x, v_x)) \texttt{Pos}_{\texttt{PMF}}(N - n - 1, \lambda_r(\pi r_o^2 - \texttt{AoI}_2(r_o, d_x, v_x))) \\
&\quad \texttt{Pos}_{\texttt{CMF}}(N_s - n - 1, \lambda_r(\pi r_x^2 - \texttt{AoI}_2(r_o, d_x, v_x))) = h_{\texttt{tag,m}_1}(r_o = \|\mathbf{r}\|, d_x, v_x),
\end{aligned} \tag{C.2}$$

where the second step follows from the fact that $\{\Phi_r \setminus \mathbf{r}\}$ is a homogeneous PPP with density λ_r and the regions in each indicator function are non-overlapping. The final result follows in two step: first we decondition over the point $\mathbf{r}$, then we decondition over Φ_u. We write this as

$$\mathbb{E}[K_N] = \mathbb{E}_{\Phi_u}\left[\sum_{\mathbf{x} \in \Phi_u} \int_{\mathbf{r} \in \mathbb{R}^2} h_{\texttt{tag,m}_1}(\|\mathbf{r}\|, d_x, v_x) \lambda_r \mathrm{d}\mathbf{r}\right]$$

$$= \mathbb{E}_{\Phi_u}\left[\sum_{\mathbf{x}\in\Phi_u} 2\pi\lambda_r \int_{r_o=0}^{\infty} h_{\texttt{tag},\texttt{m}_1}(r_o, d_x, v_x) r_o \mathrm{d}r_o\right]$$

$$= 2\pi\lambda_u\lambda_r \int_{r_o=0}^{\infty} \mathrm{d}r_o \int_{d_x=0}^{\infty} \mathrm{d}d_x \int_{v_x=0}^{2\pi} \mathrm{d}v_x h_{\texttt{tag},\texttt{m}_1}(r_o, d_x, v_x) r_o d_x,$$

where the last step follows from the application of Campbell's theorem.

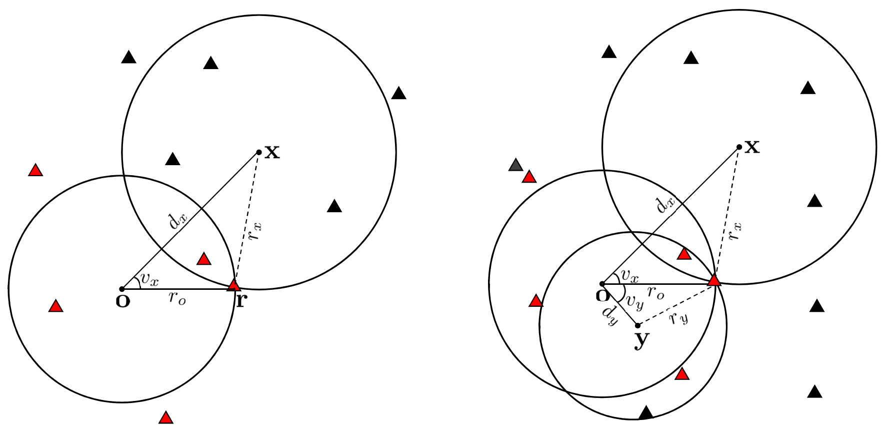

Figure C.1: The typical user is located at $\mathbf{o}$, $\mathbf{x}, \mathbf{y} \in \Phi_u$ are random user locations. The red triangles represent the serving AP locations of the typical user. The illustration is for the third nearest serving AP for the typical user.

The second moment of the load for the N-th nearest serving AP to the typical user is

$$\begin{aligned}
\mathbb{E}[|K_N|^2] =& \mathbb{E}\left[\left|\sum_{\mathbf{x}\in\Phi_u} \mathbf{1}_{|\Phi_r \cap \mathcal{B}_{r_x}(\mathbf{x})| \le N_s - 1} \mathbf{1}_{|\Phi_r \cap \mathcal{B}_{r_o}(\mathbf{o})| = N-1}\right|^2\right] \\
=& \mathbb{E}\left[\sum_{\mathbf{x}\in\Phi_u} \sum_{\mathbf{y}\in\Phi_u} \mathbf{1}_{|\Phi_r \cap \mathcal{B}_{r_x}(\mathbf{x})| \le N_s - 1} \mathbf{1}_{|\Phi_r \cap \mathcal{B}_{r_y}(\mathbf{y})| \le N_s - 1} \mathbf{1}_{|\Phi_r \cap \mathcal{B}_{r_o}(\mathbf{o})| = N-1}\right] \\
=& \mathbb{E}\left[\sum_{\mathbf{x}\in\Phi_u} \sum_{\substack{\mathbf{x}\neq\mathbf{y} \\ \mathbf{y}\in\Phi_u}} \mathbf{1}_{|\Phi_r \cap \mathcal{B}_{r_x}(\mathbf{x})| \le N_s - 1} \mathbf{1}_{|\Phi_r \cap \mathcal{B}_{r_y}(\mathbf{y})| \le N_s - 1} \mathbf{1}_{|\Phi_r \cap \mathcal{B}_{r_o}(\mathbf{o})| = N-1}\right] \\
&+ \mathbb{E}\left[\sum_{\mathbf{x}\in\Phi_u} \mathbf{1}_{|\Phi_r \cap \mathcal{B}_{r_x}(\mathbf{x})| \le N_s - 1} \mathbf{1}_{|\Phi_r \cap \mathcal{B}_{r_o}(\mathbf{o})| = N-1}\right].
\end{aligned}$$

On the right hand side of the above equation, the second summation term is the mean $\mathbb{E}[K_N]$, which has been derived above. We focus on deriving an expression for the first term (please refer to Fig. C.1 (right)). Let is Using (7.13), let us define $u_x = u(r_o, d_x, v_x)$, $u_y = u(r_o, d_y, v_y)$, and

$$u_{xy} = \begin{cases} u_x + u_y, & \{v_x < \pi, v_y > \pi\}, \\ u_x + u_y, & \{v_x > \pi, v_y < \pi\}, \\ |u_x - u_y|, & \text{Otherwise.} \end{cases} \tag{C.3}$$

Further, let us denote the region of intersection of three circles as $\mathtt{RoI_{oxy}} = \{\mathcal{B}_{r_o}(\mathbf{o}) \cap \mathcal{B}_{r_x}(\mathbf{x}) \cap \mathcal{B}_{r_y}(\mathbf{y})\}$, the region exclusive to both the circles centered at $\mathbf{o}$ and $\mathbf{x}$ as $\mathtt{RoI_{ox}} = \{\mathcal{B}_{r_o}(\mathbf{o}) \cap \mathcal{B}_{r_x}(\mathbf{x})\} \setminus \mathtt{RoI_{oxy}}$, the regions exclusive to both the circles at $\mathbf{o}$ and $\mathbf{y}$ as $\mathtt{RoI_{oy}} = \{\mathcal{B}_{r_o}(\mathbf{o}) \cap \mathcal{B}_{r_y}(\mathbf{y})\} \setminus \mathtt{RoI_{oxy}}$, and the common region exclusive to circles at $\mathbf{x}$ and $\mathbf{y}$ as $\mathtt{RoI_{xy}} = \{\mathcal{B}_{r_x}(\mathbf{x}) \cap \mathcal{B}_{r_y}(\mathbf{y})\} \setminus \mathtt{RoI_{oxy}}$. Conditioned on Φ_u and $\mathbf{r}$, we write

$$\begin{aligned}
&\mathbb{E}_{\{\Phi_r \setminus \mathbf{r}\}}\left[\mathbf{1}_{|\Phi_r \cap \mathcal{B}_{r_x}(\mathbf{x})| \le N_s - 1} \mathbf{1}_{|\Phi_r \cap \mathcal{B}_{r_y}(\mathbf{y})| \le N_s - 1} \mathbf{1}_{|\Phi_r \cap \mathcal{B}_{r_o}(\mathbf{o})| = N - 1}\right] \\
&\stackrel{(b)}{=} \mathbb{E}_{\{\Phi_r \setminus \mathbf{r}\}}\Bigg[\sum_{n=0}^{N-1} \mathbf{1}_{|\Phi_r \cap \mathtt{RoI_{oxy}}| = n} \sum_{m=0}^{N-n-1} \mathbf{1}_{|\Phi_r \cap \mathtt{RoI_{ox}}| = m} \sum_{p=0}^{N-m-n-1} \mathbf{1}_{|\Phi_r \cap \mathtt{RoI_{oy}}| = p} \mathbf{1}_{|\Phi_r \cap \{\mathcal{B}_{r_o}(\mathbf{o}) \setminus \{\mathcal{B}_{r_x}(\mathbf{x}) \cup \mathcal{B}_{r_y}(\mathbf{y})\}\}| = N-n-m-p-1} \\
&\qquad \sum_{q=0}^{\min\{N_s-n-m-1, N_s-n-p-1\}} \mathbf{1}_{|\Phi_r \cap \mathtt{RoI_{xy}}| = q} \mathbf{1}_{|\Phi_r \cap \{\mathcal{B}_{r_x}(\mathbf{x}) \setminus \{\mathcal{B}_{r_o}(\mathbf{o}) \cup \mathcal{B}_{r_y}(\mathbf{y})\}\}| \le N_s - n - m - q - 1} \\
&\qquad \mathbf{1}_{|\Phi_r \cap \{\mathcal{B}_{r_y}(\mathbf{y}) \setminus \{\mathcal{B}_{r_o}(\mathbf{o}) \cup \mathcal{B}_{r_x}(\mathbf{x})\}\}| \le N_s - n - p - q - 1}\Bigg] \\
&\stackrel{(c)}{=} \sum_{n=0}^{N-1} \mathtt{Pos_{PMF}}(n, \lambda_r \mathtt{AoI_3}(r_o, r_x, r_y, v_x, v_y)) \\
&\quad \times \sum_{m=0}^{N-n-1} \mathtt{Pos_{PMF}}(m, \lambda_r(\mathtt{AoI_2}(r_o, r_x, v_x) - \mathtt{AoI_3}(r_o, r_x, r_y, v_x, v_y))) \\
&\quad \times \sum_{p=0}^{N-n-m-1} \mathtt{Pos_{PMF}}(p, \lambda_r(\mathtt{AoI_2}(r_o, r_y, v_y) - \mathtt{AoI_3}(r_o, r_x, r_y, v_x, v_y))) \\
&\quad \times \mathtt{Pos_{PMF}}(N - n - m - p - 1, \lambda_r(\pi r_o^2 - \mathtt{AoI_2}(r_o, r_x, v_x) - \mathtt{AoI_2}(r_o, r_y, v_y) + \mathtt{AoI_3}(r_o, r_x, r_y, v_x, v_y))) \\
&\quad \times \sum_{q=0}^{\min\left\{\substack{N_s-n-m-1, \\ N_s-n-p-1}\right\}} \mathtt{Pos_{PMF}}(q, \lambda_r(\mathtt{AoI_2}(r_x, r_y, u_{xy}) - \mathtt{AoI_3}(r_o, r_x, r_y, v_x, v_y))) \\
&\quad \times \mathtt{Pos_{PMF}}(N_s - n - m - q - 1, \lambda_r(\pi r_x^2 - \mathtt{AoI_2}(r_o, r_x, v_x) - \mathtt{AoI_2}(r_x, r_y, u_{xy}) + \mathtt{AoI_3}(r_o, r_x, r_y, v_x, v_y))) \\
&\quad \times \mathtt{Pos_{PMF}}(N_s - n - p - q - 1, \lambda_r(\pi r_y^2 - \mathtt{AoI_2}(r_o, r_y, v_y) - \mathtt{AoI_2}(r_x, r_y, u_{xy}) + \mathtt{AoI_3}(r_o, r_x, r_y, v_x, v_y))) \\
&\quad = h_{\mathtt{tag,m_2}}(r_o, d_x, d_y, v_x, v_y),
\end{aligned} \tag{C.4}$$

where $r_i = \sqrt{d_i^2 + r_o^2 - 2r_o d_i \cos(v_i)}$ for $i \in \{x, y\}$, the function $\mathtt{AoI_2}(\cdot,\cdot,\cdot)$ is given in (7.12), the area of intersection of three circles is evaluated as per the procedure presented in Appendix C.4. The step (a) follows from the fact that the regions in indicator functions are non-overlapping and $\Phi_r \setminus \mathbf{r}$ is a homogeneous PPP with density λ_r. Similar to the derivation of the first moment, we obtain the final expression for the second moment by deconditioning over $\mathbf{r}$ and then over Φ_u by application of Campbell's theorem.

C.3 Proof of Lemma 7.9

Much of the derivation can be done on the similar lines as that of Appendix C.2. Since Φ_r is a homogeneous PPP, it is translation invariant. Hence, we assume that the typical AP is located at the origin. The mean load of the AP can be written as

$$\mathbb{E}[K_o] = \mathbb{E}\left[\sum_{\mathbf{x}\in\Phi_u} \mathbb{E}\left[\mathbf{1}\left(|\Phi_r \cap \mathcal{B}_{\|\mathbf{x}\|}(\mathbf{x})| \leq N_s - 1\right)\right]\right]$$
$$= 2\pi\lambda_u \int_{r=0}^{\infty} \sum_{l=0}^{N_s-1} \frac{(\pi\lambda_r r^2)^l}{l!} \exp(-\pi\lambda_r r^2) r \mathrm{d}r \quad \overset{(a)}{=} \frac{\lambda_u}{\lambda_r} \sum_{l=0}^{N_s-1} \int_{u=0}^{\infty} \frac{u^l}{l!} \exp(-u)\mathrm{d}u = \frac{N_s\lambda_u}{\lambda_r},$$

where (a) follows from replacing $u = \pi\lambda_r r^2$. The second moment of the load can be written as

$$\mathbb{E}[K_o^2] = \mathbb{E}\left[\left|\sum_{\mathbf{x}\in\Phi_u} \mathbf{1}\left(|\Phi_r \cap \mathcal{B}_{\|\mathbf{x}\|}(\mathbf{x})| \leq N_s - 1\right)\right|^2\right]$$
$$= \mathbb{E}\left[\sum_{\mathbf{x}\in\Phi_u} \sum_{\mathbf{y}\in\Phi_u}^{\mathbf{x}\neq\mathbf{y}} \mathbb{E}_{\Phi_r}\left[\mathbf{1}_{|\Phi_r\cap\mathcal{B}_{\|\mathbf{x}\|}(\mathbf{x})|\leq N_s-1} \mathbf{1}_{|\Phi_r\cap\mathcal{B}_{\|\mathbf{y}\|}(\mathbf{y})|\leq N_s-1}\right]\right] + \underbrace{\mathbb{E}\left[\sum_{\mathbf{x}\in\Phi_u} \mathbb{E}\left[\mathbf{1}_{|\Phi_r\cap\mathcal{B}_{\|\mathbf{x}\|}(\mathbf{x})|\leq N_s-1}\right]\right]}_{\mathbb{E}[K_o]}.$$

The inner expectation in the first term on the RHS can be decomposed as

$$\mathbb{E}_{\Phi_r}\left[\mathbf{1}_{|\Phi_r\cap\mathcal{B}_{\|\mathbf{x}\|}(\mathbf{x})|\leq N_s-1} \mathbf{1}_{|\Phi_r\cap\mathcal{B}_{\|\mathbf{y}\|}(\mathbf{y})|\leq N_s-1}\right] =$$
$$= \sum_{l=0}^{N_s-1} \mathbb{E}_{\Phi_r}\left[\mathbf{1}_{|\Phi_r\cap\{\mathcal{B}_{\|\mathbf{x}\|}(\mathbf{x})\cap\mathcal{B}_{\|\mathbf{y}\|}(\mathbf{y})\}|=l} \mathbf{1}_{|\Phi_r\cap\{\mathcal{B}_{\|\mathbf{y}\|}(\mathbf{y})\setminus\{\mathcal{B}_{\|\mathbf{x}\|}(\mathbf{x})\cap\mathcal{B}_{\|\mathbf{y}\|}(\mathbf{y})\}|\leq N_s-l-1}\right.$$
$$\left.\times\, \mathbf{1}_{|\Phi_r\cap\{\mathcal{B}_{\|\mathbf{x}\|}(\mathbf{x})\setminus\{\mathcal{B}_{\|\mathbf{x}\|}(\mathbf{x})\cap\mathcal{B}_{\|\mathbf{y}\|}(\mathbf{y})\}|\leq N_s-l-1}\right].$$

From the above expression, we obtain the expression for $h_{\mathtt{typ,m2}}(r_x, r_y, u)$ by taking the expectation with respect to Φ_r. Now, with the application of Campbell's formula, we get the final expression of the lemma as

$$\mathbb{E}\left[\sum_{\mathbf{x}\in\Phi_u} \sum_{\mathbf{y}\in\Phi_u}^{\mathbf{x}\neq\mathbf{y}} h_{\mathtt{typ,m2}}(r_x, r_y, u)\right] = 2\pi\lambda_u^2 \int_{r_x=0}^{\infty} \int_{r_y=0}^{\infty} \int_{u=0}^{2\pi} h_{\mathtt{typ,m2}}(r_x, r_y, u) \mathrm{d}u r_y \mathrm{d}r_y r_x \mathrm{d}r_x,$$

where r_x, r_y, and u are as depicted in Fig. C.2.

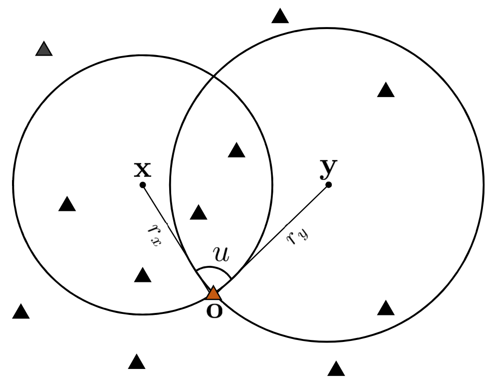

Figure C.2: **x** and **y** correspond to user locations and **o** correspond to the typical AP location. The number of APs in each non-overlapping region follow independent Poisson distribution.

C.4 Area of Intersection of Three Circles

Note that owing to the constraint that three circles have a common point of intersection, the common area of intersection will either of the following three cases: (1) a point with area zero, (2) a lens, or (3) a circular triangle. All three cases are presented in Fig. C.3. In the case, when the common area of intersection is a circular triangle (right most case in Fig. C.3), the area is given as [150]

$$
\begin{aligned}
\mathtt{AoI}_3(r_o, r_x, r_y, v_x, v_y) =& \frac{1}{4}\sqrt{(c_1+c_2+c_3)(c_2+c_3-c_1)(c_1+c_3-c_2)(c_1+c_2-c_3)} \\
&+ r_o^2 \arcsin\frac{c_1}{2r_o} - \frac{c_1}{4}\sqrt{4r_o^2 - c_1^2} + r_y^2 \arcsin\frac{c_2}{2r_y} - \frac{c_2}{4}\sqrt{4r_y^2 - c_2^2} \\
&+ r_x^2 \arcsin\frac{c_3}{2r_x} - \frac{c_3}{4}\sqrt{4r_x^2 - c_3^2},
\end{aligned}
$$

where c_1, c_2, c_3 are chord lengths as denoted in the figure. Please note that the first two cases are special cases of the third case, e.g. we can get the second case by replacing $c_2 = 0$ and $c_1 = c3$. Similarly, in the first case, $c_1 = c_2 = c_3 = 0$. Further, c_is are functions of r_o, r_x, r_y, v_x, v_y. The procedure to determine them is outlined in [150] that is followed in this work.

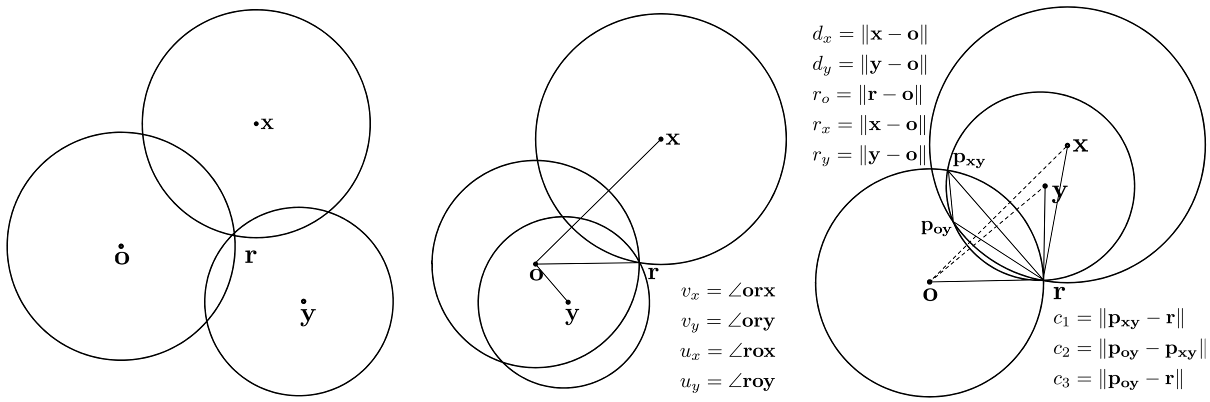

Figure C.3: Three possible configurations of three circle intersection with one common point of intersection $\mathbf{r}$. The fourth configuration in which the smallest circle lies inside the two bigger circles has been ignored as it is a zero probability event. Different distances and angles are marked in the Figure.

C.5 Proof of Proposition 6

Ignoring the pilot contamination term in the expression of achievable rate in (7.4), we can write the rate coverage as

$$R_c = \mathbb{P}\Bigg[\frac{\rho_d N}{2^{T_r}-1}\Bigg(\sum_{\mathbf{r}_l \in \Phi_{ro}} \sqrt{\gamma_{lo}(1-2^{-C_f/k_l})/K_{\mathtt{max}}}\Bigg)^2 - \rho_d N \sum_{\mathbf{r}_l \in \Phi_{ro}} \gamma_{lo} 2^{-C_f/k_l}/K_{\mathtt{max}} \\ - \rho_d \sum_{\mathbf{r}_l \in \Phi_{ro}} \beta_{lo} - 1 \geq \rho_d \sum_{\mathbf{r}_l \in \Phi_{ro}^C} \beta_{lo}\Bigg]. \tag{C.5}$$

To proceed further, we first condition on the distance to the N_s-th serving AP d_{oN_s}. Condition on this distance, we replace $\sum_{\mathbf{r}_l \in \Phi_{ro}^C} \beta_{lo}$ by its mean which is given as

$$\mathbb{E}_{\Phi_{ro}^C}[\sum_{\mathbf{r}_l \in \Phi_{ro}^C} \beta_{lo}] = 2\pi\lambda_r \int_{r=d_{oN_s}}^{\infty} l(r) r \mathrm{d}r.$$

The above result follows from the application of Campbell's theorem. Note that using the mean instead of the exact expectation has marginal impact on the accuracy of the result as $\sum_{\mathbf{r}_l \in \Phi_r} \beta_{lo}$ is dominated by contributions from the nearest N_s serving APs. Hence, we can write

$$\sum_{\mathbf{r}_l \in \Phi_r} \beta_{lo} \approx \sum_{\mathbf{r}_l \in \Phi_{ro}} \beta_{lo} + \mathbb{E}_{\Phi_{ro}^C}[\sum_{\mathbf{r}_l \in \Phi_{ro}^C} \beta_{lo}].$$

Next, the loads among the serving APs are correlated. Hence, to get the accurate result, we need to evaluate the (C.5) with respect to the joint distribution of $\{K_i\}_{i=1}^{N_s}$. However, obtaining this joint distribution is extremely challenging and is not tractable. Hence, we exactly consider the load of the nearest AP and replace the load of the rest of the APs by its effective mean. For the i-th nearest AP, the effective mean is given as $\bar{K}_i = 1 + \sum_{k_i=0}^{\infty} \min\{k_i, K_{\texttt{max}}\}\mathbb{P}[K_i = k_i]$, where K_i follows negative binomial distribution whose PMF is determined using the moment matching method presented in Sec. 7.4.1. With the above two approximation, condition on the distances to the serving APs and the load of the nearest AP to the typical user, the link rate coverage is given as

$$R_c = \mathbb{E}_{k_1, d_{o1}, \ldots, d_{oN_s}} \left[\mathbf{1} \left(2\pi\lambda_r \int\limits_{d_{oN_s}}^{\infty} l(r) r \mathrm{d}r \leq h_{\texttt{cov}}(k_1, d_{o1}, d_{o2}, \ldots, d_{oN_s}) \right) \right], \tag{C.6}$$

where $h_{\texttt{cov}}(k_1, d_{o1}, d_{o2}, \ldots, d_{oN_s})$ is given by (7.15). Note that conditioned on d_{oN_s}, d_{oi} for $1 \leq i \leq N_s - 1$ are i.i.d. distributed with following PDF [10]

$$f_{D_{oi}}(d_{oi}) = \frac{2d_{oi}}{d_{oN_s}^2}, \quad 0 \leq d_{oi} \leq d_{oN_s}.$$

Further, the PDF of D_{oN_s} is given as [10]

$$f_{D_{oN_s}}(d_{oN_s}) = \frac{2}{\Gamma(N_s)} (\pi\lambda_r)^{N_s} d^{2N_s-1} \exp(-\pi\lambda_r d_{oN_s}^2).$$

We evaluate the expectation in (C.6) using the aforementioned distance distributions along with the PMF of the load K_1 associated with the nearest tagged AP.

Appendix D

Proofs of Lemmas and Propositions of Chapter 8

D.1 Proof of Lemma 8.2

As discussed in Section 8.3, in order to evaluate the `MAP`, we ignore the effect of all the PZs except the nearest one. In addition, due to the nearest neighbor connectivity, there are no OpB BSs in $\mathcal{B}_{r_o^B}(\mathbf{u}_o^B)$ (See Fig. 8.4b). Therefore, we consider the points in the set $\{x \in \Psi_B : x \notin \{\mathcal{B}_{R_{pz}}(\mathbf{y}_{oB}^A) \cup \mathcal{B}_{r_o^B}(\mathbf{u}_o^B)\}\}$. Using (8.9), the modified MAI of the tagged BS is given as

$$\tilde{\mathcal{I}}_o^B = \prod_{\mathbf{x}_i^B \in \Psi_B \setminus \mathbf{x}_o^B} \mathbf{1}_{\mathbf{x}_i^B \notin \{\mathcal{B}_{R_{pz}}(\mathbf{y}_{oB}^A) \cup \mathcal{B}_{r_o^B}(\mathbf{u}_o^B)\}} \left(\mathbf{1}_{P_r(\mathbf{x}_o^B, \mathbf{x}_i^B) \leq \tau_{cs}} + \mathbf{1}_{P_r(\mathbf{x}_o^B, \mathbf{x}_i^B) > \tau_{cs}} \mathbf{1}_{t_{x_j}^B > t_{x_o}^B} \right). \tag{D.1}$$

Without loss of generality, we make the tagged BS as our reference point (i.e. origin) as shown in Fig. 8.4b. Let $\tilde{\Psi}_B = \{\mathbf{x} \in \Psi_B : \mathbf{x} \notin \mathcal{B}_{r_o^B}(\mathbf{u}_o^B)\}$. With application of Lemma 8.1, the density function of $\tilde{\Psi}_B$ is $\lambda_{\Psi_B}(x|r_o^B) = \mathcal{E}(x, \lambda_B, r_o^B, r_o^B)$. Now, conditioned on the distances R_o^B and $R_{o,AB} = \|\mathbf{y}_{oB}^A - \mathbf{x}_o^B\|$, and the back-off timer of the tagged BS $t_{x_o}^B = t$,

$$\begin{aligned}
&\mathbb{P}\left[\mathcal{I}_o^B = 1 \middle| t, r_{o,AB}, r_o^B\right] \\
\overset{(a)}{\geq} &\mathbb{P}\left[\tilde{\mathcal{I}}_o^B = 1 \middle| t, r_{o,AB}, r_o^B\right] = \mathbb{E}\left[\tilde{\mathcal{I}}_o^B \middle| t, r_{o,AB}, r_o^B\right] \\
= &\mathbb{E}\Bigg[\prod_{\mathbf{x}_i^B \in \tilde{\Psi}_B \setminus \{\mathcal{B}_{R_{pz}}(\mathbf{y}_{oB}^A) \cup \mathbf{x}_o^B\}} \mathbb{E}\Big[\mathbf{1}_{P_r(\mathbf{x}_o^B, \mathbf{x}_i^B) \leq \tau_{cs}} \\
&+ \mathbf{1}_{P_r(\mathbf{x}_o^B, \mathbf{x}_i^B) > \tau_{cs}} \mathbf{1}_{t < t_{x_i}^B}\Big] \Bigg| t, r_{o,AB}, r_o^B\Bigg] \\
\overset{(b)}{=} &\mathbb{E}\Bigg[\prod_{\mathbf{x}_i^B \in \tilde{\Psi} \setminus \{\mathcal{B}_{R_{pz}}(\mathbf{y}_{oB}^A) \cup \mathbf{x}_o^B\}} \left(1 - t \exp\left(-\frac{\tau_{cs} l(\|\mathbf{x}_i^B\|)}{P_B}\right)\right)\Bigg] \\
\overset{(c)}{=} &\exp\left(-\int_{\mathbf{x} \in \mathbb{R}^2 \setminus \{\mathcal{B}_{R_{pz}}(\mathbf{y}_{oB}^A) \cup \mathbf{x}_o^B\}} t \lambda_{\Psi_B}(\|\mathbf{x}\| | r_o^B) e^{-\frac{\tau_{cs} l(\|\mathbf{x}\|)}{P_B}} \mathbf{x} \mathrm{d}\mathbf{x}\right)
\end{aligned}$$

$$\overset{(d)}{=} \exp\Bigg(- t\big(2\pi \int_0^{\infty} \lambda_{\Psi_B}(y|r_o^B) e^{\frac{-\tau_{cs} l(y)}{P_B}} y \mathrm{d}y$$

$$- 2 \int_{r_{o,AB}-R_{pz}}^{r_{o,AB}+R_{pz}} \lambda_{\Psi_B}(y|r_o^B) e^{\frac{-\tau_{cs} l(y)}{P_B}} \varphi_{pz}(y|r_{o,AB}) y \mathrm{d}y\big)\Bigg), \tag{D.2}$$

where (a) follows from the fact that we are considering more number of points in $\tilde{\mathcal{I}}_o^B$ than in $\mathcal{I}_o^B$, (b) follows from the fact that small scale fading is exponentially distributed and $t_{x_i}^B$ is uniformly distributed between $[0,1]$, (c) follows from the application of the PGFL of the PPP, (d) follows from changing Cartesian co-ordinates to polar co-ordinates, and $\varphi_{pz}(y|r_{o,AB}) = \frac{r_{o,AB}^2 + y^2 - R_{pz}^2}{2yr_{o,AB}}$. The expression for $f_1(\cdot)$ in Lemma 8.2 is obtained after deconditioning over $t_{x_o}^B$, which is uniformly distributed in $[0,1]$.

D.2 Proof of Lemma 8.3

In this proof, we derive the conditional CDF of $R_{o,AB}$ for Event-2, i.e. the probability denoted by K_2 in (8.23). For notational simplicity we do not mention the condition $E_2(r_o^B) = \{N_{\Phi_B}(\mathcal{B}_{r_o^B}(\mathbf{u}_o^B)) = 0, N_{\Psi_B}(\mathcal{B}_{r_o^B}(\mathbf{u}_o^B)) = 0\}$ and implicitly consider it for all the expressions. Conditioned on R_o^B, the location of the nearest OpA BS from the typical user is constrained by the condition that it has to lie outside the circle $\mathcal{B}_{R_{pz}}(\mathbf{x}_o^B)$ (Refer to Fig. 8.6a). Now, at a distance r_o^A, the location of the nearest OpA BS lies on a ring. Hence, its location is uniformly distributed between the angles $[-\varphi_{AB}(r_o^A, r_o^B, R_{pz}), \varphi_{AB}(r_o^A, r_o^B, R_{pz})]$, where $\varphi_{AB}(r_o^A, r_o^B, R_{pz})$ is given by (8.29). Now the CDF of $R_{o,AB}$ conditioned on R_o^A, R_o^B, and Θ_A is given as

$$\mathbb{P}\left[R_{o,AB} \le r_{o,AB} \middle| r_o^A, r_o^B, \theta_A\right]$$

$$\overset{(a)}{=} \mathbb{P}\left[R_{o,AB} \le r_{o,AB} \middle| N_{\Psi_A}\left(\mathcal{C}_1(\hat{r}_{o,AB})\right) = 0, r_o^A, r_o^B, \theta_A\right]$$

$$\times \mathbb{P}\left[N_{\Psi_A}\left(\mathcal{C}_1(\hat{r}_{o,AB})\right) = 0 \middle| r_o^A, r_o^B, \theta_A\right]$$

$$+ \mathbb{P}\left[R_{o,AB} \le r_{o,AB} \middle| N_{\Psi_A}\left(\mathcal{C}_1(\hat{r}_{o,AB})\right) \neq 0, r_o^A, r_o^B, \theta_A\right]$$

$$\times \mathbb{P}\left[N_{\Psi_A}\left(\mathcal{C}_1(\hat{r}_{o,AB})\right) \neq 0 \middle| r_o^A, r_o^B, \theta_A\right]$$

$$\overset{(b)}{=} \mathbf{1}(\hat{r}_{o,AB} \le r_{o,AB}) \exp(-\lambda_A |\mathcal{C}_1(\hat{r}_{o,AB})|)$$

$$+ \mathbb{P}\left[\tilde{R}_{o,AB} \le r_{o,AB} | r_o^A, r_o^B, \theta_A\right]$$

$$\times \left(1 - \exp(-\lambda_A |\mathcal{C}_1(\hat{r}_{o,AB})|)\right), \tag{D.3}$$

where (a) follows from the application of law of total probability, and (b) follows from (8.25) and the fact that number of points in $\mathcal{C}_1(\hat{r}_{o,AB})$ is Poisson distributed with mean $\lambda_A|\mathcal{C}_1(\hat{r}_{o,AB})|$. The second term in the summation is

$$\begin{aligned}
&\mathbb{P}\left[\tilde{R}_{o,AB} \leq r_{o,AB} | r_o^A, r_o^B, \theta_A\right] \\
=&\mathbb{P}\left[R_{o,AB} \leq r_{o,AB} | N_{\Psi_A}\left(\mathcal{C}_1(\hat{r}_{o,AB})\right) \neq 0, r_o^A, r_o^B, \theta_A\right] \\
=&\frac{\mathbb{P}\left[R_{o,AB} \leq r_{o,AB}, N_{\Psi_A}\left(\mathcal{C}_1(\hat{r}_{o,AB})\right) \neq 0 | r_o^A, r_o^B, \theta_A\right]}{\mathbb{P}\left[N_{\Psi_A}\left(\mathcal{C}_1(\hat{r}_{o,AB})\right) \neq 0 | r_o^A, r_o^B, \theta_A\right]} \\
=&\begin{cases} 1 & r_{o,AB} \geq \hat{r}_{o,AB} \\ \frac{1-\exp(-\lambda_A|\mathcal{C}_1(r_{o,AB})|)}{1-\exp(-\lambda_A|\mathcal{C}_1(\hat{r}_{o,AB})|)} & r_{o,AB} < \hat{r}_{o,AB}. \end{cases}
\end{aligned} \tag{D.4}$$

Substituting (D.4) in (D.3), we get

$$\begin{aligned}
&\mathbb{P}\left[R_{o,AB} \leq r_{o,AB} | r_o^A, r_o^B, \theta_A\right] \\
=&\mathbf{1}(\hat{r}_{o,AB} \leq r_{o,AB}) \exp(-\lambda_A|\mathcal{C}_1(\hat{r}_{o,AB})|) \\
&+ \mathbf{1}(\hat{r}_{o,AB} \leq r_{o,AB})(1 - \exp(-\lambda_A|\mathcal{C}_1(\hat{r}_{o,AB})|)) \\
&+ \mathbf{1}(\hat{r}_{o,AB} > r_{o,AB})(1 - \exp(-\lambda_A|\mathcal{C}_1(r_{o,AB})|)) \\
=&\mathbf{1}(\hat{r}_{o,AB} \leq r_{o,AB}) \\
&+ \mathbf{1}(\hat{r}_{o,AB} > r_{o,AB})(1 - \exp(-\lambda_A|\mathcal{C}_1(r_{o,AB})|)).
\end{aligned} \tag{D.5}$$

The final expression in the Lemma is obtained by deconditioning (D.5) w.r.t. conditional density function of Θ_A given in (8.28).

D.3 Proof of Lemma 8.4

As per our discussion in Section 8.3.1 on Event-1 and Event-2, using the law of total probability, the distance distribution of R_o^A can be written as

$$\begin{aligned}
F_{R_o^A}(r_o^A|r_o^B) &= \mathbb{P}\left[R_o^A \leq r_o^A \middle| N_{\Phi_B}(\mathcal{B}_{r_o^B}(\mathbf{u}_o^B)) = 0, r_o^B\right] \\
=&\underbrace{\mathbb{P}\left[R_o^A \leq r_o^A \middle| E_2(r_o^B), r_o^B\right]}_{T_1} \\
&\underbrace{\mathbb{P}\left[N_{\Psi_B}(\mathcal{B}_{r_o^B}(\mathbf{u}_o^B)) = 0 | N_{\Phi_B}(\mathcal{B}_{r_o^B}(\mathbf{u}_o^B)) = 0, r_o^B\right]}_{T_2} \\
&+ \underbrace{\mathbb{P}\left[R_o^A \leq r_o^A \middle| E_1(r_o^B), r_o^B\right]}_{T_3}
\end{aligned}$$

$$\underbrace{\mathbb{P}\left[N_{\Psi_B}(\mathcal{B}_{r_o^B}(\mathbf{u}_o^B)) \neq 0 | N_{\Phi_B}(\mathcal{B}_{r_o^B}(\mathbf{u}_o^B)) = 0, r_o^B\right]}_{T_4}, \tag{D.6}$$

where the conditional CDF for Event-2 and Event-1 is denoted by T_3 and T_1, respectively.

Now for Event-2, the locations of OpA BSs follow a homogeneous PPP of density λ_A outside the circle $\mathcal{B}_{R_{pz}}(\mathbf{x}_o^B)$, which is equivalent to having a hole $\mathcal{B}_{R_{pz}}(\mathbf{x}_o^B)$ in Ψ_A. Therefore, with application of Lemma 1, the conditional CDF of R_o^A for Event-2 is

$$T_1 = 1 - \exp(-\mathcal{G}(r_o^A, \lambda_A, R_{pz}, r_o^B)). \tag{D.7}$$

On the other hand, T_3 corresponds to Event-1, where there is at least one OpA BS in $\mathcal{B}_{r_o^B+R_{pz}}(\mathbf{u}_o^B) \setminus \mathcal{B}_{R_{pz}}(\mathbf{x}_o^B)$ (Refer Fig. 8.5a). Further, to ensure that all the points of Ψ_B in $\mathcal{B}_{r_o^B}(\mathbf{u}_o^B)$ have been deleted, the conditional density of OpA BS in the $\mathcal{B}_{r_o^B+R_{pz}}(\mathbf{u}_o^B) \setminus \mathcal{B}_{R_{pz}}(\mathbf{x}_o^B)$ is likely to be higher than λ_A. Accurate characterization of this density requires exact consideration of number of PZs in the region and their relative overlaps, which is a difficult proposition. Hence, we consider the density of Ψ_A in $\mathcal{B}_{r_o^B+R_{pz}}(\mathbf{u}_o^B) \setminus \mathcal{B}_{R_{pz}}(\mathbf{x}_o^B)$ to be λ_A and obtain the CDF of T_3 given in (D.8). Note that since we are underestimating the density of Ψ_A, this conditional CDF is a lower bound on the actual CDF.

$$T_3 = \mathbb{P}\left[R_o^A \leq r_o^A \middle| E_1(r_o^B), r_o^B\right] = \begin{cases} 0 & r_o^A + r_o^B \leq R_{pz} \\ \frac{1-\exp(-\lambda_A|\mathcal{C}_2(r_o^A, r_o^B, R_{pz})|)}{1-\exp(-\lambda_A|\mathcal{C}_2(r_o^B+R_{pz}, r_o^B, R_{pz})|)} & r_o^A + r_o^B > R_{pz}, \end{cases} \tag{D.8}$$

where $\mathcal{C}_2(r_o^A, r_o^B, R_{pz}) = \mathcal{B}_{r_o^A}(\mathbf{u}_o^B) \setminus \{\mathcal{B}_{r_o^A}(\mathbf{u}_o^B) \cap \mathcal{B}_{R_{pz}}(\mathbf{x}_o^B)\}$.

In order to obtain the probabilities given by T_3 and T_4, we observe that, we first need to determine $\mathbb{P}\left[N_{\Phi_B}(\mathcal{B}_{r_o^B}(\mathbf{u}_o^B)) = 0 \middle| r_o^B\right]$, which is the complementary CDF of the contact distance of PHP, i.e. $\mathbb{P}\left[N_{\Phi_B}(\mathcal{B}_{r_o^B}(\mathbf{u}_o^B)) = 0 \middle| r_o^B\right] = 1 - F_{R_o^B}(r_o^B)$. Now T_2 can be expressed as

$$\begin{aligned} &\mathbb{P}\left[N_{\Psi_B}(\mathcal{B}_{r_o^B}(\mathbf{u}_o^B)) = 0 | N_{\Phi_B}(\mathcal{B}_{r_o^B}(\mathbf{u}_o^B)) = 0, r_o^B\right] \\ =&\frac{\mathbb{P}\left[N_{\Psi_B}(\mathcal{B}_{r_o^B}(\mathbf{u}_o^B)) = 0 | r_o^B\right]}{\mathbb{P}\left[N_{\Phi_B}(\mathcal{B}_{r_o^B}(\mathbf{u}_o^B)) = 0 | r_o^B\right]} = \frac{\exp(-\pi\lambda_A (r_o^B)^2)}{1 - F_{R_o^B}(r_o^B)}. \end{aligned}$$

On the other hand, T_4 denotes the probability of the complementary event of $E_2(r_o^B)$ and its expression is given as

$$T_4 = 1 - T_2 = 1 - \frac{\exp(-\pi\lambda_A (r_o^B)^2)}{1 - F_{R_o^B}(r_o^B)}. \tag{D.9}$$

This completes the proof of the Lemma.

D.4 Proof of Lemma 8.7

This Lemma can be proved on the similar lines as that of the proof of Lemma 8.4. First we approximate the CDF of R_o^A conditioned on Event-1, i.e. $F_{R_o^A}(r_o^A | r_o^B, E_1(r_o^B))$ presented in (D.6). As discussed earlier, conditioned on Event-1, the average number of OpA BSs in $\mathcal{B}_{r_o^B+R_{pz}}(\mathbf{u}_o^B) \setminus \mathcal{B}_{R_{pz}}(\mathbf{x}_o^B)$ is likely to be larger than $\lambda_A\pi\left((r_o^B+R_{pz})^2-R_{pz}^2\right)$. While more rigorous approach can be used to obtain an accurate approximation for the above conditional CDF, we resort to a heuristic method to provide a simpler approximate expression for $F_{R_o^A}(r_o^A|r_o^B, E_1(r_o^B))$. First, we ignore the presence of the exclusion zone around the tagged BS. However, note that when $r_o^B < R_{pz}$, there will not be any OpA BSs in $\mathcal{B}_{R_{pz}-r_o^B}(\mathbf{u}_o^B)$. We take this into account to obtain the approximate expression. An illustration of the above scenario is presented in Fig. 8.5a, where the dotted red circle represents $\mathcal{B}_{R_{pz}-r_o^B}(\mathbf{u}_o^B)$. Second, for relatively larger values of $r_o^B(> R_{pz}/2)$, the number of OpA BSs in $\mathcal{B}_{r_o^B}(\mathbf{u}_o^B)$ is likely to be non-zero. Hence, we approximate that there is at least one OpA BS in $\mathcal{B}_{r_o^B}(\mathbf{u}_o^B) \setminus \mathcal{B}_{\max(R_{pz}-r_o^B,0)}(\mathbf{x}_o^B)$. Now, depending on the relative distances of r_o^B and R_{pz}, we get the expression presented in (8.33). The expression for $F_{R_o^A}(r_o^A|r_o^B, E_2(r_o^B))$ is the same the one given in (D.7).

Now our objective is to obtain approximate expressions for T_2 and T_4 in (D.6). The complementary CDF of R_o^B can be expressed as

$$\begin{aligned}
&\mathbb{P}\left[N_{\Phi_B}(\mathcal{B}_{r_o^B}(\mathbf{u}_o^B))=0|r_o^B\right]\\
=&\sum_{n=0}^{\infty}\mathbb{P}\left[N_{\Phi_B}(\mathcal{B}_{r_o^B}(\mathbf{u}_o^B))=0|N_{\Psi_B}(\mathcal{B}_{r_o^B}(\mathbf{u}_o^B))=n, r_o^B\right]\mathrm{Poi}(n)\\
=&\exp(-\pi\lambda_B(r_o^B)^2)+\sum_{n=1}^{\infty}\mathbb{P}\left[N_{\Phi_B}(\mathcal{B}_{r_o^B}(\mathbf{u}_o^B))=0|N_{\Psi_B}(\mathcal{B}_{r_o^B}(\mathbf{u}_o^B))=n, r_o^B\right]\mathrm{Poi}(n),
\end{aligned}\tag{D.10}$$

where

$$\mathrm{Poi}(n)=\exp(-\pi\lambda_B(r_o^B)^2)\frac{(\pi\lambda_B(r_o^B)^2)^n}{n!}.\tag{D.11}$$

In (D.9), presented in Appendix D.3, if we use the approximate CDF of R_o^B given in (8.5), then T_4 can be negative with non-zero probability. This is justified by the fact that the approximate expression cannot be decomposed into the total probability expression presented in (D.10). In order to avoid this situation, we approximate the complementary CDF of R_o^B as

$$\begin{aligned}
1-F_{R_o^B}(r_o^B)=&\mathbb{P}\left[N_{\Phi_B}(\mathcal{B}_{r_o^B}(\mathbf{u}_o^B))=0|r_o^B\right]\\
\approx&\exp(-\pi\lambda_B(r_o^B)^2)+\sum_{n=1}^{\infty}\left(1-\exp(-\pi\lambda_A R_{pz}^2)\right)^n\mathrm{Poi}(n)\\
=&\exp(-\pi\lambda_B\exp(-\pi\lambda_A R_{pz}^2)(r_o^B)^2).
\end{aligned}\tag{D.12}$$

where the second step follows from the fact that there exists at least one PAL BS within R_{pz} of each of the n points so that all the n points have been deleted. Since the relative overlaps among protection zones are ignored, the above expression is an approximation. The third step follows after some algebraic manipulation. Now, the complementary CDF of R_o^B in the Lemma can be approximated by the expression presented in (D.12).

D.5 Proof of Lemma 8.8

Note that if we take into account only Event-2, then we are underestimating the density of OpA BSs in the vicinity of the tagged OpB BS. Therefore, the actual distance is stochastically dominated (first order) by the distance obtained considering only Event-2. Using this fact, we derive the lower bound on the CDF that is presented next. From (8.22), using the law of total probability we write

$$\begin{aligned}
F_{R_{o,AB}}(r_{o,AB}|r_o^B) =& \mathbb{P}\left[R_{o,AB} \le r_{o,AB}|r_o^B, N_{\Phi_B}(\mathcal{B}_{r_o^B}(\mathbf{u}_o^B)) = 0\right] \\
=& \mathbb{P}\left[R_{o,AB} \le r_{o,AB}|r_o^B, E_1(r_o^B)\right] \mathbb{P}\left[N_{\Psi_B}(\mathcal{B}_{r_o^B}(\mathbf{u}_o^B)) \neq 0|N_{\Phi_B}(\mathcal{B}_{r_o^B}(\mathbf{u}_o^B)) = 0, r_o^B\right] \\
&+ \mathbb{P}\left[R_{o,AB} \le r_{o,AB}|r_o^B, E_2(r_o^B)\right] \mathbb{P}\left[N_{\Psi_B}(\mathcal{B}_{r_o^B}(\mathbf{u}_o^B)) = 0|N_{\Phi_B}(\mathcal{B}_{r_o^B}(\mathbf{u}_o^B)) = 0, r_o^B\right] \\
\overset{(a)}{\ge}& \mathbb{P}\left[R_{o,AB} \le r_{o,AB}|r_o^B, E_2(r_o^B)\right] \\
&\Big(\mathbb{P}\left[N_{\Psi_B}(\mathcal{B}_{r_o^B}(\mathbf{u}_o^B)) \neq 0|N_{\Phi_B}(\mathcal{B}_{r_o^B}(\mathbf{u}_o^B)) = 0, r_o^B\right] \\
&+ \mathbb{P}\left[N_{\Psi_B}(\mathcal{B}_{r_o^B}(\mathbf{u}_o^B)) = 0|N_{\Phi_B}(\mathcal{B}_{r_o^B}(\mathbf{u}_o^B)) = 0, r_o^B\right]\Big) \\
\overset{(b)}{=}& \mathbb{P}\left[R_{o,AB} \le r_{o,AB}|r_o^B, E_2(r_o^B)\right],
\end{aligned}$$

where (a) follows since we are considering only Event-2 and

$$\mathbb{P}\left[R_{o,AB} \le r_{o,AB}|r_o^B, E_2(r_o^B)\right] \le \mathbb{P}\left[R_{o,AB} \le r_{o,AB}|r_o^B, E_1(r_o^B)\right]. \tag{D.13}$$

In order to evaluate the probability in (b), note that the OpA BS forms a homogeneous PPP of density λ_A beyond $\mathcal{B}_{\mathbf{x}_o^B}(R_{pz})$. Further, as discussed in Section 8.3.1, for Event-2, $R_{o,AB}$ is independent of R_o^B. Hence, using Lemma 4 in [142], we write

$$F_{R_{o,AB}}(r_{o,AB}|r_o^B) \ge 1 - \exp\left(-\pi\lambda_A((r_{o,AB})^2 - R_{pz}^2)\right),$$

and the final expression in the Lemma follows deconditioning w.r.t. R_o^B.

D.6 Proof of Lemma 8.10

In order to prove this Lemma, we first need to show that deconditioning w.r.t. $R_{o,AB}$ using a lower bound on its CDF preserves the lower bound on the conditional MAP presented in Lemma 8.2. To arrive at this conclusion, consider the expression in step (d) in (D.2) presented in Appendix D.1. The lower bound on the MAP of the tagged BS conditioned on $R_{o,AB}$, R_o^B, $t_{x_o^B}$ is given as

$$\mathbb{P}\left[\mathcal{I}_o^B|r_{o,AB}, r_o^B, t\right] \ge$$

$$\exp\Big(-t\big(2\pi\int_0^\infty \lambda_{\Psi_B}(y|r_o^B)e^{\frac{-\tau_{cs}l(y)}{P_B}}y\mathrm{d}y-2\int_{r_{o,AB}-R_{pz}}^{r_{o,AB}+R_{pz}}\lambda_{\Psi_B}(y|r_o^B)e^{\frac{-\tau_{cs}l(y)}{P_B}}\varphi_{pz}(y|r_{o,AB})y\mathrm{d}y\big)\Big)$$
$$=\exp\big(-tf_1(r_{o,AB},r_o^B)\big).$$

Since $f_1(r_{o,AB},r_o^B)$ is an increasing function w.r.t. $r_{o,AB}$, conditioned on R_o^B and $t_{x_o^B}$ we write

$$\int_{r_{o,AB}=0}^{\infty} e^{-tf_1(r_{o,AB},r_o^B)}\mathrm{d}F_{R_{o,AB}}(r_{o,AB}|r_o^B)\geq\int_{r_{o,AB}=0}^{\infty} e^{-tf_1(r_{o,AB},r_o^B)}\mathrm{d}F^{\mathtt{LB,x}}_{R_{o,AB}}(r_{o,AB}|r_o^B),\qquad\text{(D.14)}$$

where $F^{\mathtt{LB,x}}_{R_{o,AB}}(r_{o,AB}|r_o^B)$ denotes the lower bounds on the CDF of $R_{o,AB}$ presented in Lemmas 8.6 and 8.8. Now, de-conditioning the above expressions w.r.t. $t_{x_o^B}$ and R_o^B, we get

$$\mathbb{P}\left[\mathcal{I}_o^B|r_{o,AB},r_o^B,t\right]\geq\int_{r_o^B=0}^{\infty}\int_{t=0}^{1}\int_{r_{o,AB}=0}^{\infty} e^{-tf_1(r_{o,AB},r_o^B)}\times\mathrm{d}F^{\mathtt{LB,x}}_{R_{o,AB}}(r_{o,AB}|r_o^B)f_{R_o^B}(r_o^B)\mathrm{d}t\mathrm{d}r_o^B.$$

Changing the order of integration between $r_{o,AB}$ and t, and deconditioning w.r.t. $t_{x_o^B}$ we arrive at the result presented in the Lemma.

D.7 Proof of Lemma 8.14

Since the density functions in Lemmas 8.11 and 8.12 are conditioned on the distances to the nearest OpA BS and the tagged OpB BS, the correlation in node locations is effectively captured by these conditional densities in the vicinity of the typical user. Hence, conditioned on R_o^A and R_o^B, we assume that these interference powers are independent of each other.

Now, the conditional LT of the aggregate interference can be expressed as the product of the conditional LTs of interference from OpA and OpB BSs. Following the similar approach as presented in [43], the LT of interference from the interfering OpB BSs conditioned on R_o^A,

R_o^B, and $\mathcal{I}_o^B = 1$ is given as $\mathcal{L}_{I_{agg}^{BB}}(s|r_o^A, r_o^B, \mathcal{I}_o^B = 1) =$

$$\begin{aligned}
&\mathbb{E}\left[e^{-s\sum_{\mathbf{x}_j\in\Phi_B\setminus\mathbf{x}_o^B}\frac{P_B\mathcal{I}_j^B h(\mathbf{u}_o^B,\mathbf{x}_j)}{l(\|\mathbf{x}_j\|)}}\middle| r_o^A, r_o^B, \mathcal{I}_o^B = 1\right]\\
=&\mathbb{E}\left[\prod_{\mathbf{x}_j\in\Phi_B\setminus\mathbf{x}_o^B}\mathbb{E}\left[e^{\frac{-s\mathcal{I}_j^B P_B h(\mathbf{u}_o^B,\mathbf{x}_j)}{l(\|\mathbf{x}_j\|)}}\right]\middle| r_o^A, r_o^B, \mathcal{I}_o^B = 1\right]\\
\overset{(a)}{=}&\mathbb{E}\left[\prod_{\mathbf{x}_j\in\Phi_B\setminus\mathbf{x}_o^B}\frac{1}{1+\frac{s\mathcal{I}_j^B P_B}{l(\|\mathbf{x}_j\|)}}\middle| r_o^A, r_o^B, \mathcal{I}_o^B = 1\right]\\
\overset{(b)}{=}&\exp\left(-\int_{x=r_o^B}^{\infty}\int_{\theta=0}^{2\pi}\frac{\tilde{\lambda}_{\Psi_B}(x|r_o^A, r_o^B))M(\mathbf{x}(x,\theta)|r_o^B)}{l(x)(sP_B)^{-1}+1}\mathrm{d}\theta x\mathrm{d}x\right),
\end{aligned} \tag{D.15}$$

where (a) follows from the moment generating function (MGF) of the exponential fading term $h(\mathbf{u}_o^B, \mathbf{x}_j)$, (b) follows from the application of the PGFL of PPP and the retention probability of a point in Φ_B derived in Lemma 8.13. Similarly, the conditional LT of interference from the OpA BSs is $\mathcal{L}_{I_{agg}^{BA}}(s|r_o^A, r_o^B) =$

$$\begin{aligned}
&\mathbb{E}\left[e^{\left(-s\frac{P_A h(\mathbf{u}_o^B,\mathbf{x}_o^A)}{l(\|\mathbf{x}_o^A\|)}-\sum_{\mathbf{y}_j\in\Psi_A\setminus\mathbf{x}_o^A}\frac{sP_A h(\mathbf{u}_o^B,\mathbf{y}_j)}{l(\|\mathbf{y}_j\|)}\right)}\right]\\
=&\mathbb{E}_h\left[e^{\frac{-sP_A h(\mathbf{u}_o^B,\mathbf{x}_o^A)}{l(r_o^A)}}\right]\mathbb{E}_{\Psi_A}\left[\prod_{\mathbf{y}_j\in\Psi_A\setminus\mathbf{x}_o^A}\mathbb{E}_h\left[e^{\left(-\frac{sP_A h(\mathbf{u}_o^B,\mathbf{y}_j)}{l(\|\mathbf{y}_j\|)}\right)}\right]\right]\\
=&\frac{1}{1+\frac{sP_A}{l(r_o^A)}}\exp\left(-2\pi\int_{y=r_o^A}^{\infty}\frac{\mathcal{E}(y,\lambda_A,R_{pz},r_o^B)}{l(y)(sP_A)^{-1}+1}y\mathrm{d}y\right),
\end{aligned}$$

where the last step follows from the application of the PGFL of PPP, and the conditional density of Ψ_A is presented in (8.40).

D.8 Proof of Lemma 8.17

As illustrated in Fig. 8.10a, consider an OpB BS located at $\mathbf{y}_o^B$ and let $y = \|\mathbf{y}_o^B\|$. Note that Fig. 8.10a presents a representative diagram for Φ_B that has been approximated as a non-homogeneous PPP using Lemma 8.16. Hence, we have already captured the effect of all the PZs in the network. If we do not take into account the contention process among the

BSs in Φ_B, then the CDF of the distance between the typical user and the nearest interfering BS conditioned on R_o^A is given as

$$\begin{aligned} F_{D_o^B}(d_o^B|r_o^A) &= 1 - \mathbb{P}\left[N_{\Phi_B}(\mathcal{B}_{d_o^B}(\mathbf{u}_o^A)|r_o^A) = 0\right] \\ &= 1 - \exp\left(-2\pi\int_{y=0}^{d_o^B}\tilde{\lambda}_{\Psi_B}(y|r_o^A)y\mathrm{d}y\right), \end{aligned} \tag{D.16}$$

which follows from the nearest neighbor distribution of a non-homogeneous PPP. One way of interpreting this result is that all the BSs in Φ_B have a retention probability 1. On the other hand, if contention process is considered among the BSs in Φ_B, then all the BSs are not going to be active (retained), which depends on the MAP of a BS in Φ_B. Hence, the nearest BS in Φ_B may not be the first active interfering BS. In order to obtain the distance distribution to the nearest active BS, we follow the similar assumption as presented in [144, Section IV]. As per the assumption, the contention domain of a BS located at a distance y from the origin (in our case the typical OpA user) lies beyond $\mathcal{B}_y(\mathbf{u}_o^A)$. Hence, the medium access indicator for the BS at $\mathbf{y}_o^B$ is given as $\mathcal{I}_{\mathbf{y}_o}^B =$

$$\prod_{\mathbf{x}_j^B\in\Phi_B\setminus\mathcal{B}_y(\mathbf{u}_o^A)}\left(\mathbf{1}_{P_r(\mathbf{y}_o^B,\mathbf{x}_j^B)\le\tau_{cs}} + \mathbf{1}_{P_r(\mathbf{y}_o^B,\mathbf{x}_j^B)>\tau_{cs}}\mathbf{1}_{t_{x_j}^B>t_{y_o}^B}\right). \tag{D.17}$$

Now using the similar steps as presented in Appendix D.1, the MAP of a BS at a distance y from the origin is given as

$$\eta(y|r_o^A) = \mathbb{E}\left[\mathcal{I}_{\mathbf{y}_o}^B = 1\right] = \frac{1-\exp(-f_5(y,r_o^A))}{f_5(y,r_o^A)}, \tag{D.18}$$

where $f_5(y,r_o^A)$ is presented in (8.62). Above MAP can be interpreted as the retention probability of the point at $\mathbf{y}_o^B \in \Phi_B$ as an active interferer. Using the above retention probability, we assume that the active BSs in Φ_B form a non-homogeneous PPP of density $\tilde{\lambda}_{\Psi_B}(y|r_o^A)\eta(y|r_o^A)$. Hence, the CDF of distance to the nearest active OpB interfering BS conditioned on r_o^A is given as

$$F_{D_o^B}(d_o^B|r_o^A) = 1 - \exp\left(-2\pi\int_{y=0}^{d_o^B}\tilde{\lambda}_{\Psi_B}(y|r_o^A)\eta(y|r_o^A)y\mathrm{d}y\right). \tag{D.19}$$

The conditional PDF in the Lemma is obtained by taking the derivative of the above CDF w.r.t. d_o^B.

Bibliography

[1] J. Zhang, E. Björnson, M. Matthaiou, D. W. K. Ng, H. Yang, and D. J. Love, "Prospective multiple antenna technologies for beyond 5g," *IEEE Journal on Sel. Areas in Commun.*, 2020.

[2] T. L. Marzetta, "Noncooperative cellular wireless with unlimited numbers of base station antennas," *IEEE Trans. on Wireless Commun.*, vol. 9, no. 11, pp. 3590–3600, Nov. 2010.

[3] E. Bjornson, E. G. Larsson, and T. L. Marzetta, "Massive MIMO: ten myths and one critical question," *IEEE Commun. Magazine*, vol. 54, no. 2, pp. 114–123, February 2016.

[4] E. Bjornson, J. Hoydis, and L. Sanguinetti, "Massive MIMO has unlimited capacity," *IEEE Trans. on Wireless Commun.*, vol. 17, no. 1, pp. 574–590, Jan 2018.

[5] H. Q. Ngo, A. Ashikhmin, H. Yang, E. G. Larsson, and T. L. Marzetta, "Cell-free massive MIMO versus small cells," *IEEE Trans. on Wireless Commun.*, vol. 16, no. 3, pp. 1834–1850, March 2017.

[6] E. Nayebi, A. Ashikhmin, T. L. Marzetta, H. Yang, and B. D. Rao, "Precoding and power optimization in cell-free massive MIMO systems," *IEEE Trans. on Wireless Commun.*, vol. 16, no. 7, pp. 4445–4459, July 2017.

[7] J. Andrews, F. Baccelli, and R. Ganti, "A tractable approach to coverage and rate in cellular networks," *IEEE Trans. on Commun.*, vol. 59, no. 11, pp. 3122–3134, Nov. 2011.

[8] H. S. Dhillon, R. K. Ganti, F. Baccelli, and J. G. Andrews, "Modeling and analysis of K-tier downlink heterogeneous cellular networks," *IEEE Journal on Sel. Areas in Commun.*, vol. 30, no. 3, pp. 550 – 560, Apr. 2012.

[9] H. ElSawy, E. Hossain, and M. Haenggi, "Stochastic geometry for modeling, analysis, and design of multi-tier and cognitive cellular wireless networks: A survey," *IEEE Commun. Surveys and Tutorials*, vol. 15, no. 3, pp. 996–1019, Third Quarter 2013.

[10] M. Haenggi, *Stochastic Geometry for Wireless Networks.* Cambridge University Press, 2013.

[11] S. Mukherjee, *Analytical Modeling of Heterogeneous Cellular Networks: Geometry, Coverage, and Capacity*, Cambridge, Jan. 2014.

[12] J. G. Andrews, A. K. Gupta, and H. S. Dhillon, "A primer on cellular network analysis using stochastic geometry," 2016. [Online]. Available: http://arxiv.org/abs/1604.03183

[13] H. ElSawy, A. Sultan-Salem, M. S. Alouini, and M. Z. Win, "Modeling and analysis of cellular networks using stochastic geometry: A tutorial," *IEEE Commun. Surveys and Tutorials*, vol. 19, no. 1, pp. 167–203, First Quarter 2017.

[14] F. Fernandes, A. Ashikhmin, and T. L. Marzetta, "Inter-cell interference in noncooperative TDD large scale antenna systems," *IEEE Journal on Sel. Areas in Commun.*, vol. 31, no. 2, pp. 192–201, February 2013.

[15] H. Yin, D. Gesbert, M. Filippou, and Y. Liu, "A coordinated approach to channel estimation in large-scale multiple-antenna systems," *IEEE Journal on Sel. Areas in Commun.*, vol. 31, no. 2, pp. 264–273, February 2013.

[16] J. Jose, A. Ashikhmin, T. L. Marzetta, and S. Vishwanath, "Pilot contamination and precoding in multi-cell TDD systems," *IEEE Trans. on Wireless Commun.*, vol. 10, no. 8, pp. 2640–2651, August 2011.

[17] J. H. Sorensen and E. de Carvalho, "Pilot decontamination through pilot sequence hopping in massive MIMO systems," in *Proc., IEEE Globecom*, Dec 2014, pp. 3285–3290.

[18] A. S. Alwakeel and A. H. Mehana, "Achievable rates in uplink massive MIMO systems with pilot hopping," *IEEE Trans. on Commun.*, vol. PP, no. 99, pp. 1–1, 2017.

[19] I. Atzeni, J. Arnau, and M. Debbah, "Fractional pilot reuse in massive MIMO systems," in *Proc., IEEE Intl. Conf. on Commun. Workshops (ICC Workshops)*, June 2015, pp. 1030–1035.

[20] O. Y. Bursalioglu, G. Caire, R. K. Mungara, H. C. Papadopoulos, and C. Wang, "Fog massive MIMO: A user-centric seamless hot-spot architecture," *IEEE Trans. on Wireless Commun.*, vol. 18, no. 1, pp. 559–574, 2019.

[21] J. Zhang, X. Yuan, and Y. J. Zhang, "Locally orthogonal training design for cloud-rans based on graph coloring," *IEEE Trans. on Wireless Commun.*, vol. 16, no. 10, pp. 6426–6437, Oct 2017.

[22] W. Hmida, V. Meghdadi, A. Bouallegue, and J. P. Cances, "Graph coloring based pilot reuse among interfering users in cell-free massive MIMO," in *Proc., IEEE Intl. Conf. on Commun. (ICC)*, May 2020.

[23] M. Attarifar, A. Abbasfar, and A. Lozano, "Random vs structured pilot assignment in cell-free massive MIMO wireless networks," in *Proc., IEEE Intl. Conf. on Commun. Workshops (ICC Workshops)*, May 2018, pp. 1–6.

[24] H. Liu, J. Zhang, X. Zhang, A. Kurniawan, T. Juhana, and B. Ai, "Tabu-search-based pilot assignment for cell-free massive MIMO systems," *IEEE Trans. on Veh. Technology*, vol. 69, no. 2, pp. 2286–2290, 2020.

[25] M. Bartelt and V. Privman, "Kinetics of irreversible multilayer adsorption: One-dimensional models," *The Journal of chemical physics*, vol. 93, no. 9, pp. 6820–6823, 1990.

[26] ——, "Kinetics of irreversible monolayer and multilayer adsorption," *Intl. Journal of Modern Physics B*, vol. 5, no. 18, pp. 2883–2907, 1991.

[27] P. Krapivsky, "Kinetics of multilayer deposition: Models without screening," *The Journal of chemical physics*, vol. 97, no. 3, pp. 2134–2138, 1992.

[28] P. Van Tassel and P. Viot, "An exactly solvable continuum model of multilayer irreversible adsorption," *EPL (Europhysics Letters)*, vol. 40, no. 3, p. 293, 1997.

[29] S. Yang, P. Viot, and P. R. Van Tassel, "Generalized model of irreversible multilayer deposition," *Physical Review E*, vol. 58, no. 3, p. 3324, 1998.

[30] A. Burr, M. Bashar, and D. Maryopi, "Cooperative access networks: Optimum fronthaul quantization in distributed massive MIMO and cloud ran - invited paper," in *Proc., IEEE Veh. Technology Conf. (VTC)*, 2018, pp. 1–5.

[31] M. Bashar, K. Cumanan, A. G. Burr, H. Q. Ngo, and M. Debbah, "Cell-free massive MIMO with limited backhaul," in *Proc., IEEE Intl. Conf. on Commun. (ICC)*, 2018, pp. 1–7.

[32] M. Bashar, K. Cumanan, A. G. Burr, H. Q. Ngo, E. G. Larsson, and P. Xiao, "Energy efficiency of the cell-free massive MIMO uplink with optimal uniform quantization," *IEEE Trans. on Green Commun. and Networking*, vol. 3, no. 4, pp. 971–987, 2019.

[33] G. Femenias and F. Riera-Palou, "Cell-free millimeter-wave massive MIMO systems with limited fronthaul capacity," *IEEE Access*, vol. 7, pp. 44 596–44 612, 2019.

[34] M. Bashar, K. Cumanan, A. G. Burr, H. Q. Ngo, M. Debbah, and P. Xiao, "Max–min rate of cell-free massive MIMO uplink with optimal uniform quantization," *IEEE Trans. on Commun.*, vol. 67, no. 10, pp. 6796–6815, 2019.

[35] H. Masoumi and M. J. Emadi, "Performance analysis of cell-free massive MIMO system with limited fronthaul capacity and hardware impairments," *IEEE Trans. on Wireless Commun.*, vol. 19, no. 2, pp. 1038–1053, 2020.

[36] G. Femenias and F. Riera-Palou, "Fronthaul-constrained cell-free massive MIMO with low resolution adcs," *IEEE Access*, vol. 8, pp. 116 195–116 215, 2020.

[37] M. Bashar, H. Q. Ngo, K. Cumanan, A. G. Burr, P. Xiao, E. Björnson, and E. G. Larsson, "Uplink spectral and energy efficiency of cell-free massive MIMO with optimal uniform quantization," *IEEE Trans. on Commun.*, vol. 69, no. 1, pp. 223–245, 2020.

[38] S. Buzzi and C. D'Andrea, "Cell-free massive MIMO: User-centric approach," *IEEE Wireless Commun. Letters*, vol. PP, no. 99, pp. 1–1, 2017.

[39] H. Q. Ngo, L.-N. Tran, T. Q. Duong, M. Matthaiou, and E. G. Larsson, "On the total energy efficiency of cell-free massive mimo," *IEEE Trans. on Green Commun. and Networking*, vol. 2, no. 1, pp. 25–39, 2018.

[40] G. Interdonato, E. Björnson, H. Q. Ngo, P. Frenger, and E. G. Larsson, "Ubiquitous cell-free massive MIMO communications," *EURASIP Journal on Wireless Commun. and Networking*, vol. 2019, no. 1, pp. 1–13, 2019.

[41] E. Björnson and L. Sanguinetti, "Scalable cell-free massive MIMO systems," *IEEE Trans. on Commun.*, vol. 68, no. 7, pp. 4247–4261, 2020.

[42] S. Buzzi, C. D'Andrea, A. Zappone, and C. D'Elia, "User-centric 5g cellular networks: Resource allocation and comparison with the cell-free massive MIMO approach," *IEEE Trans. on Wireless Commun.*, vol. 19, no. 2, pp. 1250–1264, 2020.

[43] H. Q. Nguyen, F. Baccelli, and D. Kofman, "A stochastic geometry analysis of dense IEEE 802.11 networks," in *Proc., IEEE Int. Conf. on Comput. Commun.*, May 2007, pp. 1199–1207.

[44] T. V. Nguyen and F. Baccelli, "A probabilistic model of carrier sensing based cognitive radio," in *Proc., IEEE Symp. on New Frontiers in Dynamic Spectrum*, Apr. 2010, pp. 1–12.

[45] N. T. Viet and F. Baccelli, "Stochastic modeling of carrier sensing based cognitive radio networks," in *Proc., Modeling and Optimization in Mobile, Ad Hoc and Wireless Networks*, May 2010, pp. 472–480.

[46] G. Alfano, M. Garetto, and E. Leonardi, "New directions into the stochastic geometry analysis of dense CSMA networks," *IEEE Trans. Mobile Computing*, vol. 13, no. 2, pp. 324–336, Feb. 2014.

[47] O. Elijah, C. Y. Leow, T. A. Rahman, S. Nunoo, and S. Z. Iliya, "A comprehensive survey of pilot contamination in massive MIMO - 5G system," *IEEE Commun. Surveys and Tutorials*, vol. 18, no. 2, pp. 905–923, Secondquarter 2016.

[48] Y. Li, Y.-H. Nam, B. L. Ng, and J. Zhang, "A non-asymptotic throughput for massive MIMO cellular uplink with pilot reuse," in *Proc., IEEE Globecom*, Dec 2012, pp. 4500–4504.

[49] E. Bjornson, E. G. Larsson, and M. Debbah, "Massive MIMO for maximal spectral efficiency: How many users and pilots should be allocated?" *IEEE Trans. on Wireless Commun.*, vol. 15, no. 2, pp. 1293–1308, Feb 2016.

[50] H. ElSawy, A. Sultan-Salem, M. S. Alouini, and M. Z. Win, "Modeling and analysis of cellular networks using stochastic geometry: A tutorial," *IEEE Commun. Surveys and Tutorials*, vol. 19, no. 1, pp. 167–203, Firstquarter 2017.

[51] P. Madhusudhanan, X. Li, Y. Liu, and T. X. Brown, "Stochastic geometric modeling and interference analysis for massive MIMO systems," in *Proc., Modeling and Optimization in Mobile, Ad Hoc and Wireless Networks*, May 2013, pp. 15–22.

[52] S. Govindasamy, "Uplink performance of large optimum-combining antenna arrays in Poisson-cell networks," in *Proc., IEEE Intl. Conf. on Commun. (ICC)*, Jun. 2014, pp. 2158–2164.

[53] T. Bai and R. W. Heath, "Asymptotic coverage and rate in massive MIMO networks," in *IEEE Global Conf. on Signal and Inform. Processing*, Dec 2014, pp. 602–606.

[54] ——, "Asymptotic SINR for millimeter wave massive MIMO cellular networks," in *Proc., IEEE SPAWC*, June 2015, pp. 620–624.

[55] S. Govindasamy, "Uplink performance of large optimum-combining antenna arrays in power-controlled cellular networks," in *Proc., IEEE Intl. Conf. on Commun. (ICC)*, Jun. 2015, pp. 4137–4143.

[56] T. Bai and R. W. Heath, "Analyzing uplink SINR and rate in massive MIMO systems using stochastic geometry," *IEEE Trans. on Commun.*, vol. 64, no. 11, pp. 4592–4606, Nov 2016.

[57] E. Bjornson, L. Sanguinetti, and M. Kountouris, "Deploying dense networks for maximal energy efficiency: Small cells meet massive MIMO," *IEEE Journal on Sel. Areas in Commun.*, vol. 34, no. 4, pp. 832–847, Apr 2016.

[58] N. Liang, W. Zhang, and C. Shen, "An uplink interference analysis for massive mimo systems with MRC and ZF receivers," in *Proc., IEEE Wireless Commun. and Networking Conf. (WCNC)*, Mar. 2015, pp. 310–315.

[59] A. Shojaeifard, K. Wong, M. D. Renzo, G. Zheng, K. A. Hamdi, and J. Tang, "Massive MIMO-enabled full-duplex cellular networks," *IEEE Trans. on Commun.*, vol. 65, no. 11, pp. 4734–4750, Nov 2017.

[60] O. Y. Bursalioglu, G. Caire, R. K. Mungara, H. C. Papadopoulos, and C. Wang, "Fog massive MIMO: A user-centric seamless hot-spot architecture," *IEEE Trans. on Wireless Commun.*, vol. 18, no. 1, pp. 559–574, 2019.

[61] M. Haenggi, “User point processes in cellular networks,” *IEEE Wireless Commun. Letters*, vol. 6, no. 2, pp. 258–261, April 2017.

[62] J. Moller, “Random Johnson-Mehl Tessellations,” *Advances in Applied Probability*, vol. 24, no. 4, pp. 814–844, 1992.

[63] B. Yu, S. Mukherjee, H. Ishii, and L. Yang, “Dynamic TDD support in the LTE-B enhanced local area architecture,” in *Proc., IEEE Globecom Workshops*, Dec 2012, pp. 585–591.

[64] H. Q. Ngo, E. Larsson, and T. Marzetta, “Energy and spectral efficiency of very large multiuser MIMO systems,” *IEEE Trans. on Commun.*, vol. 61, no. 4, pp. 1436–1449, Apr. 2013.

[65] E. Pineda and D. Crespo, “Temporal evolution of the domain structure in a Poisson-Voronoi transformation,” *Journal of Statistical Mechanics: Theory and Experiment*, vol. 2007, no. 06, p. P06007, 2007.

[66] S. M. Yu and S. Kim, “Downlink capacity and base station density in cellular networks,” in *Proc., Modeling and Optimization in Mobile, Ad Hoc and Wireless Networks*, May 2013, pp. 119–124.

[67] S. Singh, H. S. Dhillon, and J. G. Andrews, “Offloading in heterogeneous networks: Modeling, analysis, and design insights,” *IEEE Trans. on Wireless Commun.*, vol. 12, no. 5, pp. 2484–2497, May 2013.

[68] P. Calka, “The distributions of the smallest disks containing the Poisson-Voronoi typical cell and the Crofton cell in the plane,” *Advances in Applied Probability*, vol. 34, no. 4, pp. 702–717, 2002.

[69] J. Gil-Pelaez, “Note on the inversion theorem,” *Biometrika*, vol. 38, no. 3-4, pp. 481–482, 1951.

[70] M. D. Renzo and P. Guan, “Stochastic geometry modeling of coverage and rate of cellular networks using the Gil-Pelaez inversion theorem,” *IEEE Commun. Lett.*, vol. 18, no. 9, pp. 1575–1578, Sep. 2014.

[71] J. Schloemann, H. S. Dhillon, and R. M. Buehrer, “Toward a tractable analysis of localization fundamentals in cellular networks,” *IEEE Trans. on Wireless Commun.*, vol. 15, no. 3, pp. 1768–1782, Mar. 2016.

[72] K. A. Hamdi, “A useful lemma for capacity analysis of fading interference channels,” *IEEE Trans. on Commun.*, vol. 58, no. 2, 2010.

[73] M. D. Renzo, A. Guidotti, and G. E. Corazza, “Average rate of downlink heterogeneous cellular networks over generalized fading channels: A stochastic geometry approach,” *IEEE Trans. on Commun.*, vol. 61, no. 7, pp. 3050–3071, July 2013.

[74] Z. Yazdanshenasan, H. S. Dhillon, M. Afshang, and P. H. J. Chong, “Poisson hole process: Theory and applications to wireless networks,” *IEEE Trans. on Wireless Commun.*, vol. 15, no. 11, pp. 7531–7546, Nov 2016.

[75] T. D. Novlan, H. S. Dhillon, and J. G. Andrews, “Analytical modeling of uplink cellular networks,” *IEEE Trans. on Wireless Commun.*, vol. 12, no. 6, pp. 2669–2679, Jun. 2013.

[76] H. ElSawy and E. Hossain, “On stochastic geometry modeling of cellular uplink transmission with truncated channel inversion power control,” *IEEE Trans. on Wireless Commun.*, vol. 13, no. 8, pp. 4454–4469, Aug 2014.

[77] S. Singh, X. Zhang, and J. G. Andrews, “Joint rate and SINR coverage analysis for decoupled uplink-downlink biased cell associations in HetNets,” *IEEE Trans. on Wireless Commun.*, vol. 14, no. 10, pp. 5360–5373, Oct 2015.

[78] W. U. Mondal and G. Das, “Uplink user process in Poisson cellular network,” *IEEE Commun. Letters*, vol. 21, no. 9, pp. 2013–2016, Sept 2017.

[79] M. Afshang and H. S. Dhillon, “Poisson cluster process based analysis of hetnets with correlated user and base station locations,” *IEEE Trans. on Wireless Commun.*, vol. 17, no. 4, pp. 2417–2431, 2018.

[80] H. Tabassum, E. Hossain, and J. Hossain, “Modeling and analysis of uplink non-orthogonal multiple access in large-scale cellular networks using Poisson cluster processes,” *IEEE Trans. on Commun.*, vol. 65, no. 8, pp. 3555–3570, Aug 2017.

[81] H. ElSawy and E. Hossain, “On stochastic geometry modeling of cellular uplink transmission with truncated channel inversion power control,” *IEEE Trans. on Wireless Commun.*, vol. 13, no. 8, pp. 4454–4469, Aug 2014.

[82] B. Blaszczyszyn, M. Karray, and H. Keeler, “Using Poisson processes to model lattice cellular networks,” in *Proc., IEEE INFOCOM*, Apr. 2013, pp. 773–781.

[83] H. S. Dhillon and J. G. Andrews, “Downlink rate distribution in heterogeneous cellular networks under generalized cell selection,” *IEEE Wireless Commun. Lett.*, vol. 3, no. 1, pp. 42 – 45, Feb. 2014.

[84] P. Madhusudhanan, J. Restrepo, Y. Liu, T. Brown, and K. Baker, “Downlink performance analysis for a generalized shotgun cellular system,” *IEEE Trans. on Wireless Commun.*, vol. 13, no. 12, pp. 6684–6696, Dec 2014.

[85] F. Baccelli and B. Bllaszczyszyn, “Stochastic geometry and wireless networks: Volume I theory,” *Found. Trends Netw.*, vol. 3, no. 3-4, pp. 249–449, Mar. 2009.

[86] A. Rényi, "On a one-dimensional problem concerning random space filling," *Publications of the Mathematical Institute of the Hungarian Academy of Sciences*, vol. 3, pp. 109–127, 1958.

[87] J. Talbot, G. Tarjus, P. Van Tassel, and P. Viot, "From car parking to protein adsorption: an overview of sequential adsorption processes," *Colloids and Surfaces A: Physicochemical and Engineering Aspects*, vol. 165, no. 1-3, pp. 287–324, 2000.

[88] S. Fleurke and H. Dehling, "The sequential frequency assignment process," in *Proceedings of the 12th WSEAS International Conference on Applied Mathematics*, ser. MATH'07. Stevens Point, Wisconsin, USA: World Scientific and Engineering Academy and Society (WSEAS), 2007, p. 280–285.

[89] S. Fleurke and C. Külske, "A second-row parking paradox," *Journal of Statistical Physics*, vol. 136, no. 2, pp. 285–295, 2009.

[90] ——, "Multilayer parking with screening on a random tree," *Journal of Statistical Physics*, vol. 139, no. 3, pp. 417–431, 2010.

[91] S. R. Fleurke and A. C. D. van Enter, *Analytical Results for a Small Multiple-Layer Parking System.* Cham: Springer International Publishing, 2014, pp. 43–53.

[92] B. Bonnier, D. Boyer, and P. Viot, "Pair correlation function in random sequential adsorption processes," *Journal of Physics A: Mathematical and General*, vol. 27, no. 11, p. 3671, 1994.

[93] P. Schaaf and J. Talbot, "Surface exclusion effects in adsorption processes," *The Journal of chemical physics*, vol. 91, no. 7, pp. 4401–4409, 1989.

[94] ——, "Kinetics of random sequential adsorption," *Physical Review Letters*, vol. 62, pp. 175–178, Jan 1989.

[95] E. Björnson, J. Hoydis, and L. Sanguinetti, "Massive MIMO has unlimited capacity," *IEEE Trans. on Wireless Commun.*, vol. 17, no. 1, pp. 574–590, Jan 2018.

[96] O. Y. Bursalioglu, C. Wang, H. Papadopoulos, and G. Caire, "Rrh based massive MIMO with "on the fly" pilot contamination control," in *Proc., IEEE Intl. Conf. on Commun. (ICC)*, May 2016, pp. 1–7.

[97] R. Sabbagh, H. Zhu, and J. Wang, "Pilot allocation and sum-rate analysis in distributed massive MIMO systems," in *Proc., IEEE Veh. Technology Conf. (VTC)*, Sep. 2017, pp. 1–5.

[98] S. Buzzi, C. D'Andrea, M. Fresia, Y.-P. Zhang, and S. Feng, "Pilot assignment in cell-free massive MIMO based on the Hungarian algorithm," *IEEE Wireless Commun. Letters*, 2020.

[99] A. Busson and G. Chelius, “Capacity and interference modeling of CSMA/CA networks using SSI point processes,” *Telecommun. Syst.*, vol. 57, no. 1, pp. 25–39, Sep. 2014.

[100] J. Talbot, G. Tarjus, P. V. Tassel, and P. Viot, “From car parking to protein adsorption: an overview of sequential adsorption processes,” *Colloids and Surfaces A: Physicochemical and Engineering Aspects*, vol. 165, no. 1, pp. 287 – 324, 2000.

[101] U. Von Luxburg, “A tutorial on spectral clustering,” *Statistics and computing*, vol. 17, no. 4, pp. 395–416, 2007.

[102] S. Boyd and L. Vandenberghe, *Convex optimization.* Cambridge university press, 2004.

[103] A. Ng, M. Jordan, and Y. Weiss, “On spectral clustering: Analysis and an algorithm,” *Adv. Neural Inf. Process. Syst.*, vol. 14, pp. 849–856, 2001.

[104] I. S. Dhillon, “Co-clustering documents and words using bipartite spectral graph partitioning,” in *Proceedings of ACM SIGKDD Int. Con. on Knowledge discovery and Data mining*, 2001, pp. 269–274.

[105] C. Barnhart, E. L. Johnson, G. L. Nemhauser, M. W. Savelsbergh, and P. H. Vance, “Branch-and-price: Column generation for solving huge integer programs,” *Operations research*, vol. 46, no. 3, pp. 316–329, 1998.

[106] A. Mehrotra and M. A. Trick, “A column generation approach for graph coloring,” *Informs Journal on Computing*, vol. 8, no. 4, pp. 344–354, 1996.

[107] L. Fu, S. C. Liew, and J. Huang, “Fast algorithms for joint power control and scheduling in wireless networks,” *IEEE Trans. on Wireless Commun.*, vol. 9, no. 3, pp. 1186–1197, 2010.

[108] M. Johansson and L. Xiao, “Cross-layer optimization of wireless networks using nonlinear column generation,” *IEEE Trans. on Wireless Commun.*, vol. 5, no. 2, pp. 435–445, 2006.

[109] A. J. Hoffman, A. W. J. Kolen, and M. Sakarovitch, “Totally-balanced and greedy matrices,” in *Selected Papers Of Alan J Hoffman: With Commentary.* World Scientific, 2003, pp. 328–337.

[110] “Guidelines for evaluation of radio interface technologies for IMT-Advanced,” *Report ITU-R*, vol. M.2135-1, Dec 2009.

[111] O. Simeone, O. Somekh, H. V. Poor, and S. Shamai (Shitz), “Downlink multicell processing with limited-backhaul capacity,” *EURASIP Journal on Advances in Signal Processing*, vol. 2009, no. 1, p. 840814, Jun 2009.

[112] R. Zakhour and D. Gesbert, "Optimized data sharing in multicell MIMO with finite backhaul capacity," *IEEE Trans. on Signal Processing*, vol. 59, no. 12, pp. 6102–6111, Dec 2011.

[113] S. H. Park, O. Simeone, O. Sahin, and S. Shamai, "Joint precoding and multivariate backhaul compression for the downlink of cloud radio access networks," *IEEE Trans. on Signal Processing*, vol. 61, no. 22, pp. 5646–5658, Nov 2013.

[114] Q. Zhang, C. Yang, and A. F. Molisch, "Downlink base station cooperative transmission under limited-capacity backhaul," *IEEE Trans. on Wireless Commun.*, vol. 12, no. 8, pp. 3746–3759, August 2013.

[115] S. H. Park, O. Simeone, O. Sahin, and S. S. Shitz, "Fronthaul compression for cloud radio access networks: Signal processing advances inspired by network information theory," *IEEE Signal Processing Magazine*, vol. 31, no. 6, pp. 69–79, Nov 2014.

[116] T. Q. Quek, M. Peng, O. Simeone, and W. Yu, *Cloud radio access networks: Principles, technologies, and applications.* Cambridge University Press, 2017.

[117] F. Baccelli and A. Giovanidis, "A stochastic geometry framework for analyzing pairwise-cooperative cellular networks," *IEEE Trans. on Wireless Commun.*, vol. 14, no. 2, pp. 794–808, 2014.

[118] G. Nigam, P. Minero, and M. Haenggi, "Coordinated multipoint joint transmission in heterogeneous networks," *IEEE Trans. on Commun.*, vol. 62, no. 11, pp. 4134–4146, 2014.

[119] R. Tanbourgi, S. Singh, J. G. Andrews, and F. K. Jondral, "A tractable model for noncoherent joint-transmission base station cooperation," *IEEE Trans. on Wireless Commun.*, vol. 13, no. 9, pp. 4959–4973, 2014.

[120] N. Lee, D. Morales-Jimenez, A. Lozano, and R. W. Heath, "Spectral efficiency of dynamic coordinated beamforming: A stochastic geometry approach," *IEEE Transactions on Wireless Communications*, vol. 14, no. 1, pp. 230–241, 2014.

[121] S. Govindasamy and I. Bergel, "Uplink performance of multi-antenna cellular networks with co-operative base stations and user-centric clustering," *IEEE Trans. on Wireless Commun.*, vol. 17, no. 4, pp. 2703–2717, 2018.

[122] W. Bao and B. Liang, "Optimizing cluster size through handoff analysis in user-centric cooperative wireless networks," *IEEE Trans. on Wireless Commun.*, vol. 17, no. 2, pp. 766–778, 2018.

[123] A. Papazafeiropoulos, P. Kourtessis, M. D. Renzo, S. Chatzinotas, and J. M. Senior, "Performance analysis of cell-free massive MIMO systems: A stochastic geometry approach," *IEEE Trans. on Veh. Technology*, vol. 69, no. 4, pp. 3523–3537, 2020.

[124] S. Kusaladharma, W.-P. Zhu, W. Ajib, and G. A. A. Baduge, “Stochastic geometry based performance characterization of swipt in cell-free massive MIMO,” *IEEE Trans. on Veh. Technology*, vol. 69, no. 11, pp. 13 357–13 370, 2020.

[125] M. Afshang and H. S. Dhillon, “Fundamentals of modeling finite wireless networks using binomial point process,” *IEEE Trans. on Wireless Commun.*, vol. 16, no. 5, pp. 3355–3370, May 2017.

[126] J. Mecke, “On the relationship between the 0-cell and the typical cell of a stationary random tessellation,” *Pattern Recognition*, vol. 32, no. 9, pp. 1645–1648, 1999.

[127] P. D. Mankar, P. Parida, H. S. Dhillon, and M. Haenggi, “Distance from the nucleus to a uniformly random point in the 0-cell and the typical cell of the Poisson–Voronoi tessellation,” *J. Stat. Phys.*, vol. 181, no. 5, pp. 1678–1698, 2020.

[128] J.-S. Ferenc and Z. Néda, “On the size distribution of poisson voronoi cells,” *Physica A: Statistical Mechanics and its Applications*, vol. 385, no. 2, pp. 518–526, 2007.

[129] F. Baccelli, M. Klein, M. Lebourges, and S. Zuyev, “Stochastic geometry and architecture of communication networks,” *Telecommunication Systems*, vol. 7, no. 1, pp. 209–227, 1997.

[130] S. K. Iyer and D. Yogeshwaran, “Percolation and connectivity in ab random geometric graphs,” *Advances in Applied Probability*, vol. 44, no. 1, pp. 21–41, 2012.

[131] M. D. Penrose, “Continuum AB percolation and AB random geometric graphs,” *Journal of Applied Probability*, vol. 51, no. A, pp. 333–344, 2014.

[132] C. Stegehuis and L. Weedage, “Degree distributions in AB random geometric graphs,” *preprint arXiv:2104.03711*, 2021.

[133] FCC, “Report and order and second further notice of proposed rule making,” FCC, Tech. Rep. GN Docket No. 12-354, Apr. 2016.

[134] J. H. Reed, A. W. Clegg, A. V. Padaki, T. Yang, R. Nealy, C. Dietrich, C. R. Anderson, and D. M. Mearns, “On the co-existence of TD-LTE and radar over 3.5 GHz band: An experimental study,” *IEEE Wireless Commun. Letters*, vol. 5, no. 4, pp. 368–371, Aug. 2016.

[135] S. Bhattarai, A. Ullah, J. M. J. Park, J. H. Reed, D. Gurney, and B. Gao, “Defining incumbent protection zones on the fly: Dynamic boundaries for spectrum sharing,” in *Proc., IEEE Intl. Symp. on Dynamic Spectrum Access Networks (DySpan)*, Sep. 2015, pp. 251–262.

[136] C. W. Kim, J. Ryoo, and M. M. Buddhikot, “Design and implementation of an end-to-end architecture for 3.5 GHz shared spectrum,” in *Proc., IEEE Intl. Symp. on Dynamic Spectrum Access Networks (DySpan)*, Sep. 2015, pp. 23–34.

[137] Y. Li, F. Baccelli, J. G. Andrews, T. D. Novlan, and J. C. Zhang, "Modeling and analyzing the coexistence of Wi-Fi and LTE in unlicensed spectrum," *IEEE Trans. on Wireless Commun.*, vol. 15, no. 9, pp. 6310–6326, Sep. 2016.

[138] C. H. Lee and M. Haenggi, "Interference and outage in Poisson cognitive networks," *IEEE Trans. on Wireless Commun.*, vol. 11, no. 4, pp. 1392–1401, Apr. 2012.

[139] X. Song, C. Yin, D. Liu, and R. Zhang, "Spatial throughput characterization in cognitive radio networks with threshold-based opportunistic spectrum access," *IEEE Journal on Sel. Areas in Commun.*, vol. 32, no. 11, pp. 2190–2204, Nov. 2014.

[140] U. Tefek and T. J. Lim, "Interference management through exclusion zones in two-tier cognitive networks," *IEEE Trans. on Wireless Commun.*, vol. 15, no. 3, pp. 2292–2302, Mar. 2016.

[141] N. Deng, W. Zhou, and M. Haenggi, "Heterogeneous cellular network models with dependence," *IEEE Journal on Sel. Areas in Commun.*, vol. 33, no. 10, pp. 2167–2181, Oct. 2015.

[142] Z. Yazdanshenasan, H. S. Dhillon, M. Afshang, and P. H. J. Chong, "Poisson hole process: Theory and applications to wireless networks," *IEEE Trans. on Wireless Commun.*, vol. 15, no. 11, pp. 7531–7546, Nov. 2016.

[143] ITU-R, "Guidelines for evaluation of radio interface technologies for IMT-Advanced," ITU-R, Tech. Rep. M.2135, 2009.

[144] A. Al-Hourani, R. J. Evans, and S. Kandeepan, "Nearest neighbor distance distribution in hard-core point processes," *IEEE Commun. Letters*, vol. 20, no. 9, pp. 1872–1875, Sep. 2016.

[145] M. X. Gong, R. Stacey, D. Akhmetov, and S. Mao, "A directional CSMA/CA protocol for mmWave wireless pans," in *Proc., IEEE Wireless Commun. and Networking Conf. (WCNC)*, Apr. 2010, pp. 1–6.

[146] X. Zhu, Z. Wang, C. Qian, L. Dai, J. Chen, S. Chen, and L. Hanzo, "Soft pilot reuse and multicell block diagonalization precoding for massive MIMO systems," *IEEE Trans. on Veh. Technology*, vol. 65, no. 5, pp. 3285–3298, May 2016.

[147] S.-H. Park, O. Simeone, O. Sahin, and S. Shamai, "Multihop backhaul compression for the uplink of cloud radio access networks," in *Proc., IEEE Intl. Symposium on Information Theory*, 2014, pp. 2704–2708.

[148] G. Caire, "On the ergodic rate lower bounds with applications to massive MIMO," *IEEE Trans. on Wireless Commun.*, 2018.

[149] M. Medard, "The effect upon channel capacity in wireless communications of perfect and imperfect knowledge of the channel," *IEEE Trans. on Info. Theory*, vol. 46, no. 3, pp. 933–946, May 2000.

[150] M. P. Fewell, "Area of common overlap of three circles," Defence Science and Technology Organisation Edinburgh (Australia), Tech. Rep., 2006.